PERFORMANCE ANALYSIS OF VIRTUAL FULL-DUPLEX AND UNDERLAY D2D BASED WIRELESS SYSTEMS

Ph.D. Thesis

by

JUSTIN JOSE

DEPARTMENT OF ELECTRICAL ENGINEERING
INDIAN INSTITUTE OF TECHNOLOGY INDORE
MAY, 2024

PERFORMANCE ANALYSIS OF VIRTUAL FULL-DUPLEX AND UNDERLAY D2D BASED WIRELESS SYSTEMS

Ph.D. THESIS

Submitted in partial fulfillment of the

requirements for the award of the degree

of

DOCTOR OF PHILOSOPHY

by

Justin Jose

DEPARTMENT OF ELECTRICAL ENGINEERING

INDIAN INSTITUTE OF TECHNOLOGY INDORE

MAY, 2024

INDIAN INSTITUTE OF TECHNOLOGY INDORE

CANDIDATE'S DECLARATION

I hereby certify that the work which is being presented in the thesis entitled "**PERFORMANCE ANALYSIS OF VIRTUAL FULL-DUPLEX AND UNDERLAY D2D BASED WIRELESS SYSTEMS**" in the partial fulfillment of the requirements for the award of the degree of DOCTOR OF PHILOSOPHY and submitted in the DEPARTMENT OF ELECTRICAL ENGINEERING, Indian Institute of Technology Indore, is an authentic record of my own work carried out during the time period from July 2019 to May 2024 under the supervision of Prof. Vimal Bhatia, Professor, Indian Institute of Technology Indore, India.

The matter presented in this thesis has not been submitted for the award of any other degree of this or any other institute.

31-05-2024

Signature of the student with date

(JUSTIN JOSE)

This is to certify that the above statement made by the candidate is correct to the best of my knowledge.

31.05.2024

Signature of Thesis Supervisor with date

(Prof. VIMAL BHATIA)

Justin Jose has successfully given his Ph.D. Oral Examination held on September 10, 2024.

10.09.2024

Signature of Thesis Supervisor with date

(Prof. VIMAL BHATIA)

ACKNOWLEDGEMENTS

I would like to take this opportunity to express my gratitude to everyone who has kindly supported me from the beginning of my Ph.D. career. First and foremost, I thank my almighty God, **Lord Jesus Christ**, for giving me good health, mercy, and abundant grace, without which this thesis would have been impossible to accomplish.

At the very outset, I would like to express my sincere and heartfelt thanks to my Ph.D. supervisor, Prof. Vimal Bhatia, for his continuous support throughout my research. His guidance at every phase of my five-year research journey has shaped this thesis into its current form. I am grateful to him for motivating me to conduct research in cutting-edge technologies, allowing me the freedom to explore, develop my ideas, and work at my own pace. I would also like to thank my PSPC committee members, Prof. Shaibal Mukherjee and Prof. Apurba K. Das, for their support and perpetual encouragement.

In addition to my supervisor, I am also grateful to other co-authors in my research, including Dr. Parvez Shaik, Dr. Anirudh Agarwal, Shubham Bisen, and Prof. Keshav Singh. I would like to extend special gratitude to Dr. Anirudh Agarwal for guiding me in pursuing Ph.D. admission under Prof. Vimal Bhatia. I also thank Vinat Goyal, Amrita Srivastava, and Shashwat Mishra, online internship students who assisted me in applying machine learning to my work.

I am grateful to all the research colleagues of the Signal and Software Group (SaSg) for their encouragement and support, never letting me feel lonely on this long journey. Special thanks to Deepak Kumar, Abhinav Singh Parihar, Anupma Sharma, Vidya Bhaskar Shukla, Vaishali Sharma, Amit Baghel, and Purva Sharma. I also thank Dr. Puneet Singh Thakur, Dr. Mahendra Singh Thakur, Abhishek Ojha, Vivek Kumar, Sukh Sagar, and Parth Toshniwal for their various forms of assistance. I would also like to thank the Finnish national agency TFK program, Finland for the financial assistance for the research visit at Oulu University, Finland. This research visit helped me meet new people and experts, and expand my research knowledge. I would like to thank the Indian Institute of Technology Indore and Ministry of Human Resource Development, Government of India for providing financial assistance.

I am deeply indebted to my parents and my sister, Jobsy Jose, to whom this dissertation is dedicated, for their unwavering and unconditional love and prayers throughout this endeavor. I also thank the servants of God and church members for keeping me in their prayers, which have uplifted me to this level.

Finally, I am once again grateful to God for bringing such blessed people to influence my life. I therefore give Him all praise, glory, and honor.

JUSTIN JOSE

Dedicated to my family

ABSTRACT

The rapid increase in mobile device usage has triggered a surge in bandwidth-intensive applications like video streaming, gaming, and more. This growth has heightened the demand for enhanced spectrum utilization and performance in upcoming wireless networks. Technologies such as virtual full-duplex (VFD) communication, underlay device-to-device (D2D) communication, reconfigurable intelligent surfaces (RIS) or intelligent reflecting surfaces, and non-orthogonal multiple access (NOMA) have emerged as promising solutions for the next generation of wireless networks. Traditional half-duplex systems, where devices can only transmit or receive at any given time, often underutilize available spectrum. Full-duplex (FD) communication overcomes this limitation by enabling simultaneous transmission and reception on the same frequency channel, effectively doubling spectral efficiency with reduced latency. However, due to the high self-interference problem in FD systems, VFD communication has emerged as an alternative with improved network performance.

Furthermore, underlay D2D communication allows devices in close vicinity to communicate directly using the same frequency bands allocated to cellular networks with interference reduction techniques via proper resource allocation, thus improving spectrum utilization. Additionally, NOMA enables efficient sharing of time-frequency resources among multiple users. Unlike traditional orthogonal multiple access (OMA) schemes, NOMA allows multiple users to transmit concurrently on the same frequency band by employing power domain multiplexing. Moreover, RIS can improve signal propagation, coverage, and reliability by intelligently manipulating the electromagnetic waves. This enhancement leads to improved rates and efficiency in wireless communication systems. Additionally, a variant of RIS known as simultaneously transmitting and reflecting RISs (STAR-RIS) not only reflects signals but also transmits them, thereby enhancing the flexibility and effectiveness of RISs to serve users on both sides of the RIS.

In this thesis, initially, a cooperative VFD-based NOMA (VFD-NOMA) system using decode-and-forward (DF) relay with successive relaying (SR) is investigated under practical constraints such as imperfect successive interference cancellation (SIC) and residual inter-relay interference (IRI). SIC is crucial in NOMA for leveraging power differences between users, although achieving perfect SIC poses challenges. Similarly, residual IRI may persist even after interference cancellation. Previous works have neglecting these practical aspects and primarily focused on analyzing performance over Rayleigh faded channels, overlooking other generalized fading models like Nakagami-m. Thus, a framework for outage probability (OP), asymptotic OP, and ergodic rate (ER) expressions is developed for the considered system model over the generalized Nakagami-m fading channels. Additionally, the performance of the considered system is compared against FD-OMA and FD-NOMA schemes, highlighting the impact of the fading parameter and inter-relay distance.

Secondly, comparing to FD systems, the SR based VFD (SR-VFD) system models studied in the literature necessitate an additional time phase and a doubled number of relays for each destination user. Therefore, this thesis introduces a novel frequency division duplex (FDD) based VFD (FDD-VFD) system model. This model not only matches FD in terms of resource utilization but also surpasses the performance of both SR-VFD and FD systems. Two practical scenarios are considered: absence of inter-relay interference (A-IRI) and presence of inter-relay interference (P-IRI). The thesis analyzes the OP and ER performance metrics of the proposed

system. Also, to mitigate the impact of inter-relay interference in the P-IRI scenario, optimization problems are investigated to minimize the system OP (SOP) and maximize the ergodic sum rate (ESR) through joint allocation of transmit power for the relays. The particle swarm optimization (PSO) algorithm and a deep neural network (DNN) architecture are employed to solve these formulated problems. Extensive evaluations are conducted across various system parameters to demonstrate the effectiveness of the proposed FDD scheme and draw significant conclusions.

Third, the thesis delves into exploring a novel system model based on NOMA-enabled underlay D2D communication to further enhance the utilization of the wireless spectrum and available resources. This model incorporates NOMA in both underlay D2D and cellular networks, offering increased spectral efficiency compared to previous underlay D2D and NOMA models and exhibiting potential for superior performance. The study presents analytical expressions for the SOP and sum ergodic rate (SER) metrics for performance evaluation. Additionally, a power control mechanism based on a DNN is proposed for minimizing SOP, complementing the analytical analysis with practical insights from simulations, showcasing the model's effectiveness over comparative schemes and highlighting the importance of optimizing power values in response to various system parameters.

Fourthly, the investigation focuses on enhancing both system performance and spectrum utilization through an novel RIS-FD system model, specifically catering to different downlink and uplink (DDU) users, unlike existing studies that predominantly consider two-way communication with the same user for both downlink and uplink (SDU). This model has applications in FD cooperative systems as well as underlay D2D communication, featuring multiple users with best downlink and uplink user selections. The study incorporates factors such as residual SI (RSI), co-channel interference (CCI), and hardware imperfections (HI), considering direct links across generalized Nakagami-m fading channels. Analytical expressions for OP, SOP, and ER are derived, alongside investigations into joint element splitting, user power allocations, and reflection amplitude with objectives of minimizing SOP and maximizing ESR.

Fifth and in the last, the thesis proposes a novel VFD communication-based scheme for STAR-RIS, referred to as VFD-STAR-RIS, aimed at mimicking and surpassing the performance of conventional FD-based STAR-RIS (FD-STAR-RIS) communication, particularly in scenarios with high RSI. The VFD-STAR-RIS model substitutes the FD access point (AP) with two half-duplex (HD) APs or remote radio units, each serving a specific downlink or uplink user. This design achieves performance improvements without the complexity of SI cancellation, while maintaining spectrum utilization akin to FD-STAR-RIS. The proposed model also finds application in FD cooperative systems and underlay D2D communication, with analytical expressions provided for OP and ER, considering multiple uplink and downlink users with user selections. Furthermore, to mitigate inter-user interferences (IUI) aided by STAR-RIS, the study investigates optimization problems involving power allocations, reflection amplitude, transmission amplitude, and STAR-RIS element partitioning for SOP minimization and ESR maximization. A solution using the PSO algorithm is employed for SOP minimization. However, due to the complexity involved in the ER expressions, applying PSO directly to the JPRTE problem of ESR maximization (JPRTE-ESR) will require significant convergence time. Thus, a machine learning (ML) approach is used to approximate ER expressions via a DNN architecture, and thereafter PSO is applied to obtain a solution having a very low computational time.

Lastly, numerical results are compared with Monte-Carlo simulations to verify the correctness of the presented expressions.

Contents

List of Figures

List of Tables

List of Abbreviations/Acronyms

5G fifth generation.

6G sixth generation.

AF amplify-and-forward.

AWGN additive white Gaussian noise.

BS base station.

CCI co-channel interference.

CDF cumulative distribution function.

CSI channel state information.

D2D device-to-device.

DDU different user for downlink and uplink.

DF decode-and-forward.

DNN deep neural network.

eLU exponential linear unit.

embb enhanced mobile broadband.

ER ergodic rate.

ESR ergodic sum rate.

FD full-duplex.

FDD frequency division duplex.

GCQ Gaussian-Chebyshev quadrature.

HD half-duplex.

HI hardware impairments.

i.i.d. independent and identically distributed.

IoT internet of things.

IRI inter-relay interference.

IRS intelligent reflecting surface.

LANs local area networks.

LoS line-of-sight.

M2M machine-to-machine.

MANET mobile ad-Hoc networks.

MIMO multiple-input and multiple-output.

ML machine learning.

MMT moment matching technique.

mmTC massive machine-type communication.

MSE mean square error.

NGMA next generation multiple access.

NLD non-linear distortion.

NLoS non-line-of-sight.

NLPA non-linear power amplifier.

NOMA non-orthogonal multiple access.

OAC optimized allocation of coefficients.

OFDM orthogonal frequency division multiplexing.

OMA orthogonal multiple access.

OP outage probability.

PA power amplifier.

PDF probability density function.

PSO particle swarm optimization.

QoS quality of service.

RAC random allocation of coefficients.

RF radio frequency.

RIS reconfigurable intelligent surface.

RSI residual self interference.

RV random variable.

SDU same user for downlink and uplink.

SER sum ergodic rate.

SI self interference.

SIC successive interference cancellation.

SINR signal-to-interference and noise ratio.

SNR signal-to-noise ratio.

SOP system outage probability.

SR successive relaying.

STAR-RIS simultaneously transmitting and reflecting reconfigurable intelligent surfaces.

UE user equipment.

URLLC ultra-reliable and low-latency communication.

V2I vehicle-to-infrastructure.

V2V vehicle-to-vehicle.

VFD virtual full-duplex.

List of Symbols

- Basic arithmetic and calculus notations with their definitions.

Elementary & Special Functions

Notation	Definition
$\Gamma(x)$	$= \int_0^\infty t^{x-1}e^{-t}\,\mathrm{d}t$ is the Gamma function.
$\Gamma(x,y)$	$= \int_y^\infty t^{x-1}e^{-t}\mathrm{d}t$ is the upper incomplete Gamma function.
$\Upsilon(x,y)$	$= \int_0^y t^{x-1}e^{-t}\mathrm{d}t$ is the lower incomplete Gamma function.

Probability & Statistics

Let X be a random variable (RV).

Notation	Definition
$\mathbb{E}[\cdot]$	statistical expectation operator
$f_X(\cdot)$	probability density function (PDF) of a RV X
$F_X(\cdot)$	cumulative distribution function (CDF) of a RV X
$\mathcal{CN}(\mu,\sigma^2)$	complex normal distribution with mean μ and variance σ^2
$Nak(a,b)$	Generalized Nakagami-m fading distribution, characterized by fading severity value a and variance b
$Uni[a,b)$	Uniform distribution bounded in the range a and b
$\Xi(s,\theta)$	Gamma distribution with scale θ and shape s

Chapter 1

Introduction

1.1 Overview

In the realm of wireless communication, achieving better spectrum utilization with high data rates, ensuring ultra-reliable and low-latency communication (URLLC), providing enhanced mobile broadband (eMBB), enabling global coverage and connectivity, and supporting massive machine-type communication (mMTC) are critical objectives for next generation networks [9]. Over the years, there has been a phenomenal increase in the number of communicating mobile devices and a subsequent growth in varied wideband applications like video streaming and sharing, gaming, mobile cloud computing etc. Consequently, it has fueled the demand for better spectrum usage in the next generation wireless networks. Further, the speed of cellular links has seen significant increments: from 50 kbps in 2G systems, 144 kbps in 2.5G systems, around 2 Mbps in 3G systems, to approximately 100 Mbps in 4G systems (3GPP-LTE and WiMAX). The advent of 5G saw speeds of around 1 Gbps, and projections for 6G systems reach approximately 1 Tbps [10]. Similarly, indoor wireless local area networks (LANs) have evolved from 11 Mbps in IEEE 802.11b to 300 Mbps in IEEE 802.11n within the last two decades [11].

Despite the high data rates provided by 4G systems, there remains a disparity between customer demands and the services available. Addressing this gap necessitates ongoing and future research focusing on next-generation wireless communication technologies such as cooperative relaying, virtual full-duplex (VFD) communication, underlay device-to-device (D2D) communication, non-orthogonal multiple access (NOMA), and reconfigurable intelligent surfaces (RIS). Efficient utilization of the globally allocated frequency spectrum for wireless communication, coupled with high data rate transmission over multipath fading channels, presents a formidable challenge in practical wireless communication systems. Consequently, the design and operation of wireless communication systems confront various challenges that require thorough study and analysis to achieve high data rate transmission with better spectrum utilization, high reliability and low latency over multipath fading channels.

1.2 Wireless Communication Channel

The wireless communication channel serves as the conduit for information signals to travel from their source to their destination, encountering several impairments along the way. This section delves into the basics of wireless propagation, multipath fading, and channel models. Additionally, it elaborates on fundamental performance metrics and provides mathematical descriptions to characterize the performance of wireless systems.

1.2.1 Multipath Fading

Fading in wireless communication refers to the fluctuation in signal attenuation over time or frequency. As the transmitted signal navigates through the wireless medium, encountering reflection, diffraction, refraction, or scattering, it follows multiple paths to reach its destination, resulting in different replicas of the signal with varying amplitudes, phases, and frequencies. These replicas converge at the receiver, where constructive or destructive interference occurs, leading to amplification or attenuation in signal power. This phenomenon directly impacts the resilience and dependability of the wireless communication system. Figure 1.1 illustrates a typical scenario of signal propagation between transmitting and receiving antennas through a multipath fading channel.

Fading can be categorized into two main types: large-scale fading and small-scale fading. Large-scale fading primarily stems from shadowing caused by large objects like hills or buildings, as well as path loss proportional to distance. On the

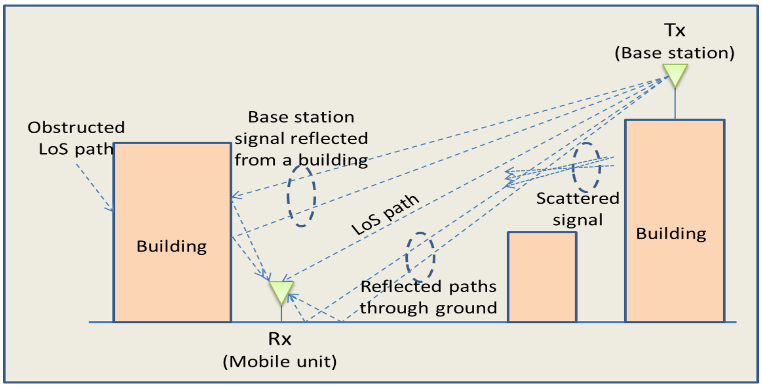

Figure 1.1: Wireless communication channel.

other hand, small-scale fading arises from the constructive or destructive interference of multiple copies of the transmitted signal as it traverses through multipath environments.

1.2.2 Channel Characterization

Mathematically describing fading poses significant challenges due to its variability across time, frequency, and geographic locations. Consequently, considerable attention has been devoted to statistically characterizing fading. Various precise and relatively straightforward statistical models have been proposed to capture the nature of fading channels, depending on the propagation environment [12, 13]. For small-scale fading, commonly utilized distributions include Rayleigh, Rician, Nakagami-m, among others, which are detailed below:

- **Rayleigh distribution:**

  The Rayleigh distribution stands out as a widely adopted approach for characterizing the statistical characteristics of radio channels. It is employed when multipath propagation occurs without a prominent line-of-sight (LoS) path between end users. This distribution models the in-phase and quadrature-phase components of the received signal as a zero-mean complex Gaussian random process, owing to the constructive or destructive interference of multipath components. Consequently, the amplitude of the received signal follows a Rayleigh distribution. The PDF of a Rayleigh-distributed signal can be formulated as follows

$$f_\gamma(x) = \frac{1}{\Omega} \exp\left(-\frac{x}{\Omega}\right), \qquad x \geq 0 \tag{1.1}$$

where Ω represents the average signal-to-noise ratio (SNR).

- **Rician distribution:**

The Rician distribution is chosen when there exists a prominent stationary non-fading (LoS) component between end users. In such scenarios, the random multipath acquires a DC component due to the summation of multipath signals, leading to the dominance of a stable non-fading component. When the strong LoS component is absent, the Rayleigh distribution becomes a specific instance of the Rician distribution. The PDF of the Rician distribution can be expressed as

$$f_\gamma(x) = \frac{(K+1)}{\Omega} \exp\left(-\left(K + \frac{(K+1)x}{\Omega}\right)\right) I_0\left(2\sqrt{K\frac{(K+1)x}{\Omega}}\right), \qquad x \geq 0 \tag{1.2}$$

where K represents the Rician K-factor which is defined as the ratio of power of the LoS component to the multipath components, and $I_v(\cdot)$ represents the v^{th} order modified Bessel function of first kind.

- **Nakagami-m distribution:**

Nakagami-m is used to characterize small-scale fading for dense signal scatters. It is also used in a variety of real-world applications such as modeling wireless signals and radio wave propagation due to its generalized fading characteristic for different values of the severity parameter m. One sided Gaussian distribution for $m = \frac{1}{2}$ and Rayleigh distribution for $m = 1$ are special cases of Nakagami-m distribution [14]. Further, the Nakagami-m model closely approximates the Hoyt and Rice distributions, and an infinite value of the fading severity represents a deterministic envelope, signifying the absence of fading. Additionally, the model offers the best representation of land-mobile propagation, indoor-mobile multipath, and ionospheric radio links. Thus, this thesis utilizes Nakagami-m distribution for the small scale fading. It is to note that as the model includes Rayleigh fading as a special case, the analytical and optimization results presented in the thesis are also applicable to the same by setting the fading severity values of each link to unity. The PDF of the Nakagami-m distribution can be expressed

$$f_\gamma(x) = \left(\frac{m}{\Omega}\right)^m \frac{1}{\Gamma(m)} x^{m-1} \exp\left(-\frac{mx}{\Omega}\right), \qquad x \geq 0 \tag{1.3}$$

1.2.3 Performance Metrics

To examine the performance of VFD and underlay D2D based wireless communication systems over fading channels, several performance metrics are used. To fix various design issues of wireless communication systems, these performance measures are used. Commonly used performance metrics in the wireless communication literature are instantaneous signal-to-noise ratio (SNR), outage probability (OP), ergodic rate (ER), and average symbol error rate (ASER) [13].

1. **Instantaneous SNR**: The instantaneous SNR is a basic performance metric that is used to quantify the signal corruption due to noise. Instantaneous SNR is related to data detection as it is measured at the output of the receiver and is an excellent indicator of the overall fidelity of the communication system. Instantaneous SNR can be expressed as

$$\gamma = \frac{\text{Received signal power at the receiver}}{\text{Received noise power at the receiver}} = \frac{P|h|^2}{\sigma^2}, \tag{1.4}$$

   where P, h, and σ^2 represent the transmit power, channel parameter, and noise variance, respectively. Due to the multipath fading in wireless communication, average SNR is a more appropriate performance metric than instantaneous SNR. Average SNR is the statistical averaging over the probability distribution of the fading and is given as $\Omega = \mathbb{E}[\gamma]$, where $\mathbb{E}[\cdot]$ represents the statistical expectation operator.

2. **Outage Probability**: OP is one of the important performance metric that depicts link failure probability and is mainly used in the case of a slow-fading scenario. It is defined as the probability that the received end-to-end instantaneous SNR (γ) of the considered system lies below a predefined threshold

(γ_{th}), which can be given as

$$\begin{aligned}\mathcal{P}_{\text{out}}(\gamma_{\text{th}}) &= \Pr\left[\gamma < \gamma_{\text{th}}\right] \\ &= \int_0^{\gamma_{\text{th}}} f_\gamma(x)\mathrm{d}x,\end{aligned} \tag{1.5}$$

where $f_\gamma(\cdot)$ represents the probability density function (PDF) of γ, $\gamma_{\text{th}} = 2^{r_{\text{th}}} - 1$, and r_{th} represents the threshold data rate.

3. **Ergodic rate**: Ergodic capacity quantifies the ultimate reliable communication limit over fading channels. Instantaneous capacity (measured in bps/Hz) is defined as the maximum rate achieved by the communication channel and can be determined as $C = \log_2(1+\gamma)$. Hence, ergodic capacity is obtained by averaging the instantaneous capacity over the PDF of the instantaneous SNR (γ), which is defined as

$$\begin{aligned}\mathcal{C}_{\text{e}} =& \mathbb{E}\left[\log_2(1+\gamma)\right] \\ =& \int_0^{\infty} \log_2(1+x) f_\gamma(x)\mathrm{d}x.\end{aligned} \tag{1.6}$$

4. **Average symbol error rate**: ASER is an important performance metric for wireless communication systems that can be determined by averaging the symbols with error at the receiver. For any digital modulation technique, the generalized ASER expression by using the CDF-based approach can be given as

$$\mathcal{P}_e = -\int_0^{\infty} \mathcal{P}_s^{'}(e|x)\mathcal{P}_{out}(x)\mathrm{d}x, \tag{1.7}$$

where $\mathcal{P}_s^{'}(e|x)$ represents the first order derivative of the conditional SEP ($\mathcal{P}_s(e|x)$) for the received SNR.

1.3 Cooperative Relaying

In wireless communication, multipath fading is one of the major impairments that cause reduced reliability, robustness, and coverage of a network. Cooperative relaying has been reckoned as an effective approach to counteract the effect of multipath fading in wireless communications. Cooperative relaying can mitigate the path-loss and shadowing effects by introducing an intermediate node i.e., a relay node in between the source and destination. In this way, three distinct gains can be achieved: (i) diversity is increased because of the additional and independent path available for signal propagation between source and destination; (ii) communication between source and destination is performed in hops i.e., the transmitter is closer to the receiver and path-loss is reduced; (iii) the smart relay position mitigates the shadowing effect [15]. The basic idea of cooperative relaying is to process the information between source and destination through alternative indirect multipath via intermediate relay nodes. The cooperative relaying has been incorporated in the standards such as LTE-Advanced and IEEE 802.16j [16]. The transmitted signal is processed through different relaying schemes. Commonly used relaying schemes are

- Amplify-and-forward (AF)

- Decode-and-forward (DF)

Amplify-and-forward: In AF relaying, the relay receives the signal coming from the source node, amplifies it, and forwards it to the destination. The signal received at the relay is affected by channel fading and noise. Hence, noise is also amplified at the relay along with the information signal. AF is the simplest relaying technique because no further processing is required at the relay. However, since a power amplifier (PA) is used to amplify the signal, AF relaying is sensitive to PA nonlinearity i.e., non-linear PA (NLPA), and the impact of NLD becomes a major issue in a multi-hop network.

Decode-and-forward: In DF relaying, the relay first decodes the received information signal from the source, and then re-encodes and transmits it to the destination. Both decoding and re-encoding are performed at the relay. Ideally, the same information is re-transmitted through the relay, so noise is not amplified and fading impairments of the source to relay channel are mitigated. However, the processing load at the relay is greater than AF relaying, and an accumulation in error occurs if there is an error in the recovery of the information signal at the relay which is also forwarded to the destination.

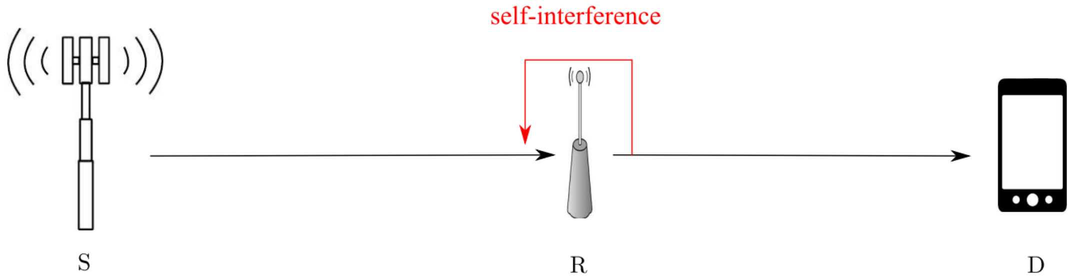

Figure 1.2: Two-hop relay network with FD relay [1].

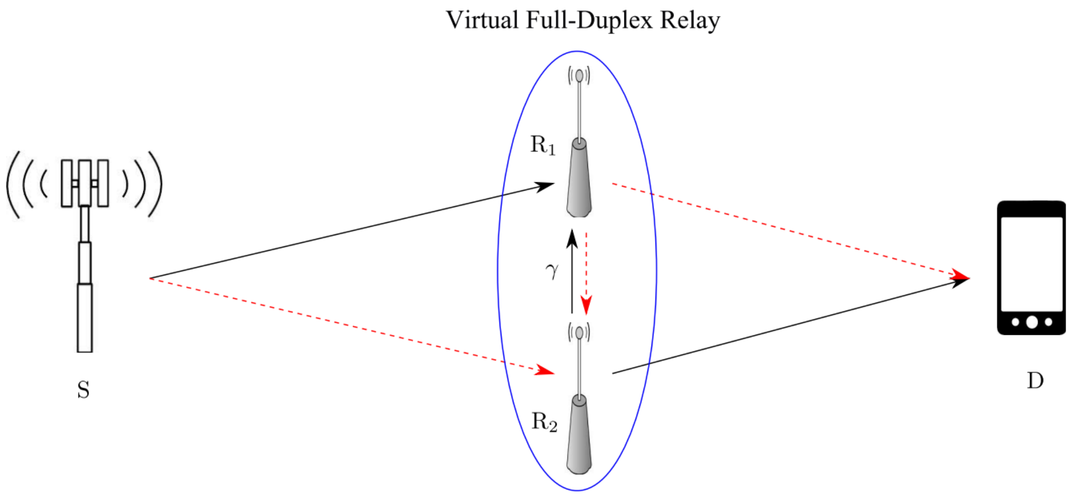

Figure 1.3: A two-hop relay network utilizing a VFD relay. The solid black lines represent active connections during even time slots, while the dashed red lines represent active connections during odd time slots [1].

1.4 Virtual Full-Duplex Communication

In recent years, VFD communication has emerged as an alternative to traditional FD communication. FD communication facilitates simultaneous transmission and reception of data within the same frequency band. In contrast to conventional half-duplex (HD) systems, which restrict devices to either transmitting or receiving data at a given moment, FD systems support two-way communication without requiring distinct time slots or antennas for transmission and reception. This advancement notably enhances data throughput and operational efficiency in wireless networks. Specifically, cooperative FD communication involves the collaboration of relay nodes in a network to facilitate simultaneous transmission and reception on the same frequency band.

Table 1.1: SI Suppression Techniques [8]

Techniques	**Capability**	**Pros**	**Cons**
Antenna directionality	30 dB	1. Easy to implement 2. Provides directional diversity 3. Suitable in narrowband scenarios	1. Suffers bandwidth constraints due to large range of wavelengths 2. Not suitable for wideband
Antenna placement	47 dB	Robust in narrowband scenarios	1. Requires 3 antennas; extra cost 2. Suffers severe amplitude mismatch 3. Requires manual tuning and so do not adapt to the environment
Antenna separation	30 dB	1. Uplink and downlink are spatially separated 2. Uses the idea of increasing path loss between transmitter and receiver antennas	1. Not applicable to point—to—point scenarios where both nodes are FD enabled 2. Not feasible with small form—factor devices 3. Suffers degradation on individual antennas radiation pattern 4. Can suppress desired signal
Cross polarisation	50 dB	1. Can be applied to both separate and shared antennas 2. Can be applied to small form-factor devices with duplexes	1. Unaware of system characteristics 2. Affected by environmental factors
Analogue cancellation in Balun circuit	45 dB	1. Generates inverted version of the Received signal for cancellation 2. Non-bandwidth limited; non—power limited 3. Adaptive to the environment	1. Incurs additional non-linearity from the noise cancelling circuit 2. Cancellation is not adequate
Digital Cancellation with analogue cancellation	60 dB	Suppresses both SI and noise	Suffers transmitter distortion due to non—ideality of transmitter and receiver components

Table 1.2: Comparison between VFD and FD communication

	Full Duplex	**Virtual Full Duplex**
Definition	Simultaneous transmission and reception of signals at the same time and over the same frequency band.	Simultaneous transmission and reception of signals by replacing the FD node by two HD nodes.
Nature of interference	Strong SI due to large power difference between device's own transmission and received signal of interest arriving from a remote transmit antenna.	Inter-node-interference from transmitting node to receiving node, which is significantly lower than SI due to large physical separation between the nodes.
Residual interference after cancellation	Current SI cancellation techniques involve mixed analog and digital mitigation schemes. However, the SI cancellation is limited by hardware imperfections such as nonlinear distortions, non-ideal frequency response of circuits, phase noise etc. Further, the large power imbalance saturates the receiver RF chain due to limited dynamic range of ADC such that digital cancellation in the receiver baseband processing is not possible, and therefore leading to high RSI.	Inter-node-interference at the receiving node is comparatively lower than RSI due to physical separation between the nodes.
Computational Complexity	High computational complexity with advanced signal processing is involved in order to cancel the strong SI, and thus there also exists a fundamental trade-off between hardware cost and SI cancellation capability.	Computational complexity is very minimal in comparison to FD systems.

Relay usage was initially standardized in IEEE802.16j [17]. Subsequently, LTE-advanced also explored various relay strategies to achieve desired throughput and coverage targets [18, 19]. In these real-world systems, relays typically function in a HD mode due to the complex challenges associated with transmitting and receiving within the same frequency band and time slot [17–19]. This HD operation leads to inefficient utilization of the radio channel resource since a HD relay requires two time slots to forward a message from source to destination. An alternative approach involves relays operating in FD mode, where they can transmit data while simultaneously receiving new data to be forwarded in the subsequent time slot. However, implementing FD relays presents practical difficulties due to significant self-interference (SI) between transmitting and receiving radio frequency (RF) chains, as depicted in Fig. 1.2. For instance, WiFi signals are transmitted with an average power of 20 dBm, while the noise floor stands at around -90 dBm. Consequently, SI must be reduced by 110 dB to match the noise level; otherwise, any residual SI treated as noise would compromise performance.

Although the theoretically ideal scenario involves perfect removal of SI from the received signal since the relay has complete knowledge of it, practical constraints arise. The large power disparity between transmitted and received signals saturates the receiver RF chain, especially the analog-to-digital converter (ADC) dynamic range, making digital interference cancellation challenging in receiver baseband processing. Recent studies [19–23] have demonstrated the practical viability of FD relays by mitigating the impact of self-interference through a combination of analog and digital methods. These architectures typically employ analog partial self-interference cancellation to prevent the receiver's ADC from being overwhelmed by the transmitter's power. Subsequently, digital SI cancellation is carried out in the baseband domain. Some of these approaches utilize multiple antennas during transmission, causing the transmit signals to cancel out in phase opposition at the receiving antennas, thus reducing SI in the analog domain. Table 1.1 summarizes various SI mitigation techniques involved in FD.

A more recent alternative [22] employs a single antenna along with a signal splitter known as a circulator, which connects the transmitter chain to the antenna and the antenna to the receiver chain while maintaining sufficient isolation between the transmitter and receiver ports. Expanding on the concept of using multiple antennas for receiver isolation, a distributed version of this approach involves physically separated nodes, each equipped with antennas. This setup allows each node to operate in a conventional HD mode. Moreover, by increasing the physical separation between nodes, the issue of receiver saturation is resolved.

Work in [1] investigates a VFD relay scheme formed by two half-duplex relays (as depicted in Fig. 1.3), building on the idea of using multiple antennas for isolation. This setup enables each relay to function in either receive or transmit mode during alternating time slots, a concept known as successive relaying (SR) [24–26]. With this approach, the source can transmit new messages to the destination in every time slot, simulating the functionality of a FD relay system. It's worth noting that the network topology resembles the well-known diamond relay network, albeit with an additional interfering link between the two relays. The primary performance bottleneck in SR is inter-relay interference, akin to SI in FD relays. The distinction between FD and VFD communication is summarized in Table 1.2. Notably, achieving effective SI cancellation requires sophisticated hardware and complex signal processing algorithms, which can increase both the complexity and cost of the system. This creates a fundamental trade-off between hardware cost and SI cancellation capability. VFD communication, on the other hand, can provide the benefits of FD communication without the need for such advanced SI cancellation techniques, making it a more cost-effective solution. Additionally, VFD can be more energy-efficient than FD systems because it avoids the additional power consumption associated with the cancellation process. This is particularly important in battery-powered devices or energy-constrained environments, where minimizing power consumption is a priority. Specifically, for the cooperative communication system models discussed in Chapters 2 and 3, VFD relaying users can replace FD relaying users due to these reasons. Interestingly, in a more practical approach, VFD can be effectively used in hybrid communication systems where both FD and VFD modes are employed depending on the specific requirements of the scenario. This hybrid approach allows the network to leverage the benefits of FD where possible, while using VFD in situations where SI cancellation is more challenging or costly.

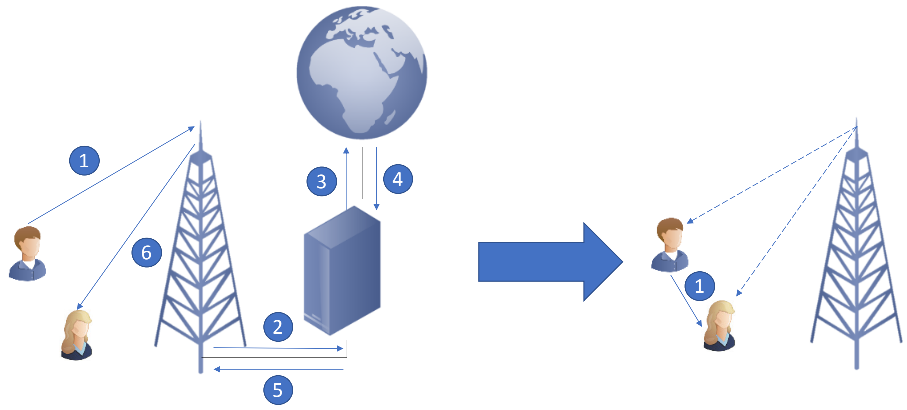

Figure 1.4: A typical communication link as compared with a D2D enabled link.

1.5 Underlay D2D Communication

In a standard cellular setup, devices link up with a base station (BS) that handles the resource distribution. However, when two nearby devices want to communicate, their data goes back and forth through the BS, causing congestion and latency, as seen in Fig. 1.4. This drawback notably decreases network effectiveness and energy usage. Allowing these devices to communicate directly, as shown in Fig. 1.4, brings several benefits. It enhances spectral and energy efficiency, substantially reduces delays, and establishes a D2D network of close-range direct connections. Research indicates that a D2D network can double network capacity, quadruple device speeds, and cut latency by three times [27].

1.5.1 Overview of D2D Communication

A D2D network allows nearby devices to communicate directly with minimal involvement from the BS. The European Union's FP7 project, METIS (Mobile and wireless communications Enablers for the Twenty-twenty Information Society), viewed D2D communication as crucial for 5G networks [28]. The METIS project conducted extensive research on D2D concepts and standards, identifying various applications for D2D networks, such as D2D-C (Critical) for low-latency applications like vehicle-to-vehicle (V2V) communication, D2D-M (machine-to-machine) for IoT applications, D2D-N (non-critical) for traffic offloading, and D2D-B (Backhaul) for enhancing cellular network performance [29].

Compared to conventional direct communication protocols like Bluetooth or Wi-

Fi Direct, D2D communication depends on the cellular network for specific control tasks such as synchronization and device discovery. It operates within cellular bands rather than ISM bands and is part of the cellular wireless protocol [30]. Unlike Mobile Ad-Hoc Networks (MANETs), a D2D network has centralized control and mainly consists of single-hop direct links instead of multi-hop links [31]. Moreover, a D2D network collaborates with the cellular network, potentially boosting data rates for cellular users at cell boundaries by using an intermediary device as a relay node [32], or distributing information to multiple recipients through traffic offloading [33]. Its opportunistic use of network resources, akin to cognitive radio networks, makes it adaptable and scalable for various envisioned B5G/6G network scenarios [34].

D2D networks are broadly categorized based on resource utilization: In-band, operating within the cellular band, and Out-band, operating outside it. In-band networks may further categorize into Underlay, Overlay, and Cellular modes based on spectrum access techniques. Underlay involves D2D pairs sharing channels with cellular users in an opportunistic shared access model, Overlay reserves a part of the cellular band for D2D operations similar to licensed shared access, and cellular mode uses D2D nodes to enhance services for cellular devices, such as employing a D2D node as a relay for users at cell edges [35]. Out-band D2D networks operate beyond the cellular band, potentially relying on the BS for network tasks in controlled mode or functioning autonomously without a BS, useful in post-disaster scenarios when the cellular network infrastructure is compromised [36].

1.5.2 Prominent D2D Applications

Besides facilitating direct communication, a D2D network can be highly beneficial for content dissemination and alleviating network traffic—such as in live-streaming sports events where multiple devices access the same video stream through different channels, causing inefficient network resource usage. Instead, employing a D2D multicast network could transmit the video stream from one device to many, offering a faster, seamless viewing experience to a larger audience. Likewise, streaming services could utilize D2D nodes as local cache storage to distribute videos to nearby devices. Exploring the delivery of emerging multimedia formats like virtual reality videos via D2D networks is also underway [37].

In the emerging field of federated learning, where machine learning (ML) tasks are distributed across numerous devices for collective learning [38], D2D networks play a vital role in sharing neural networks among collaborating devices [39]. This distributed learning process also aids network controllers in creating a "Digital Twin" of the network for optimized command and control [40]. D2D links can also serve proximity advertising purposes. For instance, a shop wanting to advertise its services to nearby individuals could use D2D links to reach their phones, offering targeted advertisements that increase footfall and provide relevant content to users.

Another critical application area for D2D is V2V and vehicle-to-infrastructure (V2I) communication, especially concerning latency-sensitive scenarios like potential collisions between vehicles on the road, where reduced latency through direct links can be life-saving. Enabling low-latency machine-to-machine (M2M) links via D2D networks also supports communications in realms like the Internet of Things, Internet of Medical Things, and by extension, Industry 4.0 [41]. Finally, D2D networks play a crucial role in public safety and disaster recovery applications [42]. From efficient early warning broadcasts during natural disasters to post-disaster rescue operations when the core cellular network may be compromised, setting up a D2D network swiftly can aid emergency services in locating and rescuing affected individuals, potentially reducing casualties [36].

1.5.3 Major Challenges with D2D Communication

Several technical hurdles need to be overcome to achieve the envisioned objectives of D2D communication. Some of the key challenges include:

- **Decentralized or Centralized Control:** D2D networks can operate with either centralized or decentralized control modes. In the decentralized mode, the BS isn't involved in resource allocation tasks. Devices must discover each other and synchronize their transmissions to minimize interference and collisions. Conversely, the centralized mode, with the BS in control, addresses these technical issues. The BS allocates resources among D2D pairs, provides a common synchronization source, and maintains a device list for faster discovery and pairing.

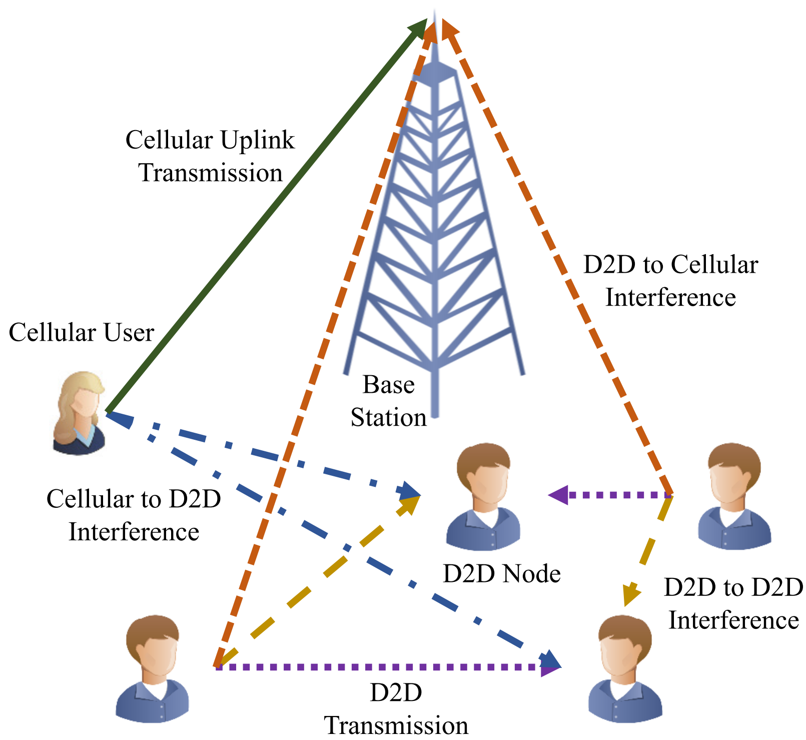

Figure 1.5: Inter- and Intra-tier interferences in a D2D network.

- **Overlay or Underlay:** In overlay D2D networks, the cellular network reserves a portion of its spectrum for D2D operations, posing optimization challenges. For instance, determining the optimal spectrum reservation to maximize overall network performance (both D2D and cellular) is crucial. Over-reserving spectrum can hinder cellular network performance, while under-reserving stifles the D2D network. The dynamic size of D2D networks adds complexity; the underlay mode often offers better spectrum efficiency due to its adaptability. Here, D2D pairs opportunistically access cellular uplink/downlink channels, ensuring the entire uplink/downlink spectrum is available when D2D users are inactive. The BS manages interference, benefiting from more resources than individual cellular users.

- **Resource Management:** Efficient resource management in D2D networks involves power and channel allocation among D2D pairs while minimizing interference on the cellular network. Managing interference is critical due to shared spectrum usage. Different types of interference in underlay D2D networks are illustrated in Fig. 1.5, highlighting the need to control interference levels for optimal performance.

1.6 Non-orthogonal Multiple Access

The multiple access scheme is defined as a technique of serving multiple users over the same channel by applying rules to cancel or limit the interference between the users, e.g., by providing orthogonality in frequency, or time, or space, etc. The use of a suitable multiple access technology is fundamental to the physical layer and has evolved with different generations of wireless communication. The type of multiple access schemes have shown significant improvements with the advancement of wireless networks. For instance, the first generation operated on frequency division multiple access, which is an analog frequency modulation scheme. The multiple access schemes were transformed into digital modulation from the second generation. The second generation utilized digital modulation and performed multiplexing in time, also known as time division multiple access (TDMA). After TDMA, Qualcomm [43] proposed another useful MA scheme, known as code division multiple access (CDMA). The use of CDMA was prominent in the third generation networks. However, CDMA was not capable of supporting data rates with high speeds, hence the 4G network adopted yet another advanced technique, the orthogonal frequency division multiple access (OFDMA) [44]. The orthogonal multiple access (OMA) techniques are widely accepted in the 4G networks [45].

NOMA has been contemplated as a potential candidate in providing superior spectral efficiency and massive connectivity. Recently, NOMA has been proposed for the 3GPP long term evolution (LTE) [46], [47]. It is worth pointing out that in long term evolution-Advanced (LTE-A), NOMA is implemented as a two-user case [48]. Broadly, NOMA is categorized as power domain (PD)-NOMA and code domain (CD)-NOMA (generally referred as sparse code multiple access). CD-NOMA includes multiple access solutions relying on low-density spreading [49], sparse code multiple access [50], multi-user shared access [51], successive interference cancellation amenable multiple access [52], etc. PD-NOMA and CD-NOMA differ in their basic principle of application. As the names suggest, while PD-NOMA exploits the power domain, CD-NOMA exploits the code domain for non-orthogonal resource allocation. However, due to simpler implementation, PD-NOMA has gained more popularity [53], since no big changes are required at the transmitter as compared to the current technology. This work utilizes PD-NOMA for multiple access. PD-NOMA exploits dimension of power domain and thus, it is capable of serving multiple users simultaneously on a given resource block (RB) by applying successive interference cancellation (SIC). The messages/signals of multiple users with different channel conditions are superimposed and transmitted. Based on the order of users' channel gain conditions, SIC is applied to decode their signal [54]. Fundamentally, the implementation of PD-NOMA (referred as NOMA hereafter) is different from the conventional approach used in OMA technologies, e.g., in frequency division multiple access, TDMA, CDMA, and OFDMA. By exploiting the power domain, NOMA is able to serve multiple users by assigning different power based on the user's channel condition, thereby is capable of utilizing the spectrum more efficiently, which is essential for the future generation networks. A theoretical comparison between the conventional OMA technique namely OFDMA and NOMA is depicted in [54]. The comparison shows that theoretically, users served using NOMA achieves improvement in their rate as compared to OFDMA. The improvement is credited to the increased bandwidth (BW) allocated to the users served using NOMA, which otherwise is distributed between the users due to the orthogonal allocation of resources under OMA. Moreover, by exploring the users' channel condition opportunistically, NOMA can serve multiple users with different requirements [55].

The major advantages of NOMA, which make it popular are, improved spectral efficiency, massive connectivity, and compatibility. The improved spectral efficiency is attributed to the fact that NOMA serves multiple users on the same resource block, i.e., the same frequency and time, which indicates efficient utilization of the spectrum and also leads to enhanced sum throughput of the system [54]. Furthermore, users are served simultaneously, which implies a larger number of active devices leading to massive connectivity. NOMA can support a larger number of users on a given resource block as compared to OMA, which dedicate an entire resource block for one user only. Moreover, the application of NOMA requires only minimal changes in the current 4G network [53]. The development of the superposition coding and SIC technologies both in theory and practice guarantees compatibility and easier implementation of NOMA.

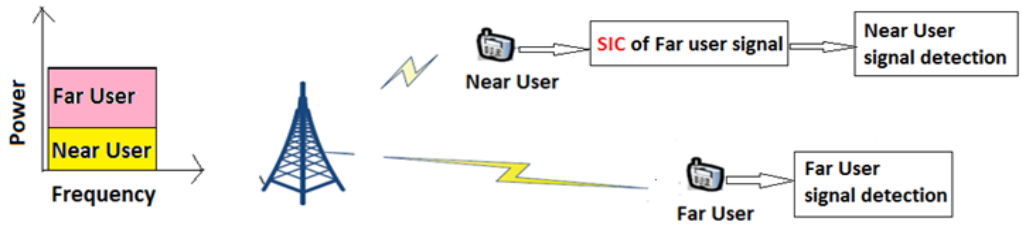

Figure 1.6: Basic principle of NOMA [2].

1.6.1 Key Technologies of NOMA

The key enabling technologies for NOMA is based on two principles, namely, superposition coding and SIC. In fact, these two technologies are not new and the roots of them can be found in many existing literature. As the two main technologies superposition coding and SIC continue to mature both in theoretical and practical aspects, NOMA is able to be applied in the next generation networks without considering the implementation issues. By invoking superposition coding technique, the BS transmits the combination of superposition coded signals of all users' messages. Without loss of generality, the channel gains of users are with respect to a particular ordering (e.g., increasing order or decreasing order). In the traditional OMA schemes, one of the popular power allocation policy is water filling policy. However, in NOMA, users with poor channel conditions are supposed to allocate more power. By doing so, it can ensure that the users with poor channel condition can decode the message of themselves by treating other users' messages as noise. For those users which are in good channel conditions, SIC technologies can be applied to enable subtract the interference from other users with poorer channel conditions.

Superposition Coding

As first proposed by Cover as early as in 1972 [56], the elegant idea of superposition coding is regarded as one of the fundamental building blocks of coding schemes to achieve the capacity on a scalar Gaussian broadcast channel [57]. More particularly, it was theoretically demonstrated that superposition coding is capable of achieving the capacities of Gaussian broadcasting channel capacity [58] and of achieving the capacities of the general degraded broadcast channel capacity . The fundamental concept of superposition coding is that it is able to encode a user with poor channel condition at a lower rate and then superimpose the signal of a user with better channel condition on it. Due to the solid foundation laid on the information perspective, researchers begin to apply superposition coding technologies to enormous channels, such as interference channels [59], relay channels [60], multiple access channels [61], and wiretap channels [62]. While the aforementioned contributions sufficiently motivate the use of superposition coding from theoretic perspective, another breakthrough which have been made on superposition coding is to bring this technique from theory to practice [63, 64]. Specifically, [63] designed an experimental platform using a software-radio system to investigate the performance of superposition coding. The set of achievable rate pairs under a packet-error constraint was determined.

Successive Interference Cancellation

Aiming to improve the network capacity with efficient managing interference, SIC is regarded as a promising technology for performing interference cancellation in wireless networks. SIC technique achieves interference cancellation with the following procedure: it enables the user with stronger link to decode the user with weaker link first. Then, it regenerates the signal of weaker user at the stronger user side and subtract the interference. At last the stronger user decodes its information without suffering the interference from the weaker user. It is demonstrated that SIC is capable of reaching the region boundaries of Shannon capacity, both in terms of the broadcast channel and multiple access networks. Additionally, one main advantage of SIC is that it requires low hardware complexity design at the receiver side [65]. As such, SIC has been widely studied and various version was been employed in practical systems such as CDMA [66] and vertical-bell laboratories layered space-time (V-BLAST) [67]. Furthermore, SIC has been exploited in several practical scenarios, such as multi-user multiple input multiple output (MIMO) networks [68], multi-hop networks [69], random access systems [70], and stochastic geometry modeled large-scale networks [71]. Another important development on SIC is that it has been implemented in some commercial systems, e.g., IEEE 802.15.4. In an imperfect SIC scenario, the interference from the stronger user's signal may not be completely removed when decoding the weaker user's signal. This residual interference can degrade the performance of users, particularly those with weaker signals, as they experience higher levels of interference. Inaccuracies in estimating the CSI and non-linearities in the transmitter or receiver hardware can contribute to errors in the SIC process.

1.7 Intelligent Reflecting Surface

The vision of a smart radio environment can be achieved by leveraging the intelligent reflecting surface (RIS)/reconfigurable intelligent surface (RIS). The RIS is one of the most promising and revolutionizing paradigm to achieve smart and reconfigurable wireless channel/radio propagation environments for beyond 5G/6G wireless communication systems [9]. It can enhance the spectrum and/or energy efficiency of wireless communication systems. RIS is a planar surface composed of various passive reflecting elements (REs), where each of the REs can independently influence the incident signal to vary in amplitude and/or phase. The reflected signals can be reconfigured to propagate in the desired directions by carefully adjusting the amplitude/phase shifts of all the REs. The wireless channels between transmitters and receivers can be easily modified by smartly placing RISs in a network and carefully coordinating their reflection coefficients. Due to rapid developments in metamaterials, the reflection coefficient of each element can be reconfigured in real-time to adapt the dynamically fluctuating wireless propagation environment.

The metasurface is a type of two-dimensional (i.e., with nearly zero thickness) artificial material that shows special electromagnetic properties depending on its structural parameters. As shown in Figure 1.7, the metasurface is made up of a large number of passive scattering elements or REs, such as metallic or dielectric particles, which can alter the impinging electromagnetic waves in various ways [72]. The direction and strength of the reflected waves are governed by the sub-wavelength structural arrangement of the REs, which affects how the incident waves are transformed. The RIS is made of a programmable metasurface that allows for complete control over the phase shifts experienced by various REs. This can be accomplished by applying external stimuli to the REs, which will modify their physical parame-

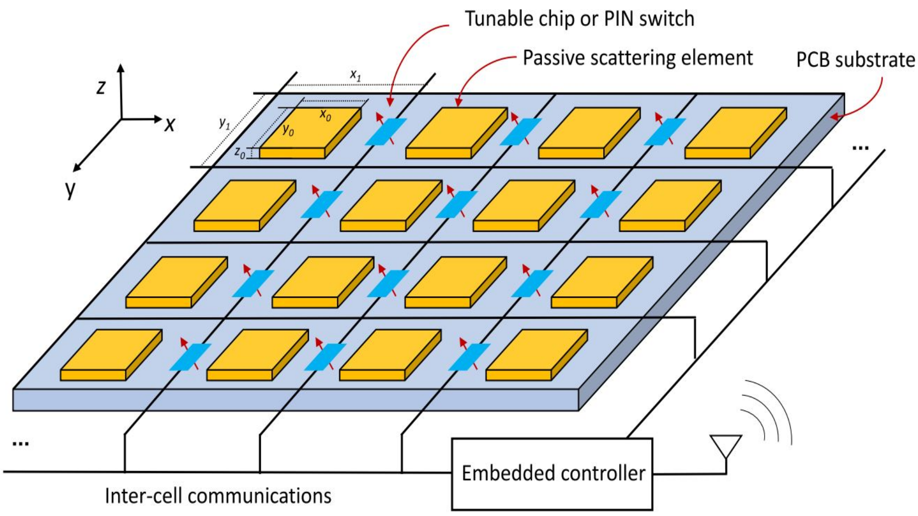

Figure 1.7: Reconfigurable metasurface with substantial number of passive scattering/reflecting elements [3].

ters and change the metasurface's electromagnetic properties without refabrication. A joint phase control of the REs allows the RIS to reconfigure its electromagnetic characteristics. This suggests integrating tunable chips into the metasurface's structure, with each tunable chip interacting locally with a RE and communicating with a central controller i.e., RIS controller [73]. In particular, the RIS controller can be implemented in a field-programmable gate array and the tunable chips are typical PIN or varactor diodes. As shown in Figure 1.7, the embedded RIS controller can communicate and receive reconfiguration requests from external devices, and then optimize and distribute its phase control decisions to all tunable chips. Each tunable chip modifies its state after receiving the control input, allowing the corresponding scattering element to alter its behavior. The RIS controller can use this sensing data to automatically alter its configuration and maintain consistent EM behavior with dynamic environmental conditions. By adjusting the phase of specific REs, the RIS can be reconfigured. The inter-cell communication among the tunable chips works together to control the REs of the metasurface that exhibits the desired tunable functions for the RIS's reconfigurability. A wide variety of tunable functions such as perfect absorption, anomalous reflection, beam shaping, and steering can be supported by the RIS [74]. The advantages of RIS-aided systems can be summarized as:

1) Flexible reconfiguration: The phase shift of all the REs i.e., passive beamforming can be achieved by coherent focused signal reflection in the desired receiver and null in the other directions. It can play an important role in performance improvement in wireless communication. The transmit beamforming, resource allocation, and power allocation can be jointly optimized to achieve performance gains [72].

2) Easy to deploy: The RIS is made of low-cost passive REs embedded in the metasurface. It is highly flexible in terms of both deployment and replacement because it can take on any shape. The RIS can be deployed on several structures such as building facades, indoor walls, aerial platforms, roadside billboards, highway polls, vehicle windows, etc.

3) Spectral/Energy efficiency enhancement: The RIS can modify the wireless propagation environment by compensating for the power loss over long distances. The sum-rate performance and better QoS can be achieved by the RIS-assisted wireless network. In contrast to AF and DF relaying protocols, RIS is capable of shaping the incoming signal by controlling the phase shift of each RE instead of employing a power amplifier. Thus, deploying RIS is more energy-efficient and environmentally friendly than AF and DF systems.

4) Compatibility: The RIS supports a FD mode of operation for transmission because it can only reflect electromagnetic waves. Additionally, RIS-aided wireless communication systems are compatible with the standards and hardware of existing wireless networks [75].

1.8 Simultaneous Transmitting and Reflecting RIS

The conventional reflecting-only RISs are limited to reflecting the incident wireless signal, requiring the transmitter and receiver to be positioned on the same side of the RIS, resulting in a half-space coverage. However, this constraint may not always be practical, restricting the flexibility and effectiveness of RISs, as users may be situated on both sides of the RIS. To address this limitation, a new concept called simultaneously transmitting and reflecting RISs (STAR-RISs) has received research attention. In STAR-RISs, the wireless signal incident on an element is divided into two parts when arriving from either side of the surface. One part, the reflected signal,

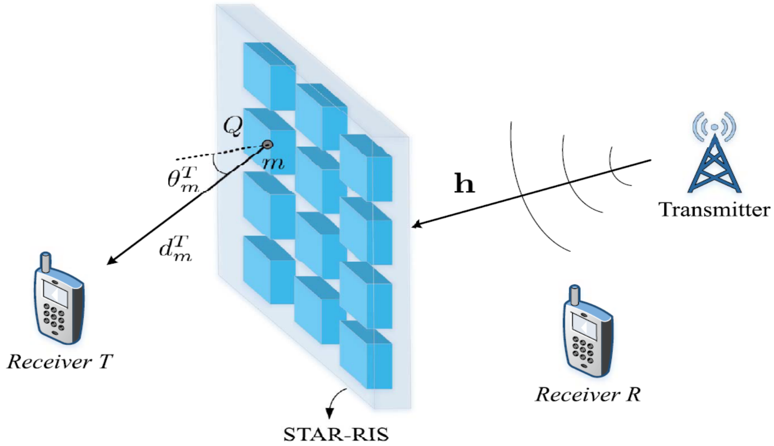

Figure 1.8: An illustration of STAR-RIS communication system [4].

is directed back into the same space as the incident signal (reflection space), while the other part, the transmitted signal, is sent to the opposite space (transmission space). By manipulating both the electric and magnetic currents of a STAR-RIS element, the transmitted and reflected signals can be reconfigured independently through two coefficients: the transmission and reflection coefficients. This enables the realization of a highly flexible full-space coverage.

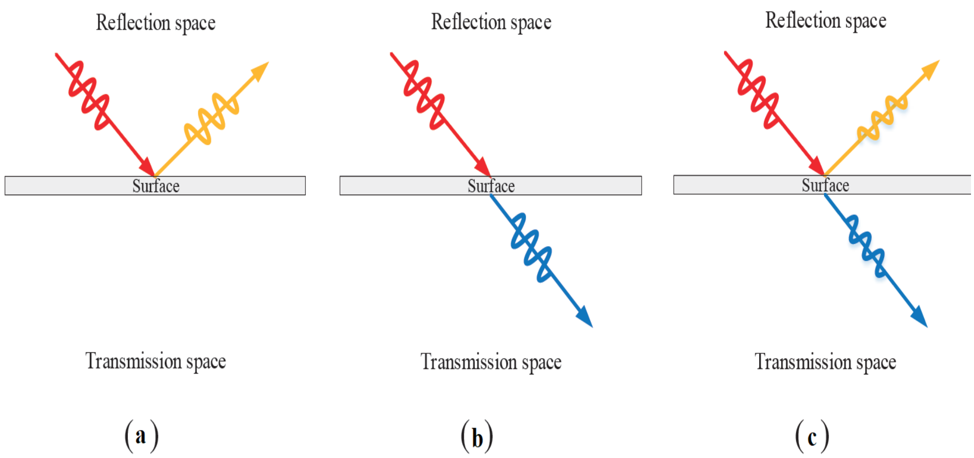

Figure 1.9: An illustration of signal propagation types of STAR-RISs: a) full reflection (conventional RIS); b) full transmission; c) STAR propagation [5].

There are three signal propagation types in STAR-RIS: full reflection, full transmission, and STAR, as demonstrated by a prototype developed by researchers at NTT DOCOMO, Japan [76]. The prototype features a metasurface covered by a transparent glass substrate. By adjusting the distance between the metasurface and the substrate, the three signal propagation types can be achieved, as illustrated in Figure 1.9. In the scenario of full reflection, incoming signals are entirely reflected and cannot penetrate the surface, a manipulation commonly explored in traditional reflecting-only RISs. Conversely, in the full transmission scenario, all incoming signals pass through the surface into the transmission space without any reflection. Lastly, in the STAR scenario, incoming signals are divided by the surface, with a portion being reflected into the reflection space and the remainder radiated into the transmission space, enabling comprehensive manipulation of signal propagation across space. Since STAR-RISs are typically designed to be optically transparent, they blend seamlessly with existing building structures like windows, ensuring no undesirable aesthetic impact, crucial for practical implementations. While the joint manipulation of transmission and reflection is not a new concept, particularly in physical and metasurface technology, several concepts similar to STAR have been proposed beyond the NTT DOCOMO prototype. For instance, in [8], frequency-selective reflection and transmission were achieved using a dual-band bi-functional metasurface structure, while [9] introduced the concept of an intelligent omni-surface (IOS), adjusting signals via a common phase shift.

Adjusting the phase shifts for transmission and reflection can typically be done separately, but the amplitudes of these coefficients must follow the law of energy conservation, ensuring that the total energy of the transmitted and reflected signals matches that of the incident signal. This means that the sum of transmission and reflection coefficients should equal one. Consequently, by adjusting these coefficients, each element in the STAR-RIS can operate in full transmission mode (T mode), full reflection mode (R mode), or both simultaneously (T&R mode). Based on this signal model, there are three practical protocols for operating STAR-RISs in wireless networks: energy splitting (ES), mode switching (MS), and time switching (TS).

- **Energy Splitting:** In this protocol, every element of the STAR-RIS is expected to function in T&R mode. Under this setup, incoming signals are divided into transmitted and reflected signals with varying energy levels, based on predetermined transmission and reflection amplitude coefficients. In practice, optimizing the amplitude and phase shift coefficients of each element for both transmission and reflection can be done together to achieve various design goals in wireless networks.

- **Mode Switching:** In the MS protocol, all elements of the STAR-RIS are divided into two groups. One group operates in T mode, while the other operates in R mode. This setup resembles a conventional RIS that reflects only and a transmitting-only RIS. In this protocol, the selection of mode for each element and the corresponding phase shift coefficients for transmission and reflection are optimized together. This approach results in an "on-off" type of protocol, meaning that each element is either transmitting or reflecting, making MS relatively easy to implement. However, MS typically cannot achieve the same level of transmission and reflection gain as ES because only a subset of elements is chosen for transmission and reflection, respectively.

- **Time switching** TS protocol involves periodically switching all elements between T mode and R mode in separate time slots, known as T period and R period. The allocation of time for full transmission and full reflection signals can be optimized to find a balance between the communication qualities of the front and back sides. TS offers the advantage that, with a given time allocation, the transmission and reflection coefficients are not linked, allowing for independent optimization. However, implementing TS requires precise time synchronization, making it more complex than ES and MS protocols.

1.9 Motivation

While SIC is crucial in NOMA for leveraging the power differences between users, achieving perfect-SIC is challenging. Similarly, residual IRI may persist even after interference cancellation. However, previous works on cooperative VFD and NOMA (VFD-NOMA) haven't explored the combined effects of residual inter-relay interference (IRI) and imperfect successive interference cancellation (SIC). Additionally, prior research in VFD-NOMA has only analyzed performance over Rayleigh faded channels, neglecting other generalized fading models like Nakagami-m. Furthermore, the VFD schemes in the literature are successive relaying based (SR-VFD), necessitating double the number of relays for each destination user and an extra time phase compared to FD, resulting in inefficient resource utilization despite improved system performance. Hence, it's imperative to propose a novel system model to improve the resource utilization with a single relay per destination user and no additional time phase. Likewise, previous works on underlay D2D and NOMA (D2D-NOMA) have focused on OMA either in the underlay D2D communication or in the cellular communication, leading to less spectrally efficient system models. Therefore, exploring a more spectrally efficient NOMA-enabled D2D (ND) communication underlaying NOMA-enabled cellular (NC) communication, i.e., a ND-NC transmission system, is crucial.

Moreover, existing RIS-based FD (RIS-FD) studies mainly concentrate on two-way communication, assuming the same user for downlink and uplink (SDU) communication, i.e., an RIS-FD-SDU system. However, in practical wireless networks, uplink and downlink transmissions may involve the same or different users. Hence, analyzing a novel RIS-FD system with different downlink and uplink (DDU) users, i.e., an RIS-FD-DDU system, is necessary. It is to note that in the RIS-FD-SDU, all RIS elements can be dedicated to the same user for coherent combining, boosting the received signal. However, in the RIS-FD-DDU system, the RIS needs spatial division into two zones: Zone-D boosts downlink transmission from the access point (AP), while Zone-U serves uplink transmissions to the AP, ensuring fairness to different users. Additionally, alternative VFD schemes should be designed for high RSI scenarios, replacing and surpassing available FD-based STAR-RIS (FD-STAR-RIS) systems in the literature. In VFD-STAR-RIS, the FD AP is substituted by two HD APs or remote radio units, with one AP serving the downlink user and the other the uplink user, leading to performance gains without SI cancellation complexity, maintaining spectrum utilization as in FD-STAR-RIS. Further enhancing system performance by managing STAR-RIS aided inter-user-interference (IUI) necessitates investigating SOP minimization and ESR maximization while adhering to user QoS requirements, optimizing power allocations, reflection amplitude, transmission amplitude, and STAR-RIS element partitioning (JPRTE).

Thus, analyzing VFD and underlay D2D based systems integrated with next-generation wireless technologies like NOMA, RIS, and STAR-RIS is crucial for designing practical communication systems for next-generation communication. This thesis aims to study these aspects under practical scenarios and optimize overall performance accordingly.

1.10 Thesis Flowchart, Outline, and Contributions

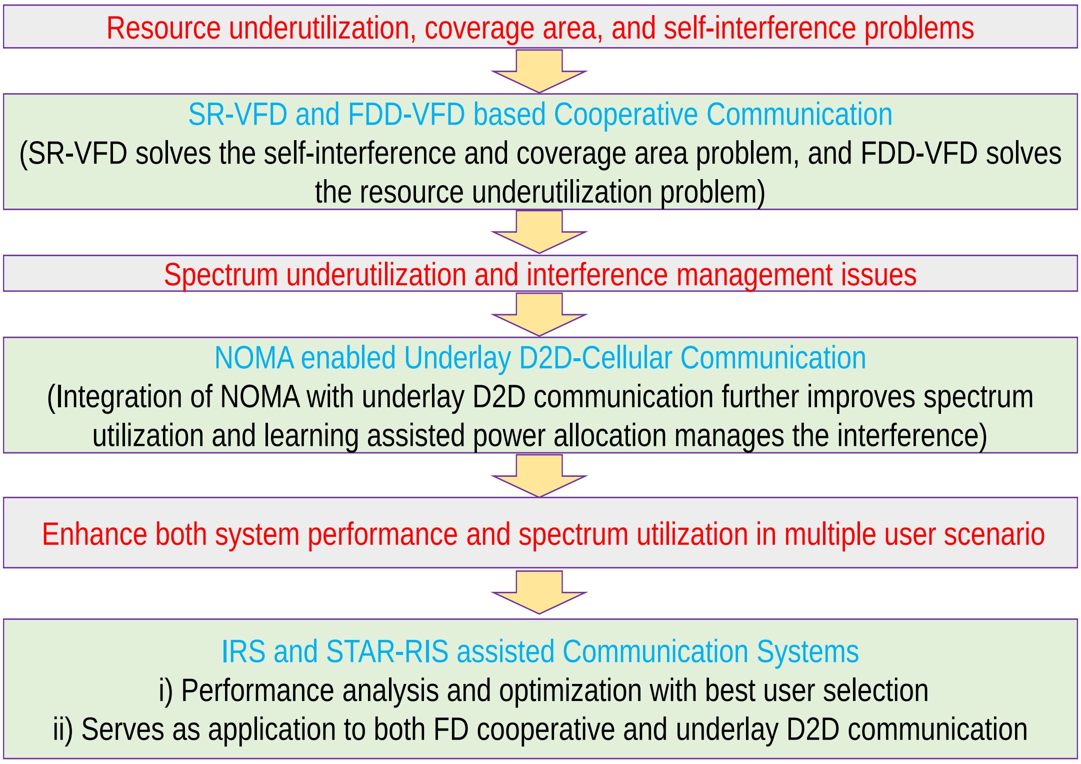

Figure 1.10: Flowchart of the thesis.

The flowchart of the thesis is shown in Figure 1.10. The thesis is organized into 7 chapters, which are briefly described with their contributions as follows:

Chapter 1. Introduction : Chapter 1 of the thesis includes a concise overview of topics such as wireless communication channels, multipath fading, channel characterization, different performance metrics, and fundamental concepts of VFD, underlay D2D, NOMA, RIS, and STAR-RIS. Additionally, it outlines the motivation behind the work and highlights the main contributions presented in the thesis.

Chapter 2. Cooperative VFD-NOMA under Imperfect SIC and Residual Inter-Relay Interference: This chapter investigates a decode-and-forward relaying based cooperative VFD-NOMA system under the impact of practical constraints like imperfect SIC and residual inter-relay interference (IRI). Framework for OP, asymptotic OP, and ER expressions is developed for the considered system model over generalized Nakagami-m fading channels. Accuracy of the derived closed-form expressions is verified through rigorous Monte-Carlo simulations. Also, the performance of the considered system is also compared against two different FD schemes, with the impact of the fading parameter and inter-relay distance also being highlighted.

Chapter 3. Frequency Division Duplexing based Cooperative VFD Communication: In comparison to FD, the VFD system models studied in the literature are based on successive relaying (SR) that require an extra time phase and a double number of relays for each destination user. Thus, in this chapter, a novel frequency division duplex (FDD) based VFD (FDD-VFD) system model is proposed that can not only match FD in terms of resource utilization but also outperform both SR-VFD and FD. Two practical scenarios of absence of IRI (A-IRI) and presence of IRI (P-IRI) are considered. We analyze the OP and ER performance metrics and present their analytical expressions in closed-form over Nakagami-m fading channels. Next, to minimize the effect of inter-relay interference in P-IRI scenario, we investigate optimization problems of minimizing the system OP (SOP) and maximizing the ergodic sum rate (ESR) for jointly allocating transmit power of the relays. We utilize particle swarm optimization (PSO) algorithm and deep neural network (DNN) architecture to solve the formulated problems. Extensive evaluations are carried out over different system parameters to prove the efficacy of proposed FDD scheme and obtain key inferences.

Chapter 4. NOMA Enabled Underlay D2D-Cellular Network: This chapter investigates a D2D underlayed cellular system where both D2D and cellular networks are NOMA enabled, which is not only more spectrally efficient than the previous D2D and NOMA models but also can outperform them. Specifically, closed-form expressions for SOP and sum ER (SER) metrics are presented for performance analysis and thereafter a DNN based power control mechanism is proposed for SOP minimization. Analytical results are validated with extensive simulations that reveal the effectiveness of the proposed model over comparative schemes and the requirement of optimizing the power values in accordance with change in different system parameters.

Chapter 5. RIS Assisted FD Systems with Different Downlink and Uplink Users: This chapter studies a FD network assisted by an RIS involving both downlink and uplink users in the same frequency band with best user selection. The RIS is partitioned into two zones to cater to each of downlink and uplink users. The analysis incorporates factors such as RSI, co-channel interference, and hardware imperfections, considering a direct link over generalized Nakagami-m fading channels. Analytical expressions for OP, SOP, and ER are derived. We also investigate the joint allocation of element splitting between the zones, user power allocations, and reflection amplitude with SOP minimization and ESR maximization as objectives. Extensive Monte-Carlo simulations are conducted to validate the analytical expressions.

Chapter 6. VFD Communication Enabled STAR-RIS Network: This chapter proposes a novel VFD communication based STAR-RIS scheme to mimic as well as outperform conventional FD based STAR-RIS communication in practical high residual self-interference scenarios. For the proposed VFD-STAR-RIS system involving multiple uplink and downlink users with user selection, analytical expressions of OP and ER are presented for downlink and uplink users. Thereafter, to minimize STAR-RIS aided inter-user interferences, we study optimization problem of JPRTE for SOP minimization and ESR maximization. A PSO algorithm based solution is used to solve the JPRTE problem of minimizing the SOP (JPRTE-SOP). However, due to the complexity involved in the ER expressions, applying PSO directly to the JPRTE problem of ESR maximization (JPRTE-ESR) will require significant convergence time. Thus, a machine learning (ML) solution is proposed where the ER expressions are first closely approximated via a ML architecture, and thereafter PSO is applied to obtain a solution having a very low computational time. Monte-Carlo simulations are carried out to demonstrate efficacy of proposed VFD-STAR-RIS scheme, JPRTE-SOP, and JPRTE-ESR solutions to draw out useful inferences.

Chapter 7. Conclusions and Future Works: All the contributions of the thesis have been summarized in this chapter, and important insights and conclusions have been presented. Further, the scope for future works is also discussed.

Chapter 2

Cooperative VFD-NOMA under Imperfect SIC and Residual Inter-Relay Interference

In recent times, NOMA and FD based transmissions have gained an increasing research attention due to their ability to bring a significant enhancement in the spectrum efficiency in comparison to traditional HD and OMA technologies. The NOMA technology utilizes superposition coding to multiplex same radio-frequency users with different fractions of the total transmission power. On other hand, in FD communications, users transmit and receive signals simultaneously over the same frequency/time resources. Additionally, FD systems can be integrated with cooperative NOMA for achieving a lower latency and ultra-reliable wireless communications [77]. In [78], the authors consider FD relaying in an AF cooperative networks and investigate the problem of optimal relay selection. Authors in [79, 80] consider FD relaying with multiple-antenna source and destination terminals. In [81], outage performance of a DF based cooperative FD system is studied. Further, in [82], the authors investigate a DF cooperative NOMA system with dedicated FD relaying to communicate with a far destination user.

However, in the FD setup, the simultaneous transmission and reception results in a very strong SI at the user equipment [83]. Further, as high computational complexity with advanced signal processing is involved in the SI cancellation process, there also exists a fundamental trade-off between hardware cost and SI cancellation capability, and thus resulting in a high RSI, as highlighted in [84, 85]. Therefore, a more recent alternative, successive relaying based VFD system has become a popular candidate over the traditional FD with reduced complexity [1, 86–89], wherein two different HD relays are used for FD such that at a time instant, one receives the signal and the other transmits alternatively. VFD provides a prominent and promising solution in combating SI by managing the IRI. In [1], the authors investigated VFD based 2-hop and the multi-hop cooperative system and considered different coding schemes such as quantize-map-and-forward and lattice-based compute-and-forward for IRI cancellation. In [86, 87], the authors considered a cooperative multi-relay VFD model and performed a Markov chain based analysis to derive closed form expressions for OP. In [88], the authors proposed a relay selection algorithm with adaptive interference management for multi-phase DF downlink VFD NOMA relay framework. Authors in [89] proposed a 3-phase transmission system in order to cancel out the IRI completely, wherein they analyzed the performance of VFD based cooperative NOMA system over Rayleigh faded channels.

2.0.1 Motivation and Contribution

The works in [88, 89] assume a perfect SIC. However, though SIC is essential in NOMA to exploit the power-difference between users, ensuring a perfect-SIC is difficult [82, 90]. Similarly, residual-IRI may exist even after interference cancellation [82]. Thus, VFD-NOMA is prone to a joint effect of residual-IRI and imperfect-SIC, the effects of which have not been studied in the existing literature. Further, the effect of large-scale path-loss is not considered in [89], thereby limiting its applicability. Furthermore, various cooperative FD and NOMA based works in [82, 91] and [92] have considered generalized Nakagami-m fading channels (for small scale fading), which can represent a variety of wireless fading environments, including distributions like Rayleigh, Rician and one-sided Gaussian as special cases. However, the previous works in VFD-NOMA in [88] and [89] have done the performance analysis over Rayleigh faded channels, and not generalized to other channel models.

Considering the aforementioned research gaps, in this chapter, detailed investigations are presented considering the joint impact of imperfect-SIC and residual-IRI on VFD-NOMA system. In particular, the significant contributions are summarized as follows:

- Nakagami-m faded links are considered along with large scale path-loss in the VFD system model.
- Closed-form expressions are derived of OP and ER for each user, with Monte-Carlo simulations being presented to verify their accuracy.
- Asymptotic OP expressions are presented along with diversity order.
- Performance of the VFD-NOMA is compared with conventional FD-NOMA and FD-OMA schemes and useful inferences are drawn out.

2.1 System Model

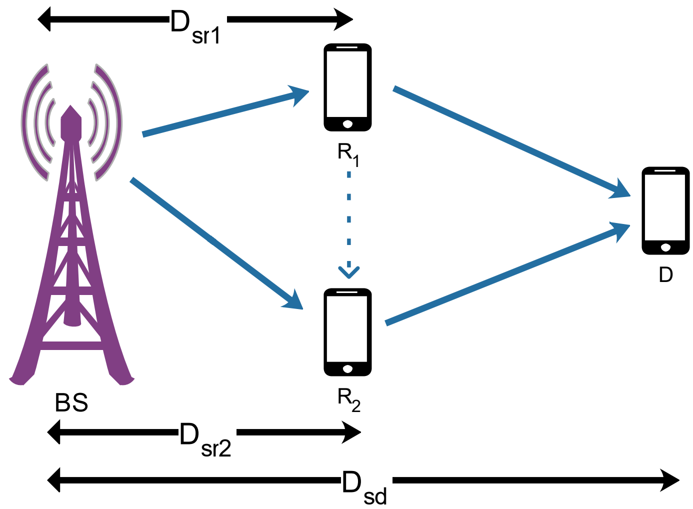

Figure 2.1: System model of VFD-NOMA.

A cooperative NOMA system is considered with a BS acting as a source (S), two single antenna users R_1 and R_2 for VFD relaying, and a single antenna user D as the destination, as shown in Figure 2.1, where D_{sd} is distance from S to D, D_{sr_1} is distance between S and R_1, and D_{sr_2} is distance between S and R_2. R_1 and R_2 are closer to BS, in comparison to D, and hence are near users in the system model, while D being considered as far user. Each ij link, where $i \in \{s, r_1, r_2\}$, $j \in \{r_1, r_2, d\}$ and $i \neq j$, is assumed to be independently flat faded Nakagami-m channel with

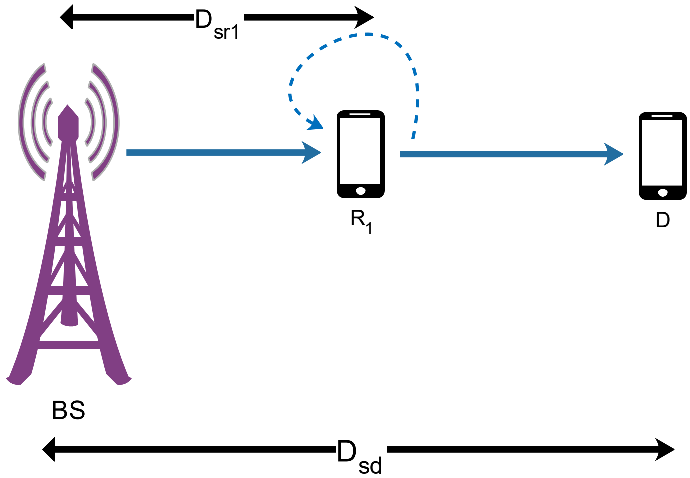

Figure 2.2: System model of FD-NOMA/FD-OMA.

distribution $Nak(m_{ij}, \overline{g}_{ij})$, where $\overline{g}_{ij} = \mathbb{E}[g_{ij}]$ and $g_{ij} = |h_{ij}|^2$. It is assumed that a direct link between S and D does not exist due to heavy shadowing. Further, it is considered that R_1 and R_2 are distant apart to avoid receiver saturation. It is to note that receiver saturation refers to the saturation of the analog-to-digital converter at the receiver. In practical wireless communication systems, each receive RF chain is characterized by a maximum input signal power level, above which saturation occurs. Thus, the SI suppression techniques in FD communication involve both the analog and digital domains, where SI is partially suppressed by analog cancellation schemes before the application of digital SI cancellation methods. On the other hand, in VFD communication, the problem of receiver saturation is eliminated by allowing a large physical separation between the half-duplex relays [93].

To improve the spectral efficiency, two users are served over same time/frequency resources using NOMA. S transmits the signal through half-duplex relays R_1 and R_2 in a successive relaying fashion where, one relay receives the signal from S and the other forwards the received signal to D alternatively and thus, effectively forming a VFD [93]. The entire transmission process is carried out in three different time phases, the details of which are explained in the next sub-section.

2.1.1 Transmission Protocol

In Phase 1, S superimposes signals $x_{r_1}(t_1)$ and $x_d(t_1)$ (i.e. signals of R_1 and D) with α and β fractions of total transmit power P_s respectively, and broadcasts it to R_1 and R_2. As in NOMA, near user is served with lower power in comparison to the far user, $\alpha < \beta$, where $\alpha + \beta = 1$ is the total power budget. R_1 and R_2 decode $x_d(t_1)$ and hence, the SINR at R_1 and R_2 are given as

$$\psi_{sr_1}^{D}(t_1) = \frac{g_{sr_1}\,\beta\,P_s}{g_{sr_1}\,\alpha\,P_s + \sigma_N^2} = \frac{g_{sr_1}\,\beta\,\rho_s}{g_{sr_1}\,\alpha\,\rho_s + 1}, \tag{2.1}$$

$$\psi_{sr_2}^{D}(t_1) = \frac{g_{sr_2}\,\beta\,\rho_s}{g_{sr_2}\,\alpha\,\rho_s + 1}, \tag{2.2}$$

where σ_N^2 is AWGN power, ρ_s is transmit SNR and $\rho_s = \frac{P_s}{\sigma_N^2}$. Then, R_1 detects its own signal $x_{r_1}(t_1)$ after removing the signal $x_d(t_1)$ through SIC. Thus, the corresponding SINR at R_1 after SIC is given as

$$\psi_{sr_1}^{R_1}(t_1) = \frac{g_{sr_1}\,\alpha\,\rho_s}{\zeta_{sr_1}\,g_{sr_1}\,\beta\,\rho_s + 1}, \tag{2.3}$$

where ζ_{sr_1} denotes the level of residual interference, with $\zeta_{sr_1} = 0$ implying perfect-SIC. In Phase 2, R_1 relays $x_d(t_1)$ to D with power $P_r = \frac{P_s}{2}$ and thus SNR at D can be given as

$$\psi_{r_1d}^{D}(t_2) = g_{r_1d}\,\rho_r. \tag{2.4}$$

where $\rho_r = \frac{P_R}{\sigma_N^2}$. Concurrently, S superimposes signals $x_{r_2}(t_2)$ and $x_d(t_2)$ (i.e. signals of R_2 and D) and transmits it to R_2. During this phase, R_2 receives a interfering signal from R_1. However, R_2 removes the IRI from R_1 through previous phase decoded signal $x_d(t_1)$. R_2 determines its own signal $x_{r_2}(t_2)$ after detecting and removing $x_d(t_2)$ through SIC. The corresponding SINR's at R_2 are given as

$$\psi_{sr_2}^{D}(t_2) = \frac{g_{sr_2}\,\beta\,\rho_s}{g_{sr_2}\,\alpha\,\rho_s + \zeta_{r_1r_2}\,g_{r_1r_2}\,\rho_r + 1}, \tag{2.5}$$

$$\psi_{sr_2}^{R_2}(t_2) = \frac{g_{sr_2}\,\alpha\,\rho_s}{g_{sr_2}\,\zeta_{sr_2}\,\beta\,\rho_s + \zeta_{r_1r_2}\,g_{r_1r_2}\,\rho_r + 1}, \tag{2.6}$$

Table 2.1: Transmission phases in VFD-NOMA, FD-NOMA and FD-OMA.

Transmission Phase	VFD-NOMA			FD-NOMA		FD-OMA	
	BS	R_1	R_2	BS	R_1	BS	R_1
1	$x_s(t_1)$	-	-	$x_s^{'}(t_1)$	$x_d(t_1)$	$x_{r_1}(t_1)$	-
2	$x_s(t_2)$	$x_d(t_1)$	-	$x_s^{'}(t_2)$	$x_d(t_2)$	$x_{r_1}(t_2)$	-
3	-	-	$x_d(t_2)$	-	-	$x_d(t_1)$	$x_d(t_1)$
4	-	-	-	-	-	$x_d(t_2)$	$x_d(t_2)$

where $\zeta_{r_1r_2}$ denotes the level of cancellation of the IRI from R_1. The transmission process completes in Phase 3 by R_2 relaying the information $x_d(t_2)$ with power P_r to D. The received SNR at D is given as

$$\psi_{r_2d}^{D}(t_3) = g_{r_2d}\,\rho_r. \tag{2.7}$$

The entire VFD-NOMA transmission protocol is summarized in Table 2.1, and compared with FD-NOMA and FD-OMA systems that require 2 and 4 transmission phases, respectively. A single relay (R_1) is employed in FD-NOMA and FD-OMA schemes as shown in Figure 2.2.

2.2 Performance Analysis

2.2.1 Outage Probability at R_1

Let u_d and u_r be target SINR's of the destination user and relays, respectively. The probability that R_1 can successfully decode the signals $x_d(t_1)$ and $x_{r_1}(t_1)$ can be given by $\Pr(g_{sr_1} \geq \frac{u_d}{\rho_s(\beta-u_d\alpha)})$ and $\Pr(g_{sr_1} \geq \frac{u_r}{\rho_s(\alpha-u_r\,\zeta_{sr_1}\beta)})$ respectively. Outage at R_1 is said to happen if it either fails to decode $x_d(t_1)$ or $x_{r_1}(t_1)$ and is obtained by applying [94, eq. 3.381.9] as

$$P_{out,R_1} = 1 - \prod_{i=\{1,2\}} \frac{\Gamma(m_{sr_1}, \mu_{sr_1}T_i)}{\Gamma(m_{sr_1})}, \tag{2.8}$$

where $T_1 = \frac{u_d}{(\beta-u_d\alpha)}$. $\mu_{sr_i} = \frac{m_{sr_i}}{\rho_s\,\bar{g}_{sr_i}}$, where $i \in \{1,2\}$ and $T_2 = \frac{u_r}{(\alpha-u_r\,\zeta_{sr_1}\beta)}$. As T_1 and T_2 are thresholds corresponding to channel gain, they cannot be negative. Thus, using (2.8), the range of α is determined as $\frac{u_r\,\zeta_{sr_1}}{1+u_r\,\zeta_{sr_1}} < \alpha < \frac{1}{1+u_d}$.

2.2.2 Outage Probability at R_2

The probability that R_2 can successfully decode the signal $x_d(t_1)$ is $\frac{\Gamma(m_{sr_2},\mu_{sr_2}\,T_1)}{\Gamma(m_{sr_2})}$. Also, the probability that R_2 can successfully decode the signals $x_d(t_2)$ and $x_{r_2(t_2)}$ are determined as $1-\Pr(\frac{c_1\,g_{sr_2}}{\zeta_{r_1r_2}\,\rho_r\,g_{r_1r_2}+1} < 1)$ and $1-\Pr(\frac{c_2\,g_{sr_2}}{\zeta_{r_1r_2}\,\rho_r\,g_{r_1r_2}+1} < 1)$ respectively, where $c_1 = \frac{\rho_s(\beta-u_d\alpha)}{u_d}$ and $c_2 = \frac{\rho_s(\alpha-u_r\,\zeta_{sr_2}\beta)}{u_r}$. Utilizing the Nakagami-m PDF expression [95] and using [94, 8.352.6, 3.381.4, 1.111], the exact closed-form OP expression of R_2 can be derived as

$$P_{out,R_2} = 1 - \frac{\Gamma(m_{sr_2},T_{51})}{\Gamma(m_{sr_2})} \prod_{i=\{1,2\}} \frac{{T_4}^{m_{r_1r_2}}}{\Gamma(m_{r_1r_2})} e^{-T_{5i}} {T_{5i}}^{n} \times \frac{\mathbb{K}_1(k,n)}{(T_{5i}+T_4)^{k+m_{r_1r_2}}}, \tag{2.9}$$

where $T_4 = \frac{\mu_{r_1r_2}}{\zeta_{r_1r_2}}$, $T_{51} = \mu_{sr_2}T_1$, $T_{52} = \frac{\mu_{sr_2}\,u_r}{\alpha-u_r\,\zeta_{sr_2}\,\beta}$ and $\mu_{r_1r_2} = \frac{m_{r_1r_2}}{\rho_r\,\bar{g}_{r_1r_2}}$. $\mathbb{K}_1(p,q) = \sum_{q=0}^{m_{sr_2}-1}\mathbb{K}_2(p,q)$ and $\mathbb{K}_2(p,q) = \sum_{p=0}^{q}\frac{\Gamma(p+m_{r_1r_2})}{p!\,(q-p)!}$.

2.2.3 Outage Probability at D

An outage event at D is defined as D fails to decode the signal transmitted by either R_1 or R_2. Therefore, exact closed-form OP expression of D can be derived as

$$P_{out,D} = 1 - \prod_{i=\{1,2\}} \frac{\Gamma(m_{sr_i},\,\mu_{sr_i}T_1)\,{T_4}^{m_{r_1r_2}}\,{T_{51}}^{n}\,\mathbb{K}_1(k,n)}{\Gamma(m_{sr_i})\,\Gamma(m_{r_1r_2})\,e^{T_{51}}\,(T_{51}+T_4)^{k+m_{r_1r_2}}} \prod_{j=\{1,2\}} \frac{\Gamma(m_{r_jd},\mu_{r_jd}\,u_d)}{\Gamma(m_{r_jd})}, \tag{2.10}$$

where $\mu_{r_id} = \frac{m_{r_id}}{\rho_r\,\bar{g}_{r_id}}$.

2.2.4 Asymptotic Analysis

In this subsection, high SNR analysis of the considered system model is performed by taking $\rho_s \to \infty$ to derive asymptotic OP expressions in the form $(G_{c,i}\rho_s)^{-G_{d,i}}$ (where $G_{d,i}$ and $G_{d,i}$ are diversity order and coding gain of the user i) corresponding to R_1, R_2, and D as

$$P^{\infty}_{out,R_1} = ({Y_{sr_1}}^{-1}\rho_s)^{-m_{sr_1}}, \tag{2.11}$$

$$P^{\infty}_{out,R_2} = ((Z_{sr_2}T_1)^{-1}\rho_s)^{-m_{sr_2}} + \mu_{sr_2}^{m_{sr_2}} Z(n, m_{sr_2}), \tag{2.12}$$

$$P^{\infty}_{out,D} = \sum_{i=\{1,2\}} ((Z_{sr_i}T_1)^{-1}\rho_s)^{-m_{sr_i}} + \sum_{j=\{1,2\}} ({Z_{r_jd}}^{-1}\rho_s)^{-m_{r_jd}} + {T_{51}}^{m_{sr_2}} Z(n, m_{sr_2}), \tag{2.13}$$

where $Z_{sr_i} = \rho_s\, \mu_{sr_i}(m_{sr_i}!)^{\frac{-1}{m_{sr_i}}}$. Further, $Z_{r_jd} = 2\,\rho_s\, \mu_{r_jd}\, u_d(m_{r_jd}!)^{\frac{-1}{m_{r_jd}}}$, $Z(n, m_{sr_2}) = \frac{\mathbb{K}_2(n,m_{sr_2})}{T_4^n\,\Gamma(m_{r_1r_2})}$ and $Y_{sr_1} = Z_{sr_1}(\sum_{i=\{1,2\}}(T_i)^{m_{sr_1}})^{\frac{-1}{m_{r_jd}}}$. From the above equations, G_{d,R_1}, G_{d,R_2} and $G_{d,D}$ can be easily obtained as m_{sr_1}, 0 and 0, respectively. Additionally, with $\zeta_{r_1r_2} = 0$, G_{d,R_2} and $G_{d,D}$ are equal to m_{sr_2} and $min(m_{sr_1}, m_{sr_2}, m_{r_1d}, m_{r_2d})$, respectively. Also, G_{c,R_1}, G_{c,R_2} can be obtained as ${Y_{sr_1}}^{-1}$ and $(Z_{sr_2}T_1)^{-1}$, respectively. Further, $G_{c,D}$ can be obtained as $(Z_{sr_1}T_1)^{-1}$, $(Z_{sr_2}T_1)^{-1}$, ${Z_{r_1d}}^{-1}$ and ${Z_{r_2d}}^{-1}$, corresponding to when $G_{d,D}$ equals m_{sr_1}, m_{sr_2}, m_{r_1d} and m_{r_1d}, respectively.

2.2.5 Ergodic Rate

The ERs of R_i (where $i \in \{1, 2\}$) and R_D can thus be expressed as

$$C_{R_i} = \frac{1}{3\ln 2}\int_0^{\frac{\alpha}{\zeta_{sr_i}\beta}} \frac{1 - F_{\psi^{R_i}_{sr_i}(t_i)}(x)}{1+x}\,dx, \tag{2.14}$$

$$C_D = \frac{1}{3\ln 2}\sum_{i=\{1,\,2\}}\int_0^{\frac{\beta}{\alpha}} \frac{1 - F_{X_i}(x_i)}{1+x_i}\,dx_i, \tag{2.15}$$

where $F_{\psi^{R_i}_{sr_i}(t_i)}(x) = Pr(\psi^{R_i}_{sr_i}(t_i) < x)$ and $X_i = \min(\psi^D_{sr_i}(t_i), \psi^D_{r_id}(t_{i+1}))$. Utilizing [94, 8.352.6, 3.381.4, 1.111] and the basic Gaussian-Chebyshev quadrature (GCQ) relation [96] given by $\int_{-1}^{1} \frac{f(x)}{\sqrt{1-x^2}}\, dx = \frac{\pi}{L} \sum_{l=1}^{L} f[\cos(\frac{(2l-1)\pi}{2L})]$, approximate ER expressions are obtained corresponding to R_1, R_2, and D, as

$$C_{R_1} = \sum_{n=0}^{m_{sr_1}-1} \frac{(\mu_{sr_1})^n}{n!}\ \mathbb{A}(1, \zeta_{sr_1}\beta, 0, \Omega_{R_1}, 1, 0), \tag{2.16}$$

$$C_{R_2} = (\mu_{sr_2})^n\, \mathbb{K}_1(k,n)\ \mathbb{A}(2, \zeta_{sr_2}\beta, 0, \Omega_{R_2}, 1, 1), \tag{2.17}$$

$$\begin{aligned} C_D = \sum_{n=0}^{m_{sr_1}-1} \frac{(\mu_{sr_1})^n}{n!} \sum_{k=0}^{m_{r_1d}-1} & \frac{(\mu_{r_1d})^k\, \mathbb{A}(1, \alpha, 1, \Omega_D, k+1, 0)}{k!} + \frac{\mathbb{K}_1(k,n)}{(\mu_{sr_2})^{-n}} \\ & \sum_{p=0}^{m_{r_2d}-1} \frac{(\mu_{r_2d})^p\, \mathbb{A}(2, \alpha, 1, \Omega_D, p+1, 1)}{p!}, \end{aligned} \tag{2.18}$$

where $\Phi_l = \frac{1+\phi_l}{1-\phi_l}$. $\Omega_{R_i} = \frac{\alpha\,(\phi_l+1)}{2\,\zeta_{sr_i}\beta}$ and $\Omega_D = \frac{\beta\,(\phi_l+1)}{2\,\alpha}$. Further

$$\begin{aligned} \mathbb{A}(i, \Delta_1, \theta_1, \Delta_2, \theta_2, \theta_3) = & \frac{\pi}{3\,L\,\ln 2}\Big(\frac{{T_4}^{m_{r_1r_2}}}{\Gamma(m_{r_1r_2})}\Big)^{\theta_3} \sum_{l=1}^{L} e^{-(\frac{\mu_{sr_i}\Phi_l}{\Delta_1}+\theta_1\mu_{r_id}\,\Omega_D)}\ \Big(\frac{\Phi_l}{\Delta_1}\Big)^n \\ & \times \frac{{\Delta_2}^{\theta_2}\sqrt{1-\phi_l^2}}{(1+\Delta_2)\,(1+\phi_l)\,(\frac{\mu_{sr_i}\Phi_l}{\Delta_1}+T_4)^{\theta_3(k+m_{r_1r_2})}}, \end{aligned} \tag{2.19}$$

where $\phi_l = \cos(\frac{(2l-1)\pi}{2L})$ and the parameter L denotes the accuracy-complexity trade-off.

2.3 Results and Discussions

This section assesses performance of the considered system using Monte-Carlo simulations, and draw out useful inferences. Considering $\overline{g}_{ij} = (\frac{D_{sd}}{D_{ij}})^{\eta}$, where D_{ij} is distance between node i and j, and η is path-loss exponent [97]. Unless otherwise specified, $P_s = 1$, $\eta = 3$, $\alpha = 0.3$, and $\zeta_{ij} = 0.3$, where $i \in \{s, r_1, r_2\}$ and $j \in \{r_1, r_2\}$. The values of $\{D_{sr_1}, D_{sr_2}, D_{r_1r_2}\}$ are taken as $\{3\,D_{sd}/7, D_{sd}/7, 3\,D_{sd}/7\}$,

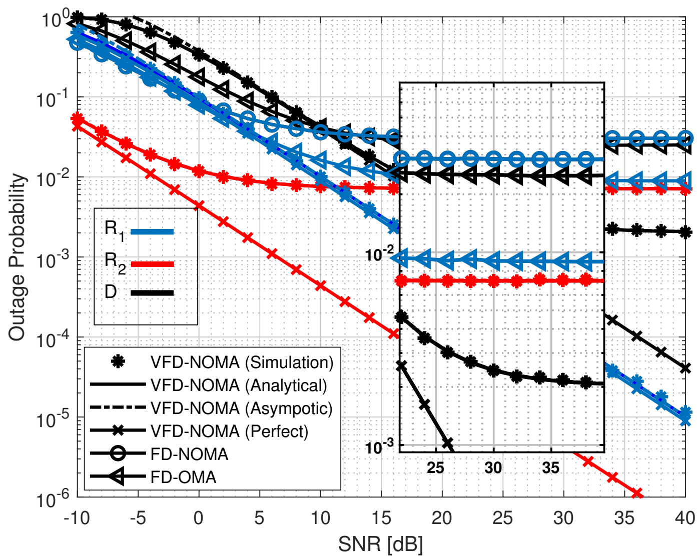

Figure 2.3: OP vs SNR for cases of imperfect-SIC/residual-IRI and perfect-SIC/perfect-IRI.

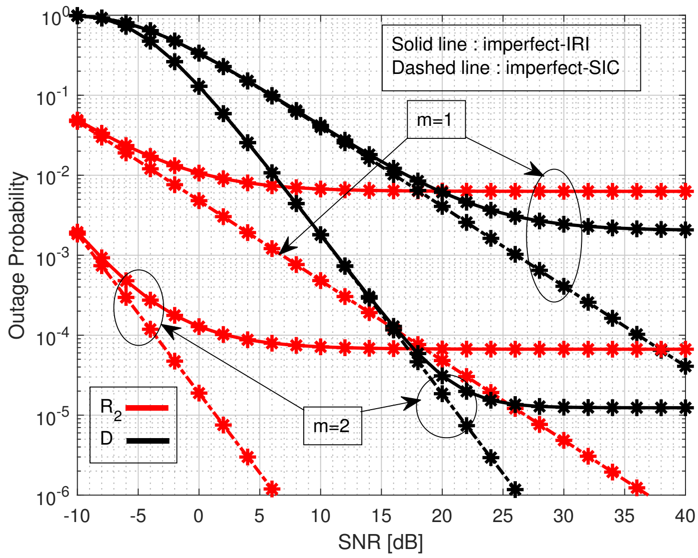

Figure 2.4: OP vs SNR for cases of perfect-SIC/residual-IRI and imperfect-SIC/perfect-IRI.

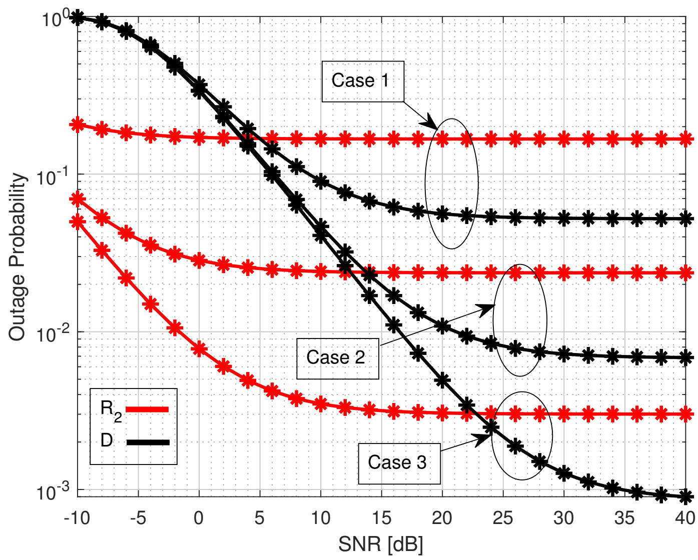

Figure 2.5: OP vs SNR comparison of R_2 and D for distinct values of inter-relay distance D_{r1r2}.

with $D_{r_1d} = 1 - D_{sr_1}$ and $D_{r_2d} = 1 - D_{sr_2}$. The results are compared with FD-NOMA and FD-OMA, that require 2 and 4 transmission phases, respectively. R_1 is employed in these schemes for FD relaying considering imperfect-SIC and a RSI of -3 dB [82]. Further, for FD-OMA, power budget is maintained.

In Figure 2.3, exact, asymptotic and simulation OP results of imperfect-SIC/residual-IRI and perfect-SIC/perfect-IRI are depicted over SNR. It is observed that there is a significant impact of both imperfect-SIC and residual-IRI on R_2 and D, with constant outage performance in the high SNR regime. On other hand, R_1 is least affected due to the presence of imperfect-SIC alone and thus is also seen to have a much higher performance than the compared FD schemes. Further, for SNR of 34 dB, R_2 is also observed to have 77% and 92% times lower OP than FD-NOMA and FD-OMA respectively. Similarly, it is observed that the outage performance of D is higher approximately by a 10 fold, in comparison to both the FD schemes. This happens due to a high RSI effect on these FD systems, in comparison to residual-IRI which depends on $D_{r_1r_2}$. Further, the derived analytical results are observed to match well with the simulation results.

Figure 2.4 shows OP performance of R_2 and D for fading parameters values $m = 1$ and $m = 2$ ($m_{ij} = m$, where $i \in \{s, r_1, r_2\}$ and $j \in \{r_1, r_2, d\}$) over scenarios of perfect-SIC/residual-IRI and imperfect-SIC/perfect-IRI. It is observed that the

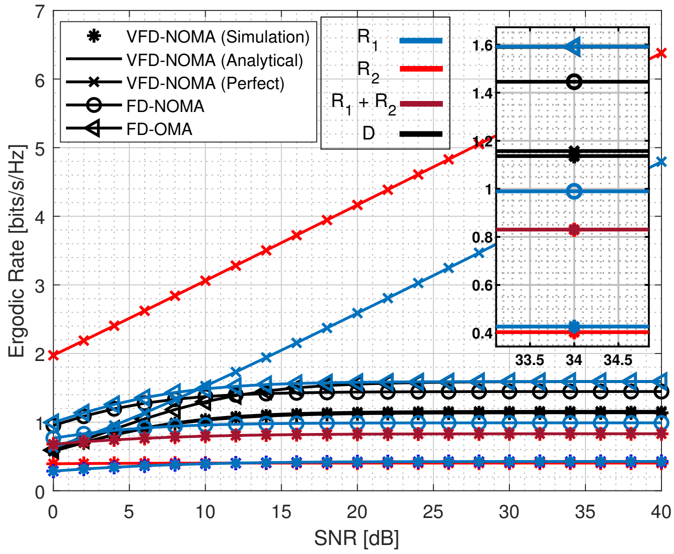

Figure 2.6: ER vs SNR for $D_{sr_1} = 3D_{SD}/7$.

system performs better as the value of m increases. Also, in a perfect-SIC/residual-IRI scenario, R_2 is observed to obtain higher OP than D as it gets affected by IRI while decoding the signal corresponding to D, prior to its own signal. Further, the presence of residual-IRI causes the VFD-NOMA system to operate in an interference limited environment, and thus the OP is seen to saturate with increase in SNR. Additionally, the non-zero outage floor explains the reason behind the zero diversity order obtained for R_2 and D. Therefore, it is reasonable to observe the impact of residual-IRI being more on the system in comparison to imperfect-SIC, especially in the high SNR region.

Figure 2.5 illustrates the outage performance comparison of R_2 and D for three distinct inter-relay distance cases $D_{r1r2} = D_{sd}/7$, $2D_{sd}/7$ and $4D_{sd}/7$. For an SNR of 34 dB, it is observed that case 2 with $D_{r1r2} = 2D_{sd}/7$ has an approximate OP improvement for R_2 and D of 86% and 87% respectively, over case 1 with $D_{r1r2} = D_{sd}/7$. For the same SNR value, case 3 with $D_{r1r2} = 4D_{sd}/7$ shows an approximate increase in the outage performance of the two users by 87% and 85%, respectively over case 2. This is because, with the increase in D_{r1r2}, the inter-relay link path-loss gain decreases, which in turn reduces residual-IRI at R_2, as can be deduced from expressions of $\psi^{D}_{sr_2}(t_2)$ and $\psi^{R_2}_{sr_2}(t_2)$. Therefore, the performance of the system can be enhanced by developing suitable strategies that aim proper selection of the near users such that the residual-IRI is minimized.

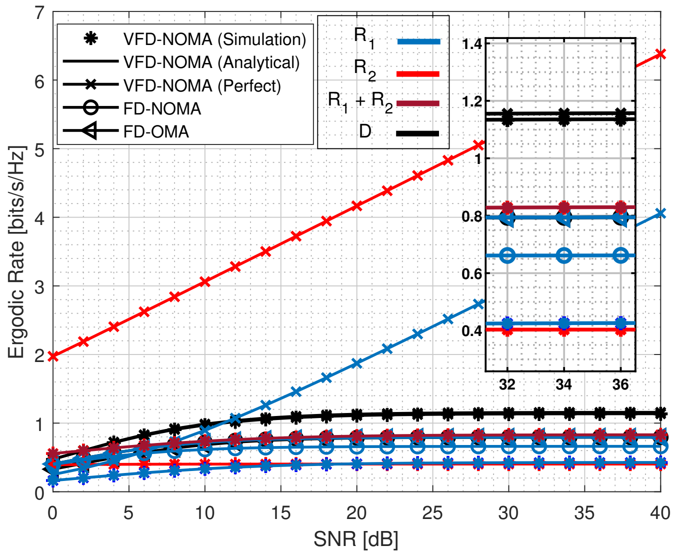

Figure 2.7: ER vs SNR for $D_{sr_1} = 5D_{SD}/7$.

In Figure 2.6 and Figure 2.7, results of ERs are presented over SNR for two distinct values of D_{sr_1}, compared with the case of perfect-SIC/perfect-IRI. It is reasonable to observe ERs of users to be lower for the imperfect case in comparison to the perfect case. Further, as seen in Figure 2.6, owing to a higher pre-log factor in FD-NOMA in comparison to VFD-NOMA (i.e., 1/2 versus 1/3) and a higher transission power of FD-OMA for R_1 (i.e., $P_s/2$ versus αP_s), the FD schemes can be seen to achieve a higher ER. It is to note (and as also mentioned earlier) that this higher rate comes at the cost of a lower outage performance. However, as shown in Figure 2.7, for a SNR of 34 dB, the ER of D is seen to be 43% higher than FD schemes. Although, the rates of R_1 and R_2 are seen to be less due to HD operation, their combined rate is seen to be 25% and 5% higher than in FD-NOMA and FD-OMA, respectively. Thus, as R_1 is located away from BS, the increased path-loss causes the RSI effect to become dominant, and thus leading to a drop in performance in the FD schemes. However, unaffected by RSI, VFD-NOMA outperforms the FD schemes even with the joint impact of imperfect-SIC and residual-IRI, and thus optimization of relay location is needed. Furthermore, the derived analytical expressions are seen to match closely with the simulation results.

2.4 Summary

This chapter investigates cooperative VFD-NOMA under the impact of imperfect SIC and residual IRI. Analytical OP and ER expressions are derived for the VFD-NOMA system under the impact of imperfect-SIC and residual-IRI over generalized Nakagami-m fading environment. The performance of the considered system is also compared against FD-NOMA and FD-OMA schemes, with the impact of the fading parameter and inter-relay distance also being highlighted. The analytical results are seen to be in close agreement with the Monte-Carlo simulation results. Furthermore, the users are observed to have better performance in comparison to the FD schemes even with the effect of imperfect-SIC and residual-IRI. The results also reveal the necessity of optimizing the relay locations. Notably, the VFD model under consideration requires twice the number of relays and an additional time phase as compared to the two counterpart FD schemes. Consequently, new VFD models to be developed that can efficiently utilize both relay and time resources.

Chapter 3

Frequency Division Duplexing based Cooperative VFD Communication

In the previous chapter and the existing works in [1, 89, 98–105], the VFD system model studied is based on SR that require a double number of relays for each destination user and an extra time phase compared to FD. Thus, the improved system performance in these SR-VFD schemes come at the price of a poor resource utilization. Thus, in this chapter, a novel FDD-VFD system model is proposed that can not only match FD in terms of resource utilization but also outperform both SR-VFD and FD.

Moreover, various VFD system models have been studied in the literature with some considering the A-IRI [98–101] assuming that the relays are located far from each other or relays with directional antennas and fixed infrastructure are used while others have analyzed the performance in the P-IRI [1, 89, 102–105]. However, majority of the previous P-IRI works study only the performance analysis part and do not focus on relay power optimization, that infact forms an important role in the design of VFD systems in order to control the IRI. Thus, in this chapter, to minimize the IRI, the problem of relay power allocation is investigated for SOP minimization and ESR maximization. The main contributions of this chapter in particular are as follows:

- A unique FDD-VFD model is proposed and compared with conventional SR-

VFD and FD models.

- For the FDD-VFD model, both the practical scenarios of A-IRI and P-IRI are investigated. Closed-form expressions of OP and ER are presented over Nakagami-m fading distribution.

- Optimization problems of power allocation of relays for P-IRI case are studied corresponding to SOP minimization and ESR maximization.

- Given the sophisticated form of the SOP expression, PSO method is utilized to obtain joint transmit power allocation for the two relays.

- Due to GCQ approach in obtaining ER, applying PSO directly to maximize the same will require a significant amount of computational time and would increase the latency. Thus, to address the issue for ultra-low latency based machine critical applications, a practically realizable DNN based solution is proposed wherein the ESR expression in the objective is first approximated utilizing a DNN architecture. Thereafter, the PSO algorithm is applied to obtain a solution with significantly reduced computational time.

- System performance is extensively analyzed for various system parameter values to evaluate the proposed FDD-VFD system and DNN-based PSO (DNN-PSO) solution, and attain useful insights.

3.1 System Model

A cooperative communication network is studied where a BS acting as a source (S) serves two far destination users D_1 and D_2 through two DF relays R_1 and R_2, respectively, as shown in Figure 6.1. It is assumed that a direct link between S and the destination users is absent due to heavy shadowing and path loss. Also, the HD relays R_1 and R_2 are able to communicate with FDD technique [106–108] and are at sufficient distance from each other such that there is no receiver saturation. Each communication link ij , where $i \in \{s, r_1, r_2\})$ and $j \in \{r_1, r_2, d_1, d_2\}$, such that $i \neq j$ is assumed to be non-identically distributed, independent, and modeled

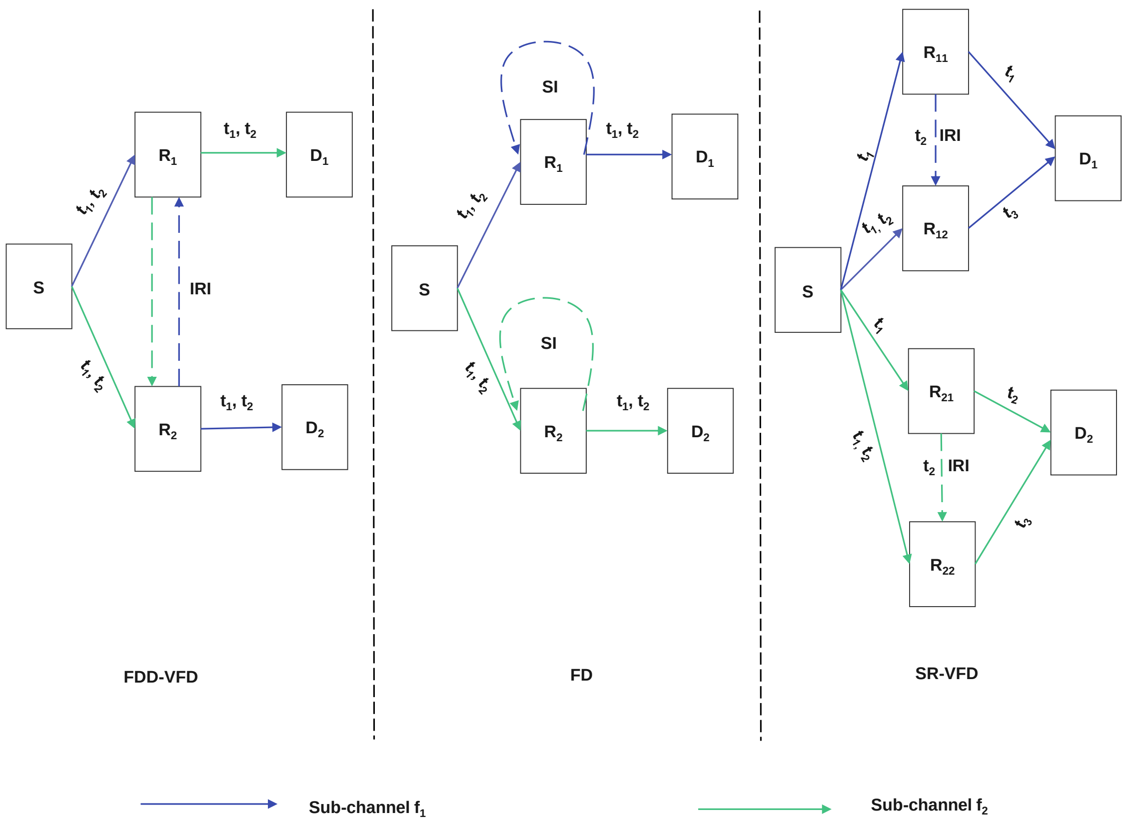

Figure 3.1: System model comparisons of FDD-VFD, FD and SR-VFD.

Table 3.1: Transmission phases in SR-VFD

Phase	S	R_{i1}	R_{i2}
t_1	$x_{d_i}(t_1)$	-	-
t_2	$x_{d_i}(t_2)$	$x_{d_i}(t_1)$	-
t_3	-	-	$x_{d_i}(t_2)$

by $Nak(m_{i,j}, \overline{g}_{i,j})$, where $\overline{g}_{i,j} = \mathbb{E}\{[|h_{i,j}|^2]\}$, $g_{ij} = |h_{ij}|^2$, and h_{ij} is channel coefficient of the link between transmitting antenna of node i and receiving antenna of node j.

Two orthogonal frequency bands or sub-channels (f_1 and f_2) are considered in the network. It is to note that there are various works in the literature which similarly consider the availability of orthogonal sub-channels in downlink communication networks and perform channel allocation to users [109–111]. Also, the FDD-VFD analysis remains relevant even when considering a single-source-single-destination network. In such a scenario, S is replaced by two distinct sources, namely S_1 and S_2. Without any loss of generality, at time t_k ($k \in \{1, 2\}$), it is assumed that BS transmits symbol $x_{d_1}(t_k)$ to R_1 using sub-channel f_1. R_1 then decodes and forwards

$x_{d_1}(t_k)$ to D_1 using the sub-channel f_2. On the contrary, R_2 receives symbol $x_{d_2}(t_k)$ from BS using channel f_2 and transmits it to D_2 using f_1. Comparatively, in FD, $S \rightarrow R_1$ and $R_1 \rightarrow D_1$ communications happen through f_1 at the time t_k. Similarly, $S \rightarrow R_2$ and $R_2 \rightarrow D_2$ communications happen through f_2. Thus, in FDD-VFD, though the two relays individually operate in HD mode, the overall communication system is virtually FD as only two frequency bands are utilized for the two destination users, thereby making the spectral efficiency same as in the case of FD. Moreover, due to the proposed channel assignment (CA), FDD-VFD is affected by distance dependent IRI in comparison to high SI and RSI in FD.

Further, the CA in SR-VFD is the same as that of FD, with the difference that each destination has to be assisted by two relays, thus requiring four relays in total (R_{11}, R_{12}, R_{21}, R_{22}) [89, 104]. Specifically, at time t_1, BS transmits $x_{d_i}(t_1)$ ($i \in \{1, 2\}$) to R_{i1} and R_{i2} using f_i. During the next time phase t_2, R_{i1} forwards $x_{d_i}(t_1)$ to D_i using f_i. At the same time and using the same channel f_i, BS transmits a new symbol $x_{d_i}(t_2)$ to R_{i2}. Thus, R_{i2} also receives an IRI from R_{i1}. Though, R_{i2} can remove the IRI through previous phase decoded signal $x_{d_i}(t_1)$, residual-IRI may still exist even after the interference cancellation process with $\zeta_r \in [0, 1]$ level of cancellation where $\zeta_r = 0$ implying perfect cancellation [104]. In the final phase t_3, R_{i2} decodes $x_{d_i}(t_2)$ and forwards to D_i. It is to note here that the SR-VFD model requires three time phases to transmit a total of two symbols. Thus, both FD and FDD will require two time slots each to transmit the two symbols as shown in Table 1. The received signal at R_1 ($y_{r_1}(t_k)$) and D_1 ($y_{d_1}(t_k)$) at k^{th} time slot (where $k \in \{1, 2\}$) is given by

$$y_{r_1}(t_k) = \sqrt{P_s}\, x_{d_1}(t_k)\, h_{sr_1} + \zeta \sqrt{P_{r_2}}\, x_{d_2}(t_k)\, h_{r_2 r_1} + n_{r_1}(t_k), \tag{3.1}$$

$$y_{d_1}(t_k) = \sqrt{P_{r_1}}\, x_{d_1}(t_k)\, h_{r_1 d_1} + n_{d_1}(t_k), \tag{3.2}$$

where P_s, P_{r_1} and P_{r_2} are transmit powers of S, R_1, and R_1, respectively. $n_i(t_k)$ is the additive white Gaussian noise (AWGN) noise at node i (where $i \in \{r_1, r_2, d_1, d_2\}$) and is modeled as $n_i \sim \mathcal{CN}(0, \sigma_n^2)$. ζ is a binary variable such that $\zeta = 0$ and $\zeta = 1$ denote A-IRI and P-IRI scenarios, respectively. Correspondingly, the SINR's at R_1

and D_1 is given by

$$\psi_{r_1}(t_k) = \frac{\rho_s \, g_{sr_1}}{\zeta \, \rho_{r_2} \, g_{r_2 r_1} + 1}, \tag{3.3}$$

$$\psi_{d_1}(t_k) = \rho_{r_1} \, g_{r_1 d_1}, \tag{3.4}$$

where $\rho_s = \frac{P_s}{\sigma_n^2}$, $\rho_{r_1} = \frac{P_{r_1}}{\sigma_n^2}$ and $\rho_{r_2} = \frac{P_{r_2}}{\sigma_n^2}$. Similarly, the received signal at R_2 and D_2 and their SINR's are given by

$$y_{r_2}(t_k) = \sqrt{P_s} \, x_{d_2}(t_k) \, h_{sr_2} + \zeta \sqrt{P_{r_1}} \, x_{d_1}(t_k) \, h_{r_1 r_2} + n_{r_2}(t_k), \tag{3.5}$$

$$y_{d_2}(t_k) = \sqrt{P_{r_2}} \, x_{d_2}(t_k) \, h_{r_2 d_2} + n_{d_2}(t_k), \tag{3.6}$$

$$\psi_{r_2}(t_k) = \frac{\rho_s \, g_{sr_2}}{\zeta \, \rho_{r_1} \, g_{r_1 r_2} + 1}, \tag{3.7}$$

$$\psi_{d_2}(t_k) = \rho_{r_2} \, g_{r_2 d_2}. \tag{3.8}$$

3.2 Performance Analysis

In this section, OP, SOP, ER, and ESR of the proposed FDD-VFD system model is analyzed. Outage probability is a very crucial metric to evaluate the reliability of slowly varying fading channels. It is defined as the probability of the end-to-end SINR of the system falling below a pre-defined threshold [112–114], where the end-to-end SINR refers to the minimum of SINR at the relay and the SINR at destination [89]. On the other hand, ER is determined by the expected value of the instantaneous mutual information between the transmitter and the receiver [115]. ER is useful for delay-insensitive services, as due to probabilistic averaging, the transmission time is required to be very long so as to reveal the long-term ergodic properties of the fading process. Let T_1 and T_2 be the target rates of the destination users D_1 and D_2, respectively. Accordingly, the OP, SOP, ER and ESR expressions are derived subsequently in the sub-sections.

3.2.1 Outage Probability for A-IRI scenario

Assuming that h_{sr_i} and $h_{r_id_i}$ are quasi-static over the two time slots and considering $\zeta = 0$ in the SINR expressions, OP of D_i (where $i \in \{1, 2\}$) for A-IRI scenario is given by

$$O_{d_i} = 1 - \Pr\left(\frac{1}{2}\log_2\left(1 + \rho_s\, g_{sri}\right) > T_i\right) \\ \times \Pr\left(\frac{1}{2}\log_2\left(1 + \rho_{r_i} g_{r_id_i}\right) > T_i\right). \tag{3.9}$$

Now, utilizing [94, eq. 3.381.9], the exact closed-form outage probability, the expression in (3.10) can be obtained as

$$O_{d_i} = 1 - \Gamma\left(m_{sr_i}, \frac{m_{sr_i}\,\delta_i}{g_{sr_i}\rho_s}\right) \frac{\Gamma\left(m_{r_id_i}, \frac{m_{r_id_i}\,\delta_i}{g_{r_id_i}\rho_{r_i}}\right)}{\Gamma\left(m_{sr_i}\right)\Gamma\left(m_{r_id_i}\right)}, \tag{3.10}$$

where $\delta_i = 2^{2T_i} - 1$.

3.2.2 Outage Probability for P-IRI scenario

OP of D_i in P-IRI scenario considering $\zeta = 1$ and quasi-static fading is given by

$$A_{i1} = \int_0^\infty \Pr(\rho_s\, g_{sr_i} > (y_1 + 1)\,\delta_i)\, f_{Y_1}(y_1)\, dy_1, \tag{3.11}$$

where $Y_1 = \rho_{r_j}\, g_{r_jr_i}$ and $f_{Y_1}(y_1)$ is the PDF of Y_1 [116]. Now, using the identities [94, eq. (3.381.9)] and [94, eq. (8.352.7)], (5.38) is resolved as

$$A_{i1} = \int_0^\infty e^{-\frac{m_{sr_i}(y_1+1)}{\rho_s\,\overline{g}_{sr_i}(\delta_i)^{-1}}} \sum_{n_1=0}^{m_{sr_i}} \left(\frac{m_{sr_i}(y_1+1)}{\rho_s\,\overline{g}_{sr_i}\delta_i^{-1}}\right)^{n_1} \\ \times \frac{1}{n_1!}\frac{e^{-\frac{m_{r_jr_i}y_1}{\rho_{r_j}\,\overline{g}_{r_jr_i}}}}{y^{1-m_{r_jr_i}}\Gamma(m_{r_jr_i})}\left(\frac{m_{r_jr_i}}{\rho_{r_j}\,\overline{g}_{r_jr_i}}\right)^{m_{r_jr_i}} dy_1. \tag{3.12}$$

Finally, using [94, eq. (1.111)] and [94, eq. (3.381.4)] in the above expression and utilizing [94, eq. 3.381.9] for A_{i2}, the final closed-form expression is obtained as

$$\hat{O}_{d_i} = 1 - \mathcal{J}_0\left(s, r_i, r_j, \frac{\rho_s\, g_{sr_i}}{\delta_i}, \rho_{r_j}\overline{g}_{r_j r_i}\right)\frac{1}{\Gamma(m_{r_i d_i})}\Gamma\left(m_{r_i d_i}, \frac{m_{r_i d_i}\delta_i}{\overline{g}_{r_i d_i}\rho_{r_i}}\right), \tag{3.13}$$

where $\mathcal{J}_0(\theta_1, \theta_2, \theta_3, \theta_4, \theta_5) = \frac{e^{-(\frac{m_{12}}{\theta_4})}}{\Gamma(m_{32})}(\frac{m_{32}}{\theta_5})^{m_{32}} \times \sum_{n_1=0}^{m_{12}-1}(\frac{m_{12}}{\theta_4})^{n_1}\sum_{n_2=0}^{n_1}\frac{\Gamma(n_2+m_{32})}{n_2!(n_1-n_2)!}(\frac{m_{12}}{\theta_4}+\frac{m_{32}}{\theta_5})^{-(n_2+m_{32})}$, $m_{xy} \triangleq m_{\theta_x\theta_y}\ \forall x, y \in \{1, 2, 3\}$.

3.2.3 System Outage Probability

The SOP of the FDD-VFD for P-IRI scenario can be defined as the probability that either of the two relays or the two destination users in the network fails to decode the corresponding symbol successfully [117]. In other words, the SOP is given by

$$\hat{O}_{SOP} = 1 - \mathcal{P}_{success}, \tag{3.14}$$

where $\mathcal{P}_{success}$ is the probability that R_1, R_2, D_1, and D_2 decode the symbols successfully. Accordingly, $\mathcal{P}_{success}$ is determined as

$$\begin{aligned}\mathcal{P}_{success} = \prod_{i=\{1,2\}} &\Pr\left(\frac{1}{2}\log_2\left(1+\psi_{r_i}(t_k)\right) > T_i\right)\\ &\times \Pr\left(\frac{1}{2}\log_2\left(1+\psi_{d_i}(t_k)\right) > T_i\right),\end{aligned} \tag{3.15}$$

Now, the closed-form expression of $\mathcal{P}_{success}$ can be derived similar as done in previous sub-sections and thereafter substituted in (3.14). Then, the exact SOP expression is given by

$$\begin{aligned}\hat{O}_{SOP} = 1 - \prod_{i=\{1,2\}} &\mathcal{J}_0\left(s, r_i, r_j, \frac{\rho_s\, g_{sr_i}}{\delta_i}, \rho_{r_j}\overline{g}_{r_j r_i}\right)\frac{1}{\Gamma(m_{r_i d_i})}\\ &\times \Gamma\left(m_{r_i d_i}, \frac{m_{r_i d_i}\delta_i}{\overline{g}_{r_i d_i}\rho_{r_i}}\right).\end{aligned} \tag{3.16}$$

3.2.4 Ergodic Rate for A-IRI scenario

The ER of D_1 is given by

$$\begin{aligned} C_{d_1} &= \mathbb{E}\left[\sum_{k=\{1,2\}} \frac{1}{2} \log_2(1 + \min\left(\rho_s\, g_{sr_1}, \rho_{r_1}\, g_{r_1 d_1}\right)) \right] \\ &= \frac{1}{2\, \ln 2} \sum_{k=\{1,2\}} \int_0^\infty \frac{1 - F_{X_1}(x_1)}{1 + x_1}\, dx_1, \end{aligned} \tag{3.17}$$

where $X_1 \triangleq \min\left(\rho_s\, g_{sr_1}, \rho_{r_1}\, g_{r_1 d_1}\right)$. Utilizing [94, eq. 3.381.9], (3.17) is further given by

$$C_{d_1} = \frac{1}{2\, \ln 2} \sum_{k=\{1,2\}} \int_0^\infty \frac{\Gamma\left(m_{sr_1}, \frac{m_{sr_1}\, x_1}{g_{sr_1} \rho_s}\right) \Gamma\left(m_{r_1 d_1}, \frac{m_{r_1 d_1}\, x_1}{g_{r_1 d_1} \rho_{r_1}}\right)}{\Gamma\left(m_{sr_1}\right) \Gamma\left(m_{r_1 d_1}\right) (1 + x_1)}\, dx_1, \tag{3.18}$$

As the assessment of (3.18) is mathematically intractable, we utilize the basic the GCQ equation [104, 118] to solve the integral by substituting $a = 0$ and $b = \delta_1$, where $x_v = \cos\left(\frac{(2v-1)\pi}{2V}\right)$, $y_v = \frac{(b-a)\, x_v}{2} + \frac{(b-a)}{2}$, L is a finite value denoting accuracy complexity trade-off, and δ_1 is set to a very high value close to infinity for numerical evaluation. Next, the ergodic rate of D_2 can be derived in the similar way and hence its proof is omitted for the sake of brevity. Thus, the ergodic rate expression of D_i, where $i \in \{1, 2\}$ for A-IRI scenario, is given by

$$\begin{aligned} C_{d_i} &= \frac{\delta_1 \pi}{4\, V \Gamma\left(m_{sr_i}\right) \Gamma\left(m_{r_i d_i}\right) \ln 2} \sum_{k=\{1,2\}} \sum_{v=1}^{V} \frac{\sqrt{1 - {x_v}^2}}{(1 + y_v)} \\ &\times \Gamma\left(m_{sr_i}, \frac{m_{sr_i}\, y_v}{g_{sr_i} \rho_s}\right) \Gamma\left(m_{r_i d_i}, \frac{m_{r_i d_i}\, y_v}{g_{r_i d_i} \rho_{r_i}}\right). \end{aligned} \tag{3.19}$$

3.2.5 Ergodic Rate for P-IRI scenario

The ER of D_1 is given by

$$\begin{aligned}\hat{C}_{d_1} &= \mathbb{E}\left[\sum_{k=\{1,2\}} \frac{1}{2}\log_2(1+\min(\frac{\rho_s\, g_{sr_1}}{\rho_{r_2}\, g_{r_2r_1}+1}, \rho_{r_1}\, g_{r_1d_1}))\right] \\ &= \frac{1}{2\ln 2}\sum_{k=\{1,2\}}\int_0^\infty \frac{1-F_{\hat{X}_1}(\hat{x}_1)}{1+\hat{x}_1}\, d\hat{x}_1, \end{aligned} \tag{3.20}$$

where $\hat{X}_1 \triangleq \min(\frac{\rho_s\, g_{sr_1}}{\rho_{r_2}\, g_{r_2r_1}+1}, \rho_{r_1}\, g_{r_1d_1})$. Utilizing [94, eq. (8.352.7)], [94, eq. (3.381.4)] and [94, eq. (1.111)], (3.20) is further given by,

$$\hat{C}_{d_1} = \frac{1}{2\ln 2}\sum_{k=\{1,2\}}\int_0^\infty \frac{\mathcal{J}_0\left(s, r_1, r_2, \frac{\rho_s\, g_{sr_1}}{\hat{x}_1}, \rho_{r_2}\overline{g}_{r_2r_1}\right)\Gamma\left(m_{r_1d_1}, \frac{m_{r_1d_1}\hat{x}_1}{\overline{g}_{r_1d_1}\rho_{r_1}}\right)}{\Gamma(m_{r_1d_1})(1+\hat{x}_1)}\, d\hat{x}_1, \tag{3.21}$$

Similar to previous sub-section, the integration in (3.21) is solved using the basic GCQ equation with $a=0$ and $b=\delta_1$. Similarly, the ergodic rate of D_2 can be derived and hence the proof is omitted for the sake of brevity. Thus, the ER expression of D_i for $i,j\in\{1,2\}$, $i\neq j$is given by

$$\begin{aligned}\hat{C}_{d_i} &= \frac{\delta_1\pi}{4\,V\Gamma(m_{r_id_i})\ln 2}\sum_{k=\{1,2\}}\sum_{v=1}^{V}\frac{\sqrt{1-{x_v}^2}}{(1+y_v)} \\ &\times \mathcal{J}_0\left(s, r_i, r_j, \frac{\rho_s\, g_{sr_i}}{y_v}, \rho_{r_j}\overline{g}_{r_jr_i}\right)\Gamma\left(m_{r_id_i}, \frac{m_{r_id_i}y_v}{\overline{g}_{r_id_i}\rho_{r_i}}\right). \end{aligned} \tag{3.22}$$

3.2.6 Ergodic Sum Rate for P-IRI scenario

The ESR of the network is defined as follows [119–121]

$$\begin{aligned}\hat{C}_{ESR} &= \mathbb{E}\left[\sum_{i=\{1,2\}}\sum_{k=\{1,2\}} \frac{1}{2}\log_2(1+\min(\frac{\rho_s\, g_{sr_i}}{\rho_{r_j}\, g_{r_jr_i}+1}, \rho_{r_i}\, g_{r_id_i}))\right] \\ &= \sum_{i=\{1,2\}}\hat{C}_{d_i}, \end{aligned} \tag{3.23}$$

where $i, j \in \{1, 2\}$ and $i \neq j$. Substituting the $\hat{C}_{d_i}$ expression from previous subsection, the ESR expression is obtained as

$$\hat{C}_{ESR} = \sum_{i=\{1,2\}} \sum_{k=\{1,2\}} \sum_{v=1}^{V} \frac{\delta_1 \pi}{4\, V \Gamma(m_{r_i d_i}) \ln 2} \frac{\sqrt{1 - {x_v}^2}}{(1 + y_v)}$$
$$\times\, \mathcal{J}_0 \left(s, r_i, r_j, \frac{\rho_s\, g_{sr_i}}{y_v}, \rho_{r_j} \overline{g}_{r_j r_i} \right) \Gamma \left(m_{r_i d_i}, \frac{m_{r_i d_i} y_v}{\overline{g}_{r_i d_i} \rho_{r_i}} \right). \tag{3.24}$$

3.3 Optimization Framework and Solution

3.3.1 Problem formulations

Clearly from the SINR expressions, the symbols corresponding to the destination users are interference limited due to IRI effect at the relays. The same can be minimized by proper allocation of the transmit power of the relays. In this context, a joint relay power allocation (JRPA) problem is mathematically formulated to minimize the SOP (JRPA-SOP) [122–124] respectively as under:

$$(\mathcal{P}0): \min_{P_{r_1}, P_{r_2}} \hat{O}_{SOP}, \tag{3.25}$$
$$\text{subject to,}$$
$$\mathcal{C}1: P_{min} < P_{r_1} < P_{max},$$
$$\mathcal{C}2: P_{min} < P_{r_2} < P_{max},$$

where constraints $\mathcal{C}1$ and $\mathcal{C}2$ correspond to ensuring that the power values lie in between a minimum and a maximum allowable level. Further, an another interesting JRPA problem is explored for ESR maximization [125] which is mathematically formulated as

$$(\mathcal{P}1): \max_{P_{r_1}, P_{r_2}} \hat{C}_{ESR}, \quad \text{subject to} \quad \mathcal{C}1 - \mathcal{C}2. \tag{3.26}$$

3.3.2 JRPA-SOP Solution

The SOP expression in (3.16) is a combination of various complex non-linear functions. Hence, a derivative-based mathematical closed-form solution to ($\mathcal{P}0$) is difficult to obtain. Thus, $P_{r_1}^* \triangleq \hat{P}_1$ and $P_{r_2}^* \triangleq \hat{P}_2$ are found utilizing an effective and derivative-free algorithm like PSO which has been used to solve such problems in various works in the literature [116, 126]. Further, PSO has a reasonable stability, fast convergence, and a better capability as compared to various other optimization algorithms.

The PSO derives its main inspiration from natural interactions like bird flocking, where c_1 number of particles try to find the best position by cooperating with each other. After evaluating using the fitting function (F_a^l), the velocity (V_a^l) and the location (L_a^l) of particle number a at the iteration number l are modified in the dimensional space. The expressions of F_a^l, V_a^l, and L_a^l are given by

$$V_a^l = c_2\, c_2^{'}\, V_a^{l-1} + c_3\, c_4^{l-1}\, (\mu_t - L_a^{l-1}) + c_5\, c_6^{l-1}\, (\mu^* - L_a^{l-1}), \tag{3.27}$$

$$L_a^i = L_a^{l-1} + V_a^l, \tag{3.28}$$

$$F_a^l = \begin{cases} \hat{O}_{SOP}, & \text{if constraints } \mathcal{C}1 \text{ and } \mathcal{C}2 \text{ get fulfilled} \\ 1, & \text{otherwise.} \end{cases} \tag{3.29}$$

where $L_a^l = ((P_{r_1})_a^l, (P_{r_2})_a^l)$ and $F_a^l \triangleq 1$ corresponds to SOP being unity when either of the two constraints does not get satisfied. c_2 and $c_2^{'}$ represent inertial weight and damping factor, respectively, c_3 and c_5 represent acceleration coefficients, and c_4^{l-1} and c_6^{l-1} are random numbers with uniform distribution in the interval $(0, 1)$ at $(l-1)^{th}$ iteration. Further, μ_a is the personal best location of the a^{th} particle with the personal best fitness Ω_a, and $\mu^* = (P_{r_1}^*, P_{r_2}^*)$ is the globally best position for the best fitness value Ω^*. The entire PSO algorithm for c_7 number of iterations is summarized in Algorithm 1.

Algorithm 1 The PSO Algorithm for JRPA

Input: Lower bound $(P_{r_1}, P_{r_2}) = P_{min}$ and upper bound $(P_{r_1}, P_{r_2}) = P_{max}$
Output: Best fitness value Ω^* and corresponding μ^*
Initialization

Initialize V_a^0 to zero and L_a^0 randomly between P_{min} and P_{max}, $\forall a \in \{1, 2, ...c_1\}$
$\mu_t = L_a^0$
Evaluate F_a^0
$\Omega_a = F_a^0$
$\Omega^* = \min\limits_{a \in \{1,2,...c_1\}} F_a^0$
$c_9 = \arg \min\limits_{a \in \{1,2,...c_1\}} F_a^0$
$\mu^* = X_{c_9}^0$
for $l \leftarrow 1$ to c_7 **do**
    for $a \leftarrow 1$ to c_1 **do**
        Update V_a^l and U_a^l in accordance with (6.51) and (6.52), respectively
        Evaluate F_a^l
        if $F_a^l < \Omega_a$ **then**
            $\Omega_a = F_a^l$
            $\mu_a = X_a^l$
        end if
        if $F_a^l < \Omega^*$ **then**
            $\Omega^* = F_a^l$
            $c_9 = a$
            $\mu^* = X_{c_9}^i$
        end if
    end for
end for

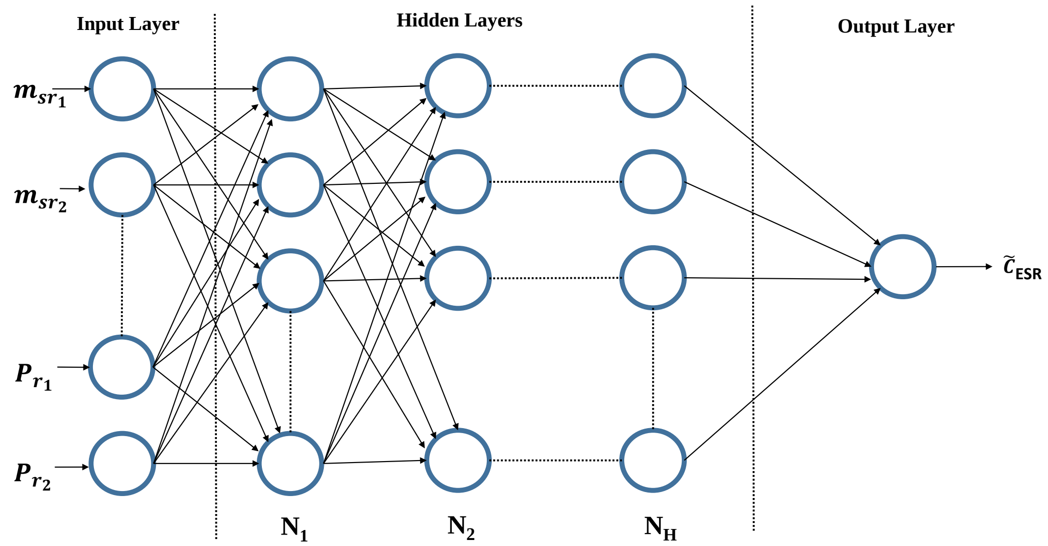

Figure 3.2: Framework for proposed neural network model for JRPA.

3.3.3 JRPA-ESR Solution

The ESR expression derived in (3.24) involves summations due to the GCQ method and non-linear functions.Thus, the PSO algorithm cannot be applied directly to solve ($\mathcal{P}1$) as it will require large number of iterations with significant computational cost which can increase the latency and thus not be usable for real-time operations. Hence, the ESR expression is first approximated using a predictive deep learning architecture which is more practical as the computational complexity is mostly shifted to offline training stage and the online implementation complexity is minimal [127].

As shown in Fig. 3.2, a fully connected feed-forward DNN model is considered with an input layer, H hidden layers, an output layer, and N_h is number of neurons in the h^{th} hidden layer. The input layer consists of 12 inputs namely m_{sr_1}, m_{sr_2}, $m_{r_1d_1}$, $m_{r_2d_2}$, $m_{r_1r_2}$, $m_{r_2r_1}$, ρ, λ_{sr_1}, λ_{sr_2}, $\lambda_{r_1r_2}$, P_{r_1}, and P_{r_2}, where $\rho = \frac{1}{\sigma_n^2}$ is the transmit SNR, λ_{sr_1} and λ_{sr_2} are normalized distances from S to R_1 and R_2, respectively, $\lambda_{r_1r_2}$ is the inter-relay normalized distance. Adam optimizer is used as the learning algorithm as it has a fast training time and can work efficiently with networks involving a lot of parameters. The learning rate, exponential decay rate and numerical stability constant are set as 0.001, 0.9 and 10^{-7}, respectively. For performance evaluation of this regression problem, we choose mean squared error

(MSE) as the loss function defined as

$$\Omega_{MSE} = \mathbb{E}[(\hat{C}_{ESR} - \tilde{C}_{ESR})^2]\,. \tag{3.30}$$

Algorithm 2 DNN Assisted ESR Prediction

Input: m_{sr_1}, m_{sr_2}, $m_{r_1d_1}$, $m_{r_2d_2}$, $m_{r_1r_2}$, $m_{r_2r_1}$, ρ, λ_{sr_1}, λ_{sr_2}, $\lambda_{r_1r_2}$, P_{r_1}, and P_{r_2}
Output: $\tilde{C}_{ESR}$

1: Data Set Generation
2: Evaluate (3.24) for each input matrix $\boldsymbol{A}$ and obtaining corresponding ESR value
3: Divide the data set to 90% and 10% for training and testing respectively
4: **while** satisfactory training and test performance is not achieved **do**
5:     Train the DNN model using eLU activation function and Adam optimizer
6:     Test the trained model using the test data
7: **end while**
8: Save the trained weights and biases
9: Utilize (6.56), (6.57) and (6.58) for ESR prediction

---

where $\tilde{C}_{ESR}$ is the predicted ESR value. Now, a dataset is created by evaluating (3.24) for different values of inputs and obtaining corresponding ESR values such that 90% of the data is used for train the DNN model and the remaining 10% for testing. For threshold operation, exponential linear unit (eLU) is used as activation function at the hidden layers (as defined in (6.55)) and linear activation function is used at the output layer [128]. The parameter values are empirically found to achieve lowest possible MSE. For the same, the best training and testing MSEs obtained are 7×10^{-4} and 8×10^{-4}, respectively, for $H = 2$ and $N_h = 500$. Now, with the optimized weights and biases, the predicted ESR value can be obtained by using (6.56), (6.57) and (6.58), where $\boldsymbol{A}$ is input matrix of order (of order 1×12) such that $\boldsymbol{A} \triangleq \{m_{sr_1}\, m_{sr_2}\, m_{r_1d_1}\, m_{r_2d_2}\, m_{r_1r_2}\, m_{r_2r_1}\, \rho\, \lambda_{sr_1}\, \lambda_{sr_2}\, \lambda_{r_1r_2}\, P_{r_1}\, P_{r_2}\}$. $\boldsymbol{W}_1$ (of order 12×500), $\boldsymbol{W}_2$ (of order 500×500), and $\boldsymbol{W}_o$ (of order 500×1) are optimized weights matrices corresponding to first hidden layer, second hidden layer and output layer, respectively. Similarly, $\boldsymbol{B}_1$ (of order 1×500), $\boldsymbol{B}_2$ (of order 1×500) and B_o (of order 1×1) are optimized bias matrices of first hidden layer, second hidden layer, and output layer, respectively. $\boldsymbol{O}_1$ and $\boldsymbol{O}_2$ are outputs corresponding to first and second hidden layer, respectively.

$$eLU(x) = \begin{cases} e^x - 1, & \text{if } x < 0 \\ x, & \text{if } x \geq 0, \end{cases} \tag{3.31}$$

$$\boldsymbol{O}_1 = eLU(\boldsymbol{A}\,\boldsymbol{W}_1 + \boldsymbol{B}_1), \tag{3.32}$$

$$\boldsymbol{O}_2 = eLU(\boldsymbol{O}_1\,\boldsymbol{W}_2 + \boldsymbol{B}_2), \tag{3.33}$$

$$\tilde{C}_{ESR} = \boldsymbol{O}_2\,\boldsymbol{W}_o + B_o. \tag{3.34}$$

The entire DNN assisted ESR prediction methodology is summarized in Algorithm 2. Finally, the PSO Algorithm 1 can now be used to maximize $\tilde{C}_{ESR}$ and hence solve ($\mathcal{P}1$) using the fitness function defined in (6.62).

$$F_a^l = \begin{cases} \tilde{C}_{ESR}, & \text{if constraints } \mathcal{C}1 \text{ and } \mathcal{C}2 \text{ get fulfilled} \\ 0, & \text{otherwise.} \end{cases} \tag{3.35}$$

3.3.4 Complexity Analysis

The computational complexity of the PSO algorithm depends on the number of particles used and number of iterations involved, and is computed as $O(c_1 \times c_7)$. Further, the computational complexity of the DNN model is measured in terms of floating-point operations (FLOPs) per second, which depends on the number of trainable weights and bias in the model. With $H = 2$ and $N_h = 500$, the number of parameters ($\mathcal{N}_{param}$) and FLOPs ($\mathcal{N}_{FLOPs}$) are given by

$$\mathcal{N}_{param} = N_I \times N_1 + N_1 + N_1 \times N_2 + N_2 + N_2 \times N_O + N_O, \tag{3.36}$$

$$\mathcal{N}_{FLOPs} = N_I \times N_1 \times 2 + N_1 + N_1 \times N_2 \times 2 + N_2 + N_2 \times N_O \times 2 + N_O, \tag{3.37}$$

where $N_I = 12$ and $N_O = 1$ refer to number of neurons in the input layer and output layer, respectively. Accordingly, the DNN model has 257501 number of parameters and 514001 FLOPs.

3.4 Results and Discussions

In this section, the performance of the FDD-VFD system is assessed using Monte-Carlo simulations and useful inferences are drawn out. Considering $\overline{g}_{ij} = 10^{-3}(\frac{\lambda_{sd}}{\lambda_{ij}})^{\eta}$, where λ_{sd} is distance from S to D_1 and D_2, λ_{ij} is distance between node i and j, and η is path-loss exponent. Due to half the number of relays required in FDD-VFD, to bring fairness in comparisons, inter-relay distance in FDD-VFD is considered to be greater than in SR-VFD. It is worth noting that the greater the distance between the relays, the higher the path loss and, consequently, the lower the impact of IRI. As a result, with only two relays used in FDD-VFD compared to four relays in SR-VFD, these two relays can be selected from the four in such a way that the inter-relay distance is maximized. Unless otherwise specified, $P_s = 1$ W, $P_{r_1} = P_{r_2} = 0.5$ W, $T_1 = T_2 = 0.1$, $P_{min} = 0$ W, $P_{max} = 1$ W, $\eta = 3$, $m_{ij} = m \triangleq 2$. The values of $\{\lambda_{sr_i}, \lambda_{r_1 r_2}\}$ (where $i \in \{1, 2\}$) are taken as $\{\lambda_{sd}/2, 3\,\lambda_{sd}/7\}$ with $\lambda_{r_i d_i} = 1 - \lambda_{sr_i}$. Moreover, $\{\lambda_{sr_{i1}}, \lambda_{sr_{i2}}, \lambda_{r_{i1} r_{i2}}\}$ is set to $\{\lambda_{sd}/2, \lambda_{sd}/2, \lambda_{sd}/7\}$ with $\lambda_{r_i d_i} = 1 - \lambda_{sr_i}$. Moreover, $c_1 = 50$, $c_2 = 1$, $c_2^{'} = 0.99$, $c_3 = c_5 = 2$ and $c_7 = 1000$. Further, RSI of -10 dB [82, 129–131] and a residual-IRI level of 0.3 is considered in FD and SR-VFD, respectively. Additionally, to analyze the effectiveness of the JRPA scheme, its performance is compared with fixed relay power allocation (FRPA) as in [116]. Monte-Carlo simulations are executed using 'Matlab' and analytical results are obtained using 'Mathematica'.

3.4.1 Outage Probability

In Figure 4.3, the performance of the proposed FDD-VFD is compared with SR-VFD and FD in terms of OP over the transmit SNR for A-IRI scenario. For a SNR of 25 dB, in FDD-VFD, the users are observed to have 90% and 99.9% times lower OP in comparison FD for $m = 1$ and $m = 3$, respectively. This is due to the severe impact of RSI in FD than in SR-VFD and FDD-VFD that leads to an outage floor at

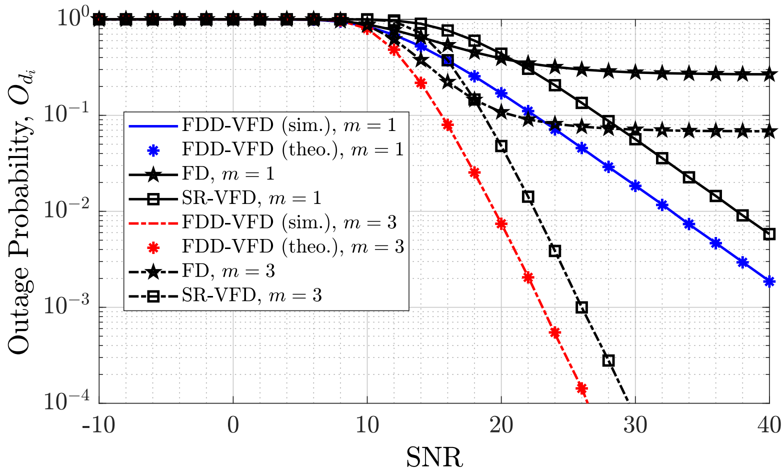

Figure 3.3: OP vs transmit SNR for FDD, SR-VFD and FD in A-IRI scenario.

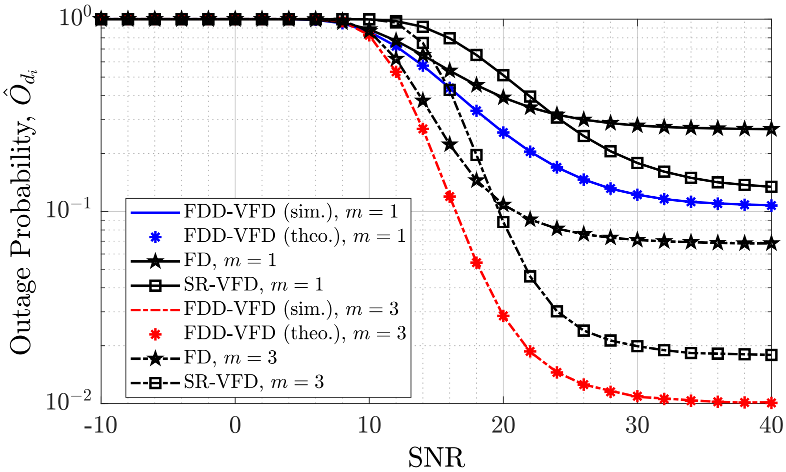

Figure 3.4: OP vs transmit SNR for FDD, SR-VFD and FD in P-IRI scenario.

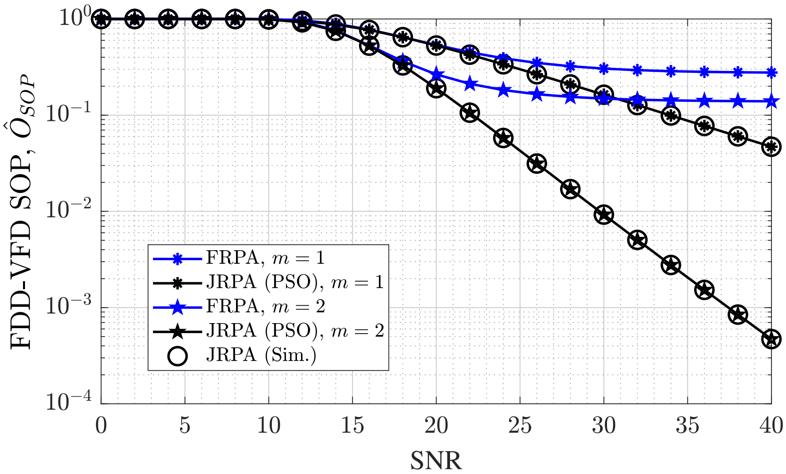

Figure 3.5: SOP performance of JRPA and FRPA with $P_{r_1} = P_{r_2} = 0.5$ W.

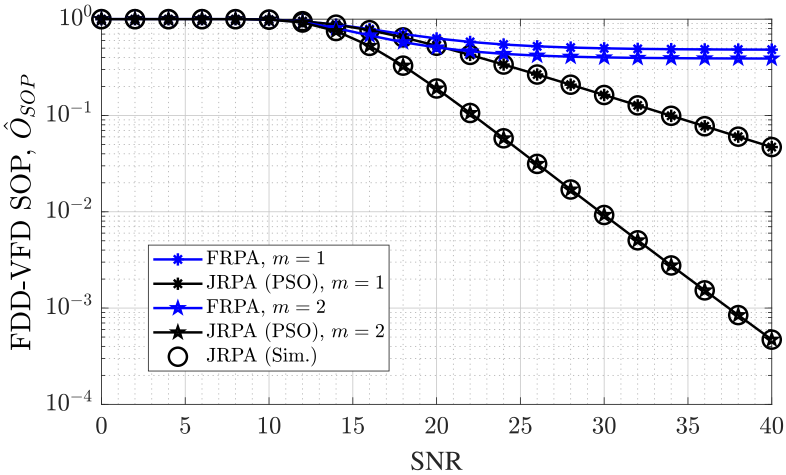

Figure 3.6: SOP performance of JRPA and FRPA with $P_{r_1} = P_{r_2} = 1$ W.

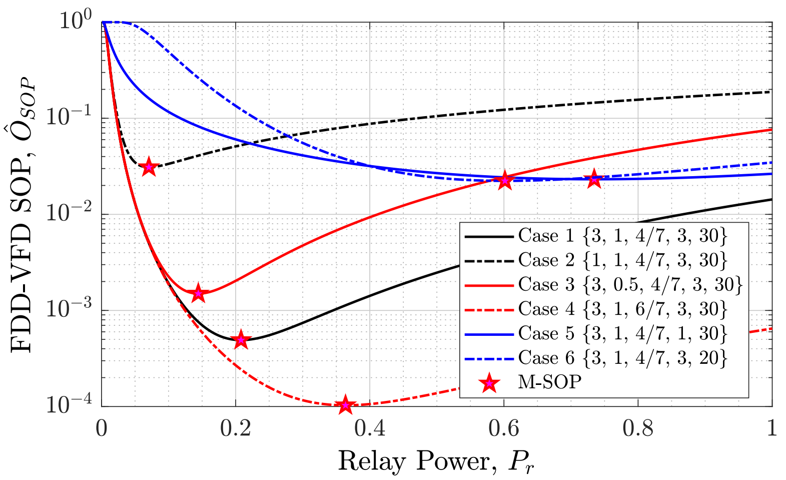

Figure 3.7: Effect of system parameters on relay power.

high SNR. On other hand, due to absence of IRI, both SR-VFD and FDD-VFD are seen to outperform FD. Further, for the same SNR value, FDD-VFD has 84% and 67% times better OP performance in comparison SR-VFD for $m = 1$ and $m = 3$, respectively. These performance gains are due to to the extra time phase in SR-VFD and hence a lower pre-log factor of 1/3 compared to 1/2 in FDD-VFD. Moreover, it can be observed that the FDD-VFD system performance improves with better fading conditions.

Figure 4.4 shows the OP vs SNR plots for P-IRI scenario. For a SNR of 25 dB, in FDD-VFD, the users are seen to have 55% and 50% times lower outage in comparison to SR-VFD for $m = 1$ and $m = 3$, respectively. This is due to a higher inter-relay distance in FDD-VFD in consequence to a lesser number of relays required, and the above mentioned higher pre-log factor. Similarly, for the same SNR value, due to high RSI, FDD-VFD has 60% and 75% times lower OP value in comparison to FD for $m = 1$ and $m = 3$, respectively. Further, it can be observed from the figure that SR-VFD outperforms FD only in the high SNR-regime as also reported in [104, 132] which further proves the efficacy of the proposed FDD-VFD model. Moreover, the presented analytical OP expression matches well with the simulation results.

In Figure 4.6, the SOP performance is shown over SNR values of the JRPA and FRPA schemes for two different m values. The relay power values in FRPA are fixed to $P_{r_1} = P_{r_2} = 0.5$ W [89, 104, 133]. It can be observed that the JRPA optimized curves plot using PSO matches closely with the simulation values. Further, for a SNR value of 30 dB, SOP in JRPA is observed to be 60% and 90% times lower than FRPA for $m = 1$ and $m = 3$, respectively. The same is a reasonable observation as the power allocations in FRPA are uniform and are not updated in accordance with the changing parameter values which further shows the requirement of the JRPA scheme in order to minimize the IRI. Further in Figure 3.6, we also compare the SOP performance of the JRPA scheme with the FRPA scheme having $P_{r_1} = P_{r_2} = 1$ W. Interestingly, as an increase in the transmit power of the relays from 0.5 to 1 W in FRPA not only enhances the received power at the destination users but also leads to an increase in IRI, we observe an overall decrease in SOP performance.

Figure 4.7, depicts variation of SOP with relay power $P_{r_1} = P_{r_2} \triangleq P_r$ for 6 differ-

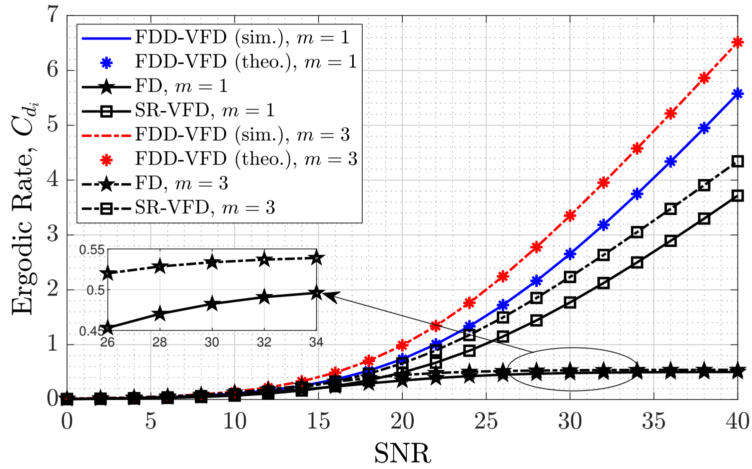

Figure 3.8: ER vs transmit SNR for FDD, SR-VFD and FD in A-IRI scenario.

ent system parameter cases that correspond to the values of $\{m_{sr}, P_s, d_{r_1r_2}, m_{rd}, \rho\}$, where $m_{sr_1} = m_{sr_2} \triangleq m_{sr}$, $m_{r_1d_1} = m_{r_2d_2} \triangleq m_{rd}$ and $\rho_s = \rho_r \triangleq \rho$. Also, the minimum SOP point and the corresponding $P^*_{r_1} = P^*_{r_2} \triangleq P^*_r$ value is shown for each case. It can be observed that for cases 2 and 3, in comparison to case 1, P^*_r decreases by 65% and 30%, respectively. This is because for lower m_{sr} and P_s values, $\psi_{r_1}(t_k)$ and $\psi_{r_2}(t_k)$ decrease as can be deduced from (3.3) and (3.7), respectively. Thus, to increase these SINRs and hence reduce the SOP, the IRI needs to be reduced by lowering the relay power. Further, comparing cases 4 and 1, an increase in $d_{r_1r_2}$ value decreases the IRI which allows a higher relay transmit power as the same increases $\psi_{d_1}(t_k)$ and $\psi_{d_2}(t_k)$ in (3.4) and (3.8), respectively. Similar results are observed for a lower m_{rd} value in case 5 where P^*_r increases approximately 3 times in order to increase $\psi_{d_1}(t_k)$ and $\psi_{d_2}(t_k)$ and hence decrease the SOP. Further, as ρ value increases from 20 dB in case 6 to 30 dB in case 4, minimum SOP and P^*_r decrease by 92% and 43%, respectively.

3.4.2 Ergodic Rate

Figure 3.8 analyzes the ER performance of the FDD-VFD with SR-VFD and FD over the transmit SNR for A-IRI scenario. Clearly, both FDD-VFD and SR-VFD outperform FD as ER in FD converges to a constant value at high SNR due to the severe impact of RSI. However, ER in FDD-VFD and SR-VFD do not converge to a constant value due to absence of IRI. Further, the proposed FDD-VFD achives

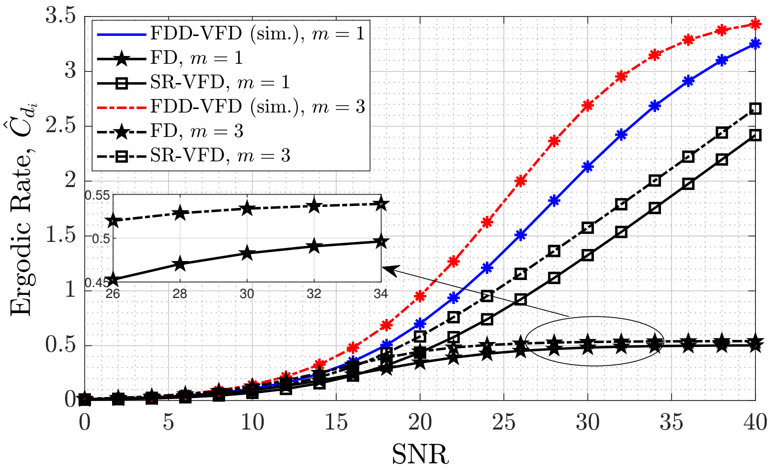

Figure 3.9: ER vs transmit SNR for FDD, SR-VFD and FD in P-IRI scenario.

Table 3.2: Average computation time for ESR optimization

Optimization Scheme	Computational time (in seconds)
Proposed DNN-PSO ($H = 1$, $N_h = 500$)	0.49
Proposed DNN-PSO ($H = 2$, $N_h = 500$)	1.01
Proposed DNN-PSO ($H = 3$, $N_h = 500$)	2.36
Analytical-PSO ($c_1 = 50$, $c_7 = 10$)	90.87
Analytical-PSO ($c_1 = 50$, $c_7 = 20$)	183.57
Analytical-PSO ($c_1 = 100$, $c_7 = 10$)	195.23

better rates than SR-VFD due to a higher pre-log factor of $1/3$ as no extra time phase is required. Further, with improved fading conditions, system performance is seen to improve. Moreover, theoretical results using the presented ER expression matches well with the simulation results.

In Figure 3.9 the ER is plot vs transmit SNR graphs for P-IRI scenario. The proposed FDD-VFD is clearly seen to have a higher ER than both SR-VFD and FD. The performance improvement observation over SR-VFD is reasonable as lesser number of relays is required in FDD-VFD which results in a higher inter-relay distance and thereby a lower IRI. For a SNR of 25 dB, in FDD-VFD, the users are seen to have 3.2 and 3.5 times higher ER in comparison to FD for $m = 1$ and $m = 3$, respectively. Further, the presented ER expression results are seen to match exactly with the simulation results.

In Table 3.2, the average computational times taken is compared for DNN-PSO and analytical-PSO based solutions for $(P1)$. In the analytical-PSO method, the PSO algortihm is applied directly using the analytical ESR expression. The com-

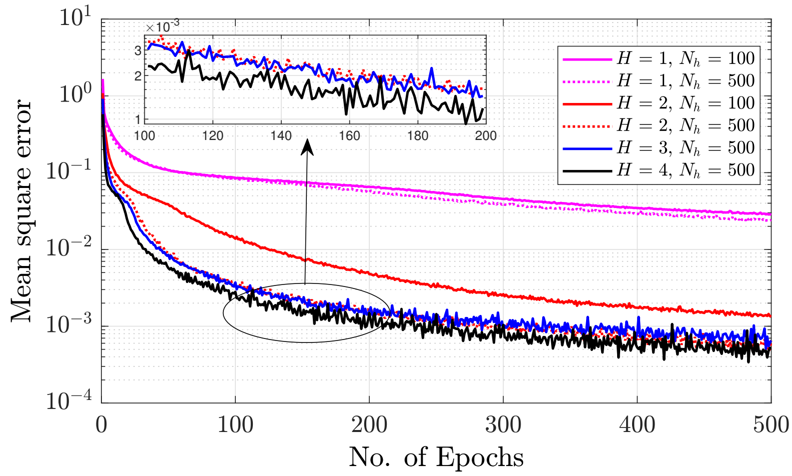

Figure 3.10: Effect of epochs on MSE for different number hidden layers and nodes.

putational times are obtained by using a computer with a 2.10 GHz Intel XEON E52620V4 X central processing unit and 64 GB RAM. It can be clearly seen that the proposed DNN-PSO solution (with $H = 2$ and $N_h = 500$) takes a very low running time in comparison to the analytical-PSO solution. Moreover, the analytical-PSO solution's runtime increases with the number of particles and the maximum number of iterations.

Further, in Figure 3.10, the effect of number of training epochs is analyzed over the achievable MSE for distinct number of hidden layers and nodes. It can be clearly seen that the training performance converges such that a choice of $H = 2$ and $N_h = 500$ is sufficient for an accurate prediction. After 300 epochs of training, the DNN model with $H = 2$ and $N_h = 500$ has 80% and 98% lower MSE as compared to models ($N_h = 100$) with $H = 2$ and $H = 1$, respectively. Moreover, an MSE of 7×10^{-4} is achieved which shows that the predicted $\tilde{C}_{ESR}$ matches well with the actual $\hat{C}_{ESR}$. Also, it can be observed that further increasing the number of hidden layers to 3 or 4 fails to bring about significant improvements in performance due to overfitting issues. Moreover, in Table 3.2, the computational time for the proposed DNN-PSO is seen to increase with increase in the number of hidden layers, thus indicating that the choice of $H = 2$ and $N_h = 500$ is sufficient and further increasing the values of H is not required.

In Figure 3.11, the ESR performance is shown over transmit SNR of the JRPA and FRPA ($P_{r_1} = P_{r_2} = 0.5$ W) schemes for fading severity values of $m = 1$ and $m = 2$. For a SNR value of 30 dB, ESR in JRPA is observed to be approximately

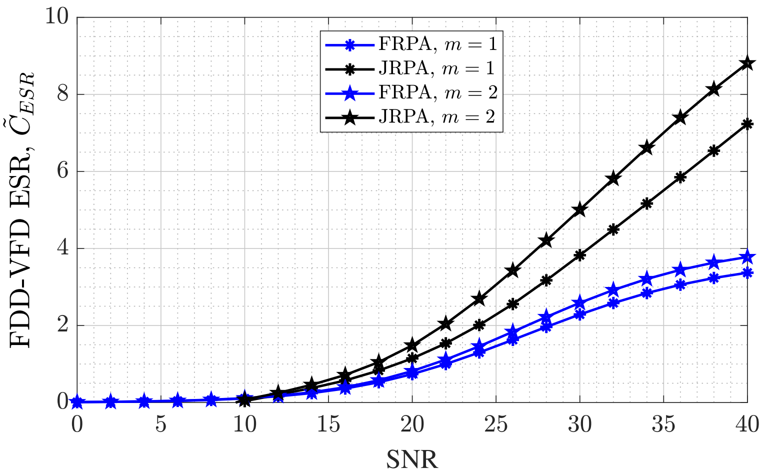

Figure 3.11: ESR performance over SNR for JRPA and FRPA with $P_{r_1} = P_{r_2} = 0.5$ W.

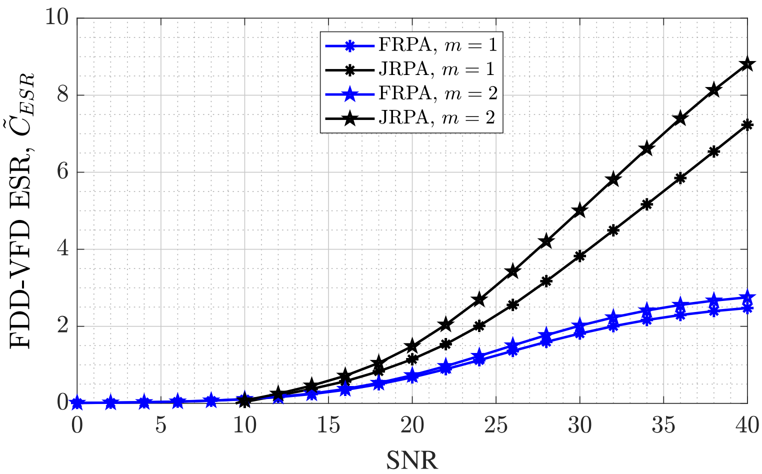

Figure 3.12: ESR performance over SNR for JRPA and FRPA with $P_{r_1} = P_{r_2} = 1$ W.

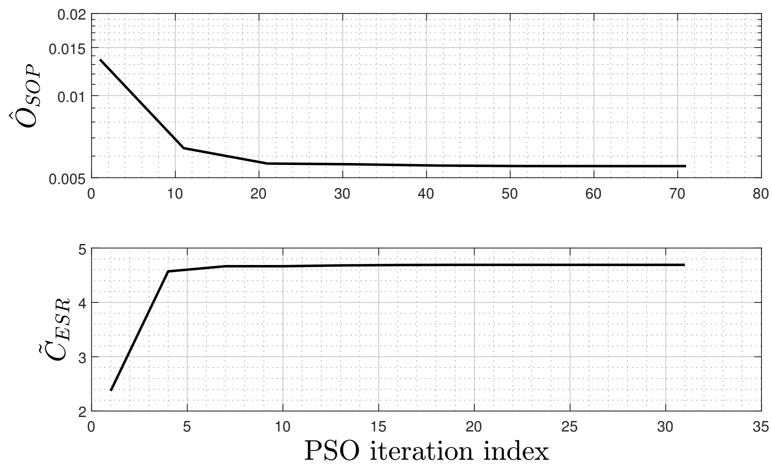

Figure 3.13: Convergence plot of the PSO algorithm for ($\mathcal{P}0$) and ($\mathcal{P}1$).

86% more than FRPA for $m = 1$. Similarly, for the same SNR value, ESR in JRPA is observed to be 95% times more than FRPA for $m = 2$. The observations made are reasonable as the P_{r_1} and P_{r_2} values in FRPA are kept to a fixed value. However, the power allocations in JRPA get updated in accordance with the change in the system parameter values. Similar observations can also be made in Figure 3.12, where the ESR performance of the JRPA scheme is compared with the FRPA scheme having $P_{r_1} = P_{r_2} = 1$ W. Furthermore, in Fig. 3.13, we plot the convergence behaviour of the PSO algorithm for $(\mathcal{P}0)$ and $(\mathcal{P}1)$. It can be observed that as the number of iterations increases, the PSO algorithm converges for both $(\mathcal{P}0)$ and $(\mathcal{P}1)$ problems.

3.5 Summary

This chapter presented performance analysis and optimization of a novel FDD-VFD system for both A-IRI and P-IRI scenarios. Specifically, OP and ER analysis were carried out over Nakagami-m channel distributions with SOP and ESR optimization for transmit power allocation of relays. The simulation results demonstrate that the proposed FDD-VFD system exhibits significantly improved OP and ER performance as compared to the conventional FD and SR-VFD schemes. Additionally, as the proposed scheme performs better utilization of resources, the same is more practical for VFD implementations. Finally, the JRPA based solution to SOP minimization and ESR maximization problems is seen to improve the system performance by minimizing the effect of IRI and thereby outperform the performance with fixed values of relay power allocations.To further enhance the utilization of the wireless spectrum and available resources, the next chapter explores a novel system model based on NOMA-enabled underlay D2D communication.

Chapter 4

NOMA Enabled Underlay D2D-Cellular Network

In the previous chapters, to enhance the spectrum utilization, VFD communication was explored as an alternative to FD. This chapter investigates underlay D2D communication and its interplay with NOMA technology which has gained significant research attention in recent years to improve the spectrum utilization and connectivity in the next-generation ultra-dense networks [122, 134–137].

Authors in [134] consider a NOMA-enabled D2D (ND) underlayed with OMA-enabled cellular (OC), i.e. ND-OC transmission for power allocation among users. Authors in [135] and [122] propose outage probability (OP) based power control (PC) for Internet-of-Things (IoT) applications. In [136], an uplink NOMA based ND-OC communication is studied. Similarly, in [137], an OMA-enabled D2D (OD) underlayed with OMA-enabled cellular (OC), i.e. OD-OC transmission system is considered. Authors in [138] investigate NOMA-enabled full-duplex D2D communication underlaid in the cellular uplink and thereby maximize the throughput by proper power control strategy. Work in [139] study a NOMA-based D2D communication network in the unlicensed band, and optimize the channel assignment and power allocation in the system.

However, due to OMA based transmission, ND-OC and OD-OC system models used in [122, 134–137] are less spectrally efficient. Hence, this chapter investigates a more spectrally efficient ND underlayed with NOMA-enabled cellular (NC), i.e. ND-NC tranmission system. Further, for performance gain over the ND-OC and the OD-OC models, a transmission protocol is proposed for the ND-NC network. SOP and sum ergodic rate (SER) analysis is performed considering the generalized Nakagami-m fading channels. Further, to control the intra-cell interferences as well as to maintain power-domain NOMA compatibility, a joint PC (JPC) problem is formulated for SOP minimization. It is worth noting that such an ND-NC system specific analysis and JPC problem is not explored in the literature.

The scope of this work is in various interference-limited peer-to-peer services, low-mobility D2D and IoT scenarios with slowly varying fading channels where only statistical channel state information (CSI) is required instead of instantaneous CSI. The key contributions of this chapter are:

- A novel ND-NC transmission protocol is proposed and investigated which is more spectrally efficient than ND-OC and OD-OC systems.
- Closed-form expressions for SOP and SER are obtained considering Nakagami-m fading.
- A JPC problem is mathematically formulated with an objective to minimize the SOP.
- A DNN based predictive JPC (P-JPC) is proposed for real-time implementations [140, 141] as JPC solution in closed-form cannot be obtained due to mathematical complexity of the SOP expression.

4.1 System Model

Consider a cellular network with base station (b) simultaneously serving two cellular users (CUs) c_1 and c_2 using NOMA, as shown in Fig. 4.1. Further, there exists a D2D group consisting of a single transmitter d_t which also utilizes NOMA to transmit to two receivers, d_1 and d_2, by reusing the CU channel. In the first time phase t_1; b and d_t transmit superimposed signals to the CUs and D2D receivers, respectively. In the next time phase t_2; d_t transmits another superimposed signal to d_1 and d_2. To transmit the same symbols, b will require two time phases in ND-OC and OD-OC systems, and d_t will require four time phases in OD-OC, as shown in Table 4.1. Each ij link, where $i \in \{b, d_t\}$ and $j \in \{c_1, c_2, d_1, d_2\}$, is assumed to be affected with

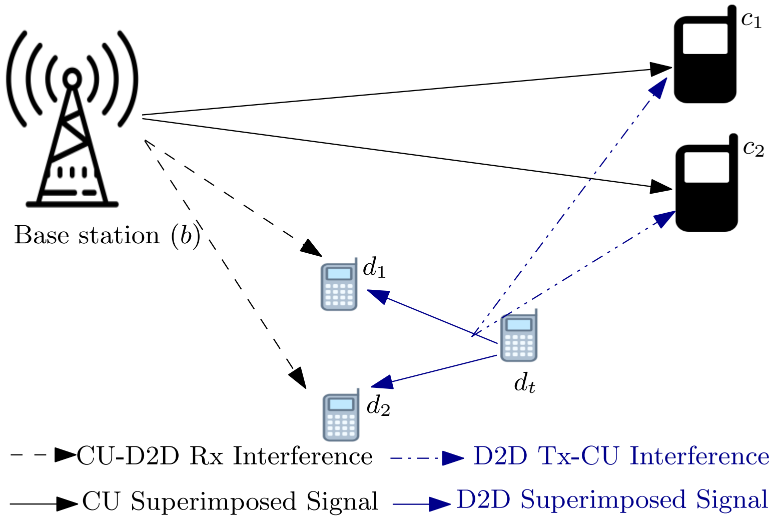

Figure 4.1: System model for ND-NC communication.

Table 4.1: Proposed ND-NC transmission protocol

System Model	t_1	t_2	t_3	t_4
ND-NC	$b \to c_1,\, c_2$ $d_t \to d_1,\, d_2$	- $d_t \to d_1,\, d_2$	- -	- -
ND-OC	$b \to c_1$ $d_t \to d_1,\, d_2$	$b \to c_2$ $d_t \to d_1,\, d_2$	- -	- -
OD-OC	$b \to c_1$ $d_t \to d_1$	$b \to c_2$ $d_t \to d_2$	- $d_t \to d_1$	- $d_t \to d_2$

path-loss and follows independent and non-identical Nakagami distribution with $Nak(m_{ij}, \overline{g}_{ij})$, where $\overline{g}_{ij} = \mathbb{E}[g_{ij}]$, $g_{ij} = |h_{ij}|^2$, and h_{ij} is the channel coefficient.

Note that in the ND-NC, as mentioned above, the symbols transmitted by d_t in the second time phase are different from the symbols sent in the first time phase. Further, though it may appear to be unfair that the cellular transmission ($b \to c_1,\, c_2$) is not allowed in t_2, the same is essential for a better performance over the considered ND-OC and OD-OC models. To demonstrate the same, a comparative ND-NC transmission protocol is also considered, where in the time phase t_2, b also transmits a new superimposed signal to the cellular users as shown in Table 4.2. Thus, a total of four time phases will be required by b in both ND-OC and OD-OC to complete the transmission process. Also, it is to be noted that in both the proposed ND-NC protocol and the comparative ND-NC protocol, the D2D communication does not allocate the time slots but instead uses the existing cellular time slots.

The NOMA users are categorized on the basis of target rates [142]. Without

Table 4.2: Comparative ND-NC transmission protocol

System Model	t_1	t_2	t_3	t_4
ND-NC	$b \to c_1,\, c_2$ $d_t \to d_1,\, d_2$	$b \to c_1,\, c_2$ $d_t \to d_1,\, d_2$	- -	- -
ND-OC	$b \to c_1$ $d_t \to d_1,\, d_2$	$b \to c_2$ $d_t \to d_1,\, d_2$	$b \to c_1$ -	$b \to c_2$ -
OD-OC	$b \to c_1$ $d_t \to d_1$	$b \to c_2$ $d_t \to d_2$	$b \to c_1$ $d_t \to d_1$	$b \to c_2$ $d_t \to d_2$

loss of generality, we assume that c_1 and d_1 are delay-sensitive users (i.e. with higher priority in successive interference cancellation (SIC) ordering) and require lower target data rate as compared to c_2 and d_2, respectively. Thus, $T_{c_1} < T_{c_2}$ and $T_{d_1} < T_{d_2}$, where T_{c_1}, T_{c_2}, T_{d_1}, and T_{d_2} are target rates for c_1, c_2, d_1 and d_2, respectively. CU c_1 detects its own symbol $x_{c_1}(t_1)$ considering the symbol $x_{c_2}(t_1)$ corresponding to c_2 as interference. However, c_2 detects $x_{c_2}(t_1)$ only after detecting and removing $x_{c_1}(t_1)$ via SIC. Hence, when b superimposes $x_{c_1}(t_1)$ and $x_{c_2}(t_1)$ with power allocation coefficients α_c and β_c, respectively, and broadcasts the same to c_1 and c_2, then $\forall\, l \in \{1,2\}$ the SINRs are given as,

$$\psi_{c_l}^{c_1}(t_1) = \frac{\alpha_c P_b\, g_{bc_l}}{\beta_c P_b\, g_{bc_l} + P_{d_t}\, g_{d_t c_l} + \sigma_{c_l}^2}, \tag{4.1}$$

$$\psi_{c_2}^{c_2}(t_1) = \frac{\beta_c P_b\, g_{bc_2}}{P_{d_t}\, g_{d_t c_2} + \sigma_{c_2}^2}, \tag{4.2}$$

where $\sigma_{c_l}^2$ is the additive white Gaussian noise (AWGN) power at node c_l, and P_b and P_{d_t} are transmit powers of b and d_t, respectively, and $\alpha_c + \beta_c = 1$.

Similarly, at time t_k, d_1 can decode its symbol $x_{d_1}(t_k)$ directly, while d_2 has to detect and remove $x_{d_1}(t_k)$ via SIC before decoding its own symbol $x_{d_2}(t_k)$. Thus, the corresponding SINRs $\forall\, l \in \{1,2\}$ are given as

$$\psi_{d_l}^{d_1}(t_k) = \frac{\alpha_d P_{d_t} g_{d_t d_l}}{\beta_d P_{d_t} g_{d_t d_l} + (2-k) P_b g_{bd_l} + \sigma_{d_l}^2}, \tag{4.3}$$

$$\psi_{d_2}^{d_2}(t_k) = \frac{\beta_d P_{d_t} g_{d_t d_2}}{(2-k) P_b g_{bd_2} + \sigma_{d_2}^2}, \tag{4.4}$$

where α_d and β_d are power coefficients for d_1 and d_2, respectively, with $\alpha_d + \beta_d = 1$ and $\sigma_{d_l}^2$ is AWGN power at d_l. Further, $k \in \{1,2\}$ and the factor $(2-k)$ ensure the presence and absence of interference from b in t_1 and t_2, respectively. $P_{d_t} = \alpha_p\, P_{max}$ with $\alpha_p \in (0,1)$ being D2D power coefficient and P_{max} being total D2D power budget.

4.2 Performance Analysis

In this section, the SOP and SER expressions are derived in closed-form for ND-NC system.

4.2.1 System Outage Probability

The successful decoding of $x_{d_1}(t_k)$ $(\forall k \in \{1,2\})$ at d_1 requires the condition $\psi_{d_1}^{d_1}(t_k) > \delta_{d_1}$ to be met and successful decoding of $x_{d_2}(t_k)$ at d_2 requires that $\psi_{d_2}^{d_1}(t_k) > \delta_{d_k}$ and $\psi_{d_2}^{d_2}(t_k) > \delta_{d_2}$, where $\delta_{d_1} = 2^{2\,T_{d_1}} - 1$ and $\delta_{d_2} = 2^{2\,T_{d_2}} - 1$. Similarly, $\psi_{c_1}^{c_1}(t_1) > \delta_{c_1}$ to decode $x_{c_1}(t_1)$, and $\psi_{c_2}^{c_1}(t_1) > \delta_{c_1}$ and $\psi_{c_2}^{c_2}(t_1) > \delta_{c_2}$ conditions for successful decoding of $x_{c_2}(t_1)$, where $\delta_{c_1} = 2^{T_{c_1}} - 1$, $\delta_{c_2} = 2^{T_{c_2}} - 1$. The SOP then can be defined as the probability that either of the users in the network fail to decode its signal successfully [119]. In other words, $\mathcal{P}_{out} = 1 - \mathcal{P}_s$, where $\mathcal{P}_s$ is the probability that all signals are successfully decoded. Accordingly, $\mathcal{P}_s$ is determined as

$$\begin{aligned}\mathcal{P}_s = \Pr[\,&\psi_{d_1}^{d_1}(t_k) > \delta_{d_1}, \psi_{d_2}^{d_1}(t_k) > \delta_{d_1}, \psi_{d_2}^{d_2}(t_k) > \delta_{d_2},\\ &\psi_{c_1}^{c_1}(t_1) > \delta_{c_1}, \psi_{c_2}^{c_1}(t_1) > \delta_{c_1}, \psi_{c_2}^{c_2}(t_1) > \delta_{c_2}\,]\\ &= A_{d_1}\, A_{d_2}\, A_{c_1}\, A_{c_2},\end{aligned} \tag{4.5}$$

where $\forall i \in \{1,2\}$, $A_{d_i} \triangleq \Pr\left(\frac{P_{d_t}\, g_{d_t d_i}}{P_b\, g_{bd_i} + \sigma_{d_i}^2} > \Phi_{d_i}, P_{d_t}\, g_{d_t d_i} > \Phi_{d_i}\right)$, $A_{c_i} \triangleq \Pr\left(\frac{P_b\, g_{bc_i}}{P_{d_t}\, g_{d_t c_i} + \sigma_{c_i}^2} > \Phi_{c_i}\right)$. Further, $\forall\, l \in \{c,d\}$, $\Phi_{l_1} \triangleq \phi_{l_1} = \frac{\delta_{l_1}}{\alpha_l - \delta_{l_1}\beta_l}$, $\Phi_{l_2} \triangleq \phi_l = \max(\phi_{l_1}, \phi_{l_2})$, $\phi_{l_2} = \frac{\delta_{l_2}}{\beta_l}$. A_{d_1} can also be written as

$$A_{d_1} = \Pr\Big(P_{d_t} g_{d_t d_1} > \max\{\Phi_{d_1}(Y_1 + \sigma_{d_1}^2), \Phi_{d_1}\sigma_{d_1}^2\}\Big), \tag{4.6}$$

where $Y_1 = P_b\, g_{bd_1}$. Now, given that Φ_{d_1}, P_b, g_{bd_1}, and $\sigma_{d_1}^2$ are all strictly positive,

$\max\{\Phi_{d_1}(Y_1+\sigma_{d_1}^2),\, \Phi_{d_1}\sigma_{d_1}^2\} = \Phi_{d_1}(Y_1+\sigma_{d_1}^2)$. Thus, A_{d_1} can now be expressed as

$$A_{d_1} = \int_0^{\infty} \Pr(P_{d_t} g_{d_t d_1} > (y_1+\sigma_{d_1}^2)\Phi_{d_1}) f_{Y_1}(y_1) dy_1, \tag{4.7}$$

Now, using the identities [94, eq. (3.381.9)] and [94, eq. (8.352.7)], (5.38) can be resolved as

$$\begin{aligned} A_{d_1} = \int_0^{\infty} \Bigg\{ & e^{-\frac{m_{d_t d_1}(y_1+1)}{P_{d_t}\,\overline{g}_{d_t d_1}(\sigma_{d_1}^2\,\Phi_{d_1})^{-1}}} \sum_{n_1=0}^{m_{d_t d_1}} \frac{1}{n_1!} \frac{e^{-\frac{m_{bd_1} y_1}{P_b\,\overline{g}_{bd_1}}}}{y^{1-m_{bd_1}}\Gamma(m_{bd_1})} \\ & \times \left(\frac{m_{d_t d_1}(y_1+1)}{P_{d_t}\overline{g}_{d_t d_1}(\sigma_{d_1}^2\Phi_{d_1})^{-1}} \right)^{n_1} \left(\frac{m_{bd_1}\sigma_{d_1}^2}{P_b \overline{g}_{bd_1}} \right)^{m_{bd_1}} \Bigg\} dy_1. \end{aligned} \tag{4.8}$$

Finally, utilizing [94, eq. (1.111)] and [94, eq. (3.381.4)]

$$A_{d_1} = \mathcal{J}_0\left(d_t, d_1, b, \frac{P_{d_t}\,\overline{g}_{d_t d_1}}{\sigma_{d_1}^2\Phi_{d_1}}, \frac{P_b\,\overline{g}_{bd_1}}{\sigma_{d_1}^2} \right). \tag{4.9}$$

Next, A_{d_2}, A_{c_1} and A_{c_2} can be expressed as

$$A_{d_2} = \int_0^{\infty} \Pr(P_{d_t} g_{d_t d_2} > (y_2+\sigma_{d_2}^2)\Phi_{d_2}) f_{Y_2}(y_2) dy_2, \tag{4.10}$$

$$A_{c_1} = \int_0^{\infty} \Pr(P_b\, g_{bc_1} > (y_3+\sigma_{c_1}^2)\,\Phi_{c_1})\, f_{Y_3}(y_3)\, dy_3, \tag{4.11}$$

$$A_{c_2} = \int_0^{\infty} \Pr(P_b\, g_{bc_2} > (y_4+\sigma_{c_2}^2)\,\Phi_{c_2})\, f_{Y_4}(y_4)\, dy_4. \tag{4.12}$$

where $Y_2 = P_b\, g_{bd_2}$, $Y_3 = P_{d_t}\, g_{d_t c_2}$ and $Y_4 = P_{d_t}\, g_{d_t c_2}$. Now, solving above integrals by the procedure followed in A_{d_1}, and substituting it in (4.5), $\mathcal{P}_{out}$ for the ND-NC network can be obtained as

$$\begin{aligned} \mathcal{P}_{out} = 1 - & \prod_{i=\{1,2\}} \mathcal{J}_0\left(d_t, d_i, b, \frac{P_{d_t}\,\overline{g}_{d_t d_i}}{\sigma_{d_i}^2\,\Phi_{d_i}}, \frac{P_b\,\overline{g}_{bd_i}}{\sigma_{d_i}^2} \right) \\ & \times \prod_{j=\{1,2\}} \mathcal{J}_0\left(b, c_j, d_t, \frac{P_b\,\overline{g}_{bc_j}}{\sigma_{c_j}^2\,\Phi_{c_j}}, \frac{P_{d_t}\,\overline{g}_{d_t c_j}}{\sigma_{c_j}^2} \right), \end{aligned} \tag{4.13}$$

where $\mathcal{J}_0(\theta_1, \theta_2, \theta_3, \theta_4, \theta_5)$ is defined as

$$\begin{aligned}\mathcal{J}_0(\theta_1, \theta_2, \theta_3, \theta_4, \theta_5) = & \frac{e^{-(\frac{m_{12}}{\theta_4})}}{\Gamma(m_{32})}(\frac{m_{32}}{\theta_5})^{m_{32}} \\ & \times \sum_{n_1=0}^{m_{12}-1}(\frac{m_{12}}{\theta_4})^{n_1}\sum_{n_2=0}^{n_1}\frac{\Gamma(n_2+m_{32})}{n_2!(n_1-n_2)!}(\frac{m_{12}}{\theta_4}+\frac{m_{32}}{\theta_5})^{-(n_2+m_{32})}\end{aligned} \tag{4.14}$$

where $m_{xy} \triangleq m_{\theta_x\theta_y}$ $\forall x, y \in \{1, 2, 3\}$.

Remarks:

1. *Range of coefficients*:The conditions $\alpha_c < \delta_{c_1}\beta_c$ and $\alpha_d < \delta_{d_1}\beta_d$, will result in A_{c_1} and A_{d_1}, respectively, becoming equal to zero, thereby causing $\mathcal{P}_s$ to become zero in (4.5). Thus, it is to note that P_{out} expressed in (4.13) holds if $\delta_{l_1}\beta_l < \alpha_l < 1$, otherwise it is unity.

2. *Fading severity*: It can be observed from the SOP expression that due to the summation operations in $\mathcal{J}_0$, with increase in the fading severity of signal link (m_{12}), $\mathcal{J}_0$ increases, which decreases $\mathcal{P}_{out}$. On the other hand, an increase in the fading severity of interference link (m_{32}), decreases $\mathcal{J}_0$, thereby causing an increase in the SOP.

3. *Target rates*: An increase in the value of target rates T_{d_1}, T_{d_2}, T_{c_1} and T_{c_2}, increases the value of δ_{d_1}, δ_{d_2}, δ_{c_1} and δ_{c_2}, respectively. The same decreases the value of $\mathcal{P}_s$, thereby causing the SOP to increase.

4.2.2 SER Analysis

The ER is determined by expected value of the instantaneous mutual information between the transmitter and the receiver. Then, the SER or the ergodic sum rate of the users can be mathematically expressed as [119]

$$\begin{aligned}\mathcal{R}_{sys} &= \mathbb{E}\left[\sum_{l=\{c,d\}}\sum_{i=\{1,2\}}\sum_{k=\{1,2\}}\xi\,\log_2(1+\psi_{l_i}^{l_i}(t_k))\right] \\ &= \sum_{i=\{1,2\}}\Big(\sum_{k=\{1,2\}}R_{d_i}(t_k)+R_{c_i}(t_1)\Big),\end{aligned} \tag{4.15}$$

where $R_{d_i}(t_k) = \mathbb{E}\left[\xi \log_2(1+\psi_{d_i}^{d_i}(t_k)\right]$, $R_{c_i}(t_1) = \mathbb{E}\left[\xi \log_2(1+\psi_{c_i}^{c_i}(t_1)\right]$, and ξ is the pre-log factor. Now, $R_{d_1}(t_1)$ can be further expressed as

$$R_{d_1}(t_1) = \frac{1}{2\ln 2}\int_0^{\frac{\alpha_d}{\beta_d}} \frac{1 - F_{\psi_{d_1}^{d_1}(t_1)}(x)}{1+x}\, dx, \tag{4.16}$$

where $\frac{1}{2}$ is pre-log factor due to two time phases required for D2D transmission. Now, utilizing [94, eq. (8.352.7)], [94, eq. (3.381.4)], [94, eq. (1.111)] and GCQ equation $\int_0^a f(x)dx{=}\mathcal{J}_1(a)f(x_r)$, we obtain

$$R_{d_1}(t_1) = \frac{1}{2\ln 2}\mathcal{J}_2\left(a_{d_1}, d_t, d_1, b, \frac{P_{d_t}\overline{g}_{d_t d_1}}{\sigma_{d_1}^2\hat{\phi}_{d_1}}, \frac{P_b\overline{g}_{bd_1}}{\sigma_{d_1}^2}\right). \tag{4.17}$$

where $\mathcal{J}_2(\theta_1,\theta_2,\theta_3,\theta_4,\theta_5,\theta_6)$ and $\mathcal{J}_1(\theta_6)$ are defined as

$$\mathcal{J}_2(\theta_1,\theta_2,\theta_3,\theta_4,\theta_5,\theta_6) \triangleq \mathcal{J}_0(\theta_1,\theta_2,\theta_3,\theta_4,\theta_5)\,\mathcal{J}_1(\theta_6)\,(1+x_r)^{-1}, \tag{4.18}$$

$$\mathcal{J}_1(\theta_6) \triangleq \frac{\theta_6\pi}{2R}\sum_{r=1}^{R}\sqrt{1-{y_r}^2}, \tag{4.19}$$

where $x_r = \frac{\theta_6 y_r}{2} + \frac{\theta_6}{2}$ and R denotes approximation order. Further, $\forall\, l \in \{c,d\}$ $a_{l_1} = \frac{\alpha_l}{\beta_l}$, $a_{l_2} = \infty$, $\hat{\phi}_{l_1} = \frac{x_r}{\alpha_l - x_r\beta_l}$, $\hat{\phi}_{l_2} = \frac{x_r}{\beta_l}$ and $\mu_{d_t d_2} = \frac{m_{d_t d_2}\sigma_{d_2}^2}{P_{d_t}\overline{g}_{d_t d_2}}$. Further, the expressions for $R_{d_2}(t_1)$, $R_{c_1}(t_1)$, $R_{c_2}(t_1)$ and $R_{d_1}(t_2)$ can be derived in similar manner. Next, using [94, eq. (3.381.9)], [94, eq. (8.352.6)], [94, eq. (3.383.10)]

$$R_{d_2}(t_2) = \frac{1}{m_{t2}}\sum_{n=0}^{m_{t2}-1}\frac{(\mu_d)^n}{n!}e^{\mu_d}\Gamma(n+1)\Gamma(-n,\mu_d). \tag{4.20}$$

where $m_{t2} \triangleq m_{d_t d_2}$. Thus, SER for ND-NC system is finally derived as

$$
\begin{aligned}
\mathcal{R}_{sys} = \frac{1}{2\,\ln 2}\Bigg(& \sum_{i=\{1,2\}} \mathcal{J}_2\bigg(a_{d_i}, d_t, d_i, b, \frac{P_{d_t}\,\overline{g}_{d_t d_i}}{\sigma_{d_i}^2 \hat{\phi}_{d_i}}, \frac{P_b\,\overline{g}_{bd_i}}{\sigma_{d_i}^2}\bigg) \\
& + \sum_{j=\{1,2\}} 2\,\mathcal{J}_2\bigg(a_{c_j}, b, c_j, d_t, \frac{P_b\,\overline{g}_{bc_j}}{\sigma_{c_j}^2 \hat{\phi}_{c_j}}, \frac{P_{d_t}\,\overline{g}_{d_t c_j}}{\sigma_{c_j}^2}\bigg) \\
& + \frac{1}{m_{d_t d_2}} \sum_{n=0}^{m_{d_t d_2}-1} \frac{(\mu_d)^n}{n!}\, e^{\mu_d}\, \Gamma(n+1)\, \Gamma(-n,\, \mu_d) \\
& + \frac{\mathcal{J}_1(a_{d_1})}{\Gamma(m_{d_t d_1})} \Gamma\bigg(m_{d_t d_1}, \frac{m_{d_t d_1}\,\sigma_{d_2}^2}{P_{d_t}\,\overline{g}_{d_t d_1}}\bigg)\Bigg),
\end{aligned}
\tag{4.21}
$$

Remarks:

1. *Choice of approximation order*: Due to the summations involved in the GCQ method to attain the analytical value of $\mathcal{R}_{sys}$, though higher values of R provide a better accuracy in the ergodic rates, the same also increases the complexity. It is to note that for low values of R, there will exist a difference between SER value obtained analytically and the simulations. Thus, with an existence of a trade-off between accuracy and complexity, even though $R \to \infty$ ideally can reduce the approximation error to zero, it can be inferred that a choice of the value of R need to be made such that the $\mathcal{R}_{sys}$ approximation attained is sufficient.

2. *Fading severity*: Similar to the insights obtained from the SOP, increase in the value of m_{12} increases $\mathcal{R}_{sys}$ due to improved fading conditions. Similarly, an increase in the value of m_{32} decreases the SER.

4.3 Optimization Framework

4.3.1 Problem formulation

To enhance the performance of the ND-NC system, the D2D interferences to CU must be kept within an acceptable level. Further, the power splits between c_1, c_2, d_1 and d_2 must be taken care of in order to maintain NOMA compatibility. In this context, we formulate a JPC problem ($P0$) to jointly obtain $\alpha_p^*, \alpha_c^*, \alpha_d^*$ that mini-

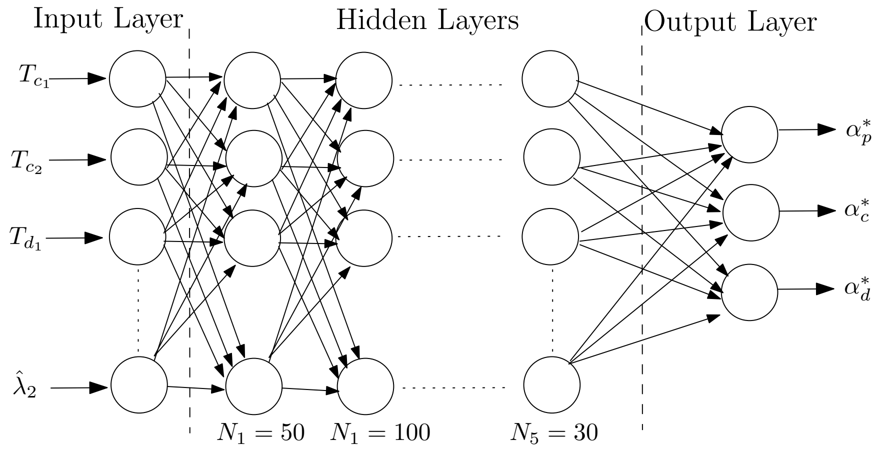

Figure 4.2: Proposed DNN framework for P-JPC.

mizes the SOP as

$$(P0): \underset{\alpha_p,\alpha_c,\alpha_d}{\text{minimize}} \quad \mathcal{P}_{out}, \quad \text{subject to} \quad \mathcal{C}1: 0 < \alpha_p < 1,$$
$$\mathcal{C}2: \alpha_c + \beta_c = 1, \quad \mathcal{C}3: \delta_{c_1}\, \beta_c < \alpha_c < 1,$$
$$\mathcal{C}4: \alpha_d + \beta_d = 1, \quad \mathcal{C}5: \delta_{d_1}\, \beta_d < \alpha_d < 1,$$
$$\mathcal{C}6: \mathcal{P}_{c_1} \leq \mathcal{P}_{th}, \quad \mathcal{C}7: \mathcal{P}_{c_2} \leq \mathcal{P}_{th},$$

where $\mathcal{C}1$, $\mathcal{C}3$ and $\mathcal{C}5$ limit the range of coefficients. $\mathcal{C}2$ and $\mathcal{C}4$ govern the power split among the NOMA users. $\mathcal{P}_{c_1} = 1 - A_{c_1}$ and $\mathcal{P}_{c_2} = 1 - A_{c_2}$ are OP experienced by c_1 and c_2, respectively. $\mathcal{C}6$ and $\mathcal{C}7$ guarantee the cellular OP's to remain below a required threshold $\mathcal{P}_{th}$.

4.3.2 Proposed P-JPC solution

As SOP expression in (4.13) is a combination of various complex non-linear functions, the derivative-based exact closed-form solution to $(P0)$ is challenging to obtain. Further, although algorithm-based solutions like full-search or brute-force can be used to solve the same by computing SOP for each value of α_p, α_c and α_d, however they require large number of iterations with significant computational complexity [140]. This can significantly increase the latency and thus are less appropriate for real-time operations. Hence, it is more practical to utilize predictive solutions based on machine learning where the computational complexity is mostly shifted to offline training with a minimal online complexity.

Now, to solve $(P0)$, we build a fully connected feed-forward DNN with an input layer, 5 hidden layers and an output layer as shown in Fig. 6.2. The input layer consists of 15 inputs namely T_{c_1}, T_{c_2}, T_{d_1}, T_{d_2}, m_{ij}, $\mathcal{P}_{th}$, $\lambda_{d_t d_1} = \lambda_{d_t d_2} \triangleq \hat{\lambda}_1$, $\lambda_{bj} = \lambda_{d_t c_1} = \lambda_{d_t c_2} \triangleq \hat{\lambda}_2$ where $i \in \{b, d_t\}$, $j \in \{c_1, c_2, d_1, d_2\}$, and λ_{ij} is the normalized distance between the transmitter node i and the receiver node j. Further, $N_1 = 50$, $N_2 = 100$, $N_3 = 250$, $N_4 = 100$, and $N_5 = 30$, where N_h is the number of neurons in the h^{th} hidden layer. Nadam, a variation of Adam optimizer [143], is used as the learning algorithm with learning rate, exponential decay rate and numerical stability constant set as 0.001, 0.9 and 10^{-7}, respectively [141]. For performance evaluation of this regression problem, MSE is choosen as the loss function defined as

$$MSE = \mathbb{E}[||\boldsymbol{\alpha} - \hat{\boldsymbol{\alpha}}||^2], \tag{4.22}$$

where $\boldsymbol{\alpha} = [\alpha_p^*, \alpha_c^*, \alpha_d^*]$ and $\hat{\boldsymbol{\alpha}} = [\hat{\alpha}_p^*, \hat{\alpha}_c^*, \hat{\alpha}_d^*]$ are actual and predicted outputs, respectively. Now, we create a dataset by solving $(P0)$ using full-search [140] for different values of inputs and obtaining corresponding output values such that 90% of the data is utilized to train the P-JPC model and the remaining 10% for testing. Note that all the above parameter values are empirically obtained to achieve the lowest possible MSE. The entire P-JPC methodology is summarized in Algorithm 3.

4.3.3 Statistical CSI

For the proposed optimization solution, only the statistical CSI (i.e. only the fading characteristics instead of instantaneous CSI) of the links is required at the base station (BS) which acts as the central controller to perform the optimization. The channel statistics of the cellular NOMA users can be obtained from the channel estimates using pilot training sequences. Similarly, the D2D-NOMA users can estimate CSI of D2D links and provide the statistics to the BS through control channels.

Notably, statistical CSI based power allocation is more practical for implementation in the scenarios in which the BS can only obtain global channel statistics especially for those links that are not directly connected to the BS. Also, acquiring instantaneous CSI would consume high feedback overhead as CSI updates will then be required frequently. On the other hand, as the statistical CSI consists of long-term channel information, frequent channel updates are not required, and is more accurate in comparison to the instantaneous CSI.

Algorithm 3 Learning Assisted P-JPC

```
Input: T_{c_1}, T_{c_2}, T_{d_1}, T_{d_2}, m_{ij}, \hat{\lambda}_1, \hat{\lambda}_2
Output: \hat{\alpha}_p^*, \hat{\alpha}_c^*, \hat{\alpha}_d^*
Data Set Generation
Multiple Nested For Loops
Solve (P0) by full-search to obtain actual \alpha_p^*, \alpha_c^* and \alpha_d^* for each input data
End For Loops
Divide the data set to 90% and 10% for training and testing respectively
while satisfactory test performance is not achieved do
    Train the model with Nadam optimizer
    Test the trained model using the test data
end while
```

4.4 Results and Discussions

In this section, the performance of the proposed scheme is numerically assessed. Unless explicitly specified, $m_{ij} \triangleq m = 2$, $P_b = 1$ W, $P_{max} = 0.2$ W, $\hat{\lambda}_1 = 0.2$ and $\hat{\lambda}_2 = 1$. $T_{c_1} = T_{d_1} \triangleq T_1 = 0.1$ bits/sec/Hz, and $T_{c_2} = T_{d_2} \triangleq T_2 = 0.5$ bits/sec/Hz, $\mathcal{P}_{th} = 0.001$, $\alpha_p = 0.5$, $\alpha_c = 0.3$ and $\alpha_d = 0.3$. Further, we consider $\overline{g}_{ij} = 10^{-3}\lambda_{ij}^{-\eta}$ and $\frac{P_i \lambda_{ij}}{\sigma_i^2} = \rho \triangleq 25$ dB [137], where $\eta = 3.5$ is the path-loss exponent.

In Figure 4.3, the performance of the ND-NC is compared with ND-OC and OD-OC systems in terms of SOP over transmit SNR. Clearly, the proposed ND-NC system is observed to experience a lower outage than both ND-OC and OD-OC. It is due to a higher pre-log factor of 1/4 in OD-OC because a total of 4 time phases are required. Further, as shown in Table 4.1, due to OMA-based cellular transmission in both ND-OC and OD-OC, the D2D transmission is interference limited in t_2 which is not the case in ND-NC. Moreover, it can be observed that the ND-NC system performance improves with better fading conditions and the analytical results presented are seen to match well with the simulation results.

Figure 4.4 and and Figure 4.5 shows SER results over SNR for the proposed and the comparative transmission protocol, respectively, where $m_x = 1, 2$, with $m_{d_t d_i} = m_{bc_i} \triangleq m_x\ \forall i \in \{1, 2\}$. The SERs of the ND-OC and the OD-OC systems, and for the comparative protocol can also be expressed similar to the ND-NC of the

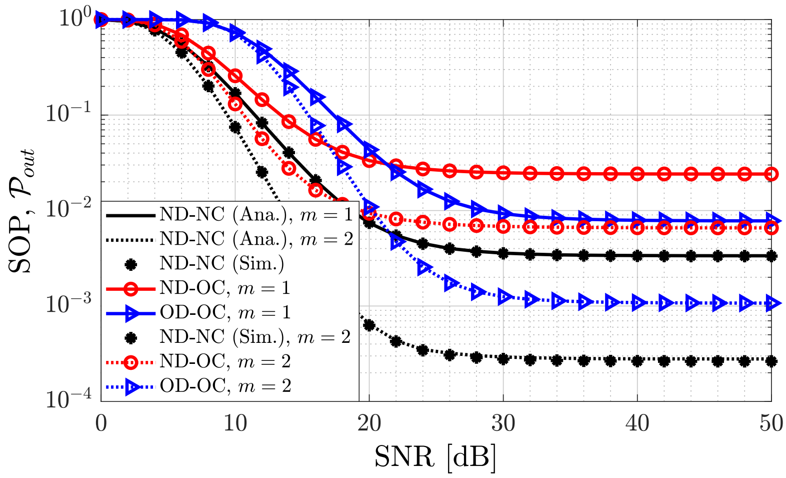

Figure 4.3: SOP vs SNR for ND-NC, ND-OC and OD-OC.

proposed protocol. It can be observed that by utilizing the proposed protocol, the ND-NC system outperforms both the ND-OC and OD-OC systems because in ND-NC, $d_t \rightarrow d_1$, d_2 transmission in t_2 is not affected by interference from b. However, by using the comparative protocol, the ND-OC system is observed to have a higher SER than ND-NC because cellular transmissions in t_3 and t_4 are not affected by interference from D2D transmitter. Further, SER is 6.25%, 7.14%, and 5.88% more in case of $m_x = 2$ than $m_x = 1$ for ND-NC, ND-OC and OD-OC, respectively as fading conditions of signal links $b \rightarrow c_i$ and $d_t \rightarrow d_i$ is improved. Moreover in both Figs. 4.3 and 4.4, despite NOMA-based D2D transmission in ND-OC, the OD-OC outperforms it as D2D transmissions in t_3 and t_4 are interference-free, which further proves the efficacy of the proposed protocol. This shows the importance of designing NOMA system models that not only more spectral efficient than OMA but also can outperform them and thus reveals the efficacy of the proposed ND-NC.

In Figure 4.6, the effect of number of epochs (E) over achievable MSE is analyzed for different hidden layers (H). After 400 epochs of training, DNN model with $H = 5$ has 95% and 67% lower MSE as compared to $H = 2$ and $H = 3$, respectively. The training performance is observed to converge at 500 epochs for $H = 5$ to attain sufficiently accurate prediction. Further, increasing the number of hidden layers to $H = 7$ or $H = 9$ does not provide remarkable performance improvement. Moreover, for $H = 5$ and $E = 400$, an MSE of 10^{-4} is achieved which shows that the predicted $\hat{\boldsymbol{\alpha}}$ matches reasonably well with the actual $\boldsymbol{\alpha}$.

In Figure 4.7, the proposed P-JPC is compared with F-JPC scheme in which

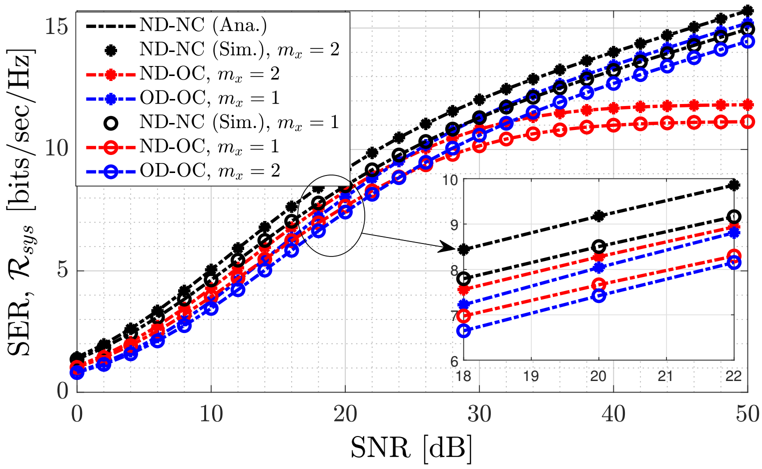

Figure 4.4: SER vs SNR for ND-NC, ND-OC and OD-OC for proposed transmission protocol.

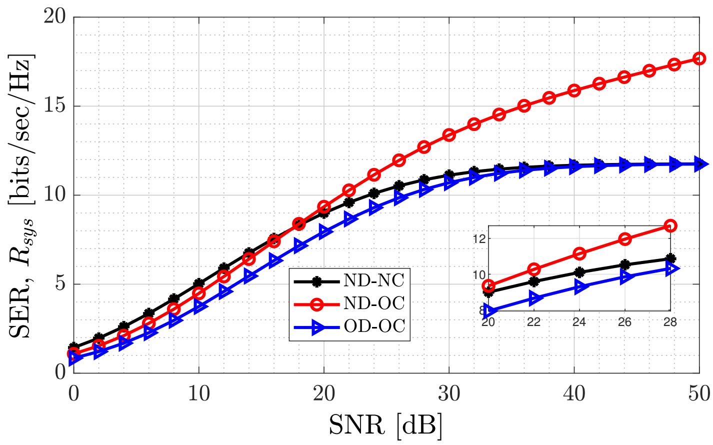

Figure 4.5: SER vs SNR for ND-NC, ND-OC and OD-OC for comparative transmission protocol.

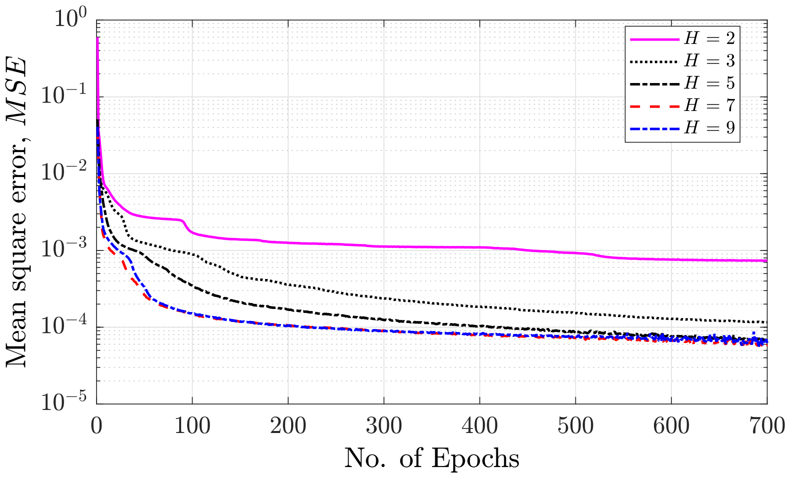

Figure 4.6: Effect of epochs on MSE for different hidden layers.

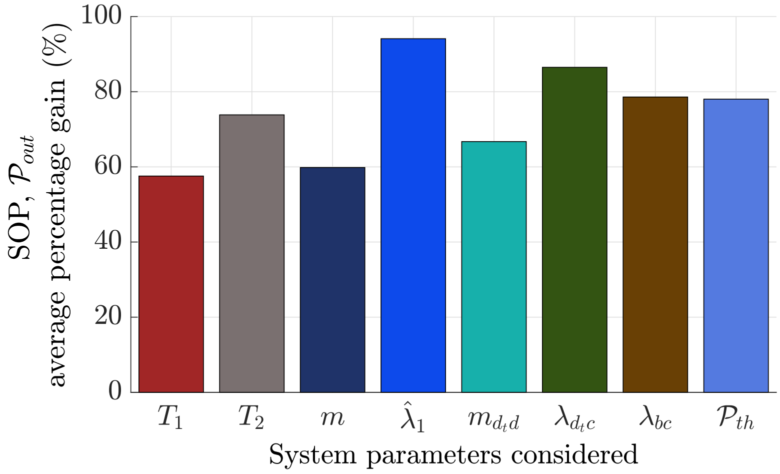

Figure 4.7: Comparison of P-JPC with F-JPC for different parameters.

$\alpha_p, \alpha_c, \alpha_d$ are fixed [140], with $m_{d_t d_i} \triangleq m_{d_t d}$, $\lambda_{d_t c_i} \triangleq \lambda_{d_t c}$ and $\lambda_{bc_i} \triangleq \lambda_{bc}$, $\forall\, i \in \{1, 2\}$. Note that an increase in either the distance or fading severity of D2D link increases the signal path-loss and thus α_p^* has to be increased. Similarly, decrease in $\lambda_{d_t c}$ increases $d_t \to c$ interference and increase in λ_{bc} increases path-loss of $d_t \to c$ link. Thus in both scenarios, the D2D interfering power is required to be lowered. Further, the NOMA power splits α_c^* and α_d^* need to be adjusted with different target rate values. Thus, clearly, the P-JPC optimized NDNC system is found to outperform F-JPC with an average improvement of 73% over all the system parameters as power allocations in the latter does not get updated adaptively to change in parameter values.

4.5 Summary

In this chapter, a novel ND-NC transmission protocol is proposed for a D2D underlayed cellular system where both D2D and cellular networks are NOMA enabled. Also, a DNN architecture is proposed to solve the JPC problem. Simulation results reveal that the proposed spectrally efficient ND-NC outperforms ND-OC and OD-OC models in terms of SOP and SER due to lower interference and lower time phases, respectively. Additionally, by using the P-JPC solution, an appreciable prediction of power allocations is achieved. Further, the closed-form expressions with Nakagami-m fading are obtained and numerically validated, along with providing various insights on SOP behaviour for different system parameters. In the following chapter, to enhance both system performance and spectrum utilization, an interesting IRS-assisted system model is investigated. This model serves as an application for both FD cooperative systems and underlay D2D communication.

Chapter 5

RIS Assisted Full-Duplex Systems with Different Downlink and Uplink Users

In this chapter, a FD network assisted by an RIS is investigated involving both downlink and uplink users in the same frequency band with best user selections. In the recent years, there has been a growing interest in the research community in integrating RIS with FD systems (RIS-FD) [144–149]. In [144, 145], the authors investigated two-way RIS-FD communication and derived analytical expressions for the OP, ER, and average symbol error rate. Work in [146] investigated the two-way RIS-FD system under the impact of imperfect channel state information and discrete phase-shift design and provide analytical insights into OP and ER, and their behavior at high transmit power regimes. Authors in [147] performed OP analysis of two-way RIS-FD system considering continuous amplitude and phase-shift, and highlighted superiority of the considered system over the one-way counterpart. In [148] a multi-RIS system was investigated and SOP was minimized to jointly optimize RIS location and number of reflecting elements. Authors in [149] considered RIS-FD with multi-user scenario and jointly optimized the precoding matrix of the base station and the reflection coefficient of the RIS to maximize the weighted minimum rate.

Since the RIS-FD works in [144–149] focus primarily on a two-way communication, they consider the SDU communication, i.e. an RIS-FD-SDU system. However, in the practical wireless communication networks, the uplink and downlink transmissions may involve the same or different users. Hence, in this work, the OP and ER analysis of a novel RIS-FD system is studied that has DDU users, i.e. an RIS-FD-DDU system. In the RIS-FD-SDU, all the elements of the RIS can be dedicated to the same user for coherent combining in order to boost the received signal. In contrast, in the RIS-FD-DDU system, to ensure fairness to the different downlink and uplink users, the RIS needs to be spatially divided into two separate zones: Zone-D and Zone-U. The elements in Zone-D are configured to boost the downlink transmission from AP, while the elements in Zone-U are configured to serve uplink transmissions to the AP. As a result, besides the direct links, both the AP and downlink users receive signals that are coherently combined from one zone and randomly combined from the other. Further, apart from RSI effect at the AP, unlike in the RIS-FD-SDU system, the downlink users also encounter CCI from uplink transmissions through a direct link and also via the RIS. These system complexities cause the performance analysis of the RIS-FD-DDU to be distinctively different from that of the RIS-FD-SDU system and considerably more challenging.

Apart from the RSI and the CCI, this work also take into account the practical constraint of HI in the system. These impairments arise from various factors, including in-phase/quadrature-phase imbalances and phase noise. Also, this work optimize the performance of the RIS-FD-DDU system by appropriately allocating transmit power coefficients, splitting RIS elements between the zones, and adjusting reflection amplitude. Also, the optimization objectives focus on minimizing SOP and maximizing ESR. Due to the intricate combination of complex non-linear functions within the mathematical expressions for SOP, OP, ER, and ESR, and the strong interdependence among the optimization variables, obtaining a closed-form solution for the problems is mathematically challenging. Therefore, to address this and determine the solution, an effective and derivative-free algorithm is employed such as particle swarm optimization (PSO).

To the best of our knowledge, this is the first study that examines the OP and the ER performance of the RIS-FD-DDU system and optimizes the same, taking into account the joint effects of CCI, RSI, and HI. The main contributions of this work are summarized as follows:

- The unique RIS-FD-DDU system model studied in this chapter is described in detail.

- Analytical OP, SOP, and ER expressions are derived over generalized Nakagami-m fading distribution using moment matching technique (MMT). The selection of the Nakagami-m distribution is driven by its flexibility and capacity to more accurately model a broader spectrum of fading scenarios, encompassing Rayleigh, Hoyt, and Rice distributions as specific instances. Additionally, among the various methods for approximating distributions, the MMT using the Gamma distribution is commonly preferred in the literature due to its effectiveness in fitting positive random variables.

- SOP minimization and ESR maximization problems are mathematically formulated constrained to QoS requirements of the users and solved via the PSO algorithm. Notably, the solution rely solely on the statistical CSI of communication links and instantaneous CSI is needed only for the desired links for configuring the optimal phase adjustments of the RIS elements.

- Validation of theoretical analysis, key system design insights, and comparison with non-RIS scenario are presented. Notably, the results show the effect on the performance of the users with different number of elements assigned to the two zones, and also with increase in the number of users and RIS elements.

This analysis is applicable to various real-world scenarios where the uplink and downlink users differ, such as intelligent transportation systems, smart manufacturing, telemedicine, smart homes, and smart grids. For instance, in a connected vehicle environment, an uplink user like a vehicle sensor system can provide traffic data and vehicle status updates to the AP for effective traffic management. Meanwhile, a downlink user, such as an autonomous vehicle, can receive navigation instructions and route updates from the AP. Similarly, in telemedicine applications, the uplink user might be a patient's wearable health monitoring device transmitting medical data to the AP through the uplink channel. Simultaneously, a healthcare professional's device can receive instructions and patient information via the downlink facilitated by the RIS. Additionally, in a smart home setup, a security camera system can transmit video footage and alerts to the AP for surveillance purposes

Table 5.1: Comparison of the presented work with other related works.

	[147]	[145]	[146]	[144]	[148]	[149]	This work
RIS-FD system	SDU	SDU	SDU	SDU	Multi-RIS assisted SDU	Multiple antenna based SDU	DDU
Multi-user scenario	✗	✗	✗	✗	✗	✓	✓
Consideration of direct link	✗	✗	✓	✗	✗	✗	✓
Fading model	Rayleigh	Rayleigh	Rayleigh	Rayleigh	Rayleigh, Rician	Rician	Generalized Nakagami-m
Hardware impairment	✗	✗	✗	✗	✗	✗	✓
Co-channel interference	✗	✗	✗	✗	✗	✓	✓
OP analysis	✓	✓	✓	✓	✓	✗	✓
ER analysis	✗	✗	✓	✗	✗	✗	✓
Performance optimization	✗	✗	✗	✓	✓	✓	✓
CSI required	-	-	-	Instantaneous CSI	Instantaneous CSI	Instantaneous CSI	Statistical CSI
Optimization objective	-	-	-	SINR maximization	SOP minimization	Weighted minimum rate maximization	SOP minimization and ESR maximization

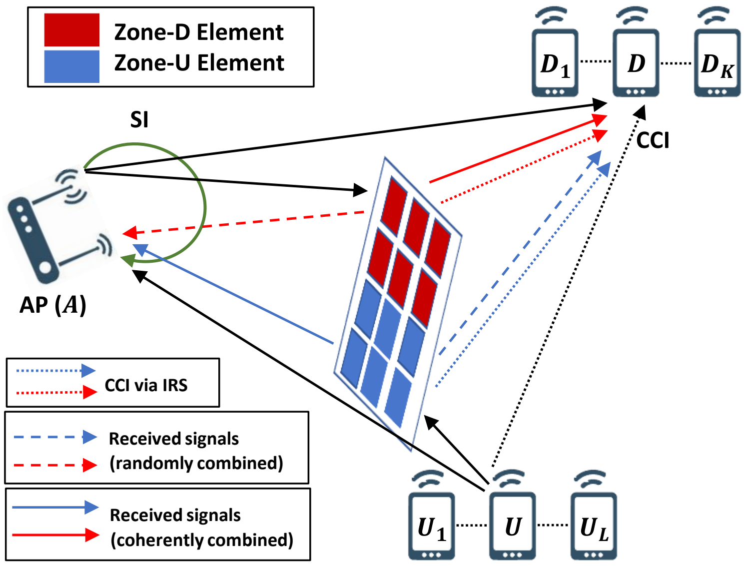

Figure 5.1: RIS-FD-DDU system model.

via the RIS. At the same time, devices like thermostats or lighting systems can receive control commands and automation settings from the AP through the downlink channel. Likewise, in a smart factory setting, a sensor node can gather real-time data from production machinery and transmit it to the AP for analysis and monitoring. Meanwhile, another user such as a robotic arm can receive control signals and commands from the AP.

5.1 System Model

A wireless network is considered where an AP (A) operating in FD serves a set of K downlink users ($\mathcal{K} = \{D_1, D_2, ..., D_K\}$) and L uplink users ($\mathcal{L} = \{U_1, U_2, ..., U_L\}$) via a N-element sized RIS. It is assumed that D and U represent the best downlink and uplink users, respectively, selected by the AP, with the user selection strategy is based on the maximum channel gain between the AP and the users. Further, the AP has two antennas, one for transmission to D and other for signal reception from U. Unlike [144–149] where the entire elements of the RIS can be configured to coherently combine the desired signal of a single user, it is considered that the RIS is divided into two zones, namely Zone-D (having N_d number of elements) and Zone-U (having N_u number of elements) to boost the downlink and uplink transmissions, respectively.For the sake of convenience and simplicity in denoting the nodes, we use the notations in both upper case (A, D, U, D_1,...D_K, U_1,...U_L) and lower case (a, d, u, d_1,...d_K, u_1,...u_L) interchangeably in the rest of the chapter. The downlink received signal (y_{d_k}) at $D_k \in \{D_1, D_2, .., D_K\}$ from A is given as

$$y_{d_k} = \underbrace{\sqrt{P_a}\,(x_{d_k} + \Phi_{ad_k})\,H_{ad_k}}_{\text{Desired signal and associated HIs}} + \underbrace{\sqrt{P_u}\,(x_u + \Phi_{ud_k})\,H_{ud_k}}_{\text{CCI and associated HIs}} + n_{d_k}, \tag{5.1}$$

where x_{d_k} and x_u represent symbols corresponding to D_k and U, respectively. $P_a = \alpha_a\,P_{max}$ and $P_u = \alpha_u\,P_{max}$ are transmission powers of A and U, respectively. α_a and α_u, bounded in the range $(0, 1]$, are coefficients of power allocation. P_{max} indicates the power allocation limit. $\Phi_{pq} \sim \mathcal{CN}(0, \phi_{pq}^2)$, where p and q belong to the set $\{a, d_k, u\}$, represents distortion noise due to the HIs with $\phi_{pq} = \sqrt{\phi_p^2 + \phi_q^2}$. ϕ_p^2 and ϕ_q^2 denote the level of HIs at the transmitter node p and the receiver node q, respectively, and ϕ_{pq} characterizes the aggregate level of HIs. $n_q \sim \mathcal{CN}(0, \sigma_q^2)$ represents the additive white Gaussian noise at node q. Further, H_{ad_k} and H_{ud_k} are given as

$$H_{ad_k} = \underbrace{h_{ad_k}}_{\text{direct link}} + \underbrace{\sum_{i_1=1}^{N_d} h_{ai_1} h_{i_1 d_k} \zeta e^{j\theta_{i_1}} + \sum_{i_2=1}^{N_u} h_{ai_2} h_{i_2 d_k} \zeta e^{j\theta_{i_2}}}_{\text{RIS reflected links}}, \tag{5.2}$$

$$H_{ud_k} = \underbrace{h_{ud_k}}_{\text{direct link}} + \underbrace{\sum_{i_1=1}^{N_d} h_{ui_1} h_{i_1 d_k} \zeta e^{j\theta_{i_1}} + \sum_{i_2=1}^{N_u} h_{ui_2} h_{i_2 d_k} \zeta e^{j\theta_{i_2}}}_{\text{RIS reflected links}}, \tag{5.3}$$

where, for each link pq (p and q belong to the set $\{a, d, u, d_k, u_l, i_1, i_2\}$ and $p \neq q$), the phase and envelope of channel co-efficient h_{pq} are characterized by distributions $\theta_{pq} \sim Uni[0, 2\pi]$ and $|h_{pq}| \sim Nak(m_{pq}, \overline{g}_{pq})$, respectively. i_1 represents the ${i_1}^{th}$ Zone-D element and i_2 signifies the ${i_2}^{th}$ Zone-U element. The parameters θ_{i_1} and θ_{i_2} represent the induced phase shifts by the RIS elements and follow the uniform distribution $Uni[0, 2\pi]$. ζ, defined in the interval $[0, 1]$, represents the reflection amplitude by the RIS elements. The uplink received signal at A (y_a) from U_l ($U_l \in \{U_1, U_2, ..., U_L\}$) is given as

$$\begin{aligned} y_a = & \underbrace{\sqrt{P_u}\left(x_{u_l} + \Phi_{u_l a}\right) H_{u_l a}}_{\text{Desired signal and associated HIs}} + \underbrace{\sqrt{P_a}\, h_{aa}(x_d + \Phi_{aa})}_{\text{SI and associated HIs}} + n_u \\ = & \sqrt{P_u}\left(x_{u_l} + \Phi_{u_l a}\right) H_{u_l a} + h_{rsi} + n_{u_l}, \end{aligned} \tag{5.4}$$

where h_{aa} denotes the self-interference (SI) between the transmitting antenna at AP and its receiving antenna. Even though the transmitted symbol x_{d_k} is known at AP, the SI cannot be perfectly suppressed due to associated HIs and significant power difference between the transmitted signal and the desired signal received from the distant user U_l. The resultant RSI can be modeled as a Rayleigh fading channel with channel co-efficient h_{rsi} and variance $\omega P_t^{\,v}$, where $\omega > 0$ and $v \in [0, 1]$. Further, $H_{u_l a}$ is given as

$$H_{u_l a} = \underbrace{h_{u_l a}}_{\text{direct link}} + \underbrace{\sum_{i_1=1}^{N_d} h_{u_l i_1} h_{i_1 a} \zeta e^{j\theta_{i_1}} + \sum_{i_2=1}^{N_u} h_{u_l i_2} h_{i_2 a} \zeta e^{j\theta_{i_2}}}_{\text{RIS reflected link}}, \tag{5.5}$$

Now, as the Zone-D and the Zone-U elements are configured to boost $A \rightarrow RIS \rightarrow D_k$ and $U_l \rightarrow RIS \rightarrow A$ transmissions for coherent combining, respectively, the same is achieved by setting $\theta^*_{i_1} = \theta_{ad_k} - \theta_{ai_1} - \theta_{i_1 d_k}$ and $\theta^*_{i_2} = \theta_{u_l a} - \theta_{u_l i_2} - \theta_{i_2 a}$. Accordingly, H_{ad_k}, $H_{u_l a}$, and H_{ud_k} are re-expressed as

$$H_{ad_k} = e^{j\theta_{ad_k}} \underbrace{\left(|h_{ad_k}| + \sum_{i_1=1}^{N_d} |h_{ai_1}||h_{i_1 d_k}|\zeta\right)}_{\text{coherently combined}} + \underbrace{\sum_{i_2=1}^{N_u} |h_{ai_2}||h_{i_2 d_k}|\zeta \Theta_{i_2}}_{\text{randomly combined}}, \tag{5.6}$$

$$H_{ud_k} = |h_{ud_k}| e^{j\theta_{ud_k}} + \underbrace{\sum_{i_1=1}^{N_d} |h_{ui_1}||h_{i_1 d_k}|\zeta \hat{\Theta}_{i_1} + \sum_{i_2=1}^{N_u} |h_{ui_2}||h_{i_2 d_k}|\zeta \hat{\Theta}_{i_2}}_{\text{randomly combined}}, \tag{5.7}$$

$$H_{u_l a} = e^{j\theta_{ua}} \underbrace{\left(|h_{u_l a}| + \sum_{i_2=1}^{N_u} |h_{u_l i_2}||h_{i_2 a}|\zeta\right)}_{\text{coherently combined}} + \underbrace{\sum_{i_1=1}^{N_d} |h_{u_l i_1}||h_{i_1 a}|\zeta \Theta_{i_1}}_{\text{randomly combined}}, \tag{5.8}$$

where Θ_{i_2}, Θ_{i_1}, $\hat{\Theta}_{i_1}$, and $\hat{\Theta}_{i_2}$ are expressed as,

$$\Theta_{i_2} \triangleq e^{j(\theta_{ai_2} + \theta_{i_2 d} + \theta_{u_l a} - \theta_{u_l i_2} - \theta_{i_2 a})}, \tag{5.9}$$

$$\Theta_{i_1} \triangleq e^{j(\theta_{u_l i_1} + \theta_{i_1 a} + \theta_{ad_k} - \theta_{ai_1} - \theta_{i_1 d_k})}, \tag{5.10}$$

$$\hat{\Theta}_{i_1} \triangleq e^{j(\theta_{ui_1}+\theta_{i_1d}+\theta_{ad_k}-\theta_{ai_1}-\theta_{i_1d_k})}, \tag{5.11}$$

$$\hat{\Theta}_{i_2} \triangleq e^{j(\theta_{ui_2}+\theta_{i_2d_k}+\theta_{u_la}-\theta_{u_li_2}-\theta_{i_2a})}. \tag{5.12}$$

It is to note, from the above equations, that the reflected signals from the RIS to the users come from all the elements instead of just N_u or N_d elements alone. The SINR at nodes D_k and A are now expressed as

$$\psi_{d_k}^{d_k} = \frac{P_a|H_{ad_k}|^2}{P_a|H_{ad_k}|^2\phi_{ad_k}^2 + P_u|H_{ud_k}|^2(1+\phi_{ud_k}^2) + \sigma_{d_k}^2}, \tag{5.13}$$

$$\psi_a^{u_l} = \frac{P_u|H_{u_la}|^2}{P_u|H_{u_la}|^2\phi_{u_la}^2 + |h_{rsi}|^2 + \sigma_a^2}. \tag{5.14}$$

For channel estimation, both "separate channel estimation" and "cascaded channel estimation" methods can be employed. In systems using semi-passive IRSs equipped with dedicated sensing devices, the channels from the BS/users to the IRS can be estimated separately at these sensing devices based on pilot signals sent by the BS/users. On the other hand, in systems with fully-passive IRSs without sensing devices, the BS-IRS and user-IRS channels cannot generally be estimated separately. Instead, only the cascaded user-IRS-BS channel can be estimated at one endpoint of the communication system, such as the BS.

Cascaded channel estimation is particularly advantageous over separate channel estimation due to its lower hardware cost and reduced energy consumption at the IRS, as it does not require active sensing devices. Specifically, for our system model, for both downlink and uplink users, the BS can send pilot signals that are reflected by the IRS to the downlink and uplink users. The users then receive these signals, estimate the combined channel and feedback the estimated cascaded channel to the BS for further processing. Based on these estimations, the BS can select the best downlink user and uplink user. Subsequently, the uplink user sends pilot signals that are reflected by the IRS to the downlink user, and the corresponding estimates are sent to the BS. The BS then communicates the required phase information to the microcontroller connected to the IRS. This information can be provided via a low-latency high-frequency (e.g., millimeter-wave) wireless link or a separate wired backhaul link.

5.2 Performance Analysis

In this section, OP and ER of the RIS-FD-DDU system are analyzed which are very crucial metrics for performance evaluation of wireless communication systems.

5.2.1 Outage Probability of Downlink User

The OP is defined as the probability of the SINR falling below a certain pre-defined threshold. Accordingly, the OP of D is given as,

$$\begin{aligned}\mathcal{O}_d &= \Pr\left(\log_2\left(1+\max\left(\psi_{d_1}^{d_1}, ...\psi_{d_K}^{d_K}\right)\right) < R_{th_d}\right) \\ &= \prod_{d_k \in \mathcal{K}} F_{\tilde{\psi}_{d_k}^{d_k}}(\tilde{\delta}_d), \end{aligned} \tag{5.15}$$

where $\tilde{\psi}_{d_k}^{d_k} \triangleq \frac{|H_{ad_k}|^2}{P_u|H_{ud_k}|^2(1+\phi_{ud_k}^2)+\sigma_{d_k}^2}$, $\tilde{\delta}_d \triangleq \frac{\delta_d}{P_a(1-\delta_d\phi_{ad_k}^2)}$, R_{th_d} is D's target rate, and $\delta_d = 2^{R_{th_d}}-1$. Note that in (5.15), $d = \underset{d_k \in \mathcal{K}}{\operatorname{argmax}}\{|H_{ad_k}|^2\}$ will also maximize the SINR $\psi_{d_k}^{d_k}$ in (5.13) as the H_{ad_k} contains N_d coherent reflections while the interference H_{ud_k} is completely randomly reflected. Now, the H_{ad_k} is a sum of channel co-efficients of a direct link, coherently combined cascaded N_d links and randomly combined cascaded N_u links. Similarly, H_{ud_k} is a sum of channel co-efficients of a direct link and randomly combined cascaded N links. Thus, it is difficult to characterize the distributions of H_{ad_k} and H_{ud_k} and obtain the exact OP expression. Hence, we resort to Gamma approximations via MMT to obtain the analytical OP expression. The first order ($\mathbb{E}[H_{ad_k,s}]$) and second order ($\mathbb{E}[H_{ad_k,s}^2]$) moments of $H_{ad_k,s} \triangleq |H_{ad_k}|^2$ are given as,

$$\mathbb{E}[H_{ad_k,s}] = \mathbb{E}[|H_{ad_k,c}|^2] + \mathbb{E}[|H_{ad_k,r}|^2], \tag{5.16}$$

$$\begin{aligned}\mathbb{E}[H_{ad_k,s}^2] = \mathbb{E}[|H_{ad_k,c}|^4] + \mathbb{E}[|H_{ad_k,r}|^4] \\ + 4\,\mathbb{E}[|H_{ad_k,c}|^2]\,\mathbb{E}[|H_{ad_k,r}|^2]),\end{aligned} \tag{5.17}$$

where $H_{ad_k,c} \triangleq e^{j\theta_{ad_k}}(|h_{ad_k}|+\sum_{i_1=1}^{N_d}|h_{ai_1}||h_{i_1d_k}|\zeta)$, and $H_{ad_k,r} \triangleq \sum_{i_2=1}^{N_u}|h_{ai_2}||h_{i_2d_k}|\zeta\Theta_{i_2}$. Due to random combining, $H_{ad_k,r}$ can be modelled as $H_{ad_k,r} \sim \mathcal{CN}(0, \bar{H}_{ad_k,r})$, where $\bar{H}_{ad_k,r} = N_u\zeta^2\bar{g}_{a\hat{i}_2}\bar{g}_{\hat{i}_2d}$, $\bar{g}_{a\hat{i}_2} \triangleq \bar{g}_{ai_2}$ and $\bar{g}_{\hat{i}_2d_k} \triangleq \bar{g}_{i_2d_k}$ ($\forall i_2 \in \{1, 2, \cdots, N_u\}$). Accordingly, $|H_{ad_k,r}|$ follows Rayleigh distribution, a specific case of the Nakagami-m fading model with unity severity, i.e. $|H_{ad_k,r}| \sim Nak(1, \bar{H}_{ad_k,r})$. Thus, the n^{th} order moment of $|H_{ad_k,r}|$ is given as [150],

$$\mathbb{E}[|H_{ad_k,r}|^n] = \Gamma(1+n/2)\,(\bar{H}_{ad_k,r})^{n/2}. \tag{5.18}$$

Now, the n^{th} order moment of $|H_{ad_k,c}| = |h_{ad_k}| + h_{ad_k,c}$,
where $h_{ad_k,c} = \sum_{i_1=1}^{N_d}|h_{ai_1}||h_{i_1d_k}|\zeta$, can be obtained as,

$$\mathbb{E}[|H_{ad_k,c}|] = \mathbb{E}[|h_{ad_k}|] + \mathbb{E}[h_{ad_k,c}], \tag{5.19}$$

$$\mathbb{E}[|H_{ad_k,c}|^2] = \mathbb{E}[|h_{ad_k}|^2] + \mathbb{E}[h^2_{ad_k,c}] + 2\,\mathbb{E}[|h_{ad_k}|]\,\mathbb{E}[h_{ad_k,c}]), \tag{5.20}$$

where $\mathbb{E}[|h_{ad_k}|^n] = \frac{\Gamma(m_{ad_k}+n/2)}{\Gamma(m_{ad_k})(m_{ad}/\bar{g}_{ad})^{n/2}}$ [150]. Further, considering the RIS-based links to be independent and identically distributed (i.i.d) and using the property $\Gamma(z+1) = z\Gamma(z)$, the first and second order moment of $h_{ad_k,c}$ can be obtained as $\mathbb{E}[h_{ad_k,c}] = N_d\zeta\delta_{ad}$ and $\mathbb{E}[h^2_{ad_k,c}] = N_d\zeta^2(1+\delta^2_{ad}(N_d-1))$, respectively. Further, $\delta_{ad_k} \triangleq \delta_{a\hat{i}_1}\,\delta_{\hat{i}_1d_k}$, $\delta_{a\hat{i}_1} \triangleq \mathbb{E}[h_{a\hat{i}_1}] = \frac{\Gamma(m_{a\hat{i}_1}+1/2)}{\Gamma(m_{a\hat{i}_1})\sqrt{m_{a\hat{i}_1}/\bar{g}_{a\hat{i}_1}}}$, $\delta_{\hat{i}_1d_k} \triangleq \mathbb{E}[h_{\hat{i}_1d_k}] = \frac{\Gamma(m_{\hat{i}_1d}+1/2)}{\Gamma(m_{\hat{i}_1d_k})\sqrt{m_{\hat{i}_1d}/\bar{g}_{\hat{i}_1d_k}}}$, where $\forall i \in \{1, 2, \cdots, N_d\}$, $h_{a\hat{i}_1} \triangleq h_{ai_1}$, $h_{\hat{i}_1d_k} \triangleq h_{i_1d_k}$, $m_{a\hat{i}_1} \triangleq m_{ai_1}$, $m_{\hat{i}_1d_k} \triangleq m_{i_1d_k}$, $\bar{g}_{a\hat{i}_1} \triangleq \bar{g}_{a\hat{i}_1}$ and $\bar{g}_{\hat{i}_1d_k} \triangleq \bar{g}_{i_1d_k}$. Now, $|H_{ad_k,c}|$ can be approximated as a Gamma RV (GRV) via MMT with parameters namely shape $s_{|H_{ad_k,c}|}$ and scale $\theta_{|H_{ad_k,c}|}$ (i.e. $|H_{ad_k,c}| \sim \Xi(s_{|H_{ad_k,c}|}, \theta_{|H_{ad_k,c}|})$) given as ,

$$s_{|H_{ad_k,c}|} = \frac{(\mathbb{E}[|H_{ad_k,c}|])^2}{Var(|H_{ad_k,c}|)}, \tag{5.21}$$

$$\theta_{|H_{ad_k,c}|} = \frac{Var(|H_{ad_k,c}|)}{\mathbb{E}[|H_{ad_k,c}|]}, \tag{5.22}$$

where $Var(|H_{ad_k,c}|) = \mathbb{E}[|H_{ad_k,c}|^2]) - (\mathbb{E}[|H_{ad_k,c}|])^2$. Now, the 4^{th} moment of the

GRV $|H_{ad_k,c}|$ is given as [150],

$$\mathbb{E}[|H_{ad_k,c}|^4] = \frac{\Gamma(s_{|H_{ad_k,c}|}+4)}{\Gamma(s_{|H_{ad_k,c}|})}(\theta_{|H_{ad_k,c}|})^4, \tag{5.23}$$

Substituting (5.18), (5.20) and (5.23) into (5.16) and (5.17), the expressions of $\mathbb{E}[H_{ad_k,s}]$ and $\mathbb{E}[H^2_{ad_k,s}]$ can be obtained. Now similar to (5.21) and (5.22), $H_{ad_k,s}$ can be approximated as a GRV via MMT with shape $s_{H_{ad_k,s}}$ and scale $\theta_{H_{ad_k,s}}$.

Next, we approximate $H_{ud_k,s} \triangleq |H_{ud_k}|^2$ as a GRV. The first order and second order moments of $H_{ud,s}$ are given as

$$\mathbb{E}[H_{ud_k,s}] = \mathbb{E}[|H_{ud_k,d}|^2] + \mathbb{E}[|H_{ud_k,r}|^2], \tag{5.24}$$

$$\begin{aligned}\mathbb{E}[H^2_{ud_k,s}] = \mathbb{E}[|H_{ud_k,d}|^4] + \mathbb{E}[|H_{ud_k,r}|^4]& \\ + 4\,\mathbb{E}[|H_{ud_k,d}|^2]\,\mathbb{E}[|H_{ud_k,d}|^2]),&\end{aligned} \tag{5.25}$$

where $H_{ud_k,d} \triangleq |h_{ud_k}|e^{j\theta_{ud_k}}$, and $H_{ud_k,r} \triangleq \sum_{i_1=1}^{N_d} |h_{ui_1}||h_{i_1d_k}|\zeta\hat{\Theta}_{i_1} + \sum_{i_2=1}^{N_u} |h_{ui_2}||h_{i_2d_k}|\zeta\hat{\Theta}_{i_2}$. Thus, $|H_{ud_k,d}| = |h_{ud_k}|$ and its n^{th} order moment is given as

$$\mathbb{E}[|H_{ud_k,d}|^n] = \frac{\Gamma(m_{ud_k}+n/2)}{\Gamma(m_{ud_k})(m_{ud_k}/P_t\bar{g}_{ud_k})^{n/2}}, \tag{5.26}$$

Further, due to random combining, $H_{ud_k,r}$ can be modelled as $H_{ud_k,r} \sim \mathcal{CN}(0, \bar{H}_{ud_k,r})$, where $\bar{H}_{ad_k,r} = N_d\zeta^2\bar{g}_{a\hat{i}_1}\bar{g}_{\hat{i}_1d} + N_u\zeta^2\bar{g}_{a\hat{i}_2}\bar{g}_{\hat{i}_2d_k}$. Thus, $|H_{ud_k,r}| \sim Nak(1, \bar{H}_{ad_k,r})$ and its n^{th} order moment is given as

$$\mathbb{E}[|H_{ud_k,r}|^n] = \Gamma(1+n/2)\,(\bar{H}_{ud_k,r})^{n/2}. \tag{5.27}$$

Equations (5.26) and (5.27) can be now be utilized to obtain (5.24) and (5.25). The first order moment and variance of $\hat{H}_{ud_k,s} \triangleq P_u|H_{ud_k}|^2(1+\phi^2_{ud_k}) + \sigma^2_d$ can be then expressed as

$$\mathbb{E}[\hat{H}_{ud_k,s}] = P_u(1+\phi^2_{ud_k})\,\mathbb{E}[H_{ud_k,s}] + \sigma^2_{d_k}, \tag{5.28}$$

$$Var(\hat{H}_{ud_k,s}) = \left(P_u(1+\phi^2_{ud_k})\right)^2 Var(H_{ud_k,s}). \tag{5.29}$$

where $Var(H_{ud_k,s}) = \mathbb{E}[H^2_{ud_k,s}]) - (\mathbb{E}[H_{ud_k,s}])^2$. Now, $\hat{H}_{ud_k,s}$ can be approximated to a GRV via MMT with shape $s_{\hat{H}_{ud_k,s}}$ and scale $\theta_{\hat{H}_{ud_k,s}}$.

Finally, as $H_{ad_k,s}$ and $\hat{H}_{ud_k,s}$ are two distinct GRVs, the ratio of the same (i.e. $\psi^{'}_{d_k} = H_{ad_k,s}/\hat{H}_{ud_k,s}$) follows a prime distribution. Its CDF is determined by the regularized incomplete beta function, as specified in (6.29).

$$F_{\tilde{\psi}^{d_k}_{d_k}}(x) \approx I\left(\frac{x\,\theta_{\hat{H}_{ud_k,s}}}{\theta_{H_{ad_k,s}} + x\,\theta_{\hat{H}_{ud_k,s}}}; s_{H_{ad_k,s}}, s_{\hat{H}_{ud_k,s}}\right). \tag{5.30}$$

Remark: By considering the approximation $1/x \approx 0$ as $x \to \infty$, the asymptotic OP in the high transmit power regime can be derived as

$$\mathcal{O}^{\infty}_d \approx \prod_{d_k \in \mathcal{K}} I\left(\frac{\hat{\delta}_d\,\theta_{H_{ud_k,s}}}{\theta_{H_{ad_k,s}} + \hat{\delta}_d\,\theta_{H_{ud_k,s}}}; s_{H_{ad_k,s}}, s_{H_{ud_k,s}}\right) \tag{5.31}$$

As the expression is independent of power P_{max}, the diversity order for D can be inferred to be zero.

5.2.2 Outage Probability of Uplink User

The OP of U is given as

$$\begin{aligned}\mathcal{O}_u &= \Pr\left(\log_2\left(1+\max\left(\psi^{u_1}_a, ...\psi^{u_L}_a\right)\right) < R_{th_u}\right)\\ &= \prod_{u_l \in \mathcal{L}} F_{\tilde{\psi}^{u_l}_a}(\tilde{\delta}_u),\end{aligned} \tag{5.32}$$

where $u = \underset{u_l \in \mathcal{L}}{\operatorname{argmax}}\{|H_{u_l a}|^2\}$ which also maximizes the corresponding SINR $\psi^{u_l}_a$. Further, $\tilde{\psi}^{u_l}_a \triangleq \frac{|H_{u_l a}|^2}{|h_{rsi}|^2+\sigma^2_a}$, $\tilde{\delta}_u \triangleq \frac{\delta_u}{P_u(1-\delta_u\phi^2_{u_l a})}$, R_{th_u} is U's target rate, and $\delta_u = 2^{R_{th_u}} - 1$. Similar to $H_{ad_k,s}$ in Lemma-1, we resort to Gamma approximations to obtain the shape $s_{H_{u_l a,s}}$ and the scale $\theta_{H_{u_l a,s}}$ of $H_{u_l a,s} \triangleq |H_{u_l a}|^2$ via MMT. A detailed proof of the same is avoided for the sake of brevity. Further, as $|h_{rsi}|$ is Rayleigh faded, $\mathbb{E}[H_{rsi}] = \mathbb{E}[|h_{rsi}|^2] = \omega P_t^v$, $\mathbb{E}[H_{rsi}^2] = \mathbb{E}[|h_{rsi}|^4] = 2(\omega P_t^v)^2$ and $Var(H_{rsi}) = (\omega P_t^v)^2$, where $H_{rsi} = |h_{rsi}|^2$. Accordingly, $\mathbb{E}[\hat{H}_{rsi}] = \mathbb{E}[H_{rsi}] + \sigma_a^2$ $\mathbb{E}[\hat{H}_{rsi}^2] = \mathbb{E}[H_{rsi}^2]$, where $\hat{H}_{rsi} = H_{rsi} + \sigma_a^2$. Thus $\hat{H}_{rsi}$ can now be converted to a GRV via MMT with shape and scale as $s_{\hat{H}_{rsi}}$ and $\theta_{\hat{H}_{rsi}}$, respectively. Now, the CDF of $H_{u_l a,s}/\hat{H}_{rsi}$ is expressed using the regularized incomplete beta function as given as

$$F_{\tilde{\psi}_a^{u_l}}(x) \approx I\left(\frac{x\,\theta_{\hat{H}_{rsi}}}{\theta_{H_{u_l a,s}} + x\,\theta_{\hat{H}_{rsi}}}; s_{H_{u_l a,s}}, s_{\hat{H}_{rsi}}\right). \tag{5.33}$$

Thus, the expression for OP of U is expressed as,

$$\mathcal{O}_u \approx \prod_{u_l \in \mathcal{L}} I\left(\frac{\tilde{\delta}_u\,\theta_{\hat{H}_{rsi}}}{\theta_{H_{u_l a,s}} + \tilde{\delta}_u\,\theta_{\hat{H}_{rsi}}}; s_{H_{u_l a,s}}, s_{\hat{H}_{rsi}}\right). \tag{5.34}$$

Remark: Utilizing [94, 8.392, 8.384.1, 8.391], the asymptotic OP for U can be obtained as

$$\mathcal{O}_u^{\infty} \approx \prod_{u_l \in \mathcal{L}} \sum_{n=0}^{\infty} (C_1\,P_{max})^{C_2} \tag{5.35}$$

where C_2 and C_1 correspond to diversity order and gain, respectively, and are given as,

$$C_2 = \Big(-(1-v)\,(s_{H_{u_l a,s}} + n)\Big), \tag{5.36}$$

$$C_1 = \left(\frac{\Gamma(s_{H_{u_l a,s}})}{n!(s_{H_{u_l a,s}} + n)\Gamma(s_{H_{u_l a,s}})}\right)^{\frac{1}{(v-1)\,(s_{H_{u_l a,s}}+n)}} \left((\hat{\delta}_u)^{-1}\,\theta_{H_{u_l a,s}}\right)^{\frac{1}{1-v}}. \tag{5.37}$$

As a special case, setting $v = 1$ will result in a zero diversity order.

5.2.3 System Outage Probability

The SOP is defined as the probability that either of the users in network fail to decode its signal successfully. In other words, the SOP is expressed as $\mathcal{O}_S = 1 - \mathcal{P}_{success}$, where $\mathcal{P}_{success}$ is the probability that symbols of both D and U are successfully decoded. Accordingly, $\mathcal{P}_{success}$ is determined as given in (5.38).

$$\begin{aligned}\mathcal{P}_{success} &= \prod_{d_k \in \mathcal{K}} \Pr(\psi_{d_k}^{d_k} < \delta_d) \prod_{u_l \in \mathcal{L}} \Pr(\psi_a^{u_l} < \delta_u) \\ &= (1 - \mathcal{O}_d)\,(1 - \mathcal{O}_u). \end{aligned} \tag{5.38}$$

Thus, the SOP expression for the RIS-FD-DDU system, is expressed as,

$$\mathcal{O}_s \approx \mathcal{O}_d + \mathcal{O}_u - \mathcal{O}_d\,\mathcal{O}_u \tag{5.39}$$

5.2.4 Ergodic Rate

The ER of D is defined as follows

$$\begin{aligned}\mathcal{R}_d &= \mathbb{E}\left[\log_2(1 + \max\left(\psi_{d_1}^{d_1}, ...\psi_{d_K}^{d_K}\right))\right] \\ &= \int_0^{\frac{1}{\phi_{ad_k}^2}} \prod_{d_k \in \mathcal{K}} \frac{1 - F_{\tilde{\psi}_{d_k}^{d_k}}(\tilde{z})}{(1+\tilde{z})\,\ln 2} d\tilde{z}, \end{aligned} \tag{5.40}$$

where $\tilde{z} = \frac{z}{P_a(1 - z\phi_{ad_k}^2)}$. Substituting (6.29) in (6.45), we obtain

$$\mathcal{R}_d = \int_0^{\frac{1}{\phi_{ad_k}^2}} \prod_{d_k \in \mathcal{K}} \frac{1 - I\left(\frac{\tilde{\delta}_d\,\theta_{\hat{H}_{ud_k},s}}{\theta_{H_{ad_k},s} + \tilde{\delta}_d\,\theta_{\hat{H}_{ud_k},s}}; s_{H_{ad_k},s}, s_{\hat{H}_{ud_k},s}\right)}{(1+\tilde{z})\,\ln 2} d\tilde{z}. \tag{5.41}$$

As the assessment of (5.41) is mathematically intractable, we utilize the basic the GCQ equation $\int_{\tilde{a}}^{\tilde{b}} f(\tilde{z})\,d\tilde{z} = \frac{(\tilde{b}-\tilde{a})\pi}{2V} \sum_{v=1}^{V} \sqrt{1 - \tilde{z}_v^2} f(y_v)$ to solve the integral by substituting $\tilde{a} = 0$ and $\tilde{b} = 1/\phi_{ad_k}^2$, where $\tilde{z}_v = \cos\left(\frac{(2v-1)\pi}{2V}\right)$, $y_v = \frac{(\tilde{b}-\tilde{a})\,x_v}{2} + \frac{(\tilde{b}-\tilde{a})}{2}$ and V is a finite value. Furthermore, the ER of U can be derived in a similar way.

Thus, the expression for ER ($\mathcal{R}_t$) of T ($\forall t \in \{d,u\}$ and $\forall T \in \{D,U\}$) is given as

$$\mathcal{R}_t \approx \prod_{\tau_t} \frac{\pi}{\phi_t'^2 \; 2V \ln 2} \sum_{v=1}^{V} \frac{\sqrt{1-{z_v}^2}}{(1+y_v)} \mathcal{I}_t, \tag{5.42}$$

where $\phi_d' \triangleq \phi_{ad_k}$, $\phi_u' \triangleq \phi_{u_l a}$, $\hat{H}_d \triangleq \hat{H}_{ud_k,s}$, $\hat{H}_u \triangleq \hat{H}_{rsi}$. $H_d \triangleq H_{ad_k,s}$, $H_u \triangleq H_{u_l a,s}$, τ_d denotes $d_k \in \mathcal{K}$, τ_u denotes $u_l \in \mathcal{L}$, and $\mathcal{I}_t \triangleq 1 - I\Big(\frac{\tilde{z}\,\theta_{\hat{H}_t}}{\theta_{H_t}+\tilde{z}\,\theta_{\hat{H}_t}}; s_{H_t}, s_{\hat{H}_t}\Big)$.

Remark: Although higher values of V can provide better accuracy for ER, the same also increases the complexity. Therefore, due to a trade-off between accuracy and complexity, a correct choice of V must be made accordingly to ensure the ER achieved is sufficiently accurate.

5.3 Optimization of SOP and ESR

To enhance the performance of the RIS-FD-DDU system, optimization problems are formulated to allocate transmit power coefficients, split RIS elements between the zones, and adjust reflection amplitude. The mathematical formulations for SOP minimization and ESR ($\mathcal{R}_{sys}$) maximization are as follows:

$$(P1): \min_{\alpha_a,\alpha_u,\alpha_d,\zeta} \mathcal{O}_S, \quad \text{subject to} \quad C1: \mathcal{O}_d < \mathcal{O}_{th_d},$$

$$C2: \mathcal{O}_u < \mathcal{O}_{th_u}, \qquad C3:\; 0 < \alpha_a, \alpha_u, \alpha_d, \zeta \le 1,$$

$$(P2): \max_{\alpha_a,\alpha_u,\alpha_d,\zeta} \mathcal{R}_{sys}, \quad \text{subject to } C3,$$

$$C6: \mathcal{R}_d > \mathcal{R}_{th_d}, \qquad C7: \mathcal{R}_u > \mathcal{R}_{th_u},$$

where $\mathcal{R}_{sys} = \mathcal{R}_d + \mathcal{R}_u$ and $\alpha_d \triangleq N_d/N$. $\mathcal{O}_{th_d}$ and $\mathcal{O}_{th_u}$ denote the threshold OPs for users D and U, respectively. Constraints $C1$ and $C2$ ensure QoS by limiting the maximum acceptable OP for each user. Similarly, constraints $C6$ and $C7$ impose ER constraints for QoS. $\mathcal{R}_{th_d}$ and $\mathcal{R}_{th_u}$ signify the minimum essential rates required for users D and U, respectively. Now, due to the intricate combination of complex non-linear functions within the mathematical expressions for SOP, OP, ER, and ESR, and the strong interdependence among the four optimization variables, obtaining a

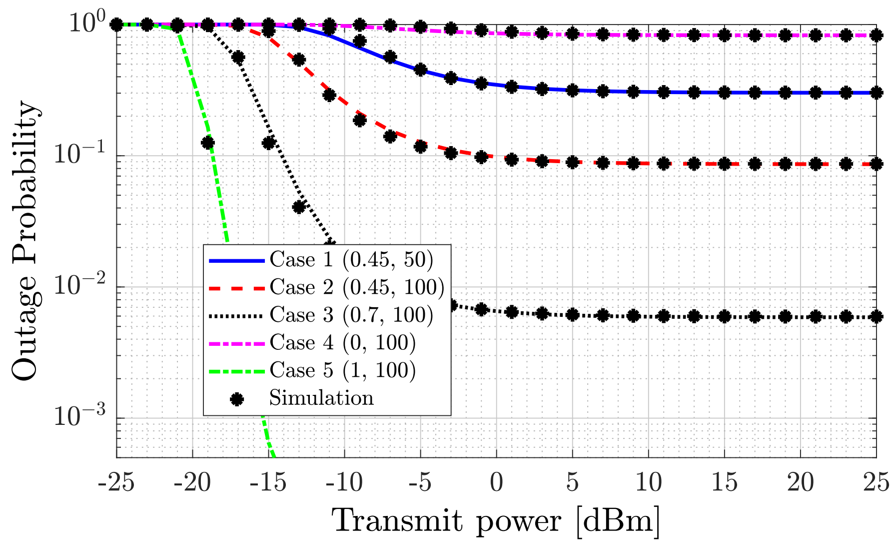

Figure 5.2: $\mathcal{O}_d$ performance w.r.t. P_{max}.

closed-form solution for the problems is mathematically challenging. Therefore, to address this and determine the solution, we employ an effective and derivative-free algorithm such as PSO. The PSO is a population-based algorithm inspired by the social behavior of bird flocking, where a group consisting of $\varkappa_1$ particles simulates movement to find a common objective and locate the best position representing the solution to the optimization problem. Each particle adjusts its position based on its own best-known solution and the global best-known solution found by any particle in the swarm, aiming to converge towards minimum SOP and maximum ESR in problems $P1$ and $P2$, respectively.

5.4 Results and Discussions

In this section, the key numerical insights into the RIS-FD-DDU system are presented. Unless explicitly stated, $N = 50$, $K = 2$, $L = 2$, $V = 100$, $\varkappa_1 = 50$, $\alpha_d = 0.7$, $\alpha_a = \alpha_u = 1$, $P_{max} = 10$ dBm, $\zeta = 1$, $R_{th_d} = R_{th_u} = 3$ bits/sec/Hz, $R_{th_t} = 1$ bits/sec/Hz, $\omega = 10^{-5}$, and $\phi_{ad} = \phi_{ud} = \phi_{ua} \triangleq \phi = 0.2$. Further, $m_{pq} = 2.5$ (where $p, q \in \{a, i_1, i_2, d, u\}$ and $p \neq q$), $\overline{g}_{pq} = r_{pq}{}^{-v}$ [145], $v = 3$, $r_{z_1} = 20$ m, $r_{z_2} = 10$ m, where $z_1 \in \{ad_k, ud_k, u_l a\}$, $z_2 \in \{ai_t, i_t d, ui_t, i_t a\}$, and $t \in \{1, 2\}$. σ_a^2 and σ_d^2 are set to -50 dBm to model a more noisy environment [144].

In Fig. 5.2 and Fig. 5.3, the OP performance is plot with respect to the maximum transmit power P_{max} for users D and U, respectively, considering ten different cases

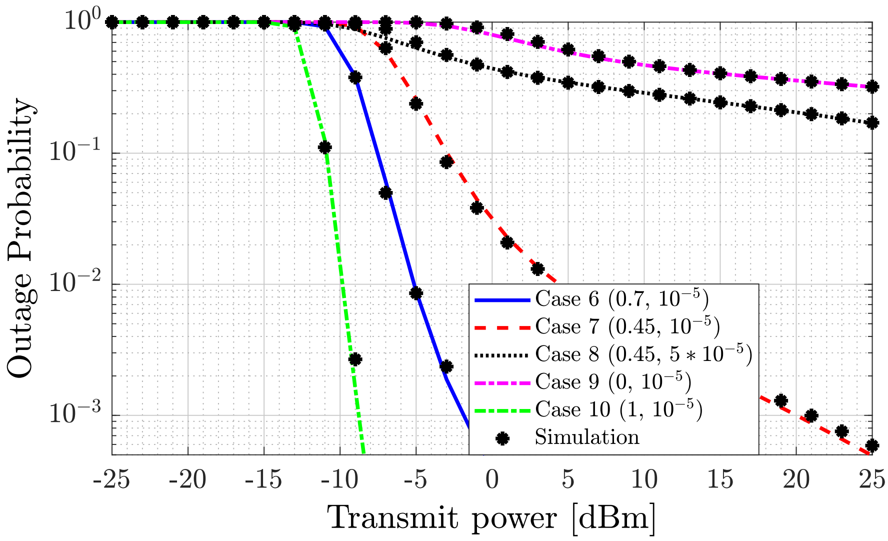

Figure 5.3: $\mathcal{O}_u$ performance w.r.t. P_{max}.

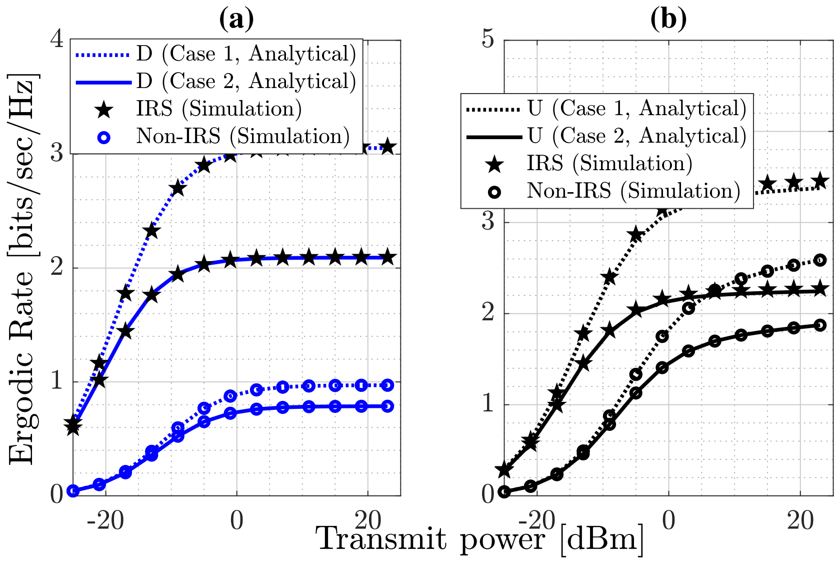

Figure 5.4: ER performance w.r.t. P_{max}.

Table 5.2: Comparison of cases for Fig. 5.2 and Fig. 5.3.

Cases	α_d	N	β_u	ω
1	0.45	50	-	-
2	0.45	100	-	-
3	0.7	100	-	-
4	0	100	-	-
5	1	100	-	-
6	-	-	0.7	10^{-5}
7	-	-	0.45	10^{-5}
8	-	-	0.45	$5*10^{-5}$
9	-	-	0	10^{-5}
10	-	-	1	10^{-5}

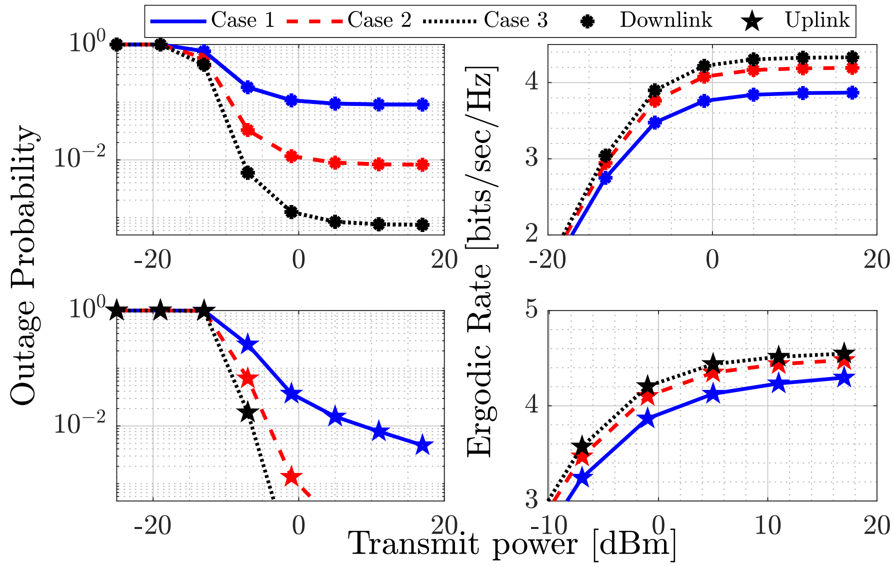

Figure 5.5: OP vs P_{max} for different number of downlink and uplink users.

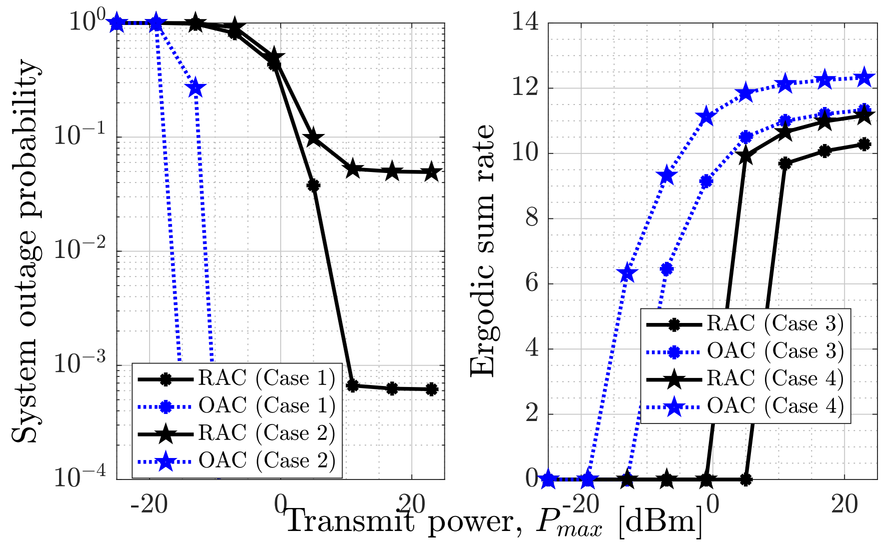

Figure 5.6: SOP and ESR optimized performance w.r.t. P_{max}.

for analysis. Cases $1-5$ and $6-10$ correspond to the values of $\{\alpha_d, N\}$ and $\{\beta_u, \omega\}$, respectively, where $\beta_u = 1 - \alpha_d$. The figures demonstrate that the curves obtained from the analytical expressions closely agree with the simulation results. The figures demonstrate that as α_d increases, the OP performance of user D improves, which is reasonable as it leads to a higher number of Zone-D elements for coherently combined links and fewer randomly combined links. Similarly, an increase in β_u increases N_u, resulting in more coherently combined links at user U and fewer randomly combined links, thereby leading to a lower value of $\mathcal{O}_u$. Additionally, the OP performance for U can be seen to be worst and best for cases 9 and 10, respectively. This is because $\beta_u = 0$ makes all the N RIS elements to randomly reflect the uplink transmission by U, whereas on the other hand, $\beta_u = 1$ ensures coherent combining of the transmitted signal by all the N RIS elements. A similar observation can also be made for user D in cases 4 and 5. Moreover, as the number of RIS elements increases, the performance of D improves, and a decrease in the value of ω reduces the RSI at the AP, thereby enhancing the outage performance of the uplink user. Also, due to the CCI effect, the OP saturates at higher values of P_{max}.

In Figure 5.4, the ER performance of the users is shown, along with a comparison with the non-RIS scenario. Cases 1 and 2 correspond to ϕ values of 0.3 and 0.5. A decrease in ϕ value from 0.5 to 0.3 reduces the impact of HI and, as a result, increases the ER of both D and U. Moreover, the users are observed to experience significantly higher rates compared to a non-RIS scenario, which justifies the integration of RIS in FD systems having different uplink and downlink users. Specifically, the ER for user D at $P_{\max} = 5$ dB is observed to be 3 and 4.7 times that of the non-RIS scenario for cases 1 and 2, respectively. Similarly, for the same $P_{\max}$ value, the ER experienced by user U is observed to be 2.1 and 1.5 times that of the non-RIS scenario for cases 1 and 2, respectively. Additionally, the derived analytical results obtained from $\mathcal{R}_d$ and $\mathcal{R}_u$ expressions closely match the simulation values.

In Fig. 5.5, OP and ER results are depicted for three different cases corresponding to number of downlink and uplink users. Cases 1, 2, and 3 correspond to K and L values of 1, 2, and 3, respectively. It can be observed that the outage performance is seen to improve with increase in the values of K and L as more number of users are available for selection. A similar enhancement can be observed in the ER of the

Table 5.3: Accuracy of ER validated by different values of V.

V	$\mathcal{R}_d$		$\mathcal{R}_u$	
	Simulation	**Analytical**	**Simulation**	**Analytical**
10	5.214	5.581	5.658	6.033
25	5.214	5.265	5.658	5.718
50	5.214	5.225	5.658	5.678
100	5.214	5.216	5.658	5.669

selected users with increase in number of downlink and uplink users. Furthermore, in Table 5.3, we validate accuracy of ER expressions against simulation values for different values of V. It is evident that the difference between the analytical ER and the simulated ER decreases as V increases. Therefore, while it is true that, in an ideal scenario, increasing V to infinity could reduce the approximation error to zero, it can be inferred that selecting a value of V close to 100 is sufficient for accurate results, considering the trade-off between accuracy and complexity.

In Fig. 5.6, SOP and ESR curves are depicted for our proposed optimized allocation of coefficients (OAC) solution, and compare it with random allocation of coefficients (RAC) where the values of α_a, α_u, α_d, and ζ are either randomly selected or fixed to a certain value. We consider four distinct cases (with $\mathcal{O}_{th_d} = \mathcal{O}_{th_u} = 0.1$), which represent different combinations of $\{\mathcal{R}_d, \mathcal{R}_u, N\}$. Specifically, Case 1, 2, 3, and 4 correspond to $\{1.5, 0.5, 50\}$, $\{2.5, 0.5, 50\}$, $\{0.5, 3.5, 50\}$, and $\{0.5, 3.5, 100\}$, respectively. It can be observed that the proposed OAC solutions outperform the comparative RAC scheme, as the values of α_a, α_u, α_d, and ζ in RAC are not updated according to the changing system parameter values. At a P_{max} value of -5 dBm, $\mathcal{R}_d = 1.5$, $\mathcal{R}_u = 0.5$, and $N = 50$, the SOP is minimized with the parameter values set at $\alpha_a = 0.89$, $\alpha_u = 0.29$, $\alpha_d = 0.61$, and $\zeta = 0.99$. Similarly, at a P_{max} value of 13 dBm, $\mathcal{R}_d = 0.5$, $\mathcal{R}_u = 3.5$, and $N = 50$, the ESR is maximized with the optimized parameter values of $\alpha_a = 0.90$, $\alpha_u = 0.72$, $\alpha_d = 0.53$, and $\zeta = 0.99$. Furthermore, the performance improves with a decrease in the values of $\mathcal{R}_d$ and $\mathcal{R}_u$, and with an increase in the number of RIS elements.

5.5 Summary

In conclusion, this chapter focused on performance analysis and optimization of RIS-FD-DDU system considering multiple uplink and downlink users and the effects of RSI, CCI, and HI. The analytical expressions derived for both OP and ER closely align with the simulation results. Further, the proposed OAC solution to the optimization problems outperform the comparative RAC scheme which indicate the requirement of optimizing the values of α_a, α_u, α_d, and ζ. The influence of key parameters, such as the number of RIS elements, RSI levels, and HI, were examined on performance of the users. The simulation results show significantly improved user rates due to the integration of the RIS compared to the non-RIS scenario. Additionally, the performance of users is seen to improve with an increasing number of RIS elements. Further, though RIS-FD-DDU system serves models both FD cooperative systems and underlay communication, RIS can provide coverage only to users that are located on the same side of the RIS incident plane and cannot serve users behind the incident plane. Therefore, in the next chapter, a STAR-RIS assisted system model is investigated.

Chapter 6

VFD Communication Enabled STAR-RIS Network

RIS stands as one of the transformative and key enabling technologies for the realization of the futuristic 6G communication networks [72, 151]. However, as the conventional RIS configuration focuses only on passive reflection, it can provide coverage only to users that are located on the same side of the RIS incident plane and cannot serve users behind the incident plane. Therefore, a novel concept of STAR-RIS having transmitting capabilities along with reflecting functionalities, has attracted significant research interest [5].

In the recent years, there has been a growing research interest in integrating FD with both RIS and STAR-RIS [6, 7, 144, 145, 152–156]. In [144, 145], the authors investigated two-way FD-based RIS communication and derived analytical expressions for the OP, ER, and average symbol error rate. The authors in [152] explored a FD enabled RIS setup, where an AP communicates concurrently with a downlink user and an uplink user, and thus perform transmit power minimization while ensuring that the rate requirements of the users are met. Work in [153] considered a cognitive radio setup with FD communication and RIS assistance, consisting of a secondary AP and multiple users. The optimization problem of maximizing the secondary network sum rate was studied, all the while ensuring minimal interference to the primary users.

Authors in [6, 7, 154–156] investigated FD-based STAR-RIS (FD-STAR-RIS) communication system. In [154], the authors investigated the OP and ER performance of a FD enabled two-way device-to-device communication system utilizing the STAR-RIS technology. Works in [6] and [7] studied sum rate maximization problem of a FD-STAR-RIS system where an FD AP establishes communication with a downlink user and an uplink user located at opposite ends of the STAR-RIS. Authors in [155, 156] studied the performance analysis of the FD-STAR-RIS set-up considered in [6, 7]. Work in [156] also investigated the problem of maximizing the ER performance of the uplink and the downlink users.

In recent years, various virtual FD (VFD) schemes have emerged to replicate FD functionality by replacing a single FD device with two HD devices [1, 98, 100, 102–104, 157–160]. The underlying principle in VFD is to exploit significant physical separation between devices to emulate FD, thereby minimizing interference between HD devices, which is significantly lower than SI. In cooperative communication scenarios, VFD schemes have been proposed where a FD relay node is replaced by two distinct HD relay nodes to forward messages from source to destination [1, 98, 100, 102–104]. Symbol transmission from the source node to the destination node occurs in a successive relaying manner, with one relay receiving the signal from the source and the other relay transmitting to the destination in an alternating fashion. In [157, 158], VFD systems are proposed to virtually realize FD operations in cell-free massive MIMO systems by substituting FD APs with HD APs. Additionally, in [159], a VFD scheme is proposed by replacing the conventional FD-enabled base station with two geographically distributed HD remote radio units, with one dedicated to uplink transmission and the other to downlink transmission.

Similarly, for high RSI scenarios, the design and analysis of alternative VFD schemes to replace the FD-STAR-RIS systems needs to investigated, which is missing in the current literature. Hence, to bridge this gap, this chapter proposes a novel VFD-based STAR-RIS (VFD-STAR-RIS) scheme to mimic and outperform the FD-STAR-RIS operation in [6, 7] by replacing the FD AP by two HD APs or remote radio units as in [157–159] wherein one AP serves the downlink user and the other AP serves the uplink user. Notably, as no SI cancellation process is involved, the performance gains in the VFD-STAR-RIS are obtained with minimal computation complexity, with the spectrum utilization same as in the FD-STAR-RIS. For the proposed system, OP and ER analysis is done for performance evaluation. To further enhance the system performance by managing the STAR-RIS aided inter-user-interference (IUI), this work also investigates problems of SOP minimization and ESR maximization constrained to user OP and ER requirements, respectively, to jointly optimize power allocations, reflection amplitude, transmission amplitude and STAR-RIS element partitioning (JPRTE).

Given that the formulated JPRTE optimization problems involve OP and ER as objectives and constraints, the solution relies solely on statistical CSI of communication links. Instantaneous CSI is only required for desired links to configure optimal phase adjustments of STAR-RIS elements. This approach is particularly useful in scenarios where acquiring instantaneous CSI of IUI links is challenging due to limited coordination between users, and given that associated channel training and feedback overhead scales proportionally with size of RIS [161, 162].

The proposed work can guide the design of practical systems for extension of coverage in which the wireless communication links are severely blocked by obstacles, including vehicular scenarios where the STAR-RIS is mounted on the windows of cars, aircraft and others [5]. Further, our investigations are also applicable for cognitive radio scenarios with either of the uplink or downlink users being considered as primary and the other as secondary [163]. Also, it will be useful for various low-latency applications such as mission critical services, advanced driver assistance, remote patient monitoring and others [164]. Major contributions of this work are summarized as follows:

- A VFD-STAR-RIS alternative system model is proposed to mimic the FD-STAR-RIS operations in practical high RSI scenarios. Multiple uplink and downlink users are considered with the best user selections.

- Analytical expressions of OP are presented for downlink and uplink users using the MMT considering generalized Nakagami-m distribution. Further, employing GCQ approach, the analytical expressions for ER are also derived.

- Two different JPRTE optimization problems are formulated to minimize the effects of STAR-RIS aided IUI considering SOP minimization (i.e. JPRTE-SOP) and ESR maximization (i.e. JPRTE-ESR) as the objectives. The same are subjected to a threshold OP and a target rate for each user. Due to complexity of the mathematical expressions for SOP and OP, and the strong interdependence among optimization variables, obtaining a closed-form solution for the minimization of SOP is mathematically challenging. Therefore, an effective and derivative-free algorithm like PSO is used to solve the JPRTE-SOP problem.

- However, due to the complexity involved in the ER expressions, applying PSO directly to solve the JPRTE-ESR will require a significant amount of convergence time and would increase the latency. Thus, to address the issue for ultra-low latency based machine critical applications, a practically realizable ML based PSO (ML-PSO) solution is proposed wherein the ER expressions in the objective and constraints are first approximated utilizing a ML model. Thereafter, the PSO algorithm is applied to obtain solution with a significantly low computational time.

- Performance of the proposed VFD-STAR-RIS system and solutions to the optimization problems are extensively analyzed for various system parameter values to obtain various useful design insights and compared with benchmark schemes.

6.1 System Model

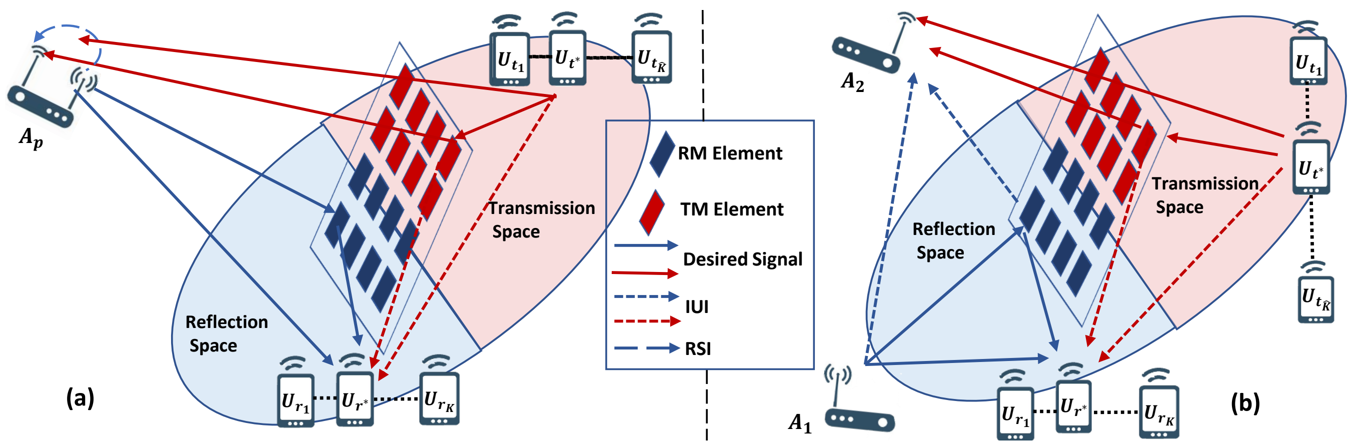

Figure 6.1: System models: (a) FD-STAR-RIS in [6, 7]. (b) Proposed VFD-STAR-RIS.

A wireless network is considered with N-element sized STAR-RIS implemented by a uniform planar array with $N = N_v \times N_h$, where N_v and N_h are the number of elements in the vertical and horizontal directions, respectively. K downlink users and $\hat{K}$ uplink users are considered on the reflection side and the transmission side of the STAR-RIS, respectively. User selection strategy is adopted based on the maximum channel gain between the AP and the users such that U_{r^*} and U_{t^*} denote the best downlink and uplink users, respectively, selected by the AP. The STAR-RIS is divided into N_t number of TM elements and N_r number of RM elements with $N_t + N_r = N$. It is to note that as from implementation complexity point of view, MS protocol is practically more convenient to apply in comparison to both ES and TS protocols due to its simple on-off kind of switching [5, 165], and as the primary objective of this work is to study a VFD alternative solution to the FD-STAR-RIS in high RSI scenario and thereby investigate the performance, inline with the performance analysis works in [165–168], this work only considers the MS protocol. As the OP and ER analysis with ES or TS protocol will be entirely different from the current work, they are defered as a subject of future studies. As shown in Fig. 1, in the FD-STAR-RIS system, U_{r^*} and U_{t^*} are served by a single FD AP (A_p) [6, 7, 156]. On the other hand, in the proposed VFD-STAR-RIS system, A_p is replaced by two HD AP's (A_1 and A_2) or remote radio units as in [157–159] for uplink and downlink transmission, respectively. It is to note that for mathematical tractability, the FD-STAR-RIS works in [6, 7] consider the FD AP (A_p) to possess only two antennas, one for signal transmission and the other for reception. On similar lines, to analyze the VFD-STAR-RIS system, a single transmission antenna is considered at A_1 and a single antenna at A_2 for reception. The analysis can be later be extended to scenario with multi-antenna based APs with transmit and receive antenna selection schemes. Notably, A_2 receives IUI from A_1 reflected by the RM elements while A_p is affected with RSI due to concurrent transmission and reception. Similarly, U_{r^*} is affected with IUI from U_{t^*} via the TM elements in both the FD and VFD systems.

For each link pq, where p and q belong to the set $\{a, a_1, a_2, t^*, r^*, i, k\}$ and $p \neq q$, the phase and envelope of channel co-efficient h_{pq} are characterized by distributions $\phi_{pq} \sim Uni[0, 2\pi]$ and $|h_{pq}| \sim Nak(m_{pq}, \overline{g}_{pq})$, respectively, where A_p, A_1, A_2, U_{t^*} and U_{r^*} are also denoted by a, a_1, a_2, t^*, r^*, respectively. Additionally, i represents the i^{th} RM element and k signifies the k^{th} TM element.

6.1.1 SINR expressions in VFD-STAR-RIS

The received signal y_{r^*} at U_{r^*} (from A_1) and y_{a_2} at A_2 (from U_{t^*}) are given as

$$
\begin{aligned}
y_{r^*} = \sqrt{P_{a_1}} x_{r^*} (h_{a_1 r^*} + \sum_{i=1}^{N_r} h_{a_1 i} v_i h_{i r^*}) + n_{r^*} \\
\underbrace{+ \sqrt{P_{t^*}} x_t (h_{t^* r^*} + \sum_{k=1}^{N_t} h_{t^* k} v_k h_{k r^*})}_{I_{r^*}},
\end{aligned} \tag{6.1}
$$

$$
\begin{aligned}
y_{a_2} = \sqrt{P_{t^*}} x_{t^*} (h_{t^* a_2} + \sum_{k=1}^{N_t} h_{t^* k} v_k h_{k a_2}) + n_{a_2} \\
\underbrace{+ \sqrt{P_{a_1}} x_{r^*} (h_{a_1 a_2} + \sum_{i=1}^{N_r} h_{a_1 i} v_i h_{i a_2})}_{I_{a_2}},
\end{aligned} \tag{6.2}
$$

where x_{t^*} and x_{r^*} represent symbols of U_{t^*} and U_{r^*}, respectively. Further, $P_{t^*} = \alpha_t \, P_{max}$ and $P_{a_1} = \alpha_{a_1} \, P_{max}$ are transmission powers of U_{t^*} and A_1, respectively. Also, α_{a_1} and α_t, bounded in the range $(0, 1]$, are coefficients of power allocation, and P_{max} indicates the power allocation limit. The parameters $v_k = \zeta_t \, e^{j\theta_k}$ and $v_i = \zeta_r \, e^{j\theta_i}$ denote the k^{th} TM element's transmission coefficient and i^{th} RM element's reflection coefficient, respectively, where θ_i and θ_k represent the induced phase shifts and follow the uniform distribution $Uni[0, 2\pi]$, and ζ_r and ζ_t, defined in the interval $[0, 1]$, represent the amplitude. Further, I_{r^*} and I_{a_2} are IUIs via the STAR-RIS, and for $q \in \{a_2, t^*\}$, $n_q \sim \mathcal{CN}(0, \sigma_q^2)$ represents the noise at node q. The SINR $\psi_{r^*}^{r^*}$ (corresponding to U_{r^*}) and $\psi_{a_2}^{t^*}$ (corresponding to U_{t^*}) in the VFD-STAR-RIS system are expressed as [169, 170]

$$
\psi_{r^*}^{r^*} = \frac{P_{a_1} \, |h_{a_1 r^*} + \sum_{i=1}^{N_r} h_{a_1 i} \, \zeta_r \, e^{j\theta_i} \, h_{i r^*}|^2}{P_{t^*} \, |h_{t^* r^*} + \sum_{k=1}^{N_t} h_{t^* k} \, \zeta_t \, e^{j\theta_k} \, h_{k r^*}|^2 + \sigma_{r^*}^2}, \tag{6.3}
$$

$$
\psi_{a_2}^{t^*} = \frac{P_{t^*} \, |h_{t^* a_2} + \sum_{k=1}^{N_t} \, h_{t^* k} \, \zeta_t \, e^{j\theta_k} \, h_{k a_2}|^2}{P_{a_1} |h_{a_1 a_2} + \sum_{i=1}^{N_r} h_{a_1 i} \zeta_r \, e^{\theta_i} \, h_{i a_2}|^2 + \sigma_{a_2}^2}. \tag{6.4}
$$

From (6.3) and (6.4), it is evident that the optimal phase shifts θ_i^* and θ_k^* should be such that there is coherent combining at the destinations and the IUIs combine randomly to reduce the interference effect. Accordingly, the SINR's are re-expressed as [165, 171, 172]

$$\psi_{r^*}^{r^*} = \frac{P_{a_1}\left(|h_{a_1r^*}| + \sum_{i=1}^{N_r} |h_{a_1i}|\zeta_r|h_{ir^*}|\right)^2}{P_{t^*}\,|h_{t^*r^*} + \sum_{k=1}^{N_t} h_{t^*k}\,\zeta_t\, e^{j\theta_k^*}\, h_{kr^*}|^2 + \sigma_{r^*}^2}, \tag{6.5}$$

$$\psi_{a_2}^{t^*} = \frac{P_{t^*}\left(|h_{t^*a_2}| + \sum_{k=1}^{N_t} |h_{t^*k}|\zeta_t|h_{ka_2}|\right)^2}{P_{a_1}|h_{a_1a_2} + \sum_{i=1}^{N_r} h_{a_1i}\zeta_r\, e^{j\theta_i^*}\, h_{ia_2}|^2 + \sigma_{a_2}^2}. \tag{6.6}$$

6.1.2 SINR expressions in FD-STAR-RIS

For the FD-STAR-RIS system, the SINR ($\hat{\psi}_{r^*}^{r^*}$) of U_{r^*} and SINR ($\hat{\psi}_{a}^{t^*}$) corresponding to U_{t^*} can be expressed as

$$\hat{\psi}_{r^*}^{r^*} = \frac{P_a\,|h_{ar^*} + \sum_{i=1}^{N_r} h_{ai}\,\zeta_r\, e^{j\hat{\theta}_i}\, h_{ir^*}|^2}{P_{t^*}\,|h_{t^*r^*} + \sum_{k=1}^{N_t} h_{t^*k}\,\zeta_t\, e^{j\hat{\theta}_k}\, h_{kr^*}|^2 + \sigma_{r^*}^2}, \tag{6.7}$$

$$\hat{\psi}_{a}^{t^*} = \frac{P_{t^*}\,|h_{t^*a} + \sum_{k=1}^{N_t} h_{t^*k}\,\zeta_t\, e^{j\hat{\theta}_k}\, h_{ka}|^2}{|h_{RSI}|^2 + \sigma_a^2}, \tag{6.8}$$

where $P_a = \alpha_a\, P_{max}$ is transmit power of A_p, $\alpha_a \in (0, 1]$. Further, h_{RSI} corresponds to the RSI having Rayleigh distribution with variance $\omega {P_{t^*}}^v$ [173], $\omega > 0$ and $v \in [0, 1]$. Further, setting $\hat{\theta}_i^*$ and $\hat{\theta}_k^*$ coherent combining at the destinations, the SINRs are re-expressed as

$$\hat{\psi}_{r^*}^{r^*} = \frac{P_a\left(|h_{ar^*}| + \sum_{i=1}^{N_r} |h_{ai}|\zeta_r|h_{ir^*}|\right)^2}{P_{t^*}\,|h_{t^*r^*} + \sum_{k=1}^{N_t} h_{t^*k}\,\zeta_t\, e^{j\hat{\theta}_k^*}\, h_{kr^*}|^2 + \sigma_{r^*}^2}, \tag{6.9}$$

$$\hat{\psi}_{a}^{t^*} = \frac{P_{t^*}\left(|h_{t^*a}| + \sum_{k=1}^{N_t} |h_{t^*k}|\zeta_t|h_{ka}|\right)^2}{|h_{RSI}|^2 + \sigma_a^2}. \tag{6.10}$$

6.2 Performance Analysis

In this section, OP and ER of the VFD-STAR-RIS system is analyzed. OP is a very suitable measure to assess the reliability and performance of wireless systems with slowly varying fading channels. On the other hand, ER is a very crucial metric for performance evaluation that indicates the averaged achievable rate. Accordingly, in the subsequent lemmas, we derive the analytical expressions of OP, SOP and ER for U_{r^*} and U_{t^*}.

6.2.1 Performance Analysis

6.2.2 Outage Probability of U_{r^*}

The OP is defined as the probability of the SINR falling below a certain pre-defined threshold [104]. Further, with $r^* = \arg \max\limits_{q \in \{1,2,..,K\}} \{\left(|h_{a_1 r_q}| + \sum_{i=1}^{N_r} |h_{a_1 i}|\zeta_r|h_{ir_q}|\right)^2\}$, as in (6.5), $A_1 \to$ STAR-RIS $\to U_{r^*}$ and $U_{t^*} \to$ STAR-RIS $\to U_{r^*}$ transmissions are coherently and randomly combined, respectively, the corresponding SINR ($\psi_{r^*}^{r^*}$) of U_{r^*} is also maximum among the K downlink users. Accordingly, the OP of U_{r^*} is given as

$$
\begin{aligned}
\mathcal{O}_{r^*} &= \Pr\left(\log_2\left(1+\psi_{r^*}^{r^*}\right) < R_{th_r}\right) = \Pr(\psi_{r^*}^{r^*} < \delta_r) \\
&= \Pr(\max\left(\psi_{r_1}^{r_1}, ...\psi_{r_K}^{r_K}\right) < \delta_r) \\
&= \prod_{q=\{1,...K\}} \Pr(\psi_{r_q}^{r_q} < \delta_r) \\
&= \prod_{q=\{1,...K\}} F_{\psi_{r_q}^{r_q}}(\delta_r),
\end{aligned} \tag{6.11}
$$

where R_{th_r} is the target rate, $\delta_r = 2^{R_{th_r}} - 1$, and $\psi_{r_q}^{r_q} = \frac{P_{a_1}\left(|h_{a_1 r_q}| + \sum_{i=1}^{N_r} |h_{a_1 i}|\zeta_r|h_{ir_q}|\right)^2}{P_{t^*}\,|h_{t^* r_q} + \sum_{k=1}^{N_t} h_{t^* k}\,\zeta_t\, e^{j\theta_k^*}\, h_{kr_q}|^2 + \sigma_r^2}$. The term $\Lambda_1 \triangleq \sqrt{P_{a_1}} \sum_{i=1}^{N_r} |h_{a_1 i}|\zeta_r|h_{ir_q}|$ can be approximated via MMT as a Gamma random variable (GRV) characterized with parameters namely shape s_{Λ_1} and scale θ_{Λ_1} (i.e. $\Lambda_1 \sim \Xi(s_{\Lambda_1}, \theta_{\Lambda_1})$) given as

$$
s_{\Lambda_1} = \frac{(\mathbb{E}[\Lambda_1])^2}{\mathbb{E}[\Lambda_1^2]) - (\mathbb{E}[\Lambda_1])^2}, \tag{6.12}
$$

$$
\theta_{\Lambda_1} = \frac{\mathbb{E}[\Lambda_1]}{s_{\Lambda_1}}, \tag{6.13}
$$

where $\mathbb{E}[\Lambda_1] = \sqrt{P_{a_1}}\zeta_r N_r \delta_1$ and $\mathbb{E}[\Lambda_1^2] = \sqrt{P_{a_1}}\zeta_r N_r(1 + \delta_1^2(N_r - 1))$ are the first and second order moments of Λ_1, respectively. Also, $\delta_1 \triangleq \delta_{a_1\hat{i}}\delta_{\hat{i}r_q}$, $\delta_{a_1\hat{i}} \triangleq \mathbb{E}[h_{a_1\hat{i}}] = \frac{\Gamma(m_{a_1\hat{i}}+\frac{1}{2})}{\Gamma(m_{a_1\hat{i}})\sqrt{m_{a_1\hat{i}}/\bar{g}_{a_1\hat{i}}}}$, $\delta_{\hat{i}r_q} \triangleq \mathbb{E}[h_{\hat{i}r_q}] = \frac{\Gamma(m_{\hat{i}r_q}+\frac{1}{2})}{\Gamma(m_{\hat{i}r_q})\sqrt{m_{\hat{i}r_q}/\bar{g}_{\hat{i}r_q}}}$ [150], where $\forall i \in \{1, 2, \cdots, N_r\}$, $h_{a_1\hat{i}} \triangleq h_{a_1 i}$, $h_{\hat{i}r_q} \triangleq h_{ir_q}$, $m_{a_1\hat{i}} \triangleq m_{a_1 i}$, $m_{\hat{i}r_q} \triangleq m_{ir_q}$, $\bar{g}_{a_1\hat{i}} \triangleq \bar{g}_{a_1 i}$ and $\bar{g}_{\hat{i}r_q} \triangleq \bar{g}_{ir_q}$.

Further, with $\Lambda_{2,q} = (\tilde{\Lambda}_1 + \Lambda_1)^2$, where $\tilde{\Lambda}_1 \triangleq \sqrt{P_{a_1}}|h_{a_1 r_q}|$, the terms $\mathbb{E}[\Lambda_{2,q}]$ and $\mathbb{E}[\Lambda_{2,q}^2]$ can be given as

$$\begin{aligned}\mathbb{E}[\Lambda_{2,q}] &= \mathbb{E}[(\tilde{\Lambda}_1 + \Lambda_1)^2] \\ &= \mathbb{E}[\tilde{\Lambda}_1^2] + \mathbb{E}[\Lambda_1^2] + 2\,\mathbb{E}[\tilde{\Lambda}_1]\,\mathbb{E}[\Lambda_1],\end{aligned} \tag{6.14}$$

$$\begin{aligned}\mathbb{E}[\Lambda_{2,q}^2] &= \mathbb{E}[(\tilde{\Lambda}_1 + \Lambda_1)^4] \\ &= \mathbb{E}[\tilde{\Lambda}_1^4] + \mathbb{E}[\Lambda_1^4] + 4(\mathbb{E}[\tilde{\Lambda}_1^3]\,\mathbb{E}[\Lambda_1] + \mathbb{E}[\tilde{\Lambda}_1]\,\mathbb{E}[\Lambda_1^3]) \\ &+ 6\,\mathbb{E}[\tilde{\Lambda}_1^2]\,\mathbb{E}[\Lambda_1^2],\end{aligned} \tag{6.15}$$

where $\mathbb{E}[\Lambda_1^3]$, $\mathbb{E}[\Lambda_1^4]$, and the n^{th} order moment of $\tilde{\Lambda}_1$ are given as [150],

$$\begin{aligned}\mathbb{E}[\Lambda_1^3] &= \frac{\Gamma(s_{\Lambda_1} + 3)}{\Gamma(s_{\Lambda_1})(1/\theta_{\Lambda_1})^3} \\ &= \prod_{\hat{n}=\{1,2\}} (s_{\Lambda_1} + \hat{n})(\theta_{\Lambda_1})^3,\end{aligned} \tag{6.16}$$

$$\begin{aligned}\mathbb{E}[\Lambda_1^4] &= \frac{\Gamma(s_{\Lambda_1} + 4)}{\Gamma(s_{\Lambda_1})(1/\theta_{\Lambda_1})^4} \\ &= \prod_{\hat{n}=\{1,2\,3\}} (s_{\Lambda_1} + \hat{n})(\theta_{\Lambda_1})^4,\end{aligned} \tag{6.17}$$

$$\mathbb{E}[\tilde{\Lambda}_1^n] = \frac{\Gamma(m_{a_1 r_q} + \frac{n}{2})}{\Gamma(m_{a_1 r_q})(m_{a_1 r_q}/P_{a_1}\bar{g}_{a_1 r_q})^{\frac{n}{2}}} \tag{6.18}$$

Now substituting the above expressions in, $\Lambda_{2,q}$ can be similarly approximated as a GRV, i.e. $\Lambda_{2,q} \sim \Xi(s_{\Lambda_{2,q}}, \theta_{\Lambda_{2,q}})$ using MMT as

$$s_{\Lambda_{2,q}} = \frac{(\mathbb{E}[\Lambda_{2,q}])^2}{\mathbb{E}[\Lambda_{2,q}^2]) - (\mathbb{E}[\Lambda_{2,q}])^2}, \tag{6.19}$$

$$\theta_{\Lambda_{2,q}} = \frac{\mathbb{E}[\Lambda_{2,q}]}{s_{\Lambda_{2,q}}}, \tag{6.20}$$

Next, in (6.5), as the IUIs at U_{r^*} combine randomly, the term Λ_3 can be expressed and modelled as [174],

$$\Lambda_3 \triangleq \sqrt{P_{t^*}} \sum_{k=1}^{N_t} h_{t^*k} \zeta_t e^{j\theta_k^*} h_{kr_q}, \tag{6.21}$$

$$\Lambda_3 \sim \mathcal{CN}(0, \bar{\Lambda}_3), \tag{6.22}$$

where $\bar{\Lambda}_3 = P_{t^*} N_t {\zeta_t}^2 \bar{g}_{t^*\hat{k}} \bar{g}_{\hat{k}r_q}$, $\bar{g}_{t^*\hat{k}} \triangleq \bar{g}_{t^*k}, \bar{g}_{\hat{k}r_q} \triangleq \bar{g}_{kr_q} \forall k \in \{1, 2, \cdots, N_t\}$. Accordingly, $|\Lambda_3|$ follows Rayleigh distribution, which is a specific case of the Nakagami-m fading model with unity severity $|\Lambda_3| \sim Nak(1, \bar{\Lambda}_3)$. Further, for the term $\Lambda_4 = (\tilde{\Lambda}_3 + \Lambda_3)^2$, where $\tilde{\Lambda}_3 \triangleq \sqrt{P_{t^*}} h_{t^*r_q}$, $\mathbb{E}[\Lambda_4]$ and $\mathbb{E}[\Lambda_4^2]$ can be given as [175],

$$\mathbb{E}[\Lambda_4] = \mathbb{E}[|\tilde{\Lambda}_3|^2] + \mathbb{E}[|\Lambda_3|^2], \tag{6.23}$$

$$\mathbb{E}[\Lambda_4^2] = \mathbb{E}[|\tilde{\Lambda}_3|^4] + \mathbb{E}[|\Lambda_3|^4] + 4\,\mathbb{E}[|\tilde{\Lambda}_3|^2]\,\mathbb{E}[|\Lambda_3|^2]), \tag{6.24}$$

where the n^{th} order moments of $\tilde{\Lambda}_3$ and Λ_3 are given as,

$$\mathbb{E}[|\tilde{\Lambda}_3|^n] = \frac{\Gamma(m_{t^*r_q} + \frac{n}{2})}{\Gamma(m_{t^*r_q})(m_{t^*r_q}/P_{t^*}\bar{g}_{t^*r_q})^{\frac{n}{2}}}, \tag{6.25}$$

$$\mathbb{E}[|\Lambda_3|^n] = \Gamma(1 + \frac{n}{2})\,(\bar{\Lambda}_3)^{\frac{n}{2}}. \tag{6.26}$$

Now, Λ_3 can be similarly approximated as a GRV with parameters s_{Λ_4} and θ_{Λ_4}. Thereafter, the term $\Lambda_{5,q} \triangleq \Lambda_4 + \sigma_r^2$ can be expressed as a new GRV with parameters $s_{\Lambda_{5,q}}$ and $\theta_{\Lambda_{5,q}}$ derived as

$$s_{\Lambda_{5,q}} = \frac{(\mathbb{E}[\Lambda_4] + \sigma_{r_q}^2)^2}{\mathbb{E}[\Lambda_4^2]) - (\mathbb{E}[\Lambda_4])^2}, \tag{6.27}$$

$$\theta_{\Lambda_{5,q}} = \frac{\mathbb{E}[\Lambda_4] + \sigma_r^2}{s_{\Lambda_{5,q}}}. \tag{6.28}$$

Finally, as $\Lambda_{2,q}$ and $\Lambda_{5,q}$ are two distinct GRVs, the ratio of the same (i.e. $\Lambda_{2,q}/\Lambda_{5,q}$) follows a prime distribution. Its CDF is determined by the regularized incomplete beta function, as specified in (6.29).

$$F_{\psi_{r_q}}(x) = I\left(\frac{x\theta_{\Lambda_{5,q}}}{\theta_{\Lambda_{2,q}} + x\theta_{\Lambda_{5,q}}}; s_{\Lambda_{2,q}}, s_{\Lambda_{5,q}}\right). \tag{6.29}$$

Substituting (6.29) in (6.11), the final expression for OP ($\mathcal{O}_{r^*}$) of U_{r^*} is expressed as

$$\mathcal{O}_{r^*} \approx \prod_{q=\{1,\ldots K\}} I\left(\frac{\delta_r\theta_{\Lambda_{5,q}}}{\theta_{\Lambda_{2,q}} + \delta_r\theta_{\Lambda_{5,q}}}; s_{\Lambda_{2,q}}, s_{\Lambda_{5,q}}\right). \tag{6.30}$$

6.2.3 Outage Probability of U_{t^*}

From (6.6), it can be seen that as $U_{t^*} \to$ STAR-RIS $\to A_2$ transmission is coherently combined and the interference $A_1 \to$ STAR-RIS $\to A_2$ is independent of the selected downlink user U_{r^*}, $t^* = \arg \max\limits_{q\in\{1,2,..,\hat{K}\}} \{\left(|h_{t^*a_2}| + \sum_{k=1}^{N_t} |h_{t^*k}||\zeta_t||h_{ka_2}|\right)^2\}$ also maximizes the corresponding SINR ($\psi_{a_2}^{t^*}$) of U_{t^*}. Accordingly, the OP of U_{t^*} is given as where R_{th_t} is target rate, $\delta_t = 2^{R_{th_t}} - 1$, and,

$$\psi_{a_2}^{t_q} = \frac{P_{t^*}\left(|h_{t_q a_2}| + \sum_{k=1}^{N_t} |h_{t_q k}|\zeta_t|h_{k a_2}|\right)^2}{P_{a_1}|h_{a_1 a_2} + \sum_{i=1}^{N_r} h_{a_1 i}\zeta_r\, e^{j\theta_i^*}\, h_{i a_2}|^2 + \sigma_{a_2}^2}. \tag{6.31}$$

As in Lemma-1, we first approximate the coherently combined term $\Lambda_6 \triangleq \sqrt{P_{t^*}}\sum_{k=1}^{N_t} |h_{t_q k}|\zeta_t|h_{k a_2}|$ as $\Lambda_6 \sim \Xi(s_{\Lambda_6}, \theta_{\Lambda_6})$ with $\mathbb{E}[\Lambda_6] = \sqrt{P_{t^*}}\zeta_t N_t \delta_3$ and $\mathbb{E}[\Lambda_6^2] = \sqrt{P_{t^*}}\zeta_t N_t(1 + \delta_3^2(N_t - 1))$, where $\delta_3 = \frac{\Gamma(m_{t_q\hat{k}}+\frac{1}{2})\Gamma(m_{\hat{k}a_2}+\frac{1}{2})}{\Gamma(m_{t_q\hat{k}})\Gamma(m_{\hat{k}a_2})\sqrt{(m_{t_q\hat{k}}/\bar{g}_{t_q\hat{k}})(m_{\hat{k}a_2}/\bar{g}_{\hat{k}a_2})}}$, $m_{t_q\hat{k}} \triangleq m_{t_q k}$ and $m_{\hat{k}a_2} \triangleq m_{k a_2}$, $\bar{g}_{t_q\hat{k}} \triangleq \bar{g}_{t_q k}$, and $\bar{g}_{\hat{k}a_2} \triangleq \bar{g}_{k a_2}, \forall i \in 1, 2, ...N_t)$. Further, $\Lambda_{7,q} = (\tilde{\Lambda}_6 + \Lambda_6)^2$, where $\tilde{\Lambda}_6 \triangleq \sqrt{P_{t_q}}|h_{t_q a_2}|$, is approximated via the MMT to $\Lambda_{7,q} \sim \Xi(s_{\Lambda_{7,q}}, \theta_{\Lambda_{7,q}})$ using $\mathbb{E}[\Lambda_{7,q}]$ and $\mathbb{E}[\Lambda_{7,q}^2]$ expressed as

$$\mathbb{E}[\Lambda_{7,q}] = \mathbb{E}[\tilde{\Lambda}_6^2] + \mathbb{E}[\Lambda_6^2] + 2\,\mathbb{E}[\tilde{\Lambda}_6]\,\mathbb{E}[\Lambda_6], \tag{6.32}$$

$$\begin{aligned}\mathbb{E}[\Lambda_{7,q}^2] = {} & \mathbb{E}[\tilde{\Lambda}_6^4] + \mathbb{E}[\Lambda_6^4] + 4(\mathbb{E}[\tilde{\Lambda}_6^3]\,\mathbb{E}[\Lambda_6] + \mathbb{E}[\tilde{\Lambda}_6]\,\mathbb{E}[\Lambda_6^3]) \\ & + 6\,\mathbb{E}[\tilde{\Lambda}_6^2]\,\mathbb{E}[\Lambda_6^2],\end{aligned} \tag{6.33}$$

where the terms $\mathbb{E}[\Lambda_6^3]$, $\mathbb{E}[\Lambda_6^4]$, and $\mathbb{E}[\tilde{\Lambda}_6^n]$ are given as

$$\mathbb{E}[\Lambda_6^3] = \prod_{\hat{n}=\{1,2\}} (s_{\Lambda_6} + \hat{n})(\theta_{\Lambda_6})^3, \tag{6.34}$$

$$\mathbb{E}[\Lambda_6^4] = \prod_{\hat{n}=\{1,2\,3\}} (s_{\Lambda_6} + \hat{n})(\theta_{\Lambda_6})^4, \tag{6.35}$$

$$\mathbb{E}[\tilde{\Lambda}_6^n] = \frac{\Gamma(m_{t_q a_2} + \frac{n}{2})}{\Gamma(m_{t_q a_2})(m_{t_q a_2}/P_{a_1}\bar{g}_{t_q a_2})^{\frac{n}{2}}}. \tag{6.36}$$

Since $\Lambda_8 \triangleq |\sqrt{P_{a_1}}\sum_{i=1}^{N_r} h_{a_1 i}\zeta_r e^{j\theta_i^*} h_{i a_2}|$ is Rayleigh faded due to random combining, $|\Lambda_8| \sim Nak(1, \bar{\Lambda}_8)$, where $\bar{\Lambda}_8 = P_{a_1}N_r{\zeta_r}^2\bar{g}_{a_1\hat{i}}\bar{g}_{\hat{i}a_2}$, $\bar{g}_{a_1\hat{i}} \triangleq \bar{g}_{a_1 i}, \bar{g}_{\hat{i}a_2} \triangleq \bar{g}_{i a_2}(\forall i \in \{1, 2, \cdots, N_r\})$. Thus, similar to Lemma-1, $\Lambda_9 = (\tilde{\Lambda}_8 + \Lambda_8)^2$ (where $\tilde{\Lambda}_8 \triangleq \sqrt{P_{a_1}}h_{a_1 a_2}$)

can be approximated as a GRV utilizing $\mathbb{E}[\Lambda_9]$ and $\mathbb{E}[\Lambda_9^2]$ expressed as

$$\mathbb{E}[\Lambda_9] = \mathbb{E}[|\tilde{\Lambda}_8|^2] + \mathbb{E}[|\Lambda_8|^2], \tag{6.37}$$

$$\mathbb{E}[\Lambda_9^2] = \mathbb{E}[|\tilde{\Lambda}_8|^4] + \mathbb{E}[|\Lambda_8|^4] + 4\,\mathbb{E}[|\tilde{\Lambda}_8|^2]\,\mathbb{E}[|\Lambda_8|^2]), \tag{6.38}$$

where $\mathbb{E}[|\tilde{\Lambda}_8|^n]$ and $\mathbb{E}[|\Lambda_8|^n]$ are given as

$$\mathbb{E}[|\tilde{\Lambda}_8|^n] = \frac{\Gamma(m_{a_1a_2} + \frac{n}{2})}{\Gamma(m_{a_1a_2})(m_{a_1a_2}/P_{t_q}\bar{g}_{a_1a_2})^{\frac{n}{2}}}, \tag{6.39}$$

$$\mathbb{E}[|\Lambda_8|^n] = \Gamma(1 + \frac{n}{2})\,(\bar{\Lambda}_8)^{\frac{n}{2}}. \tag{6.40}$$

Thus, $\Lambda_{10,q} \triangleq \Lambda_9 + \sigma_{a_2}^2$ can be similarly approximated to a GRV with parameters $s_{\Lambda_{10,q}}$ and $\theta_{\Lambda_{10,q}}$. Now, the CDF of the ratio $\Lambda_{7,q}/\Lambda_{10,q}$ is the regularized incomplete beta function. Hence, substituting the same, the final OP expression can be obtained as

$$\mathcal{O}_{t^*} \approx \prod_{q=\{1,\ldots \hat{K}\}} I\left(\frac{\delta_t\theta_{\Lambda_{10,q}}}{\theta_{\Lambda_{7,q}} + \delta_t\theta_{\Lambda_{10,q}}}; s_{\Lambda_{7,q}}, s_{\Lambda_{10,q}}\right). \tag{6.41}$$

6.2.4 System Outage Probability

The SOP of VFD-STAR-RIS network can be defined as the probability that either of the users in the network fail to decode its signal successfully [119]. In other words, the SOP can be expressed as

$$\mathcal{O}_S = 1 - \mathcal{P}_{success}, \tag{6.42}$$

where $\mathcal{P}_{success}$ is the probability that signals of both U_{r^*} and U_{t^*} are successfully decoded. Accordingly, $\mathcal{P}_{success}$ is determined as

$$\begin{aligned}
\mathcal{P}_{success} &= \Pr\left(\log_2\left(1+\psi_{r^*}^{r^*}\right) > T_r, \log_2\left(1+\psi_{a2}^{t^*}\right) > T_t\right) \\
&= \Pr\left(\log_2\left(1+\psi_{r^*}^{r^*}\right) > T_r\right) \\
&\times \Pr\left(\log_2\left(1+\psi_{a2}^{t^*}\right) > T_t\right) \\
&= \prod_{q=\{1,\ldots K\}} I\left(\frac{\delta_r \theta_{\Lambda_{5,q}}}{\theta_{\Lambda_{2,q}} + \delta_r \theta_{\Lambda_{5,q}}}; s_{\Lambda_{2,q}}, s_{\Lambda_{5,q}}\right) \\
&\times \prod_{q=\{1,\ldots \hat{K}\}} I\left(\frac{\delta_t \theta_{\Lambda_{10,q}}}{\theta_{\Lambda_{7,q}} + \delta_t \theta_{\Lambda_{10,q}}}; s_{\Lambda_{7,q}}, s_{\Lambda_{10,q}}\right),
\end{aligned} \tag{6.43}$$

Substituting (6.43) in (6.42), the final expression in (6.44) can be obtained as

$$\begin{aligned}
\mathcal{O}_S \approx &\prod_{q=\{1,\ldots K\}} I\left(\frac{\delta_r \theta_{\Lambda_{5,q}}}{\theta_{\Lambda_{2,q}} + \delta_r \theta_{\Lambda_{5,q}}}; s_{\Lambda_{2,q}}, s_{\Lambda_{5,q}}\right) \\
+ &\prod_{q=\{1,\ldots \hat{K}\}} I\left(\frac{\delta_t \theta_{\Lambda_{10,q}}}{\theta_{\Lambda_{7,q}} + \delta_t \theta_{\Lambda_{10,q}}}; s_{\Lambda_{7,q}}, s_{\Lambda_{10,q}}\right) \\
- &\prod_{q=\{1,\ldots K\}} \prod_{q=\{1,\ldots \hat{K}\}} I\left(\frac{\delta_r \theta_{\Lambda_{5,q}}}{\theta_{\Lambda_{2,q}} + \delta_r \theta_{\Lambda_{5,q}}}; s_{\Lambda_{2,q}}, s_{\Lambda_{5,q}}\right) \\
\times &I\left(\frac{\delta_t \theta_{\Lambda_{10,q}}}{\theta_{\Lambda_{7,q}} + \delta_t \theta_{\Lambda_{10,q}}}; s_{\Lambda_{7,q}}, s_{\Lambda_{10,q}}\right)
\end{aligned} \tag{6.44}$$

6.2.5 Ergodic Rate of of U_{r^*}

The ER of U_{r^*} is defined as follows [176]

$$\begin{aligned}
R_{r^*} &= \mathbb{E}\left[\log_2(1+\psi_{r^*}^{r^*})\right] \\
&= \int_0^\infty \prod_{q=\{1,\ldots K\}} \frac{1 - F_{\psi_{rq}^{rq}}(z)}{(1+z)\ln 2} dz.
\end{aligned} \tag{6.45}$$

Substituting (6.29) in (6.45), we obtain

$$R_{r^*} = \int_0^\infty \prod_{q=\{1,\ldots K\}} \frac{1 - I\left(\frac{z\theta_{\Lambda_{5,q}}}{\theta_{\Lambda_{2,q}} + z\theta_{\Lambda_{5,q}}}; s_{\Lambda_{2,q}}, s_{\Lambda_{5,q}}\right)}{(1+z)\ln 2} dz. \tag{6.46}$$

As the assessment of above equation is mathematically intractable, to solve the integral, we utilize the basic the GCQ equation [104, 118] given as

$$\int_{\hat{a}}^{\hat{b}} f(z)\,dz = \frac{(\hat{b}-\hat{a})\pi}{2V} \sum_{v=1}^{V} \sqrt{1-{z_v}^2} f(y_v). \tag{6.47}$$

where $z_v = \cos\left(\frac{(2v-1)\pi}{2V}\right)$, $y_v = \frac{(\hat{b}-\hat{a})\,x_v}{2} + \frac{(\hat{b}-\hat{a})}{2}$, V is a finite value representing the trade-off between accuracy and complexity. Substituting $\hat{a}=0$ and $\hat{b}=\Delta_1$, where Δ_1 is assigned a large value approaching infinity for numerical assessment, the final expression can be obtained as

$$\begin{aligned} R_{r^*} &\approx \frac{\Delta_1\,\pi}{2V\ln 2} \sum_{v=1}^{V} \frac{\sqrt{1-{z_v}^2}}{(1+y_v)} \\ &\times \left(1 - \prod_{q=\{1,\ldots K\}} I\left(\frac{y_v\theta_{\Lambda_{5,q}}}{\theta_{\Lambda_{2,q}} + y_v\theta_{\Lambda_{5,q}}}; s_{\Lambda_{2,q}}, s_{\Lambda_{5,q}}\right)\right). \end{aligned} \tag{6.48}$$

6.2.6 Ergodic Rate of of U_{t^*}

The ER of U_{t^*} is defined as follows

$$\begin{aligned} R_{t^*} &= \mathbb{E}\left[\log_2(1+\psi_{a_2}^{t^*})\right] \\ &= \int_0^\infty \prod_{q=\{1,\ldots \hat{K}\}} \frac{1-F_{\psi_{a_2}^{t_q}}(z)}{(1+z)\,\ln 2} dz \\ &= \int_0^\infty \frac{1-\prod_{q=\{1,\ldots \hat{K}\}} I\left(\frac{z\theta_{\Lambda_{10,q}}}{\theta_{\Lambda_{7,q}}+z\theta_{\Lambda_{10,q}}}; s_{\Lambda_{7,q}}, s_{\Lambda_{10,q}}\right)}{(1+z)\,\ln 2} dz. \end{aligned} \tag{6.49}$$

Similar to Lemma-3, the integration in (6.49) is solved using the basic GCQ equation given in (6.47) as

$$R_{t^*} \approx \frac{\Delta_1 \pi}{2V \ln 2} \sum_{v=1}^{V} \frac{\sqrt{1 - {z_v}^2}}{(1 + y_v)} \times \left(1 - \prod_{q=\{1,\ldots \hat{K}\}} I\left(\frac{y_v \theta_{\Lambda_9}}{\theta_{\Lambda_{7,q}} + y_v \theta_{\Lambda_{10,q}}}; s_{\Lambda_{7,q}}, s_{\Lambda_{10,q}}\right)\right). \tag{6.50}$$

6.3 JPRTE Optimization

In this section, two different optimization problems are investigated namely, JPRTE-SOP and JPRTE-ESR, and thereby their proposed solutions are presented.

6.3.1 Problem Formulations

From the above SINR expressions in (6.5) and (6.6), it is evident that the effects of the STAR-RIS aided IUI need to be minimized so that both U_{r^*} and U_{t^*} can experience a lower OP and a higher rate. The same can be achieved by optimizing the user power allocation coefficients (α_{a_1}, α_t), transmission amplitude (ζ_t), reflection amplitude (ζ_r), and RIS element partitioning between N_r and N_t. In this context, we explore two different JPRTE problems namely JPRTE-SOP ($P1$) and JPRTE-ESR ($P2$) of minimizing SOP and maximizing the ESR (R_{sys}), respectively, by jointly allocating α_{a_1}, α_t, ζ_t, ζ_r, N_r and N_t, where $R_{sys} \triangleq R_{r^*} + R_{t^*}$ [120]. The JPRTE problems are mathematically formulated as under:

$$\begin{aligned}
(P1)\colon \; & \min_{\alpha_{a_1},\alpha_t,\zeta_r,\zeta_t,N_r,N_t} \mathcal{O}_S, \quad \text{subject to,} \\
& C1\colon \mathcal{O}_{r^*} < \mathcal{O}_{th_r}, \qquad\qquad C2\colon \mathcal{O}_{t^*} < \mathcal{O}_{th_t}, \\
& C3\colon\; 0 < \alpha_{a_1}, \alpha_t, \zeta_r, \zeta_t \leq 1, \quad C4\colon\; N_r + N_t = N, \\
& C5\colon\; N_r, N_t \in \{1, 2, ..., N\},
\end{aligned}$$

$$\begin{aligned}
(P2)\colon \; & \max_{\alpha_{a_1},\alpha_t,\zeta_r,\zeta_t,N_r,N_t} R_{sys}, \quad \text{subject to } C3 - C5, \\
& C6\colon R_{r^*} > R_{th_r}, \qquad\qquad C7\colon R_{t^*} > R_{th_t},
\end{aligned}$$

where $\mathcal{O}_{th_r}$ and $\mathcal{O}_{th_t}$ are threshold OPs for U_{r^*} and U_{t^*}, respectively. Constraints $C1$ and $C2$ are to ensure quality of service (QoS) for each user in terms of a maximum permissible OP [161, 177]. Likewise, $C6$ and $C7$ represent ER constraints for QoS. Further, R_{th_t} and R_{th_r} denote the minimum essential rates for U_{t^*} and U_{r^*}, correspondingly.

Now, $(P1)$ and $(P2)$ are optimization problems that contain α_{a_1}, α_t, ζ_r, and ζ_t as continuous optimization variables along with N_r and N_t as discrete variables. Thus, it is challenging to tackle the JPRTE problems in their current form. To address the same, we first introduce a new continuous optimization variable $\beta_r \triangleq \frac{Nr}{N}$. Therefore, after optimizing the variable β_r, the optimized value of N_r and N_t can then be given as $N_r^* = \beta_r^* N$ and $N_t^* = N - N_r^*$, respectively, and thereafter rounded to nearest integer values. Correspondingly, the original JPRTE-SOP and JPRTE-ESR problems are re-formulated as $(P3)$ and $(P4)$, respectively, and are expressed below:

$$(P3): \min_{\alpha_{a_1},\alpha_t,\zeta_r,\zeta_t,\beta_r} \mathcal{O}_S, \quad \text{subject to } C1 - C3,$$
$$C8: 0 < \beta_r < 1.$$

$$(P4): \max_{\alpha_{a_1},\alpha_t,\zeta_r,\zeta_t,\beta_r} R_{sys}, \quad \text{subject to } C3, C6 - C8.$$

6.3.2 PSO based JPRTE-SOP Solution

Due to the intricate combination of complex non-linear functions within the OP and SOP expressions presented in equations (6.30), (6.41) and (6.44), and also considering the strong interdependence of the optimization variables α_{a_1}, α_t, ζ_r, ζ_t, and β_r, deriving a closed-form mathematical solution for $(P3)$ becomes challenging. Therefore, to address the same and determine the solution, we undertake an effective and derivative-free algorithm like PSO which has been used to solve various such complicated problems in the wireless communication literature [116, 178]. Further, its simplicity, fast convergence, and efficiency in comparison to various other algorithms makes it a popular choice for many optimization tasks.

The PSO is a population-based algorithm inspired by the social behavior of bird flocking, where the movement of a group consisting of $\varkappa_1$ particles is simulated to find a common objective and locate the best position (representing solution to the optimization problem). At the q^{th} iteration of the algorithm, particle p adjusts its position and velocity in accordance with (6.51) and (6.52), respectively, after evaluating the quality of the solution using the fitting function (F_p^q) in (6.53), where $P_p^q = ((\alpha_{a_1})_p^q, (\alpha_t)_p^q, (\zeta_r)_p^q, (\zeta_t)_p^q, (\beta_r)_p^q)$ and $F_p^q \triangleq 1$ indicates that $\mathcal{O}_S$ is set to a value of one when at least one of the constraints remains unsatisfied. Parameter $\varkappa_2$ represents inertial weight, $\varkappa_3$ and $\varkappa_5$ are acceleration coefficients, and ${\varkappa_4}^{q-1}$ and ${\varkappa_6}^{q-1}$ represent random numbers $\sim Uni(0,1)$ at $(q-1)^{th}$ iteration. Moreover, μ_p denotes the personal best position of the of the p^{th} particle, characterized by its personal best fitness Ω_p, while $\mu^* = (\alpha_{a_1}^*, \alpha_t^*, \zeta_r^*, \zeta_t^*, \beta_r^*)$ represents the globally best location associated with the best fitness value Ω^*. The complete PSO algorithm, is executed for $\varkappa_7$ stall iterations and a maximum iteration limit of $\varkappa_8$.

$$V_p^q = \varkappa_2\, V_p^{q-1} + \varkappa_3\, {\varkappa_4}^{q-1}\, (\mu_t - L_p^{q-1}) + \varkappa_5\, {\varkappa_6}^{q-1}\, (\mu^* - L_p^{q-1}), \tag{6.51}$$

$$L_p^i = L_p^{q-1} + V_p^q, \tag{6.52}$$

$$F_p^q = \begin{cases} \mathcal{O}_S, & \text{if } C1 - C3 \text{ and } C8 \text{ get fulfilled} \\ 1, & \text{otherwise.} \end{cases} \tag{6.53}$$

6.3.3 ML-PSO based JPRTE-ESR Solution

The ER expressions derived are cumbersome. Thus, unlike ($\mathcal{P}3$), the PSO algorithm cannot be applied directly to solve ($\mathcal{P}4$) as it will require significant computational cost which can increase latency and thus not be usable for real-time operations. Hence, the ER expressions are first approximated using a predictive ML architecture which is more practical as the computational complexity is mostly shifted to offline training stage and the online implementation complexity is minimal [127].

As shown in Fig. 6.2, a fully connected feed-forward DNN model is considered with an input layer, H hidden layers, an output layer, and N_h is number of neurons in the h^{th} hidden layer. The input layer consists of 22 inputs namely $m_{a_1\hat{i}}$, $m_{\hat{i}r}$, $m_{t\hat{k}}$, $m_{\hat{k}r}$, m_{a_1r}, m_{tr}, σ_r^2, P_{max}, $\bar{g}_{a_1\hat{i}}$, $\bar{g}_{\hat{i}r}$, $\bar{g}_{t\hat{k}}$, $\bar{g}_{\hat{k}r}$, $\bar{g}_{a_1r}$, $\bar{g}_{tr}$, N, K, $\hat{K}$, α_{a_1}, α_t, β_r ,

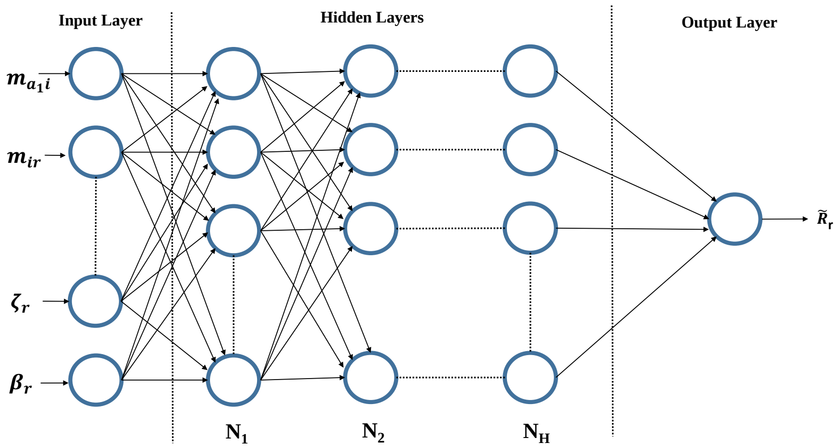

Figure 6.2: Proposed deep neural network framework for ML-PSO.

ζ_t, and ζ_r. Further, N_h is number of neurons in the h^{th} hidden layer. The output layer consists of a single neuron to predict the ER of U_{r^*}. Adam optimizer is used as the learning algorithm as it has a fast training time and can work efficiently with networks involving a lot of parameters. The learning rate, exponential decay rate and numerical stability constant are set as 0.001, 0.9 and 10^{-7}, respectively. For performance evaluation of this regression problem, MSE is chosen as the loss function defined as

$$\Omega_{MSE} = \mathbb{E}[(R_{r^*} - \tilde{R}_{r^*})^2], \tag{6.54}$$

Algorithm 4 ML Assisted ER Prediction

Inputs: $m_{a_1\hat{i}}$, $m_{\hat{i}r}$, $m_{t\hat{k}}$, $m_{\hat{k}r}$, m_{a_1r}, m_{tr}, σ_r^2, P_{max}, $\bar{g}_{a_1\hat{i}}$, $\bar{g}_{\hat{i}r}$, $\bar{g}_{t\hat{k}}$, $\bar{g}_{\hat{k}r}$, $\bar{g}_{a_1r}$, $\bar{g}_{tr}$, N, K, $\hat{K}$, α_{a_1}, α_t , ζ_t, ζ_r and β_r
Output: $\tilde{R}_r$

```
Data Set Generation
Evaluate (5.42) for each input matrix A_r and obtaining corresponding ER value
Divide the data set to 90% and 10% for training and testing respectively
while satisfactory training and test performance is not achieved do
    Train the neural network model using eLU activation function and Adam optimizer
    Test the trained model using the test data
end while
Save the trained weights and biases
Utilize (6.56), (6.57) and (6.58) for ER prediction
```

where $\tilde{R}_r$ is the predicted R_r value. Now, a dataset of 50,000 samples is created by evaluating (5.42) for different values of inputs and obtaining corresponding ER values such that 90% of the data is used for training the DNN model and the remaining 10% for testing. For threshold operation, linear activation function is used at the output layer and eLU is used as activation function at the hidden layers defined as

$$eLU(x) = \begin{cases} e^x - 1, & \text{if } x < 0 \\ x, & \text{if } x \geq 0, \end{cases} \tag{6.55}$$

The parameter values are found empirically to achieve lowest possible MSE. For the same, the best training and testing MSEs obtained are 5×10^{-4} and 7×10^{-4}, respectively, for $H = 2$ and $N_h = 500$. Now, with the optimized weights and biases, the predicted ER value for U_{r^*} can be obtained by using (6.56), (6.57) and (6.58) as

$$\boldsymbol{O}_{1,r} = eLU(\boldsymbol{A_r}\, \boldsymbol{W}_{1,r} + \boldsymbol{B}_{1,r}), \tag{6.56}$$

$$\boldsymbol{O}_{2,r} = eLU(\boldsymbol{O}_{1,r}\, \boldsymbol{W}_{2,r} + \boldsymbol{B}_{2,r}), \tag{6.57}$$

$$\tilde{R}_{r^*} = \boldsymbol{O}_{2,r}\, \boldsymbol{W}_{o,r} + B_{o,r}. \tag{6.58}$$

where $\boldsymbol{A_r}$ is input matrix of order (of order 1×22) such that
$\boldsymbol{A_r} \triangleq \{m_{a_1\hat{i}}\, m_{\hat{i}r}\, m_{t\hat{k}}\, m_{\hat{k}r}\, m_{a_1r}\, m_{tr}\, \sigma^2_{a_2}\, P_{max}\, \overline{g}_{a_1\hat{i}}\, \overline{g}_{\hat{i}r}\, \overline{g}_{t\hat{k}}\, \overline{g}_{\hat{k}r} \overline{g}_{a_1r}\, \overline{g}_{tr}\;\, N\, K\, \hat{K}\, \alpha_{a_1}\, \alpha_t\, \zeta_t \zeta_r\, \beta_r\}$. The term $\boldsymbol{W}_{1,r}$ (of order 22×500), $\boldsymbol{W}_{2,r}$ (of order 500×500), and $\boldsymbol{W}_{o,r}$ (of order 500×1) are optimized weights matrices corresponding to first hidden layer, second hidden layer and output layer, respectively. Similarly, $\boldsymbol{B}_{1,r}$ (of order 1×500), $\boldsymbol{B}_{2,r}$ (of order 1×500) and B_o (of order 1×1) are optimized bias matrices of first hidden layer, second hidden layer, and output layer, respectively. Term $\boldsymbol{O}_{1,r}$ and $\boldsymbol{O}_{2,r}$ are outputs corresponding to first and second hidden layer, respectively.

The predicted ER ($\tilde{R}_{t^*}$) for U_{t^*} can be similarly obtained by using (6.59), (6.60) and (6.61) as

$$\boldsymbol{O}_{1,t} = eLU(\boldsymbol{A_t}\, \boldsymbol{W}_{1,t} + \boldsymbol{B}_{1,t}), \tag{6.59}$$

$$\boldsymbol{O}_{2,t} = eLU(\boldsymbol{O}_{1,t}\,\boldsymbol{W}_{2,t} + \boldsymbol{B}_{2,t}), \tag{6.60}$$

$$\tilde{R}_{t^*} = \boldsymbol{O}_{2,t}\,\boldsymbol{W}_{o,t} + B_{o,t}. \tag{6.61}$$

where $\boldsymbol{A_t} \triangleq \{m_{t\hat{k}}\, m_{\hat{k}a_2}\, m_{a_1\hat{i}}\, m_{\hat{i}a_2}\, m_{ta_2}\, m_{a_1a_2}\, \sigma_t^2\, P_{max}\, \overline{g}_{t\hat{k}}\, \overline{g}_{\hat{k}a_2}\, \overline{g}_{a_1\hat{i}}\, \overline{g}_{\hat{i}a_2}\, \overline{g}_{ta_2}\, \overline{g}_{a_1a_2}\, N\, K\, \hat{K}$ $\alpha_t\, \alpha_{a_1}\, \zeta_r\, \zeta_t\, \beta_t\}$ and $\beta_t = 1 - \beta_r$.

The entire ML assisted ER prediction method is summarized in Algorithm 4. $(P4)$ is now re-formulated as,

$$(P5): \max_{\alpha_{a_1},\alpha_t,\zeta_r,\zeta_t,\beta_r} \tilde{R}_{sys}, \quad \text{subject to } C3, C8,$$
$$C9: \tilde{R}_{r^*} > R_{th_r}, \qquad\qquad C10: \tilde{R}_{t^*} > R_{th_t},$$

where $\tilde{R}_{sys} \triangleq \tilde{R}_{r^*} + \tilde{R}_{t^*}$. Finally, the PSO Algorithm 1 is now used to maximize $\tilde{R}_{sys}$ and hence solve $(P5)$ using the fitness function defined as

$$F_a^l = \begin{cases} \tilde{R}_{sys}, & \text{if constraints } \mathcal{C}3,\ \mathcal{C}8 \text{ - } \mathcal{C}10, \text{ are satisfied} \\ 0, & \text{if constraints are not satisfied.} \end{cases} \tag{6.62}$$

6.4 Results and Discussions

In this section, the performance of the VFD-STAR-RIS system is assessed using Monte-Carlo simulations, and various valuable insights are drawn. Unless mentioned otherwise, $N = 40$, $\alpha_a = 0.5$, $\alpha_{a_1} = 0.5$, $\alpha_t = 0.5$, $P_{max} = 1$ W, $\zeta_t = 0.5$, $\zeta_r = 0.5$, $\beta_r = 0.6$, $R_{th_r} = 3$ bits/sec/Hz, $R_{th_t} = 1$ bits/sec/Hz, and $\omega = 10^{-5}$ [118, 145, 175, 179]. Also, $K = 3$, $\hat{K} = 3$, $\Delta_1 = 10^4$, $L = 10^5$, $\varkappa_1 = 40$, $\varkappa_2 = 1$, $\varkappa_3 = \varkappa_5 = 1.49$, $\varkappa_7 = 20$ and $\varkappa_8 = 800$. Further, $m_{pq} \triangleq m = 2.5$ (where $p, q \in \{a, a_1, a_2, t, r\}$), $\overline{g}_{z_1} = -60$ dB, $\overline{g}_{z_2} = -30$ dB, where $z_1 \in \{ar, ta, tr, a_1r, ta_2, a_1a_2\}$ and $z_2 \in \{ai, ir, tk, ka, kr, a_1i, ka_2, ia_2\}$. The values of σ_a^2 and σ_t^2 are set to -50 dBm to simulate a more noise-prone scenario [144]. OP and ER performance are compared with the FD-STAR-RIS. The OP for U_{r^*} and U_{t^*} can be expressed as in (6.63) and (6.64), respectively. Similarly, the ER for U_{r^*} and U_{t^*} can be expressed

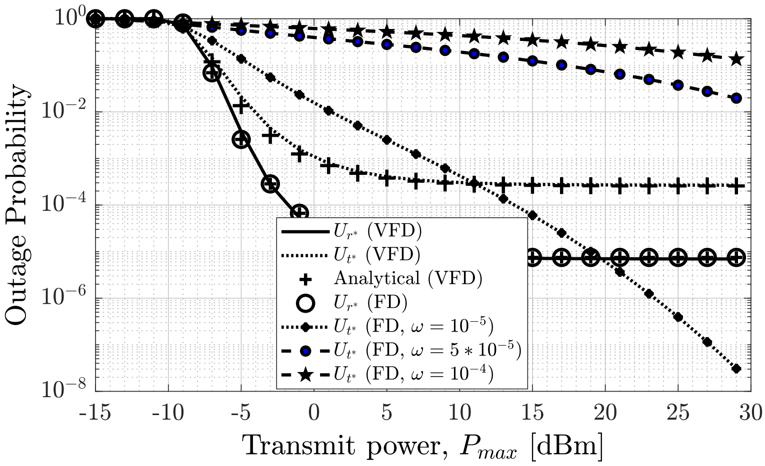

Figure 6.3: OP vs P_{max} for VFD-STAR-RIS and FD-STAR-RIS for different levels of RSI.

as in (6.65) and (6.66), respectively.

$$\hat{\mathcal{O}}_{r^*} = \Pr\left(\log_2\left(1 + \hat{\psi}_{r^*}^{r^*}\right) < R_{th_r}\right), \tag{6.63}$$

$$\hat{\mathcal{O}}_{t^*} = \Pr\left(\log_2\left(1 + \hat{\psi}_{a}^{t^*}\right) < R_{th_t}\right), \tag{6.64}$$

$$\hat{R}_{r^*} = \mathbb{E}\left[\log_2(1 + \hat{\psi}_{r^*}^{r^*})\right], \tag{6.65}$$

$$\hat{R}_{t^*} = \mathbb{E}\left[\log_2(1 + \hat{\psi}_{a}^{t^*})\right]. \tag{6.66}$$

6.4.1 Outage Probability

In Figure 6.3, we compare the OP results of the proposed VFD-STAR-RIS for both U_{r^*} and U_{t^*}. Clearly, U_{t^*} has lower OP in the VFD-STAR-RIS than the FD-STAR-RIS. Also, with increase in the value of ω, the OP gap between the two schemes is seen to further increase. The observations are reasonable as the effect of the IUI is significantly lower in comparison to the SI and RSI due to physical separation between A_1 and A_2 in the VFD and thus resulting in propagation loss, which lowers the interference. Notably, a lower OP for U_{t^*} is observed in FD-STAR-RIS only at a low RSI value of $\omega = 10^{-5}$ and a very high P_{max} value, which further proves

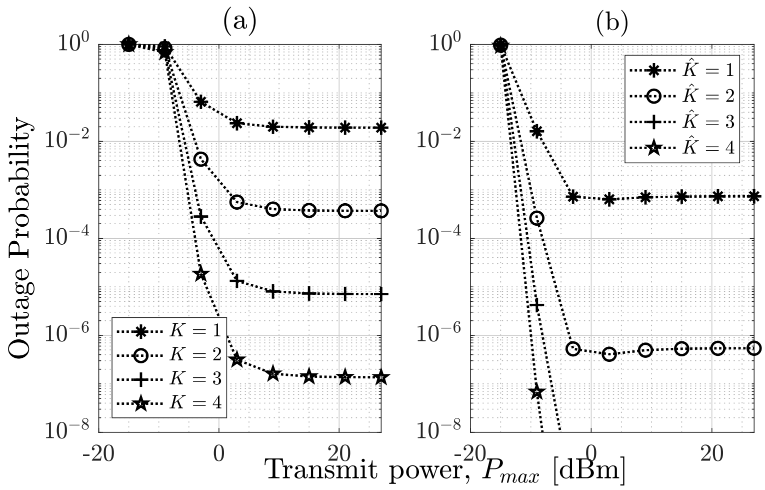

Figure 6.4: OP vs P_{max} for different number of (a) downlink users and (b) uplink users.

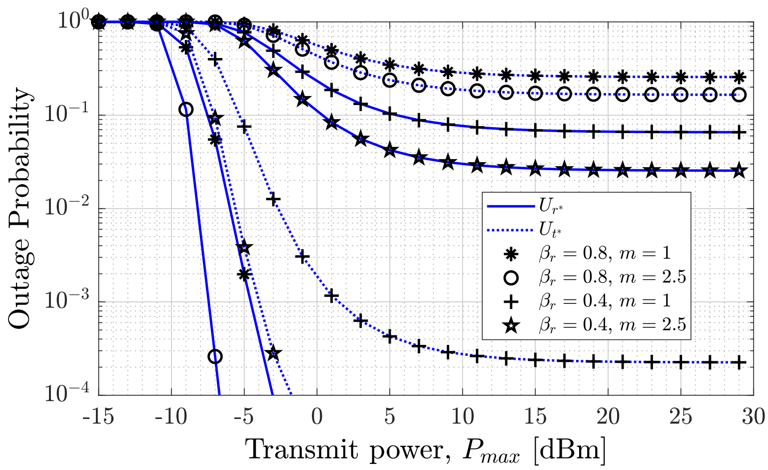

Figure 6.5: OP plot for users U_{r^*} and U_{t^*} for different values of fading severity and β_r.

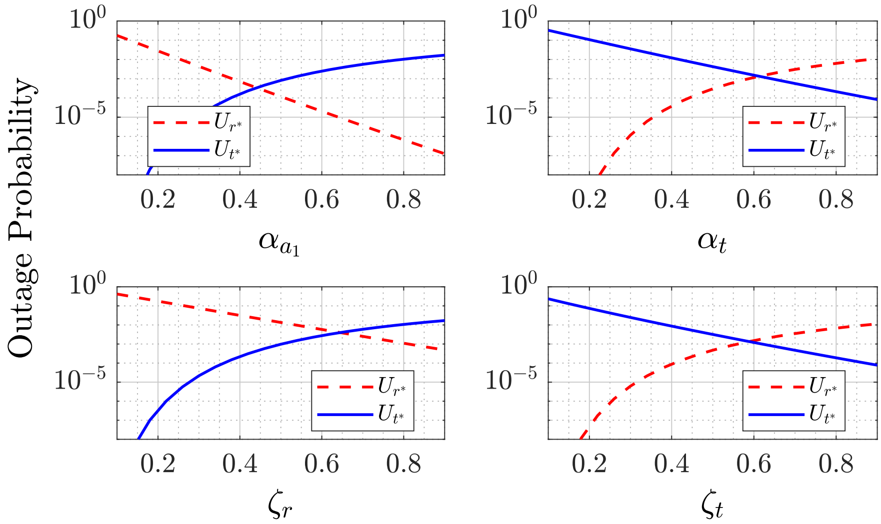

Figure 6.6: OP of the users for different values of α_{a_1}, α_t, ζ_r, and ζ_t.

the efficacy of the proposed VFD-STAR-RIS. Moreover, the performance of U_{r^*} in FD and VFD matches as both are affected by IUI. Further, U_{r^*} has better outage performance than U_{t^*} as $\beta_r = 0.6$ and thus a higher number of TR elements. Also, it can be observed that the analytical results for the presented OP closely agree with the results obtained from Monte-Carlo simulations. Further, in Figure 6.4, where OP results are plot for different number of downlink and uplink users, it can be observed that the outage performance is seen to improve with increase in the values of K and $\hat{K}$ as more number of users are available for selection.

Figure 6.5 plots the OP performance with P_{max} for the users for various values of β_r and m. For a m value of 1, as β_r increases from 0.4 to 0.8, the OP of U_{r^*} is seen to decrease by 99.37% and OP of U_{t^*} is seen to become 100 times. This is because with the increase in β_r, N_r increases and N_t decreases. The same causes increase and decrease in the values of ψ_r and $\psi_{a_2}^{t^*}$, respectively. Further, the performance of U_{t^*} and U_{r^*} is seen to improve with better fading conditions. For a OP of 10^{-3} and $\beta_r = 0.8$, as m increases from 1 to 2.5, U_{r^*} is seen to have SNR gain of approximately 4 dBm. Similarly, for P_{max} of 10 dBm and $\beta_r = 0.4$, the OP of the U_{r^*} is seen to approximately decrease by 20%.

Fig. 6.6 depicts the OP of U_{r^*} and U_{t^*} for various values of α_{a_1}, α_t, ζ_r, and ζ_t. It is evident that the OP of U_{r^*} and U_{t^*} are seen to decrease and increase, respectively, as α_{a_1} increases. A similar trend is observed for ζ_r. This is reasonable as increase

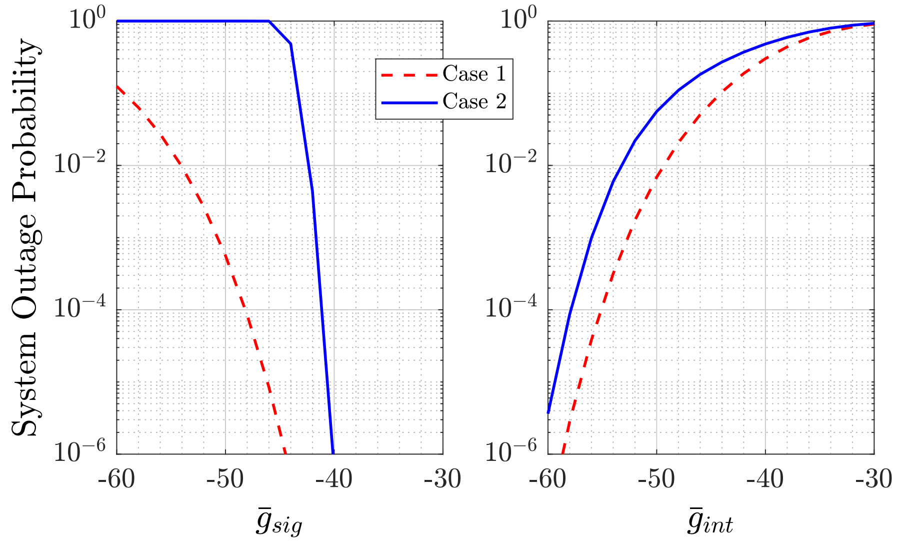

Figure 6.7: SOP of the VFD-STAR-RIS network for different values of desired signal link variance and interference link variance.

in the values of α_{a_1} (which increases the transmit power of A_1) and ζ_r improves the the SINR at U_{r^*}. However, the same also increases the SI and RSI at A_1, thereby reducing the SINR. On the contrary, OP of U_{r^*} and U_{t^*} are seen to increase and decrease, respectively, as α_t and ζ_t increase. This occurs because higher values of α_t and ζ_t enhance the SINR of U_{t^*} while simultaneously increasing the IUI at U_{r^*} from U_{t^*}.

Fig. 6.7 illustrates the SOP of the VFD-STAR-RIS network for different values of $\bar{g}_{sig}$ and $\bar{g}_{int}$, where $\bar{g}_{sig} \in \{\bar{g}_{a_1 r^*}, \bar{g}_{t^* a_2}, \bar{g}_{ir^*}, \bar{g}_{ka_2}\}$ (corresponding to desired signal links), $\bar{g}_{int} \in \{\bar{g}_{t^* r^*}, \bar{g}_{a_1 a_2}, \bar{g}_{kr^*}, \bar{g}_{ia_2}\}$ (corresponding to interference links). Cases 1 and 2 correspond to the value of $\sigma^2 = -110$ dBm and $\sigma^2 = -50$ dBm, respectively, where $\sigma^2 \triangleq \sigma_{a_2}^2 = \sigma_{r^*}^2$. It is evident that the SOP of the network is superior in a low-noise scenario in Case 1 compared to the higher noise scenario in Case 2. Furthermore, the SOP decreases with an increase in $\bar{g}_{sig}$, since increasing $\bar{g}_{sig}$ enhances the received signal strength, thereby improving the SINR at U_{r^*} and U_{t^*}. Similarly, an increase in $\bar{g}_{int}$ increases the impact of interference, leading to an increasing trend in SOP.

Figure 6.8 presents results of the JPRTE-SOP solution for two cases of $R_{thr} = R_{tht} \triangleq R_{th}$. We compare its performance with a baseline scheme where fixed values of power allocations, reflection amplitude, transmission amplitude and element partitioning (FPRTE) are used. We also compare with the conventional RIS based VFD-STAR-RIS where A_1 and A_2 serve U_{r^*} and U_{t^*}, respectively, via two different

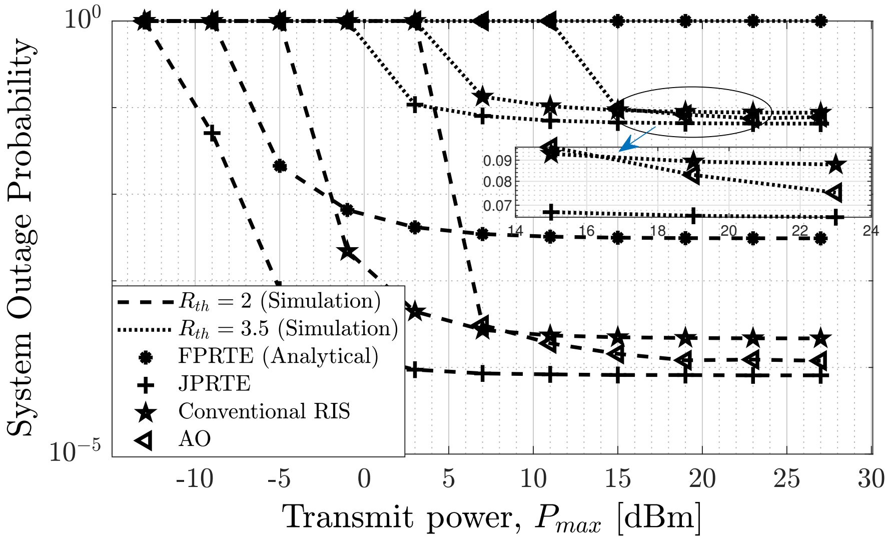

Figure 6.8: SOP performance comparison for JPRTE with FPRTE, Conventional RIS, and AO.

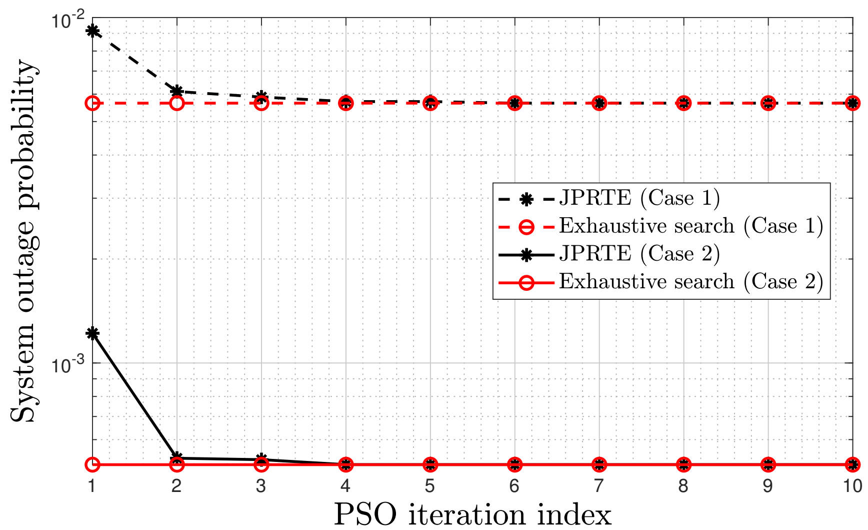

Figure 6.9: SOP vs PSO iteration index compared with exhaustive search.

reflecting only RIS. The same can also be seen as a special case of the STAR-RIS in which the number of RM and TM elements are fixed, and thus only the power allocations, reflection amplitude and transmission amplitude are jointly optimized [6, 7]. Additionally, the performance is also compared with another state-of-the-art method namely alternating optimization (AO) algorithm [180, 181]. In the AO method, the original problems are decoupled into sub-problems. Each of the sub-problem is solved via exhaustive search iteratively for the respective optimization variable while fixing the rest of the variables until convergence is obtained. For a P_{max} value of 10 dB, SOP in JPRTE is observed to be 92% and 96% times lower than FPRTE for $R_{th} = 1.5$ and $R_{th} = 2.5$, respectively. The observation is reasonable as the values of the optimization variables in FPRTE are uniform and are not updated in accordance with the changing system parameter values which further shows the requirement of the JPRTE scheme in order to minimize the IUI. Similarly, the JPRTE also has a superior SOP performance over the conventional RIS due to the number of elements being fixed in both the reflecting-only RIS. Also, the JPRTE exhibits better performance compared to the AO, showcasing the effectiveness of the PSO-based solution, which optimizes variables jointly, unlike AO, which divides the original problem into sub-problems. Further, it can be observed from the FPRTE curves that the SOP values obtained from the analytical expression in (6.44) matches closely with the simulation values.

In Fig. 6.9, we depict the SOP against the PSO iteration index. We consider two scenarios: Case 1, where $N = 60$ and $R_{th} = 3$, and Case 2, where $N = 40$ and $R_{th} = 2$, with $R_{th_r} = R_{th_t} \triangleq R_{th}$. It can be observed that the proposed solution for SOP converge to the global solution obtained through exhaustive search. Case 2 yields a lower SOP due to its lower target rate. Additionally, it is important to note that the computational burden of exhaustive search depends on the number of optimization variables and the size of the search space. Thus, with five optimization variables in ($P3$), and considering a step size of 0.001 in the search space, the exhaustive search method necessitates 1000^5 computations, rendering it impractical for implementation.

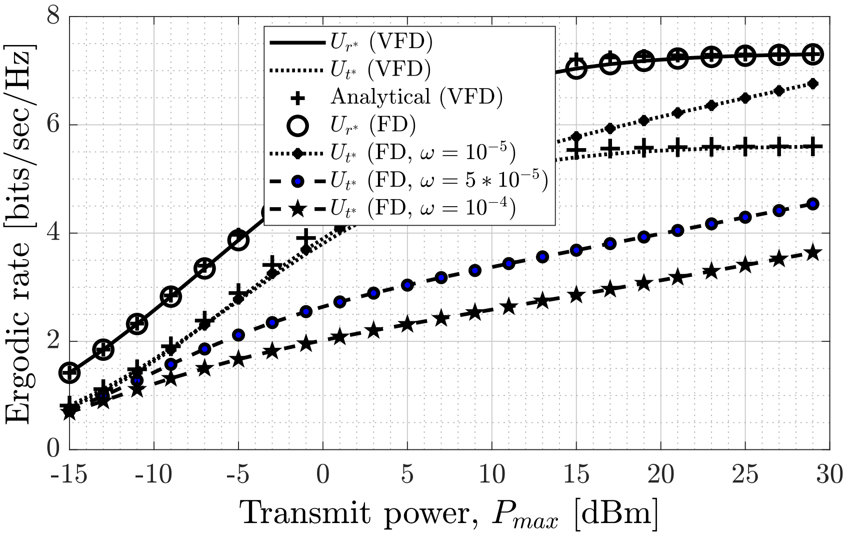

Figure 6.10: ER vs P_{max} for VFD-STAR-RIS and FD-STAR-RIS for different levels of RSI.

6.4.2 Ergodic Rate

In Figure 6.10, we compare the ER performance with P_{max} for both the downlink and uplink users. The derived analytical ER results are seen to match well with the Monte-Carlo simulations. Moreover, the proposed VFD-STAR-RIS can be observed to have a better ER performance than the FD-STAR-RIS for the uplink user. For a P_{max} of 10 dBm, U_{t^*} is observed to have 1.8 times higher ER for VFD-STAR-RIS in comparison to the FD-STAR-RIS with $\omega = 5 * 10^{-5}$. Similarly, for the same maximum transmit power value, U_{t^*} is observed to approximately have 90% higher ER for VFD-STAR-RIS in comparison to the FD-STAR-RIS with $\omega = 10^{-4}$. Further, similar to OP performance in Figure 6.3, U_{t^*} has better ER in FD-STAR-RIS only at a low RSI value of $\omega = 10^{-5}$ and a very high P_{max} value. Moreover, in Figure 6.11, where we plot ER results for different values of K and $\hat{K}$, it can be observed that the ER of users are seen to improve with increase in the number of downlink and uplink users.

Figure 6.12 plots the ER performance with P_{max} for the users for different values of β_r and m. The performance of both the users is seen to improve with increasing value of fading severity. For a P_{max} of 10 dBm and $\beta_r = 0.8$, as m increases from 1 to 2.5, the ER of the U_{t^*} and U_{r^*} is seen to approximately increase by 6% and 10%, respectively. Further, as β_r decreases from 0.8 to 0.4, the ER of U_{r^*} and U_{t^*} is

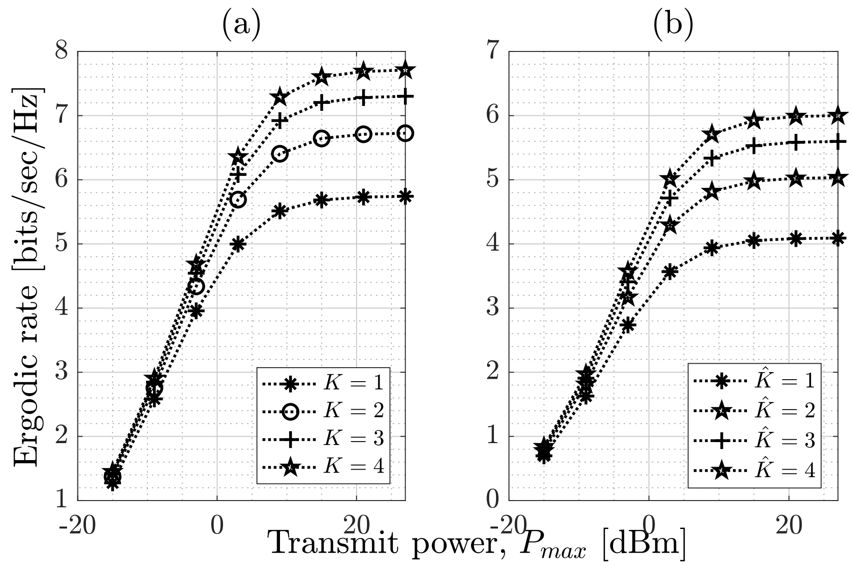

Figure 6.11: ER vs P_{max} for different number of (a) downlink users and (b) uplink users.

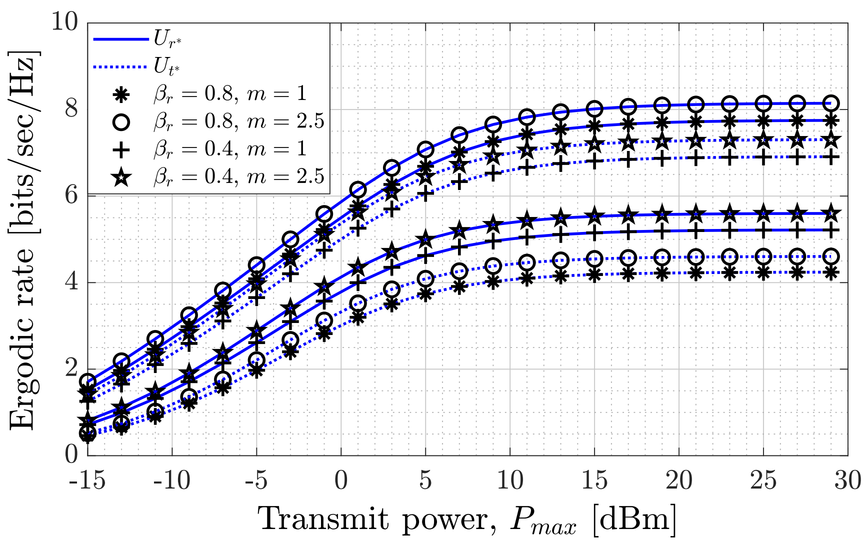

Figure 6.12: ER plot for users U_{r^*} and U_{t^*} for different values of fading severity and β_r.

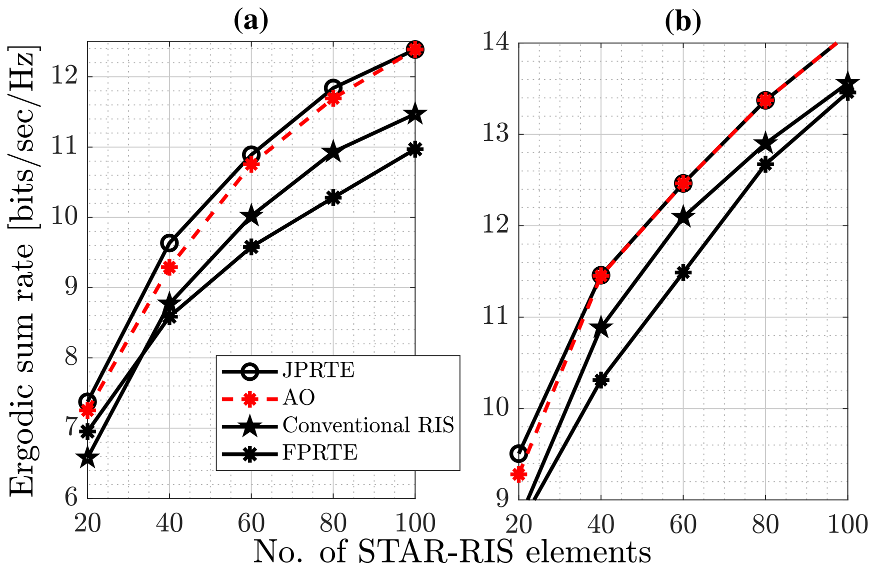

Figure 6.13: ESR performance comparison for JPRTE with FPRTE, Conventional RIS and AO for (a) $K = \hat{K} = 1$ and (a) $K = \hat{K} = 2$.

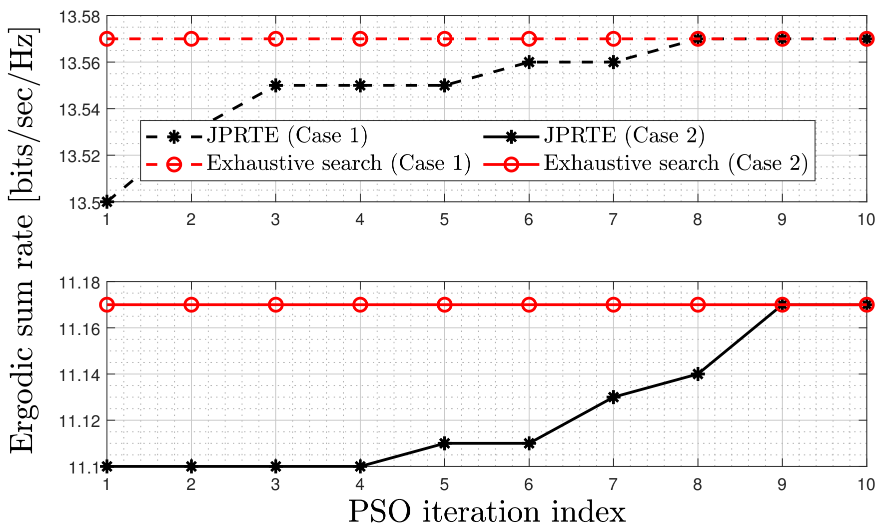

Figure 6.14: ESR vs PSO iteration index compared with exhaustive search.

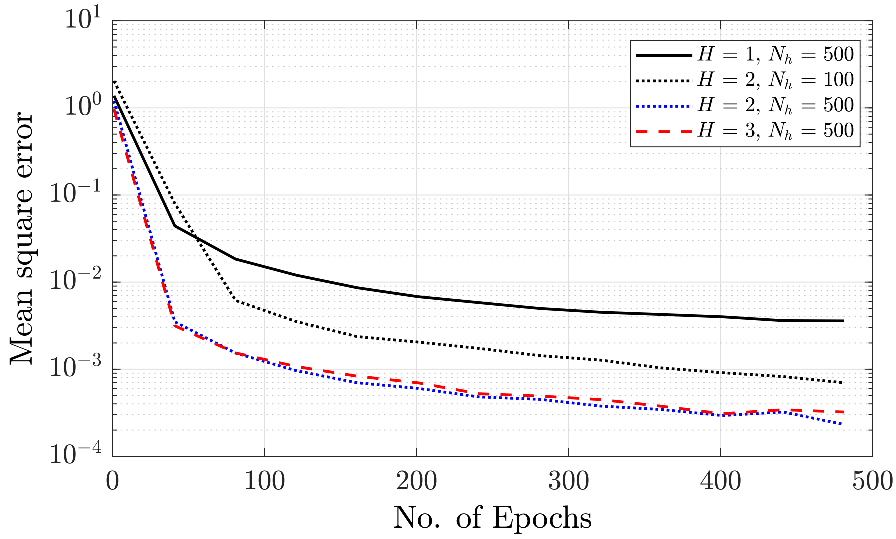

Figure 6.15: Effect of number of epochs on the MSE for different hidden layers.

Table 6.1: Average computation time for various schemes for ESR optimization

Optimization Scheme	**Computational time (in seconds)**
Proposed ML-PSO ($H = 1$, $N_h = 500$)	2.06
Proposed ML-PSO ($H = 2$, $N_h = 500$)	2.95
Alternating Optimization	3.31
Proposed ML-PSO ($H = 3$, $N_h = 500$)	5.53
Analytical-PSO ($\varkappa_1 = 50$, $\varkappa_8 = 10$)	179.45
Analytical-PSO ($\varkappa_1 = 50$, $\varkappa_8 = 20$)	344.92
Analytical-PSO ($\varkappa_1 = 100$, $\varkappa_8 = 10$)	357.15

seen to decrease and increase, respectively. Similar to Figure 6.5, the observations are reasonable as decrease in β_r causes decrease in the number of RM elements and increase in the number of TM elements.

In Figure 6.13, we depict the ESR performance over number of STAR-RIS elements of the JPRTE-ESR optimization in VFD-STAR-RIS. We compare its performance with the AO, the conventional-RIS and the FPRTE scheme. The proposed JPRTE-ESR solution is seen to outperform both the baseline schemes. Moreover, in Table 6.1, we compare the average computational times taken for different optimization schemes including analytical-PSO based solution for JPRTE-ESR where the PSO is applied directly to solve the problem ($P4$) using the analytical ER expressions. The computational times are obtained by using a computer with a 2.10 GHz Intel XEON E52620V4 X central processing unit and 64 GB RAM. It can be clearly seen that the proposed ML-PSO solution (with $H = 2$ and $N_h = 500$) takes a very low running time in comparison to the analytical-PSO solution. This is because of the complexity involved in the analytical expressions. Further, the analytical-PSO solution consumes more time with increase in the number of particles and maximum number of iterations. Further, in Fig. 6.14, we illustrate the ESR against the PSO iteration index for both Case 1 and Case 2. It can be observed that both proposed JPRTE-ESR converge to the global solution obtained through the exhaustive search. Case 2 yields a higher ESR due to greater number of STAR-RIS elements. Also, it is worth noting that although the ESR performance of AO becomes comparable to JPRTE for $K = \hat{K} = 2$, as shown in the table, this comes at a greater computational cost (3.31 seconds) compared to JPRTE (which takes 2.95 seconds), attributed to AO's higher number of iterations.

In Figure 6.15, we examine the impact of the number of training epochs on the attainable MSE for prediction the ERs by varying numbers of hidden layers and nodes within each layer. The analysis reveals a convergence in training performance to a very low value of MSE. After a training period of 400 epochs, the ML model with $H = 2$ and $N_h = 500$ showcases an MSE substantially lower by 90% and 95% in comparison to models with $H = 2$ ($N_h = 100$) and $H = 1$ ($N_h = 500$), respectively. The model also achieves an training MSE of 5×10^{-4} and test MSE of 7×10^{-4} which demonstrates a strong alignment between the predicted ER and the actual ER. Further, it can be observed that further increasing the number of hidden layers to 3 fails to bring about significant improvements in performance due to overfitting issues. Moreover, in Table 6.1, the computational time for the proposed ML-PSO is seen to increase with increase in the number of hidden layers and the neurons, thus indicating that the choice of $H = 2$ and $N_h = 500$ is sufficient and further increasing the values of H and N_h is not required.

6.5 Summary

In this chapter, a novel VFD-STAR-RIS system is proposed as an alternative to high RSI-affected FD-STAR-RIS by replacing the FD AP with two HD APs. We consider multi-user scenario with best downlink and uplink user selection, present OP and ER analysis for both U_{r^*} and U_{t^*}, and thereafter perform JPRTE optimization.

The proposed VFD model is seen to have superior performance over FD-STAR-RIS for the uplink user as IUI has a lower impact than the RSI due to propagation loss in the former. Further, apart from spectral utilization being same as the FD-STAR-RIS, these performance gains come with a minimal computational load as no SI mitigation process is involved, thus making it a practically viable solution. Further, the proposed solutions to JPRTE problems are observed to outperform the conventional-RIS and the FPRTE schemes where the optimization variables have fixed values. Also, the proposed solutions exhibit superior performance compared to AO, showcasing the effectiveness of the PSO-based solution, which optimizes variables jointly, unlike AO, which divides the original problem into sub-problems. Moreover, the solutions converge to the global solution obtained through exhaustive search. Also, interestingly, the ML-PSO based JPRTE-ESR solution is seen to have a very low computational time in comparison the analytical-PSO solution, and thus can be utilized in real-time scenarios. Moreover, we have analyzed the impact of system parameters like number of STAR-RIS elements, element partitioning, noise variances, variances of signal and interference links, fading severity and number of hidden layers on the performance of the system.

Chapter 7

Conclusions and Future Works

7.1 Conclusions

This thesis focuses on the study of novel VFD and underlay D2D-based systems. To enhance spectrum utilization and improve performance, these systems have been integrated with technologies like NOMA, RIS, and STAR-RIS. The analyzed system models are evaluated using performance measures such as OP, SOP, and ER, and SOP minimization and ESR maximization problems are studied to enhance overall performance. The main contributions and insights are summarized as follows:

Initially, the thesis explores cooperative VFD-NOMA in the presence of imperfect SIC and residual IRI. Analytical expressions are presented for OP and ER to analyze the performance of the VFD-NOMA system under imperfect SIC and residual IRI, considering generalized Nakagami-m fading. Comparative analysis against benchmark FD-NOMA and FD-OMA schemes emphasizes the impact of fading parameters and inter-relay distances. The analytical findings closely align with Monte Carlo simulation results. Despite imperfect SIC and residual IRI, both relay and destination users experience superior performance compared to FD-NOMA and FD-OMA schemes. Additionally, the findings underscore the importance of optimizing relay placements to further improve the outage performance of the VFD system.

Furthermore, a new FDD-VFD model has been developed to address the limitations of the SR-VFD model found in existing literature, which demands double the number of relays and an additional time phase compared to two counterpart FD schemes. This novel model efficiently utilizes both relay and time resources. Performance analysis and optimization have been conducted for A-IRI and P-IRI scenarios. Specifically, OP and ER analyses have been carried out considering Nakagami-m channel distributions, while optimizing the SOP and ESR through relay transmit power allocation. Simulation results demonstrate that the proposed FDD-VFD system exhibits significantly improved OP and ER performance compared to conventional FD and SR-VFD schemes. Additionally, due to its enhanced resource utilization, the proposed scheme is more practical for VFD implementations. Moreover, the solution based on JRPA for the optimization problems mitigates the impact of IRI, thereby outperforming fixed relay power allocations.

In Chapter 4, a new transmission protocol called ND-NC is introduced for a D2D underlayed cellular system, where both D2D and cellular networks utilize NOMA. Additionally, a DNN architecture is proposed to tackle the JPC problem. Simulation results indicate that the proposed spectrally efficient ND-NC protocol outperforms ND-OC and OD-OC models in terms of performance parameters like SOP and SER due to reduced interference and fewer time phases, respectively. Moreover, using the learning-based P-JPC solution achieves appreciable prediction of power allocations. Closed-form expressions considering Nakagami-m fading are derived and numerically validated, shedding light on SOP behavior under various system parameters.

Finally, chapters 5 and 6 delve into the investigation of RIS-FD-DDU and VFD-STAR-RIS systems, respectively, aimed at enhancing both system performance and spectrum utilization. These system models serve as applications for both FD cooperative systems and underlay D2D communication scenarios. In particular, for the RIS-FD-DDU system, performance analysis and optimization are conducted considering multiple uplink and downlink users, along with the effects of RSI, CCI, and HI. The derived analytical expressions for both OP and ER closely match the simulation results. Furthermore, the proposed OAC solution for optimization problems outperforms the comparative RAC scheme. The impact of crucial parameters, including the number of RIS elements, RSI levels, and HI, on user performance is examined. Simulation results demonstrate significantly enhanced user rates with the integration of RIS compared to the non-RIS scenario. Additionally, the performance of users is observed to improve with an increasing number of RIS elements.

Further, the new VFD-STAR-RIS system is introduced as an alternative to the high RSI-affected FD-STAR-RIS, where the FD AP is replaced with two HD APs. The multi-user scenario is considered with optimal selection of both downlink and uplink users. OP and ER analyses are presented for users, followed by JPRTE optimization. The proposed VFD model demonstrates superior performance over FD-STAR-RIS for the uplink user, as IUI has a lower impact compared to RSI due to propagation loss in the former. Moreover, in addition to maintaining the same spectral utilization as FD-STAR-RIS, these performance improvements come with minimal computational overhead since no SI mitigation process is required, rendering it practically feasible. Furthermore, the proposed solutions to JPRTE problems outperform conventional-RIS and FPRTE schemes, where optimization variables are fixed. Additionally, the proposed solutions exhibit superior performance compared to AO, highlighting the effectiveness of the PSO-based solution, which optimizes variables jointly, unlike AO, which divides the original problem into sub-problems. Moreover, these solutions converge to the global solution obtained through exhaustive search. Interestingly, the ML-PSO approach for JPRTE-ER solution demonstrates significantly lower computational time compared to the analytical PSO solution, making it suitable for real-time scenarios.

7.2 Future Works

- Investigating the performance of the FDD-VFD system incorporating NOMA in scenarios involving multiple destination users. Additionally, multiple relays scenarios can be considered, incorporating relay and user selections, and channel allocation.

- Analyzing the performance of the RIS-FD-DDU and VFD-STAR-RIS systems with discrete phase shifts and multiple antennas. Additionally, a VFD alternative solution can be proposed for the RIS-FD-DDU system in high RSI scenarios.

- Investigating underlay D2D and NOMA based system with multiple users with user selection and channel allocation strategies.

- Investigating the performance analysis and optimization of the VFD-STAR-

RIS system with energy splitting and time splitting protocols of the STAR-RIS.

- Optimizing the performance of the investigated systems in scenarios where full CSI knowledge is available. For this purpose, problems with objectives such as sum-rate maximization and power minimization can be explored.

References

[1] S.-N. Hong and G. Caire, "Virtual full-duplex relaying with half-duplex relays," *IEEE Trans. Inf. Theory*, vol. 61, no. 9, pp. 4700–4720, Jul. 2015.

[2] Y. Liu, Z. Qin, M. Elkashlan, Z. Ding, A. Nallanathan, and L. Hanzo, "Nonorthogonal Multiple Access for 5G and Beyond," *IEEE Proc.*, vol. 105, no. 12, pp. 2347–2381, Dec. 2017.

[3] S. Gong, X. Lu, D. Hoang, D. Niyato, L. Shu, D. Kim, and Y. Liang, "Towards smart radio environment for wireless communications via intelligent reflecting surfaces: A comprehensive survey," *IEEE Commun. Surveys Tuts.*

[4] J. Xu, Y. Liu, X. Mu, and O. A. Dobre, "STAR-RISs: Simultaneous transmitting and reflecting reconfigurable intelligent surfaces," *IEEE Commun. Lett.*, vol. 25, no. 9, pp. 3134–3138, Sep. 2021.

[5] Y. Liu, X. Mu, J. Xu, R. Schober, Y. Hao, H. V. Poor, and L. Hanzo, "STAR: Simultaneous transmission and reflection for 360° coverage by intelligent surfaces," *IEEE Wireless Commun.*, vol. 28, no. 6, pp. 102–109, Dec. 2021.

[6] P. P. Perera, V. G. Warnasooriya, D. Kudathanthirige, and H. A. Suraweera, "Sum rate maximization in STAR-RIS assisted full-duplex communication systems," in *IEEE Int. Conf. Commun. (ICC)*. IEEE, May 2022, pp. 1–6.

[7] A. Papazafeiropoulos, P. Kourtessis, and I. Krikidis, "STAR-RIS assisted full-duplex systems: Impact of correlation and maximization," *IEEE Commun. Lett.*, vol. 26, no. 12, pp. 3004–3008, Sep. 2022.

[8] C. D. Nwankwo, L. Zhang, A. Quddus, M. A. Imran, and R. Tafazolli, "A

survey of self-interference management techniques for single frequency full duplex systems," *IEEE Access*, vol. 6, pp. 30 242–30 268, 2018.

[9] Q. Wu, S. Zhang, B. Zheng, C. You, and R. Zhang, "Intelligent reflecting surface-aided wireless communications: A tutorial," *IEEE Trans. Commun.*, vol. 69, no. 5, pp. 3313–3351, May 2021.

[10] B. Zheng, C. You, W. Mei, and R. Zhang, "A survey on channel estimation and practical passive beamforming design for intelligent reflecting surface aided wireless communications," *IEEE Commun. Surv. Tutor.*, vol. 24, no. 2, pp. 1035–1071, 2nd Quart. 2022.

[11] D. Raychaudhuri and N. B. Mandayam, "Frontiers of wireless and mobile communications," *IEEE Proceed.*, vol. 100, no. 4, pp. 824–840, Feb. 2012.

[12] T. S. Rappaport, *Wireless Communications– Principles and Practice.* Horizon House Publications, Inc., 2002, vol. 45, no. 12.

[13] M. K. Simon and M.-S. Alouini, *Digital Communication over Fading Channels.* John Wiley & Sons, 2005, vol. 95.

[14] N. C. Beaulieu and C. Cheng, "Efficient Nakagami-m fading channel simulation," *IEEE Trans. Veh. Technol.*, vol. 54, no. 2, pp. 413–424, Apr. 2005.

[15] N. Nomikos, T. Charalambous, I. Krikidis, D. N. Skoutas, D. Vouyioukas, M. Johansson, and C. Skianis, "A survey on buffer-aided relay selection," *IEEE Commun. Surv. Tutor.*, vol. 18, no. 2, pp. 1073–1097, 2nd Quart. 2016.

[16] C. Hoymann, D. Astely, M. Stattin, G. Wikstrom, J.-F. Cheng, A. Hoglund, M. Frenne, R. Blasco, J. Huschke, and F. Gunnarsson, "LTE release 14 outlook," *IEEE Commun. Mag.*, vol. 54, no. 6, pp. 44–49, Jun. 2016.

[17] S. W. Peters and R. W. Heath Jr., "The future of wimax: Multihop relaying with ieee 802.16j," *IEEE Commun. Mag.*, vol. 47, no. 1, pp. 104–111, 2009.

[18] S. W. Peters, A. Y. Panah, K. T. Truong, and R. W. Heath, "Relay architectures for 3gpp lte-advanced," *EURASIP J. Adv. Signal*

Process, vol. 2009, no. 1, p. 618787, Jul 2009. [Online]. Available: https://doi.org/10.1155/2009/618787

[19] S. Parkvall, E. Dahlman, A. Furuskar, Y. Jading, M. Olsson, S. Wänstedt, and K. Zangi, "Lte-advanced - evolving lte towards imt-advanced," 09 2008, pp. 1–5.

[20] D. W. Bliss, P. A. Parker, and A. R. Margetts, "Simultaneous transmission and reception for improved wireless network performance," in *IEEE/SP 14th Workshop Statist. Signal Process., Washington, DC, USA*, 2007, pp. 478–482.

[21] M. Duarte and A. Sabharwal, "Full-duplex wireless communications using off-the-shelf radios: Feasibility and first results," in *Asilomar Conf. Signals Syst., Pacific Grove, CA, USA,*, 2010, pp. 1558–1562.

[22] D. Bharadia, E. McMilin, and S. Katti, "Full duplex radios," *ACM SIGCOMM Conf. Appl., Technol., Archit., Protocols Comput. Commun., Hong Kong*, vol. 43, no. 4, p. 375–386, Aug. 2013. [Online]. Available: https://doi.org/10.1145/2534169.2486033

[23] M. Duarte, C. Dick, and A. Sabharwal, "Experiment-driven characterization of full-duplex wireless systems," *IEEE Trans. Wireless Commun*, vol. 11, no. 12, pp. 4296–4307, 2012.

[24] T. Oechtering and A. Sezgin, "A new cooperative transmission scheme using the space-time delay code," in *ITG Workshop Smart Antennas*, 2004, pp. 41–48.

[25] S. S. C. Rezaei, S. O. Gharan, and A. K. Khandani, "Cooperative strategies for the half-duplex gaussian parallel relay channel: Simultaneous relaying versus successive relaying," in *Proc. 46th Allerton Conf. Commun., Control, Comput., Monticello, IL, USA,*, 2008, pp. 1309–1316.

[26] H. Bagheri, A. Motahari, and A. Khandani, "On the capacity of the diamond half-duplex relay channel," 05 2008, p. 649–653.

[27] H. Tullberg, P. Popovski, Z. Li, M. A. Uusitalo, A. Hoglund, O. Bulakci, M. Fallgren, and J. F. Monserrat, "The METIS 5G system concept: Meeting

the 5G requirements," *IEEE Communications magazine*, vol. 54, no. 12, pp. 132–139, 2016.

[28] I. F. Akyildiz, S. Nie, S.-C. Lin, and M. Chandrasekaran, "5G roadmap: 10 key enabling technologies," *Computer Networks*, vol. 106, pp. 17–48, 2016.

[29] Z. Li, M. Moisio, M. A. Uusitalo, P. Lunden, C. Wijting, F. S. Moya, A. Yaver, and V. Venkatasubramanian, "Overview on initial metis D2D concept," in *1st International Conference on 5G for Ubiquitous Connectivity.* IEEE, 2014, pp. 203–208.

[30] A. Asadi, Q. Wang, and V. Mancuso, "A survey on device-to-device communication in cellular networks," *IEEE Communications Surveys & Tutorials*, vol. 16, no. 4, pp. 1801–1819, 2014.

[31] X. Lin, J. G. Andrews, A. Ghosh, and R. Ratasuk, "An overview of 3GPP device-to-device proximity services," *IEEE Communications Magazine*, vol. 52, no. 4, pp. 40–48, 2014.

[32] M. N. Tehrani, M. Uysal, and H. Yanikomeroglu, "Device-to-device communication in 5G cellular networks: challenges, solutions, and future directions," *IEEE Communications Magazine*, vol. 52, no. 5, pp. 86–92, 2014.

[33] X. Wang, R. Li, C. Wang, X. Li, T. Taleb, and V. C. Leung, "Attention-weighted federated deep reinforcement learning for device-to-device assisted heterogeneous collaborative edge caching," *IEEE Journal on Selected Areas in Communications*, vol. 39, no. 1, pp. 154–169, 2020.

[34] S. Zhang, J. Liu, H. Guo, M. Qi, and N. Kato, "Envisioning device-to-device communications in 6G," *IEEE Network*, vol. 34, no. 3, pp. 86–91, 2020.

[35] P. Mach, Z. Becvar, and T. Vanek, "In-band device-to-device communication in OFDMA cellular networks: A survey and challenges," *IEEE Communications Surveys & Tutorials*, vol. 17, no. 4, pp. 1885–1922, 2015.

[36] W. Yu, H. Xu, J. Nguyen, E. Blasch, A. Hematian, and W. Gao, "Survey of public safety communications: User-side and network-side solutions and future directions," *Ieee Access*, vol. 6, pp. 70 397–70 425, 2018.

[37] J. Dai, G. Yue, S. Mao, and D. Liu, "Sidelink-aided multiquality tiled 360° virtual reality video multicast," *IEEE Internet of Things Journal*, vol. 9, no. 6, pp. 4584–4597, 2021.

[38] M. A. Hossain, A. R. Hossain, and N. Ansari, "AI in 6G: Energy-efficient distributed machine learning for multilayer heterogeneous networks," *IEEE Network*, vol. 36, no. 6, pp. 84–91, 2022.

[39] R. Fantacci and B. Picano, "A D2D-aided federated learning scheme with incentive mechanism in 6G networks," *IEEE Access*, vol. 11, pp. 107–117, 2022.

[40] A. Mozo, A. Karamchandani, S. Gómez-Canaval, M. Sanz, J. I. Moreno, and A. Pastor, "B5GEMINI: AI-driven network digital twin," *Sensors*, vol. 22, no. 11, p. 4106, 2022.

[41] C. Chakraborty and J. J. Rodrigues, "A comprehensive review on device-to-device communication paradigm: trends, challenges and applications," *Wireless Personal Communications*, vol. 114, no. 1, pp. 185–207, 2020.

[42] S.-Y. Lien, C.-C. Chien, F.-M. Tseng, and T.-C. Ho, "3GPP device-to-device communications for beyond 4G cellular networks," *IEEE Communications Magazine*, vol. 54, no. 3, pp. 29–35, 2016.

[43] K. S. Gilhousen, I. M. Jacobs, R. Padovani, A. J. Viterbi, L. A. Weaver, and C. E. Wheatley, "On the capacity of a cellular cdma system," *IEEE transactions on vehicular technology*, vol. 40, no. 2, pp. 303–312, 1991.

[44] J. Li, X. Wu, and R. Laroia, *OFDMA mobile broadband communications: A systems approach*. Cambridge University Press, 2013.

[45] E. Access, "Further advancements for E-UTRA physical layer aspects," *3GPP Technical Specification TR*, vol. 36, p. V2, 2010.

[46] Z. Ding, Y. Liu, J. Choi, Q. Sun, M. Elkashlan, I. Chih-Lin, and H. V. Poor, "Application of non-orthogonal multiple access in LTE and 5G networks," *IEEE Commun. Magazine*, vol. 55, no. 2, pp. 185–191, 2017.

[47] Y. Saito, A. Benjebbour, Y. Kishiyama, and T. Nakamura, "System-level performance evaluation of downlink non-orthogonal multiple access (NOMA)," in *2013 IEEE 24th annual international symposium on personal, indoor, and mobile radio communications (PIMRC)*, 2013, pp. 611–615.

[48] J. M. Meredith, "Study on downlink multiuser superposition transmission for LTE," in *TSG RAN Meeting*, vol. 67, 2015.

[49] R. Hoshyar, F. P. Wathan, and R. Tafazolli, "Novel low-density signature for synchronous CDMA systems over AWGN channel," *IEEE Trans. Signal Process.*, vol. 56, no. 4, pp. 1616–1626, 2008.

[50] Y. Du, B. Dong, Z. Chen, J. Fang, and X. Wang, "A fast convergence multiuser detection scheme for uplink SCMA systems," *IEEE Wireless Commun. Lett.*, vol. 5, no. 4, pp. 388–391, 2016.

[51] Z. Yuan, G. Yu, W. Li, Y. Yuan, X. Wang, and J. Xu, "Multi-user shared access for internet of things," in *2016 IEEE 83rd Veh. Technol. Conf. (VTC Spring)*. IEEE, 2016, pp. 1–5.

[52] X. Dai, S. Chen, S. Sun, S. Kang, Y. Wang, Z. Shen, and J. Xu, "Successive interference cancelation amenable multiple access (SAMA) for future wireless communications," in *2014 IEEE Int. Conf. Commun. systems*. IEEE, 2014, pp. 222–226.

[53] M. Vaezi, G. A. A. Baduge, Y. Liu, A. Arafa, F. Fang, and Z. Ding, "Interplay between NOMA and other emerging technologies: A survey," *IEEE Trans. Cognit. Commun. Netw.*, vol. 5, no. 4, pp. 900–919, 2019.

[54] Y. Saito, Y. Kishiyama, A. Benjebbour, T. Nakamura, A. Li, and K. Higuchi, "Non-orthogonal multiple access (NOMA) for cellular future radio access," in *2013 IEEE 77th Veh. Techno. Conf. (VTC Spring)*. IEEE, 2013, pp. 1–5.

[55] Z. Ding, P. Fan, and H. V. Poor, "Impact of user pairing on 5G nonorthogonal multiple-access downlink transmissions," *IEEE Trans. Veh. Technol.*, vol. 65, no. 8, pp. 6010–6023, 2015.

[56] T. Cover, “Broadcast channels,” *IEEE Trans. Inf. Theory*, vol. 18, no. 1, pp. 2–14, 1972.

[57] T. M. Cover, *Elements of information theory.* John Wiley & Sons, 1999.

[58] P. Bergmans, “Random coding theorem for broadcast channels with degraded components,” *IEEE Trans. Inf. Theory*, vol. 19, no. 2, pp. 197–207, 1973.

[59] A. Carleial, “Interference channels,” *IEEE Trans. Inf. Theory*, vol. 24, no. 1, pp. 60–70, 1978.

[60] T. Cover and A. E. Gamal, “Capacity theorems for the relay channel,” *IEEE Trans. Inf. Theory*, vol. 25, no. 5, pp. 572–584, 1979.

[61] A. J. Grant, B. Rimoldi, R. L. Urbanke, and P. A. Whiting, “Rate-splitting multiple access for discrete memoryless channels,” *IEEE Trans. Inf. Theory*, vol. 47, no. 3, pp. 873–890, 2001.

[62] I. Csiszár and J. Korner, “Broadcast channels with confidential messages,” *IEEE transactions on information theory*, vol. 24, no. 3, pp. 339–348, 1978.

[63] S. Vanka, S. Srinivasa, Z. Gong, P. Vizi, K. Stamatiou, and M. Haenggi, “Superposition coding strategies: Design and experimental evaluation,” *IEEE Trans. Wireless Commun.*, vol. 11, no. 7, pp. 2628–2639, 2012.

[64] P. Bergmans, “A simple converse for broadcast channels with additive white gaussian noise (corresp.),” *IEEE Trans. Inf. Theory*, vol. 20, no. 2, pp. 279–280, 1974.

[65] J. G. Andrews, “Interference cancellation for cellular systems: a contemporary overview,” *IEEE Wireless Commun.*, vol. 12, no. 2, pp. 19–29, 2005.

[66] P. Patel and J. Holtzman, “Analysis of a simple successive interference cancellation scheme in a ds/cdma system,” *IEEE J. Sel. Areas Commun.*, vol. 12, no. 5, pp. 796–807, 1994.

[67] P. W. Wolniansky, G. J. Foschini, G. D. Golden, and R. A. Valenzuela, “V-blast: An architecture for realizing very high data rates over the rich-scattering

wireless channel," in *International symposium on signals, systems, and electronics.* IEEE, 1998, pp. 295–300.

[68] E. Gelal, J. Ning, K. Pelechrinis, T.-S. Kim, I. Broustis, S. V. Krishnamurthy, and B. D. Rao, "Topology control for effective interference cancellation in multiuser mimo networks," *IEEE/ACM Trans. Netw.*, vol. 21, no. 2, pp. 455–468, 2012.

[69] C. Jiang, Y. Shi, Y. T. Hou, W. Lou, S. Kompella, and S. F. Midkiff, "Squeezing the most out of interference: An optimization framework for joint interference exploitation and avoidance," in *IEEE INFOCOM.* IEEE, 2012, pp. 424–432.

[70] C. Xu, L. Ping, P. Wang, S. Chan, and X. Lin, "Decentralized power control for random access with successive interference cancellation," *IEEE J. Sel. Areas Commun.*, vol. 31, no. 11, pp. 2387–2396, 2013.

[71] J. Lee, J. G. Andrews, and D. Hong, "Spectrum-sharing transmission capacity with interference cancellation," *IEEE Trans. Commun.*, vol. 61, no. 1, pp. 76–86, 2012.

[72] S. Gong, X. Lu, D. T. Hoang, D. Niyato, L. Shu, D. I. Kim, and Y.-C. Liang, "Toward smart wireless communications via intelligent reflecting surfaces: A contemporary survey," *IEEE Commun. Sur. Tutor.*, vol. 22, no. 4, pp. 2283–2314, 4th Quart. 2020.

[73] F. Liu and *et. al.*, "Programmable metasurfaces: State of the art and prospects," in *IEEE Inter. Symp. Circuits Syst. (ISCAS).* IEEE, May 2018, pp. 1–5.

[74] F. Ding, A. Pors, and S. I. Bozhevolnyi, "Gradient metasurfaces: a review of fundamentals and applications," *Rep. Progr. Phys.*, vol. 81, no. 2, p. 026401, Dec. 2017.

[75] S. Zhou, W. Xu, K. Wang, M. Di Renzo, and M.-S. Alouini, "Spectral and energy efficiency of IRS-assisted MISO communication with hardware impair-

ments," *IEEE Wireless Commun. Lett.*, vol. 9, no. 9, pp. 1366–1369, Sep. 2020.

[76] NTT DOCOMO, "Docomo Conducts World's First Successful Trial of Transparent Dynamic Metasurface." [Online]. Available: https://www.docomo.ne.jp/english/info/media_center/pr/2020/0117_00.html

[77] M. Mohammadi, X. Shi, B. K. Chalise, Z. Ding, H. A. Suraweera, C. Zhong, and J. S. Thompson, "Full-duplex non-orthogonal multiple access for next generation wireless systems," *IEEE Commun. Mag.*, vol. 57, no. 5, pp. 110–116, May 2019.

[78] I. Krikidis, H. A. Suraweera, P. J. Smith, and C. Yuen, "Full-duplex relay selection for amplify-and-forward cooperative networks," *IEEE Trans. Wireless Commun.*, vol. 11, no. 12, pp. 4381–4393, Oct. 2012.

[79] H. A. Suraweera, I. Krikidis, G. Zheng, C. Yuen, and P. J. Smith, "Low-complexity end-to-end performance optimization in mimo full-duplex relay systems," *IEEE Trans. Wireless Commun.*, vol. 13, no. 2, pp. 913–927, Feb. 2014.

[80] B. C. Nguyen, T. M. Hoang, and P. T. Tran, "Improving the performance of spatial modulation full-duplex relaying system with hardware impairment using transmit antenna selection," *IEEE Access*, vol. 8, pp. 20 191–20 202, Jan. 2020.

[81] C. Li, Z. Chen, Y. Wang, Y. Yao, and B. Xia, "Outage analysis of the full-duplex decode-and-forward two-way relay system," *IEEE Trans. Veh. Technol.*, vol. 66, no. 5, pp. 4073–4086, May 2017.

[82] V. Aswathi and A. Babu, "Full/half duplex cooperative NOMA under imperfect successive interference cancellation and channel state estimation errors," *IEEE Access*, vol. 7, pp. 179 961–179 984, Dec. 2019.

[83] H. Alves, T. Riihonen, and H. A. Suraweera, *Full-Duplex Communications for Future Wireless Networks.* Springer, 2020.

[84] Z. Zhang, K. Long, A. V. Vasilakos, and L. Hanzo, "Full-duplex wireless communications: Challenges, solutions, and future research directions," *IEEE Proc.*, vol. 104, no. 7, pp. 1369–1409, Jul. 2016.

[85] C. D. Nwankwo, L. Zhang, A. Quddus, M. A. Imran, and R. Tafazolli, "A survey of self-interference management techniques for single frequency full duplex systems," *IEEE Access*, vol. 6, pp. 30 242–30 268, Nov. 2017.

[86] Y. Kim, W. Choi, B. C. Jung, and A. Nosratinia, "A dynamic paradigm for spectrally efficient half-duplex multi-antenna relaying," *IEEE Trans. Wireless Commun.*, vol. 12, no. 9, pp. 4680–4691, Aug. 2013.

[87] Q. Li, M. Yu, A. Pandharipande, X. Ge, J. Zhang, and J. Zhang, "Performance of virtual full-duplex relaying on cooperative multi-path relay channels," *IEEE Trans. Wireless Commun.*, vol. 15, no. 5, pp. 3628–3642, May 2016.

[88] Y. Kim, K. Yamazaki, and B. C. Jung, "Virtual Full-Duplex Cooperative NOMA: Relay Selection and Interference Cancellation," *IEEE Trans. Wireless Commun.*, vol. 18, no. 12, pp. 5882–5893, Dec. 2019.

[89] Q. Y. Liau and C. Y. Leow, "Cooperative NOMA System With Virtual Full Duplex User Relaying," *IEEE Access*, vol. 7, pp. 2502–2511, Dec. 2018.

[90] L. Dai, B. Wang, Z. Ding, Z. Wang, S. Chen, and L. Hanzo, "A survey of non-orthogonal multiple access for 5G," *IEEE Commun. Surv. Tut.*, vol. 20, no. 3, pp. 2294–2323, May 2018.

[91] D. Wan, M. Wen, F. Ji, Y. Liu, and Y. Huang, "Cooperative noma systems with partial channel state information over nakagami-m fading channels," *IEEE Trans. Commun.*, vol. 66, no. 3, pp. 947–958, 2017.

[92] Y. Wang, Y. Xu, N. Li, W. Xie, K. Xu, and X. Xia, "Relay selection of full-duplex decode-and-forward relaying over Nakagami-m fading channels," *IET Commun.*, vol. 10, no. 2, pp. 170–179, Jan. 2016.

[93] S.-N. Hong and G. Caire, "Virtual full-duplex relaying with half-duplex relays," *IEEE Trans. Inf. Theory*, vol. 61, no. 9, pp. 4700–4720, Jul. 2015.

[94] I. S. Gradshteyn and I. M. Ryzhik, *Table of Integrals, Series, and Products.* 8th ed. New York, NY, USA: Academic Press, 2014.

[95] P. K. Singya, N. Kumar, V. Bhatia, and M.-S. Alouini, “On performance of hexagonal, cross, and rectangular QAM for multi-relay systems,” *IEEE Access*, vol. 7, pp. 60 602–60 616, May 2019.

[96] F. B. Hildebrand, *Introduction to Numerical Analysis.* Courier Corporation, 1987.

[97] P. Shaik, P. K. Singya, and V. Bhatia, “Performance analysis of QAM schemes for non-regenerative cooperative MIMO network with transmit antenna selection,” *AEU-Int. J. Electron. Commun.*, vol. 107, pp. 298–306, Jul. 2019.

[98] M. Oiwa and S. Sugiura, “Generalized virtual full-duplex relaying protocol based on buffer-aided half-duplex relay nodes,” in *IEEE Glob. Commun. Conf.*, 2017, pp. 1–6.

[99] A. K. Shukla, B. Manoj, and M. R. Bhatnagar, “Virtual full-duplex relaying in a buffer-aided multi-hop cooperative network,” in *Proc. Int. Conf. Signal Process. Commun. (SPCOM).* IEEE, 2020, pp. 1–5.

[100] A. Shehni and M. F. Flanagan, “Virtual full-duplex distributed spatial modulation: A new protocol for cooperative diversity,” *IEEE Access*, vol. 7, pp. 87 634–87 646, Jun. 2019.

[101] A. Ikhlef, J. Kim, and R. Schober, “Mimicking full-duplex relaying using half-duplex relays with buffers,” *IEEE Tran. Veh. Technol.*, vol. 61, no. 7, pp. 3025–3037, May 2012.

[102] S.-N. Hong, D. Hui, I. Marić, and G. Caire, “On the achievable rates of virtual full-duplex relay channel,” *IEEE Trans. Inf. Theory*, vol. 65, no. 1, pp. 354–367, Sep. 2019.

[103] Q. Y. Liau and C. Y. Leow, “Successive user relaying in cooperative NOMA system,” *IEEE Wireless Commun. Lett.*, vol. 8, no. 3, pp. 921–924, Feb. 2019.

[104] J. Jose, S. Parvez, and V. Bhatia, "VFD-NOMA Under Imperfect SIC and Residual Inter-Relay Interference Over Generalized Nakagami-m Fading Channels," *IEEE Commun. Lett.*, vol. 25, no. 2, pp. 646–650, Oct. 2020.

[105] D. H. Woo and H. Y. Hwang, "A virtual full-duplex relaying scheme and adjustment algorithms for enhancing spectral efficiency in UAV-aided communication networks," *IEEE Access*, vol. 11, pp. 12 698–12 709, Jan. 2023.

[106] S. Eom, H. Lee, J. Park, and I. Lee, "UAV-aided two-way mobile relaying systems," *IEEE Commun. Lett.*, vol. 24, no. 2, pp. 438–442, Nov. 2020.

[107] X. Jiang, Z. Wu, Z. Yin, Z. Yang, and N. Zhao, "Power consumption minimization of UAV relay in NOMA networks," *IEEE Wireless Commun. Lett.*, vol. 9, no. 5, pp. 666–670, Jan. 2020.

[108] A. Gouissem, L. Samara, R. Hamila, N. Al-Dhahir, and S. Foufou, "Relay selection in FDD amplify-and-forward cooperative networks," in *IEEE Annual Int. Symp. Pers., Indoor, and Mobile Radio Commun. (PIMRC).* IEEE, 2017, pp. 1–7.

[109] Y. Pan, C. Pan, Z. Yang, and M. Chen, "Resource allocation for D2D communications underlaying a NOMA-based cellular network," *IEEE Wireless Commun. Lett.*, vol. 7, no. 1, pp. 130–133, Oct. 2017.

[110] N. B. Khalifa, V. Angilella, M. Assaad, and M. Debbah, "Low-complexity channel allocation scheme for URLLC traffic," *IEEE Trans. Commun.*, vol. 69, no. 1, pp. 194–206, Jan. 2021.

[111] F. Liu and M. Petrova, "Performance of dynamic power and channel allocation for downlink mc-noma systems," *IEEE Trans. Wireless Commun.*, vol. 19, no. 3, pp. 1650–1662, 2019.

[112] D. Kumar, P. K. Singya, and V. Bhatia, "Performance analysis of hybrid two-way relay network with NLPA and hardware impairments," in *2021 IEEE Wireless Commun. Netw. Conf. (WCNC).* IEEE, May 2021, pp. 1–6.

[113] ——, "ASER analysis of hybrid receiver based SWIPT two-way relay network," *IEEE Trans. Veh. Technol.*, vol. 70, no. 10, pp. 10 018–10 030, Oct. 2021.

[114] P. Shaik, P. K. Singya, N. Kumar, K. K. Garg, and V. Bhatia, "On Impact of Imperfect CSI over SWIPT Device-to-Device (D2D) MIMO Relay Systems," in *Proc. Int. Conf. Signal Process. Commun. (SPCOM).* IEEE, Jul. 2020, pp. 1–5.

[115] S. Parvez, P. K. Singya, and V. Bhatia, "On ASER analysis of energy efficient modulation schemes for a device-to-device MIMO relay network," *IEEE Access*, vol. 8, pp. 2499–2512, Dec. 2019.

[116] S. Bisen, P. Shaik, and V. Bhatia, "On performance of energy harvested cooperative NOMA under imperfect CSI and imperfect SIC," *IEEE Trans. Veh. Technol.*, vol. 70, no. 9, pp. 8993–9005, Jul. 2021.

[117] V. Aswathi and A. V. Babu, "Outage and throughput analysis of full-duplex cooperative NOMA system with energy harvesting," *IEEE Trans. Veh. Technol.*, vol. 70, no. 11, pp. 11 648–11 664, 2021.

[118] D. Kumar, P. K. Singya, O. Krejcar, K. Choi, and V. Bhatia, "On performance of intelligent reflecting surface aided wireless powered iot network with HIs," *IEEE Commun. Lett.*, vol. 27, no. 2, pp. 502–506, Feb. 2023.

[119] J. Bae and Y. Han, "Joint power and time allocation for two-way cooperative noma," *IEEE Trans. Veh. Technol.*, vol. 68, no. 12, pp. 12 443–12 447, Dec. 2019.

[120] Z. Ding, Z. Yang, P. Fan, and H. V. Poor, "On the performance of non-orthogonal multiple access in 5G systems with randomly deployed users," *IEEE Signal Process. Lett.*, vol. 21, no. 12, pp. 1501–1505, Jul. 2014.

[121] M. F. Kader, M. B. Shahab, and S. Y. Shin, "Exploiting non-orthogonal multiple access in cooperative relay sharing," *IEEE Commun. Lett.*, vol. 21, no. 5, pp. 1159–1162, May 2017.

[122] J. Jose, A. Agarwal, V. Bhatia, and O. Krejcar, "Outage probability minimization based power control and channel allocation in underlay D2D-NOMA for IoT networks," *Trans. Emerg. Tel. Tech.*, vol. 33, no. 9, p. e4568, Sep. 2022.

[123] J. Jose, A. Agarwal, O. Krejcar, and V. Bhatia, "Power controlled outage-aware optimal protocol for NOMA-assisted underlay D2D networks," *AEU-Int. J. of Electron. and Commun.*, vol. 157, p. 154418, Dec. 2022.

[124] A. Agarwal and D. Mishra, "Altitude optimization for DF relaying trajectory of UAV in cooperative FANET," in *Proc. IEEE Global Commun. Conf. (GLOBECOM)*, Dec. 2020, pp. 1–6.

[125] Q. Sun, S. Han, I. Chin-Lin, and Z. Pan, "On the ergodic capacity of MIMO NOMA systems," *IEEE Wireless Commun. Lett.*, vol. 4, no. 4, pp. 405–408, Aug. 2015.

[126] M.-T. Nguyen, T.-H. Vu, and S. Kim, "Performance Analysis of Wireless Powered Cooperative NOMA-Based CDRT IoT Networks," *IEEE Syst. J.*, vol. 16, no. 4, pp. 6501–6512, Dec. 2022.

[127] C. Zhang, P. Patras, and H. Haddadi, "Deep learning in mobile and wireless networking: A survey," *IEEE Commun. Surveys Tuts.*, vol. 21, no. 3, pp. 2224–2287, 3rd Quart. 2019.

[128] C. K. Singh, P. K. Upadhyay, and J. Lehtomäki, "Performance analysis and deep learning assessment of full-duplex overlay cognitive radio noma networks under non-ideal system imperfections," *IEEE Trans. Cogn. Commun. Netw.*, Early Access, Feb. 2023.

[129] L. Yuan, Q. Du, and F. Fang, "Performance analysis of full-duplex cooperative NOMA short-packet communications," *IEEE Trans. Veh. Technol.*, vol. 71, no. 12, pp. 13 409–13 414, Dec. 2022.

[130] S. Khisa, M. Almekhlafi, M. Elhattab, and C. Assi, "Full duplex cooperative rate splitting multiple access for a MISO broadcast channel with two users," *IEEE Commun. Lett.*, vol. 26, no. 8, pp. 1913–1917, Aug. 2022.

[131] A. Mukherjee, P. Chakraborty, S. Prakriya, and A. K. Mal, "Performance of novel adaptive schemes for cognitive full-duplex relaying-based downlink cooperative noma," *IEEE Trans. Wireless Commun.*, vol. 22, no. 5, pp. 3161–3179, May 2022.

[132] J. Jose, P. Shaik, S. Bisen, and V. Bhatia, "On outage probability analysis of uplink cooperative VFD-NOMA over nakagami-m faded channels," in *Proc. IEEE Nat. Conf. Commun. (NCC).* IEEE, 2021, pp. 1–6.

[133] J. Jose, P. Shaik, and V. Bhatia, "Performance of Cooperative NOMA with Virtual Full-Duplex based DF Relaying in Nakagami-m Fading," in *Proc. 93rd Veh. Technol. Conf. (VTC).* IEEE, 2021, pp. 1–6.

[134] M. W. Baidas, M. S. Bahbahani, E. Alsusa, K. A. Hamdi, and Z. Ding, "Joint D2D group association and channel assignment in uplink multi-cell NOMA networks: A matching-theoretic approach," *IEEE Trans. Commun.*, vol. 67, no. 12, pp. 8771–8785, Sept. 2019.

[135] B. M. ElHalawany, R. Ruby, and K. Wu, "D2D communication for enabling Internet-of-Things: Outage probability analysis," *IEEE Trans. Veh. Technol.*, vol. 68, no. 3, pp. 2332–2345, Mar. 2019.

[136] R. Li, P. Hong, K. Xue, M. Zhang, and T. Yang, "Resource allocation for uplink NOMA-based D2D communication in energy harvesting scenario: A two-stage game approach," *IEEE Trans. Wireless Commun.*, vol. 21, no. 2, pp. 976–990, Feb. 2022.

[137] D.-W. Lim and J. Kang, "Outage-optimal and suboptimal power control for D2D communications in SWIPT cellular networks with local CSI," *IEEE Wireless Commun. Lett.*, vol. 9, no. 10, pp. 1795–1798, June. 2020.

[138] K. Agrawal, S. Parihar, P. Chakraborty, and S. Prakriya, "Performance of NOMA-enabled cooperative FD D2D communication in cellular underlay," *IEEE Trans. Cogn. Commun. Netw.*, vol. 8, no. 4, pp. 1730–1742, Dec. 2022.

[139] M. Le, Q.-V. Pham, H.-C. Kim, and W.-J. Hwang, "Enhanced resource allo-

cation in D2D communications with NOMA and unlicensed spectrum," *IEEE Syst. J.*, vol. 16, no. 2, pp. 2856–2866, Jun. 2022.

[140] F. Kara, H. Kaya, and H. Yanikomeroglu, "A lightweight machine learning assisted power optimization for minimum error in NOMA-CRS over Nakagami-m channels," *IEEE Trans. Veh. Technol.*, vol. 70, no. 10, pp. 11 067–11 072, Oct. 2021.

[141] G. Qian, Z. Li, C. He, X. Li, and X. Ding, "Power allocation schemes based on deep learning for distributed antenna systems," *IEEE Access*, vol. 8, pp. 31 245–31 253, Feb. 2020.

[142] Z. Ding, R. Schober, and H. V. Poor, "Unveiling the importance of SIC in NOMA systems—Part 1: State of the art and recent findings," *IEEE Commun. Lett.*, vol. 24, no. 11, pp. 2373–2377, Jul. 2020.

[143] T. Dozat, "Incorporating nesterov momentum into adam," in *Proc. ICLR Workshop*, 2016, pp. 1–4.

[144] S. Atapattu, R. Fan, P. Dharmawansa, G. Wang, J. Evans, and T. A. Tsiftsis, "Reconfigurable intelligent surface assisted two–way communications: Performance analysis and optimization," *IEEE Trans. Commun.*, vol. 68, no. 10, pp. 6552–6567, Jul. 2020.

[145] D. Kumar, P. K. Singya, O. Krejcar, K. Choi, and V. Bhatia, "Performance of IRS-aided FD two-way communication network with imperfect SIC," *IEEE Trans. Veh. Technol.*, pp. 1–6, Jan. 2023.

[146] T.-H. Vu and S. Kim, "Performance analysis of full-duplex two-way RIS-based systems with imperfect CSI and discrete phase-shift design," *IEEE Commun. Lett.*, vol. 27, no. 2, pp. 512–516, Feb. 2022.

[147] B. Lu, R. Wang, and Y. Liu, "Outage probability of intelligent reflecting surface assisted full duplex two-way communications," *IEEE Commun. Lett.*, vol. 26, no. 2, pp. 286–290, Feb. 2022.

[148] C. N. Efrem and I. Krikidis, "Joint IRS location and size optimization in multi-IRS aided two-way full-duplex communication systems," *IEEE Trans. Wireless Commun.*, vol. 22, no. 10, pp. 6518–6533, Oct. 2023.

[149] Z. Peng, Z. Zhang, C. Pan, L. Li, and A. L. Swindlehurst, "Multiuser full-duplex two-way communications via intelligent reflecting surface," *IEEE Trans. Signal Process.*, vol. 69, pp. 837–851, Jan. 2021.

[150] M. K. Simon and M.-S. Alouini, *Digital communication over fading channels*. New York: Wiley, 2001.

[151] M. Di Renzo, A. Zappone, M. Debbah, M.-S. Alouini, C. Yuen, J. de Rosny, and S. Tretyakov, "Smart radio environments empowered by reconfigurable intelligent surfaces: How it works, state of research, and the road ahead," *IEEE J. Sel. Areas Commun.*, vol. 38, no. 11, pp. 2450–2525, Jul. 2020.

[152] Y. Cai, M.-M. Zhao, K. Xu, and R. Zhang, "Intelligent reflecting surface aided full-duplex communication: Passive beamforming and deployment design," *IEEE Trans. Wireless Commun.*, vol. 21, no. 1, pp. 383–397, Jul. 2022.

[153] D. Xu, X. Yu, Y. Sun, D. W. K. Ng, and R. Schober, "Resource allocation for IRS-assisted full-duplex cognitive radio systems," *IEEE Trans. Commun.*, vol. 68, no. 12, pp. 7376–7394, Sep. 2020.

[154] T. H. Nguyen and T. T. Nguyen, "On performance of STAR-RIS-enabled multiple two-way full-duplex D2D communication systems," *IEEE Access*, vol. 10, pp. 89 063–89 071, Aug. 2022.

[155] F. Karim, S. K. Singh, K. Singh, and F. Khan, "STAR-RIS-aided full duplex communications with FBL transmission," in *IEEE Wireless Commun. Netw. Conf. (WCNC)*, 2023, pp. 1–6.

[156] J. Jose, P. Shaik, S. Bisen, and V. Bhatia, "Ergodic rate analysis and optimization of full-duplex STAR-RIS communication systems," in *Proc. Joint Eur. Conf. Netw. Commun. 6G Summit (EuCNC/6G Summit)*. IEEE, 2023, pp. 1–6.

[157] A. Chowdhury, R. Chopra, and C. R. Murthy, “Can dynamic TDD enabled half-duplex cell-free massive MIMO outperform full-duplex cellular massive MIMO?” *IEEE Trans. Commun.*, vol. 70, no. 7, pp. 4867–4883, Jul. 2022.

[158] M. Mohammadi, T. T. Vu, B. N. Beni, H. Q. Ngo, and M. Matthaiou, “Virtually full-duplex cell-free massive MIMO with access point mode assignment,” in *2022 IEEE 23rd International Workshop on Signal Processing Advances in Wireless Communication (SPAWC).* IEEE, 2022, pp. 1–5.

[159] Y. Zhang and S. Feng, “Performance analysis of the virtual full-duplex non-orthogonal multiple access systems,” in *Proc. IEEE Wireless Commun. Netw. Conf. (WCNC).* IEEE, May 2020, pp. 1–6.

[160] M. Mohammadi, H. A. Suraweera, and C. Tellambura, “Uplink/downlink rate analysis and impact of power allocation for full-duplex cloud-RANs,” *IEEE Trans. Wireless Commun.*, vol. 17, no. 9, pp. 5774–5788, 2018.

[161] R. Li, P. Hong, K. Xue, M. Zhang, and T. Yang, “Energy-efficient resource allocation for high-rate underlay D2D communications with statistical CSI: A one-to-many strategy,” *IEEE Trans. Veh. Technol.*, vol. 69, no. 4, pp. 4006–4018, Apr. 2020.

[162] Y. Yang, B. Zheng, S. Zhang, and R. Zhang, “Intelligent reflecting surface meets OFDM: Protocol design and rate maximization,” *IEEE Trans. Commun.*, vol. 68, no. 7, pp. 4522–4535, Mar. 2020.

[163] C. Zhou, B. Lyu, Y. Feng, and D. T. Hoang, “Transmit power minimization for STAR-RIS empowered symbiotic radio communications,” *IEEE Trans. Cogn. Commun. Netw.*, Early Access, Aug. 2023.

[164] B. Smida, A. Sabharwal, G. Fodor, G. C. Alexandropoulos, H. A. Suraweera, and C.-B. Chae, “Full-duplex wireless for 6G: Progress brings new opportunities and challenges,” *IEEE J. Sel. Areas Commun.*, Early Access, Jun. 2023.

[165] H. Liu, G. Li, X. Li, Y. Liu, G. Huang, and Z. Ding, “Effective capacity analysis of STAR-RIS-assisted NOMA networks,” *IEEE Wireless Commun. Lett.*, vol. 11, no. 9, pp. 1930–1934, Sep. 2022.

[166] T. Wang, M.-A. Badiu, G. Chen, and J. P. Coon, "Outage probability analysis of STAR-RIS assisted NOMA network with correlated channels," *IEEE Commun. Lett.*, vol. 26, no. 8, pp. 1774–1778, Aug 2022.

[167] M. Aldababsa, A. Khaleel, and E. Basar, "Simultaneous transmitting and reflecting intelligent surfaces-empowered NOMA networks," *arXiv preprint arXiv:2110.05311*, 2021.

[168] X. Yue, J. Xie, Y. Liu, Z. Han, R. Liu, and Z. Ding, "Simultaneously transmitting and reflecting reconfigurable intelligent surface assisted noma networks," *IEEE Trans. Wireless Commun.*, vol. 22, no. 1, pp. 189–204, Jan. 2023.

[169] F. Kilinc, R. A. Tasci, A. Celik, A. Abdallah, A. M. Eltawil, and E. Basar, "RIS-assisted grant-free NOMA: User pairing, RIS assignment, and phase shift alignment," *IEEE Trans. Cogn. Commun. Netw.*, Early Access, Jun. 2023.

[170] X. Gu, G. Zhang, B. Zhuo, W. Duan, J. Wang, M. Wen, and P.-H. Ho, "On the performance of cooperative noma downlink: A RIS-aided D2D perspective," *IEEE Trans. Cogn. Commun. Netw.*, Early Access, Aug. 2023.

[171] D. Selimis, K. P. Peppas, G. C. Alexandropoulos, and F. I. Lazarakis, "On the performance analysis of ris-empowered communications over nakagami-m fading," *IEEE Commun. Lett.*, vol. 25, no. 7, pp. 2191–2195, Jul. 2021.

[172] T. Van Chien, L. T. Tu, S. Chatzinotas, and B. Ottersten, "Coverage probability and ergodic capacity of intelligent reflecting surface-enhanced communication systems," *IEEE Commun. Lett.*, vol. 25, no. 1, pp. 69–73, Jan. 2020.

[173] S. Atapattu, P. Dharmawansa, M. Di Renzo, C. Tellambura, and J. S. Evans, "Multi-user relay selection for full-duplex radio," *IEEE Trans. Commun.*, vol. 67, no. 2, pp. 955–972, Oct. 2019.

[174] Z. Ding, R. Schober, and H. V. Poor, "On the impact of phase shifting designs on IRS-NOMA," *IEEE Wireless Commun. Lett.*, vol. 9, no. 10, pp. 1596–1600, Apr. 2020.

[175] B. Tahir, S. Schwarz, and M. Rupp, "Analysis of uplink IRS-assisted NOMA under Nakagami-m fading via moments matching," *IEEE Wireless Commun. Lett.*, vol. 10, no. 3, pp. 624–628, Dec. 2021.

[176] H. A. Suraweera, P. J. Smith, and M. Shafi, "Capacity limits and performance analysis of cognitive radio with imperfect channel knowledge," *IEEE Trans. Veh. Technol.*, vol. 59, no. 4, pp. 1811–1822, May 2010.

[177] P. Sun, K. G. Shin, H. Zhang, and L. He, "Transmit power control for D2D-underlaid cellular networks based on statistical features," *IEEE Trans. Veh. Technol.*, vol. 66, no. 5, pp. 4110–4119, May 2017.

[178] Z. Abdullah, S. Kisseleff, K. Ntontin, W. A. Martins, S. Chatzinotas, and B. Ottersten, "Successive decode-and-forward relaying with reconfigurable intelligent surfaces," in *IEEE Int. Conf. Commun. (ICC)*. IEEE, May 2022, pp. 1–6.

[179] Z. Chu, P. Xiao, D. Mi, W. Hao, Z. Lin, Q. Chen, and R. Tafazolli, "Wireless powered intelligent radio environment with non-linear energy harvesting," *IEEE Inter. Things J.*, vol. 9, no. 18, pp. 18 130–18 141, Sep. 2022.

[180] S. Kurma, M. Katwe, K. Singh, T. Q. Duong, and C.-P. Li, "Spectral-energy efficient resource allocation in RIS-aided FD-MIMO systems," *IEEE Trans. Wireless Commun.*, 2023.

[181] R. Allu, O. Taghizadeh, S. K. Singh, K. Singh, and C.-P. Li, "Robust beamformer design in active RIS-assisted multiuser MIMO cognitive radio networks," *IEEE Trans. Cogn. Commun. Netw.*, vol. 9, no. 2, pp. 398–413, Apr. 2023.

List of Publications

Journal Papers:

1. **J. Jose**, P. Shaik, and V. Bhatia, "VFD-NOMA Under imperfect SIC and residual inter-relay interference over generalized Nakagami-m fading channels" *in IEEE Commun. Lett.*, vol. 25, no. 2, pp. 646–650. IEEE, Oct. 2020.

2. **J. Jose**, A. Agarwal, V. Bhatia, and O. Krejcar, "Outage probability minimization based power control and channel allocation in underlay D2D-NOMA for IoT networks" *in Trans. Emerg. Tel. Tech.*, vol. 33, no. 9, pp. e4568. Wiley Online Library, Sep. 2022.

3. **J. Jose**, A. Agarwal, O. Krejcar, and V. Bhatia., "Power controlled outage-aware optimal protocol for NOMA-assisted underlay D2D networks" *in AEU-Int. J. of Electron. and Commun.*, vol. 157, pp. 154418. Elsevier, Dec. 2022.

4. **J. Jose**, A. Agarwal, P. Shaik, V. Goyal, K. Choi, and V. Bhatia, "Performance analysis and learning-assisted power control for NOMA enabled D2D-cellular network" *in IEEE Syst. J*, Nov. 2023., vol. 18, no. 1, pp. 646–650, Mar. 2024.

5. **J. Jose**, P. Shaik, S. Bisen, A. Srivastava, V. Bhatia, and K. Choi, "Performance analysis and optimization of frequency division duplex based virtual full-duplex communication systems" *in Ad Hoc Networks*, vol. 154, pp. 103379. Elsevier, Dec. 2023.

6. **J. Jose**, S. Bisen, P. Shaik, S. Biswas, K. Singh, and V. Bhatia, "Performance analysis of IRS assisted full-duplex systems with different downlink and uplink users" *in IEEE Trans. Veh. Technol.* (Early Access)

7. **J. Jose**, P. Shaik, S. Bisen, O. Krejcar, K. Choi, and V. Bhatia, "Virtual full-duplex communication enabled STAR-RIS: Performance analysis and machine

learning-assisted optimization" *in IEEE Trans. Cog. Commun. Network.* (Minor Revision)

8. S. Bisen, **J. Jose**, V. Bhatia, A. Mishra, and K. Choi, "Hybrid backscatter NOMA under imperfect CSI and hardware impairments" *in IEEE Commun. Lett.*, vol. 27, no. 11, pp. 3078 – 3082, 2023.

9. S. Bisen, P. Shaik, **J. Jose**, J. Nebhen, O. Krejcar, and V. Bhatia, "ASER analysis of generalized hexagonal QAM schemes for NOMA systems over Nakagami-m fading channels" *in Int J Commun Syst.*, vol. 36, no. 6, pp. e5440. Wiley Online Library, Jan. 2023.

10. S. Bisen, **J. Jose**, Z. Ding, K. Choi, and V. Bhatia, "On performance of backscatter-NOMA systems: Symbiotic communication for IoT devices" *in IEEE Trans. Veh. Technol.* (Early Access)

Conference Papers:

1. **J. Jose**, P. Shaik, and V. Bhatia, "Performance of cooperative NOMA with virtual full-duplex based DF relaying in Nakagami-m fading" *In Proc. 93rd Veh. Technol. Conf. (VTC)* pp. 1–6. IEEE, 2021.

2. **J. Jose**, P. Shaik, S. Bisen, and V. Bhatia, "On outage probability analysis of uplink cooperative VFD-NOMA over nakagami-m faded channel" *in In Proc. Nat. Conf. Commun. (NCC)* pp. 1–6. IEEE, 2021.

3. **J. Jose**, P. Shaik, , S. Bisen, V. Goyal, and V. Bhatia, "Frequency division duplex based cooperative VFD: Outage analysis and relay power allocation" *In 15th Int. Conf. Commun. Sys. Net. (COMSNETS)* pp. 1–7. IEEE, 2023. (**Best paper award**)

4. **J. Jose**, P. Shaik, S. Bisen, and V. Bhatia, "Ergodic rate analysis and optimization of full-duplex STAR-RIS communication system" *In 2023 Joint European Conf. on Net. and Commun. & 6G Summit (EuCNC/6G Summit)* pp. 1–6. IEEE, 2023.

5. S. Mishra, S. Panda, **J. Jose**, V. Bhatia, and S. Pandey, "On improving radial basis function neural networks for regression" *In 2023 Conf. on Inf. and Commun. Tech. (CICT)* pp. 1–6. IEEE, 2023. (**Best paper award**)

6. A. Srivastava, S. Panda, **J. Jose**, Karapureddy Jaswanth Reddy, Sree Teja Nadella, V. Bhatia and S. Pandey, "A comparative study on effect of activation function placement in neural network architecture for regression problems" *In 2023 Conf. on Inf. and Commun. Tech. (CICT)* pp. 1–6. IEEE, 2023.